Dissertation

submitted to the

Combined Faculty of Mathematics, Engineering and Natural Sciences

of Heidelberg University, Germany

for the degree of

Doctor of Natural Sciences

Put forward by

Iván Domingo Muñoz Molina, M.Sc.

born in: Mexico City, Mexico

Oral examination: July 10, 2024

Printed and/or published with the support of the
German Academic Exchange Service.

Assessment of linear energy transfer and relative biological effectiveness in proton-beam therapy and ion-beam therapy with Al_2O_3:C,Mg detectors

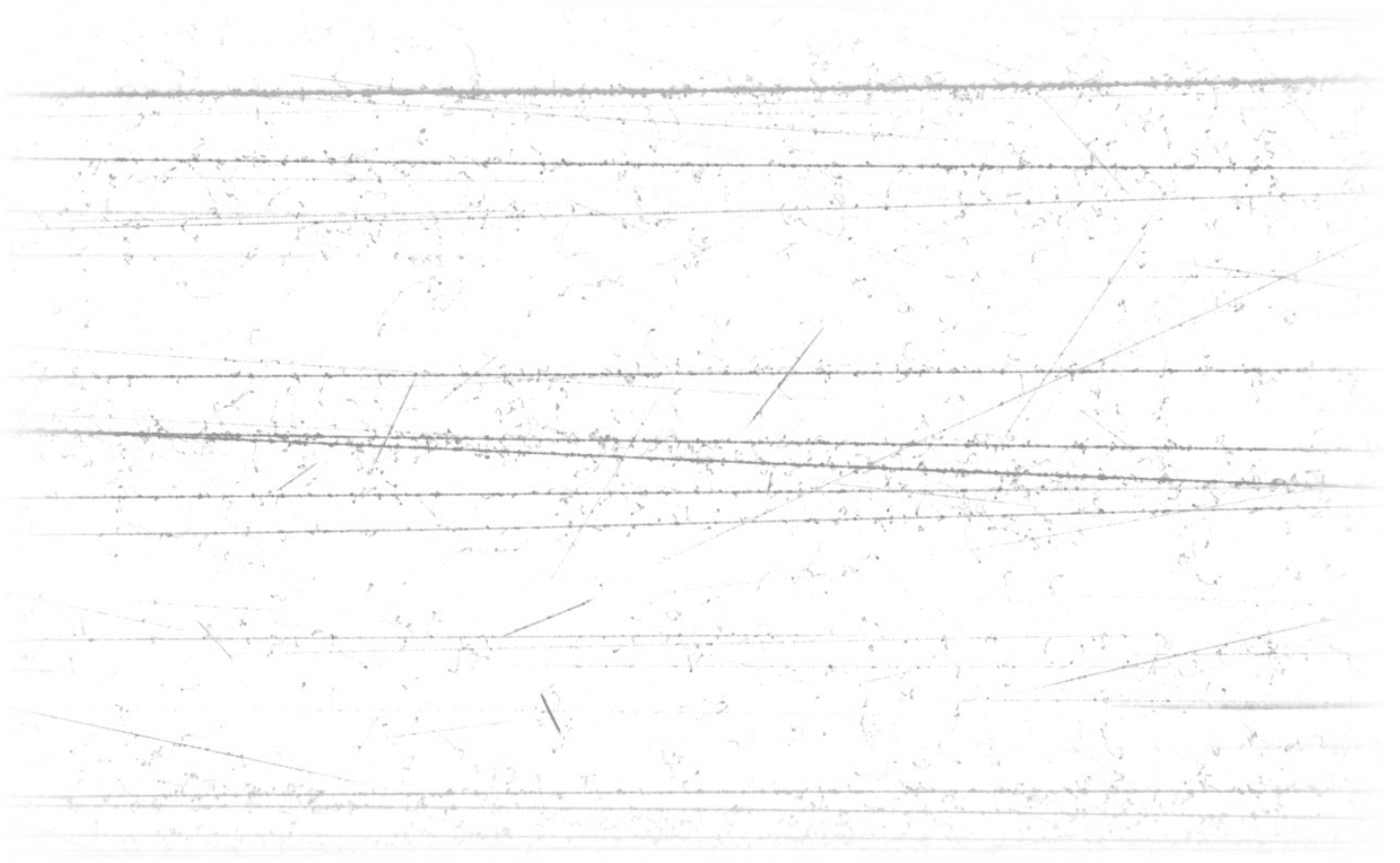

Referees: **Prof. Dr. Oliver Jäkel**
German Cancer Research Center, Heidelberg

Prof. Dr. Mark E. Ladd
German Cancer Research Center, Heidelberg

Conducted at:
the German Cancer Research Center
(DKFZ; Heidelberg, Germany)
Under supervision of:
Prof. Dr. Oliver Jäkel,
head of the Division of Medical Physics in Radiation Oncology
As a member of:
the Helmholtz International Graduate School of Cancer Research
While enrolled at:
the Department of Physics and Astronomy
of the University of Heidelberg
As a member of:
the Heidelberg Graduate School for Physics

In collaboration with:
Dr. Jeppe Brage Christensen
Paul Scherrer Institute
(PSI; Villigen, Switzerland)

The author received full financial support from:
the German Academic Exchange Service (DAAD)
Through the program:
Research Grants – Doctoral Programmes in Germany
Program number:
57440921

Enclosed publications reprinted with permission of:
Wiley Publishing LLC
IOP Publishing
Elsevier
Under the terms and conditions of:
Creative Commons (CC) licensing

Typesetting:
LaTeX by the author
Figures design:
by the author and, when required, with acknowledgement and references to original data sources.
Printing and binding:
in Heidelberg, Germany

Title page image:
Light-ion tracks obtained from a fluorescent nuclear track detector exposed to ^{12}C-ions and imaged with laser scanning confocal microscopy.
Design by:
the author

In memory of my father:
Ulises A. Muñoz Gallegos

“Science is built up of facts, as a house is built of stones;
but an accumulation of facts is no more a science than
a heap of stones is a house.”

– Jules Henri Poincaré –

Abstract

In proton-beam therapy (PBT) and ion-beam therapy (IBT), treatment fields exhibit non-homogeneous linear energy transfer (LET) distributions, which can cause variations in the relative biological effectiveness (RBE). Although these quantities are taken into account during treatment planning, there is currently no dedicated tool for the experimental assessment of LET and RBE in clinical practice. This lack of measurement tools poses a challenge to validating predictions from treatment planning systems, as is routinely done for absorbed dose. To address this gap, this thesis introduces novel methods for measuring LET and estimating RBE in PBT and IBT using aluminum oxide doped with carbon and magnesium (Al_2O_3:C,Mg) luminescent detectors. A method was developed to address variable sensitivity among individual fluorescent nuclear track detectors (FNTDs). Calibrations, enabling LET measurements in PBT and IBT, were established for both FNTDs and optically stimulated luminescence detectors (OSLDs). RBE models were integrated into the FNTDs workflow to predict RBE for protons and He-ions. Measurements to assess LET and RBE were conducted using proton and He-ion beams, and validated both *in-vitro* and *in-silico*. Finally, the developed techniques were applied during a measurement campaign aimed at identifying suitable detectors for LET measurements in PBT.

Zusammenfassung

Bei der Protonenstrahltherapie (PBT) und der Ionenstrahltherapie (IBT) weisen die Behandlungsfelder nicht-homogene Verteilungen des linearen Energietransfers (LET) auf, die zu Variationen in der relativen biologischen Wirksamkeit (RBE) führen können. Obwohl diese Größen bei der Bestrahlungsplanung berücksichtigt werden, gibt es derzeit kein dediziertes Werkzeug für die experimentelle Bewertung von LET und RBE in der klinischen Praxis. Dieser Mangel an Messwerkzeugen stellt eine Herausforderung für die Validierung von Vorhersagen aus Bestrahlungsplanungssystemen dar, wie sie routinemäßig für die absorbierte Dosis erfolgt. Um diese Lücke zu schließen, führt diese Arbeit neue Methoden zur Messung des LET und zur Schätzung der RBE in der PBT und der IBT unter Verwendung von Lumineszenz-Detektoren aus Kohlenstoff- und Magnesium-dotiertem Aluminiumoxid (Al_2O_3:C,Mg) ein. Es wurde eine Methode entwickelt, um die variable Empfindlichkeit einzelner fluoreszierender Kernspurdetektoren (FNTDs) zu adressieren. Kalibrierungen, die LET-Messungen in der PBT und der IBT ermöglichen, wurden sowohl für FNTDs als auch für optisch stimulierbare Lumineszenzdetektoren (OSLDs) etabliert. RBE-Modelle wurden in den FNTD-Arbeitsablauf integriert, um die RBE für Protonen und Helium-Ionen vorherzusagen. Messungen zur Beurteilung des LET und RBE wurden mit Protonen- und Helium-Ionenstrahlen durchgeführt und sowohl *in-vitro* als auch *in-silico* validiert. Schließlich wurden die entwickelten Techniken während einer Messkampagne angewendet, die darauf abzielte, geeignete Detektoren für LET-Messungen in PBT zu identifizieren.

Contents

Abstract vii

Zusammenfassung vii

Preface xi

List of publications xiii

Contributions at scientific events xv

List of Figures xvii

List of Tables xix

List of Acronyms xxi

1. Introduction 1
- 1.1. Motivation . . . 1
- 1.2. State of the art in measuring LET and RBE . . . 2
  - 1.2.1. LET . . . 2
  - 1.2.2. RBE . . . 5
- 1.3. Rationale of the thesis . . . 8
- 1.4. Aim of the thesis . . . 8

2. Background 11
- 2.1. Cancer . . . 11
  - 2.1.1. What is cancer? . . . 11
  - 2.1.2. Cancer epidemiology . . . 11
  - 2.1.3. Cancer treatment and management . . . 12
- 2.2. Ionizing radiation . . . 12
  - 2.2.1. Interactions of γ- and X-rays with matter . . . 14
  - 2.2.2. Interactions of charged particles with matter . . . 15
  - 2.2.3. Quantities used to describe the ionizing radiation . . . 19
    - 2.2.3.1. Absorbed dose . . . 19
    - 2.2.3.2. LET . . . 19
- 2.3. Radiobiology . . . 20
  - 2.3.1. Linear-quadratic model . . . 22
  - 2.3.2. RBE . . . 23
  - 2.3.3. RBE models . . . 24
- 2.4. Radiotherapy . . . 26
  - 2.4.1. Conventional external radiotherapy . . . 27
  - 2.4.2. Proton-beam therapy and ion-beam therapy . . . 28
  - 2.4.3. Clinical workflow: Importance of LET and RBE measurements . . . 30

2.5. Luminescence dosimetry . . . 32
2.5.1. FNTDs . . . 33
2.5.2. OSLDs . . . 35

3. Publications **37**
3.1. Overview of the publications . . . 37
3.2. Methodological developments . . . 37
3.2.1. FNTDs sensitivity correction . . . 37
3.2.2. Calibration curve for LET measurements with FNTDs . . . 38
3.2.3. Calibration curves for LET measurements with OSLDs . . . 38
3.2.4. Integration of RBE models . . . 38
3.3. Clinical tests . . . 39
3.3.1. LET measurements in clinical proton and ^{4}He-ion beams . . . 39
3.3.2. RBE measurements in clinical proton and ^{4}He-ion beams . . . 39
3.3.3. Luminescent detectors comparison study . . . 39
3.4. Graphical overview . . . 40
3.5. Publication I . . . 41
3.6. Publication II . . . 59
3.7. Publication III . . . 74
3.8. Publication IV . . . 86

4. Discussion **113**
4.1. Methodological developments . . . 113
4.1.1. FNTDs sensitivity correction . . . 113
4.1.2. Calibration curve for LET measurements with FNTDs . . . 114
4.1.3. Calibration curves for LET measurements with OSLDs . . . 115
4.1.4. Integration of RBE models . . . 116
4.2. Clinical tests . . . 116
4.2.1. LET measurements in clinical proton and ^{4}He-ion beams . . . 116
4.2.2. RBE measurements in clinical proton and ^{4}He-ion beams . . . 118
4.2.3. Luminescent detectors comparison study . . . 119

5. Summary and conclusions **121**

Appendices **123**
A. Specifications of the readout systems . . . 123
B. Intersession correction factor . . . 123

Bibliography **125**

Preface

This thesis represents the culmination of my doctoral research conducted between October 2019 and April 2024 in the Division of Medical Physics in Radiation Oncology at the German Cancer Research Center. It is intended for anyone interested in the applications of fluorescent nuclear track detectors or optically stimulated luminescent detectors in the context of ion beams. I hope that this thesis will be helpful for future students and researchers at all levels, both within my host group and elsewhere. It is my aim for this thesis to serve as a valuable written contribution to the topic and a comprehensive guide to my work. Hopefully, it will prove as beneficial to others as previous theses have been in my own research journey.

The **first chapter** begins with a concise introduction to the context in which this thesis was developed, avoiding overly technical details. Given the goal of developing a system for assessing linear energy transfer and relative biological effectiveness, the chapter is followed by a more technical and in-depth review of current and past techniques used to measure these quantities. At the end of this chapter the rationale and aim of the thesis are presented.

The **second chapter** provides the theoretical framework for this thesis. It begins with a comprehensive definition of cancer, highlighting its importance through epidemiologic figures, and providing a brief overview of treatment options. Shifting to some of the most relevant physics of radiotherapy, it presents a comprehensive definition of ionizing radiation and some basics of radiation interaction with matter, focusing on charged particles. Detailed and rigorous definitions of linear energy transfer and absorbed dose are included. The biological effects of radiation are then presented, covering relative biological effectiveness, the linear-quadratic model, and the phenomenological models used in this thesis. The chapter also briefly discusses the physical and technological aspects of modern radiotherapy. While the main focus is on proton-beam therapy and ion-beam therapy, aspects of X-ray and electron radiotherapy are also discussed to highlight the rationale for using and studying protons and heavier ions in radiotherapy. An overview of a typical radiotherapy workflow is provided, emphasizing the importance of performing linear energy transfer and relative biological effectiveness measurements, as well as potential stages for integrating these measurements into the workflow. The chapter concludes with solid-state luminescence dosimetry, explaining the functioning of fluorescent nuclear track detectors and optically stimulated luminescence detectors, as well as insights into the rationale behind certain directions taken during the research.

Since this thesis is presented in a cumulative form, the **third chapter** presents all the publications derived from the research work. In order to provide narrative coherence, this chapter begins with an overview where efforts have been made to establish connections between the publications and to show how they build upon each other. Furthermore, aiming to present the entire work in a progressive manner, each step of the research and its purpose is presented separately within a structure consisting of independent subsections. Each publication is preceded by a title page listing all authors, the journal in which the publication was published, licensing details, and the main contributions of each author. The **fourth chapter** provides a detailed discussion of the results and, where relevant, suggests possible future research directions. With the idea of facilitating a connection to the publications overview, the discussion follows the same subsection structure introduced in the previous chapter. Finally, the **fifth chapter** summarizes the work and the main conclusions of the thesis.

Recognizing that most dissertations are rarely read from cover to cover, great effort has been made to ensure that all chapters, tables, and figures are self-contained to assist the casual reader looking for single pieces of information. Therefore, acronyms, abbreviations, and quantities are redefined in each new chapter or within the respective captions.

I would like to take some space here to express my personal belief in the potential of fluorescent nuclear track detectors and optically stimulated luminescence detectors as tools for research and clinical applications in ion-beam dosimetry. I sincerely hope that my contribution can be used in the future to further push the boundaries of these techniques. To those who are willing to follow this path, I wish you all the best and good luck in your quest.

Heidelberg
April 11, 2024

Iván D. Muñoz

List of publications

Publications directly related to the thesis

Publications I, II, and III were submitted as part of the cumulative thesis application, which was accepted by the Department of Physics and Astronomy of the University of Heidelberg. Publications I to IV are included in this thesis and consist of full research articles. Publication V is a review article, and Publication VI is a review article in conference proceedings. The status of the publications is reported as of May 2024.

I I. D. Muñoz, L. N. Burigo, T. Gehrke, S. Brons, S. Greilich, and O. Jäkel. Sensitivity correction of Fluorescent Nuclear Track Detectors using alpha particles: determining LET spectra of light ions with enhanced accuracy, *Medical Physics*; 50-4 (2023), 2385–2401. DOI: http://doi.org/10.1002/mp.16083.

II J. B. Christensen, I. D. Muñoz, N. Bassler, C. Stengl, L. Bossin, M. Togno, S. Safai, O. Jäkel, and E. G. Yukihara. Optically stimulated luminescence detectors for dosimetry and LET measurements in light ion beams, *Physics in Medicine & Biology*; 68-15 (2023), 155001. DOI: http://doi.org/10.1088/1361-6560/acdfb0.

III I. D. Muñoz, D. García-Calderón, R. Felix-Bautista, L. N. Burigo, J. B. Christensen, S. Brons, A. Runz, P. Häring, S. Greilich, J. Seco, and O. Jäkel. Linear Energy Transfer Measurements and Estimation of Relative Biological Effectiveness in Proton and Helium-Ion Beams Using Fluorescent Nuclear Track Detectors, *International Journal of Radiation Oncology · Biology · Physics*; In Press (2024). DOI: https://doi.org/10.1016/j.ijrobp.2024.02.047.

IV I. D. Muñoz, O. Van Hoey, A. Parisi, N. Bassler, L. Grzanka, M. De Saint-Hubert, A. Vaniqui, P. Olko, M. Sądel, L. Stolarczyk, A. Vestergaard, O. Jäkel, E. G. Yukihara, and J. B. Christensen. Assessment of fluence- and dose-averaged linear energy transfer with passive luminescence detectors in clinical proton beams, *Physics in Medicine & Biology*; Accepted manuscript (2024). DOI: https://doi.org/10.1088/1361-6560/ad4e8e

V J. B. Christensen, I. D. Muñoz, P. Bilski, V. Conte, P. Olko, L. Bossin, A. Vestergaard, S. Agosteo, A. Rosenfeld, L. Tran, Ž. Knežević, M. Majer, I. Ambrožová, A. Parisi, T. Gehrke, M. Martišíková, and N. Bassler. Status of LET assessment with active and passive detectors in light ion beams, *Radiation Measurements*; Under Review (2024).

VI J. B. Christensen, L. Bossin, I. D. Muñoz, C. Stengl, J. Vedelago, and E. G. Yukihara. Optically stimulated luminescence detectors for LET determination and dosimetry in ion beam therapy, *Radiation Measurements*; Under Review (2024).

Publications not directly related to the thesis

All publications were either published or submitted, and the work was performed within the doctoral research timeframe. The status of the publications is reported as of May 2024.

VII J. Vedelago, F. A. Geser, I. D. Muñoz, A. Stabilini, E. G. Yukihara, and O. Jäkel. Assessment of secondary neutrons in particle therapy by Monte Carlo simulations, *Physics in Medicine & Biology*; 67-1 (2022), 015008. DOI: http://doi.org/10.1088/1361-6560/ac431b.

VIII C. Stengl, K. Panow, E. Arbes, I. D. Muñoz, J. B. Christensen, C. Neelsen, F. Dinkel, A. Weidner, A. Runz, W. Johnen, J. Liermann, G. Echner, J. Vedelago, and O. Jäkel. A phantom to simulate organ motion and its effect on dose distribution in carbon ion therapy for pancreatic cancer, *Physics in Medicine & Biology*; 68-24 (2023), 245013. DOI: http://doi.org/10.1088/1361-6560/ad0902.

IX F. A. Geser, A. Stabilini, J. P. Christensen, I. D. Muñoz, E. G. Yukihara, O. Jäkel, and J. Vedelago. A Monte Carlo study on the secondary neutron generation by oxygen ion beams for radiotherapy and its comparison to lighter ions, *Physics in Medicine & Biology*; 69-1 (2024), 015027. DOI: http://doi.org/10.1088/1361-6560/ad0f45.

X C. Stengl, I. D. Muñoz, E. Arbes, E. Rauth, J. B. Christensen, J. Vedelago, A. Runz, O. Jäkel, and J. Seco. Assessing the impact of breathing-induced motion during carbon ion mini-beam irradiation: A phantom study, *Medical Physics*; In Press (2024). DOI: https://doi.org/10.1002/mp.17077.

Contributions at scientific events

- I. D. Muñoz, D. García-Calderón, R. Félix-Bautista, L. N. Burigo, A. Runz, S. Brons, S. Greilich, J. Seco, and O. Jäkel. **Oral presentation:** Direct linear energy transfer measurements and indirect estimation of the relative biological effectiveness in therapeutic proton and helium-ion beams using fluorescent nuclear track detectors. *20th International Conference on Solid State Dosimetry (SSD20).* Viareggio, Italy; 2023.

- J. B. Christensen, I. D. Muñoz, C. Stengl, M. Togno, S. Safai, L. Bossin, O. Jäkel, and E. G. Yukihara. **Oral presentation:** Feasibility of dose and LET measurements in light ion beams with pointlike OSL detectors. *61st Annual Conference of the Particle Therapy Co-Operative Group (PTCOG61).* Madrid, Spain; 2023.

- C. Stengl, K. Panow, E. Arbes, I. D. Muñoz, J. B. Christensen, C. Neelsen, W. Johnen, A. Runz, J. Liermann, G. Echner, J. Vedelago, and O. Jäkel. **Poster presentation:** PPIeT: Pancreas Phantom for Carbon Ion beam Therapy. *5th Scientific Retreat - National Center for Radiation Oncology (NCRO).* Heidelberg, Germany; 2023.

- I. D. Muñoz and O. Jäkel. **Invited Talk:** Measuring LET track by track using Fluorescent Nuclear Track Detectors. *Danish Center for Particle Therapy Workshop: Linear Energy Transfer.* Aarhus, Denmark; 2022.

- I. D. Muñoz, L. N. Burigo, S. Greilich, and O. Jäkel. **Poster presentation:** Lineal energy distributions and moments of protons using track structure and condensed history Monte Carlo simulations. *International Conference on Individual Monitoring of Ionising Radiation (IM2022) and Neutron and Ion Dosimetry Symposium (NEUDOS-14).* Krakow, Poland; 2022.

- I. D. Muñoz, L. N. Burigo, S. Greilich, and O. Jäkel. **Poster presentation:** Enhanced LET spectra measurements with Fluorescent Nuclear Track Detectors: Applications to radiotherapy with light-ions. *2021 German Cancer Research Center (DKFZ) PhD Poster Presentation.* Heidelberg, Germany; 2021. **Poster Prize - Helmholtz International Graduate School for Cancer Research.**

- I. D. Muñoz, L. N. Burigo, S. Greilich, and O. Jäkel. **Poster presentation:** Fluorescent Nuclear Track detectors: when color matters. *2021 German Cancer Research Center (DKFZ) PhD retreat.* Heidelberg, Germany; 2021.

- I. D. Muñoz, L. N. Burigo, S. Greilich, and O. Jäkel. **Poster presentation:** Estimation of Relative Biological Effectiveness on proton and ^{4}He Spread-Out Bragg Peaks with Fluorescent Nuclear Tracks Detectors. *59th Annual Conference of the Particle Therapy Co-Operative Group (PTCOG59).* Online; 2021.

- I. D. Muñoz, S. Greilich, L. N. Burigo, J. Vedelago, and O. Jäkel. **Poster presentation:** Fluorescent Nuclear Track Detectors for microdosimetry of ion beams: microdosimetric distributions and track average lineal energy. *66th Annual International Meeting Radiation Research Society (RRS).* Online; 2020.

List of Figures

1.1. Thesis roadmap. 9

2.1. Cancer incidence and mortality. 12
2.2. Relative importance of the photoelectric effect, Compton effect and pair production. 14
2.3. Mass electronic stopping power of heavy charged particles. 16
2.4. Mass total, electronic, and radiative stopping powers of electrons. 16
2.5. Nucleus-to-nucleus absorption cross section. 17
2.6. Attenuation of ^{12}C-ions in water. 18
2.7. Landau distribution for energy straggling. 18
2.8. Direct and indirect action of radiation. 21
2.9. Survival fraction as a function of the absorbed dose for two α/β-ratio values. 23
2.10. Survival curves for radiations with different linear energy transfer, and relative biological effectiveness as a function of the linear energy transfer for various particle species. 24
2.11. Number of radiotherapy machines per geographic region, and number of proton-beam therapy and ion-beam therapy centers over time. 26
2.12. MV X-ray spectra, and depth dose profiles of X-rays and electrons. 27
2.13. Depth dose profiles of X-rays and light-ions, and dose average linear energy transfer profiles of protons and ^{4}He-ions. 29
2.14. Two-dimensional dose distributions of protons, ^{12}C-ions, and X-rays. 30
2.15. Radiotherapy workflow. 31
2.16. Band diagram depicting the stages in luminescence processes. 32
2.17. Laser scanning confocal microscope and fluorescent nuclear track detector readout. 33
2.18. Fluorescence intensity images from fluorescent nuclear track detectors exposed to light-ions. 34
2.19. Optically stimulated luminescence decay curves, and relative efficiency for aluminum oxide doped with carbon. 36

3.1. Graphical overview showing connections between publications. 40

B.1. Fluorescence intensity image of the reference fluorescent nuclear track detector, and intersession correction factor in time. 124

List of Tables

1.1. Detectors and methods for measuring linear energy transfer 5
1.2. Settings and methods for assessing the relative biological effectiveness. 7

2.1. Phenomenological relative biological effectiveness models. 25

A.1. Characteristics and technical details of the laser scanning confocal microscope. 123
A.2. Characteristics and technical details of the optically stimulated luminescence reader. 123

List of Acronyms

Al_2O_3:C,Mg	Aluminum oxide doped with carbon and magnesium
Al_2O_3:C	Aluminum oxide doped with carbon
Al_2O_3	Aluminum oxide
CT	Computed tomography
DCPT	Danish Center for Particle Therapy
DKFZ	German Cancer Research Center
DSB	Double-strand break
EURADOS	European Radiation Dosimetry Group
FNTD	Fluorescent nuclear track detector
GCO	Global Cancer Observatory
HIT	Heidelberg Ion-Beam Therapy Center
HLTR	High- to low-temperature ratio
IAEA	International Atomic Energy Agency
IBT	Ion-beam therapy
ICRU	International Commission on Radiation Units and Measurements
IFJ	Institute of Nuclear Physics, Polish Academy of Sciences
LEM	Local effect model
LET	Linear energy transfer
LiF	Lithium fluoride
LQM	Linear-quadratic model
LSCM	Laser scanning confocal microscopy
MKM	Microdosimetric kinetic model
mMKM	Modified microdosimetric kinetic model
MRI	Magnetic resonance imaging
NTCP	Normal tissue complication probability
OSL	Optically stimulated luminescence
OSLD	Optically stimulated luminescence detector
PBT	Proton-beam therapy
PSI	Paul Scherrer Institute
RBE	Relative biological effectiveness
RPL	Radiophotoluminescence
RPLD	Radiophotoluminescent detector
SCK-CEN	Belgian Nuclear Research Center
SOBP	Spread-out Bragg peak
SOI	Silicon on insulator
SSB	Single-strand break
TCP	Tumor control probability

TED	Track etch detector
TEPC	Tissue equivalent proportional counter
TL	Thermoluminescence
TLD	Thermoluminescent dosimeter
TPS	Treatment planning system
WHO	World Health Organization

Chapter 1 Introduction

1.1. Motivation

Presently, cancer is ranked among the leading causes of death worldwide [1]. Alongside surgery and chemotherapy, radiotherapy is one of the main pillars of cancer treatment [2]. Radiotherapy employs ionizing radiation to induce damage in the DNA of malignant cells, preventing them from further dividing. However, exposure of healthy tissue to ionizing radiation is unavoidable with current radiotherapy technologies, potentially causing unintended damage. Therefore, seeking a balance between controlling or curing the disease and reducing side-effects to patients, radiotherapy is constantly evolving to achieve the challenging task of conforming the radiation dose to the diseased tissue to the greatest extent possible [3].

To improve the conformity of the radiation dose, various approaches have been considered, such as using different types of particles. Currently, high-energy (energies on the order of MeV) photons and electrons stand out as the most widely used particles for cancer treatment. However, light-ions, including protons,[1.a] are increasingly recognized as promising options, generating growing interest [5]. Arguably, the main advantage of light-ions is their depth dose profile, which is characterized by a sharp increase in dose towards the end of the particle range followed by a steep fall [6], known as Bragg peak. This property is exploited by selecting the energy of the particles in such a way that they stop within the treated volume, hence delivering the maximum dose at the target site. In addition, light-ions are known to be more effective at inducing cell death than high-energy photons and electrons [7, 8]. Furthermore, this effectiveness is enhanced near to the point where the particles stop, further expanding the therapeutic advantage of light-ions. The enhanced biological effect of light-ions is related to the ionization density,[1.b] which is usually quantified by the linear energy transfer (LET) and is often described by the relative biological effectiveness (RBE) [4].[1.c] The advantageous properties of light-ions and technological developments in recent decades have led to an increased availability of proton-beam therapy (PBT) and ion-beam therapy (IBT) [9].[1.d]

In general, the biological response to ionizing radiation is influenced by several factors [10], including dose, dose rate, LET, the type of tissue or biological system, oxygenation, and the cell cycle, among others. The most important physical quantity to be considered is the absorbed dose. For this reason, and due to the fact that the RBE is regarded to be largely constant within the radiation field, conventional radiotherapy treatment plans are

[1.a] The International Commission on Radiation Units and Measurements (ICRU; Bethesda, MD, USA) and the International Atomic Energy Agency (IAEA; Vienna, Austria) recommend referring to ions with an atomic number less than or equal to 10, including protons, as light-ions [4]. Protons will only be explicitly differentiated when necessary. Ions with an atomic number greater than 10 will be referred to as heavy-ions.

[1.b] Ionization density, often expressed in units of energy per path length ($\mathrm{keV\,\mu m^{-1}}$), refers to the frequency of successive ionizing events within a given volume or per unit path length. The term beam quality is reserved for describing the penetration ability of radiation beams, as measured by parameters such as Half Value Layer, Tissue Phantom Ratio, Half Value Range, and Practical Range.

[1.c] For formal definitions of LET and RBE the reader is referred to sections 2.2.3.2 and 2.3.2, respectively.

[1.d] In this thesis, the term particle therapy is avoided when referring to both PBT and IBT, as photons and electrons, which are also used in radiotherapy, are also considered particles. Strictly speaking, PBT falls within the realm of IBT, but these techniques are differentiated for practical reasons.

optimized solely in terms of absorbed dose.[1.e] In the case of PBT and IBT, variations in LET and RBE need to be considered, and consequently treatment planning systems (TPSs) have been developed that take these quantities into account [12–18].[1.f] These systems can be used to avoid placing high-LET or -RBE components in or close to sensitive organs or substructures [20], increase the LET on the target volume [21], and to evaluate side-effects during patient follow-up [22]. However, unlike absorbed dose, there are currently no guidelines or standard equipment for measuring LET and RBE in routine clinical practice. This hinders the ability to experimentally verify these quantities and to validate the predictions made by TPSs, as it is routinely done for the absorbed dose. The inability to readily measure LET or RBE can introduce unnoticed creeping differences that can lead to compromised or suboptimal clinical outcomes. In the case of LET, it could be argued that it is a quantity that can be calculated using Monte Carlo simulations to validate the analytical approaches commonly implemented in TPSs. However, LET values may show noticeable changes from one code to another or even using different scoring and averaging techniques within the same code [23–25]. In addition, access to reliable experimental tools capable of measuring LET in research settings may be beneficial, as it could help standardize procedures in fields such as radiobiology and radiation metrology [26].

1.2. State of the art in measuring LET and RBE

1.2.1. LET

Over the years, various types of detectors have been proposed and studied for LET measurements. These detectors range from passive solid-state detectors to active gas-filled detectors, each with its own advantages and disadvantages. The ideal device should be capable of measuring LET over the full range of LET values that may be encountered, should be able to withstand the doses and fluence rates used clinically, and should be highly reproducible and accurate. In addition, for measurements in regions with high-LET gradients, detectors should have high spatial resolution, which is most often achieved by using a small sensitive volume. For applications in mixed-ion fields, the response should be independent of the type of particle. Different devices that have been investigated for LET measurements are presented below and summarized at the end of this section in Table 1.1.

Of all passive solid-state detectors, thermoluminescent dosimeters (TLDs) have been the most extensively studied. For some materials, it has been shown that the shape of the thermoluminescence (TL) glow curve can be related to the ionization density of the radiation to which they are exposed [27, 28]. In particular, the relative intensity between the high- and low-temperature components of the glow curve can be correlated with the LET and is usually quantified by the high- to low-temperature ratio (HLTR) [29, 30]. However, it has been systematically observed that the HLTR depends on the particle type, making it difficult to apply this technique to mixed particle fields [29]. Another approach, conceptually similar to the HLTR method, is to relate the ratio of the relative efficiencies of two thermoluminescent materials to the LET [31, 32]. An additional advantage of these methods is that the information regarding the LET can be used to correct for the reduced efficiency of the dosimetric

[1.e] Conventional radiotherapy refers to all techniques using high-energy photons and electrons. It should be noted that the RBE of photons and electrons generally increases with decreasing energy [11], but this effect is sufficiently small to be neglected in conventional radiotherapy.

[1.f] Current clinical practice is to use a constant RBE of 1.1 in PBT [19]. However, there is compelling evidence for an increasing RBE in the distal regions of proton beams [7]. Whether to use a constant or variable RBE in PBT is a matter of hot debate. For ions heavier than protons, there is a general consensus that variable RBE approaches should be adopted [4].

signal to accurately measure the absorbed dose. Thus, both the LET and absorbed dose can be measured simultaneously [27, 31].

Over the last two decades optically stimulated luminescence detectors (OSLDs) have gained increased interest for LET measurements in PBT and IBT [33–36]. For aluminum oxide doped with carbon (Al_2O_3:C), which is the prime material used as OSLD, it has been shown that the shape of the optically stimulated luminescence (OSL) curve changes with the ionization density of the radiation to which this material is exposed, allowing the LET of the radiation field to be measured [33, 34]. Also for Al_2O_3:C, and conceptually similar to the HLTR for TLDs, it has been shown that the ratio between the OSL signals emitted in the blue and UV bands (blue- to UV-signal ratio) can be related to the LET [35]. Both of these methods have been used to measure the LET of clinical proton beams, with the blue- to UV-signal ratio proving to be more accurate [33, 37]. As with TLDs, OSLDs can be used to measure both LET and absorbed dose with a single detector by applying an LET-dependent correction factor to the dosimetric signal [35, 37]. As in the case of the HLTR and the ratio of relative efficiencies, the blue- to UV-signal ratio of Al_2O_3:C exhibits a strong dependence on the particle type, which may limit its application to mixed-ion fields [35].

While not as extensively studied as TLDs and OSLDs, there is evidence to suggest that radiophotoluminescent detectors (RPLDs) can be used to measure the LET. Specifically, it has been shown that the radiophotoluminescence (RPL) emission spectrum of silver- (Ag^+-) doped phosphate glass reflects changes in ionization density when exposed to 30 kV X-rays and α-particles [38]. In this case, the relative intensity between the blue and yellow RPL emissions can, in principle, be correlated with the LET. However, as of the present date, no dedicated studies have been conducted in this direction.

Unlike TLDs, OSLDs, and RPLDs, which yield a signal integrated over the entire detector volume, fluorescent nuclear track detectors (FNTDs) allow the interrogation of micrometer-sized subvolumes through fluorescence microscopy techniques [39–42]. This type of readout results in high spatial resolution fluorescence images that enable the analysis of single ion-tracks. Several studies have shown that the fluorescence intensity of recorded tracks depends on the local energy deposition and, thus, can be related to the LET of the particles giving rise to the signal [43–45]. This relationship allows for the measurement of the LET spectra of a given ion field by obtaining the LET for each recorded track. Nowadays the primary – and only commercially available – material used as FNTD is aluminum oxide doped with carbon and magnesium (Al_2O_3:C,Mg) [39]. One of the main challenges when measuring LET spectra with this material is the non-homogeneous sensitivity, also known as coloration, between single crystals [44, 46, 47]. Assuming that the measured spectra are only displaced in the LET space due to different sensitivities, a correction factor based on Monte Carlo simulations has been proposed to match the position of the measured and simulated spectra [47, 48]. However, this approach requires a rather detailed knowledge of the experimental setup, which might not be always available. FNTDs have been used to measure LET spectra in clinical ion beams [47, 48] and to spatially correlate DNA damage with ion tracks [49, 50]. The main advantage of measuring LET spectra is that it opens the possibility to analyze the components of each ion type within mixed-ion fields.

Like FNTDs, track etch detectors (TEDs) can record single ion-tracks. However, TEDs rely on the differential effect of chemical etching between undamaged and radiation-damaged polymeric chains [51]. The purpose of etching is to enlarge the damage so that it can be visualized on a microscope for analysis. The morphology of the track spots can then be used to calculate the LET of single ions and derive the LET spectrum of the ion field to which the detector was exposed [52]. Particularly, the length of the major and minor axes of the

elliptical etched pit are used as the figures of interest, which are related to the ratio of the etching rates at the track and bulk material. One limitation of TEDs is that their lower LET detection threshold does not cover the entire range encountered in PBT and IBT [53, 54]. However, studies have shown that the dynamic range of these detectors is sufficient to partially measure the LET spectra of mixed-ion fields produced by ^{12}C-ions [55, 56].[1.g]

Regarding active detectors, tissue equivalent proportional counters (TEPCs) were originally designed to measure the specific energy (z) and lineal energy (y) [57, 58], which are the stochastic equivalents of absorbed dose and LET, respectively. Both z and y are defined within the context of microdosimetry to account for the random nature of energy deposition of radiation in matter and effects due to δ-rays [59].[1.h] While it is possible to link y with LET [61], most studies involving TEPCs focus on measuring y [62–64]. The latter follows from the fact that y can also be related to the RBE, eliminating the need to convert between quantities [65, 66]. TEPCs consist of a cavity filled with tissue-equivalent gas (either propane- or methane-based) at low pressure to simulate a micrometer-sized domain. The energy of each event is measured by applying a voltage between an anode and a cathode, which generates an electron avalanche and increases the signal [59]. TEPCs are highly sensitive and can measure y over a wide range. However, this high sensitivity, coupled with limitations in electronic readout systems, limits their application to clinically relevant fluence rates. These detectors have been extensively used to measure y and estimate the RBE in PBT and IBT [62–64].

Silicon on insulator (SOI) detectors use arrays of micrometer-sized silicon volumes in a SOI wafer to measure the energy deposited by ionizing particles [67]. This approach contrasts with that of TEPCs, which employ a macroscopic cavity for energy deposition measurements. In SOI detectors, the energy deposition is measured in each individual volume. Therefore, it is important for the size of the sensitive volumes to be well-defined and to avoid charge sharing between them. The current generation of SOI detectors allows for measurements at the fluence rates commonly used in clinical settings [68, 69]. Additionally, the detectors have a dynamic range in y suitable for applications in PBT and IBT [68, 70]. However, conversion coefficients from silicon to tissue or water are necessary [71]. It is worth noting that SOI detectors, like TEPCs, are designed for measuring microdosimetric quantities and not LET, although it is theoretically possible to assess the LET from these measurements [72]. This type of detectors have found extensive application in research involving clinical light-ion beams [68, 73].

Another type of silicon-based device that can be used for LET measurements is the Timepix detector. For this detector, a radiation-sensitive volume consisting of a silicon sensor layer is bump-bonded to a readout chip, known as Timepix chip. The Timepix chip consists of a densely packed matrix of electrodes with independent readout electronics for each pixel [74]. One key feature of the Timepix detector is its ability to resolve single charged-particle tracks in time. The capability to measure energy loss [75, 76], enables to perform LET spectra measurements in light-ion beams [77]. Moreover, the Timepix detector is capable to measure the LET within the entire range of interest for PBT and IBT [77, 78]. However, the data readout speed of this detector is not suitable for measurements at the fluence rates used in the clinical routine and high-energy depositions may cause saturation effects. Similar to SOI detectors, conversion factors are necessary to report the LET in biologically relevant materials [78, 79].

[1.g] For the sake of brevity, when referring to specific ion species, only the chemical symbol will be stated. If necessary, the isotope will also be explicitly given.

[1.h] Generally speaking, y is defined as the ratio of the energy imparted by a single track in a given volume (ϵ_i) to the mean chord length of that volume. z is defined as the ratio of ϵ_i to the mass of the volume [60].

Table 1.1.: Detectors and methods for measuring linear energy transfer (LET).

Mode	Type of detector	Method	Reference
Passive	Thermoluminescent dosimeters (TLDs)	High- to low-temperature ratio.	[29, 30]
		Relative efficiency ratio of two detector types.	[31, 32]
	Optically stimulated luminescence detectors (OSLDs)	Shape of the optically stimulated luminescence decay curve.	[33]
		Ratio between two different optically stimulated luminescence emission bands.	[35, 36]
	Radiophotoluminescent detectors (RPLDs)	Ratio between two different radiophotoluminescence emission bands.	[38]
	Fluorescent nuclear track detectors (FNTDs)	Fluorescence intensity of the trackspots.	[43–45]
	Track etch detectors (TEDs)	Morphology of the trackspots.	[52, 56]
Active	Tissue equivalent proportional counters (TEPCs)*	LET derived from microdosimetric quantities.	[61]
	Silicon on insulator (SOI)* detectors	LET derived from microdosimetric quantities.	[72]
	Timepix detector	Energy deposition from single ion-tracks.	[77]

*Primarily designed to measure lineal energy, which is the stochastic equivalent of the linear energy transfer.

1.2.2. RBE

The RBE is defined in its most general form as the ratio between two doses that result in the same biological effect (Equation 2.16). Thus, it can be measured using a variety of systems and techniques. However, under otherwise fixed conditions, the RBE can vary significantly depending on the system and biological endpoint used for its measurement. Although the endpoint can be chosen arbitrarily, it should preferably be relevant to the biological or clinical effect being studied. Since the RBE is a relative quantity, it is of utmost importance to consider the type of reference radiation for its evaluation and when comparing independent studies [7]. Due to their relevance to radiation oncology and associated low-LET, 6 MV X-rays or ^{60}Co γ-rays are preferred as reference radiation. However, due to their availability and ease of irradiation conditions, (200 to 250) kV X-rays are also often used.

The RBE can be assessed either *in-vivo* [80, 81] or *in-vitro* [82, 83]. *In-vivo* settings enable the study of RBE under the inherent complexity of living organisms (e.g., tumor microenvironment, cell architecture, and vasculature), better representing a clinical scenario. *In-vitro* experiments provide more simplified conditions, with the advantage of more controlled parameters and higher experimental throughput. Approaches used to assess the RBE in both types of settings are presented below and summarized at the end of this section in Table 1.2.

Clonogenic cell survival assays are the most common type of biological experiment used to study the RBE of light-ions. These studies examine the ability of cells to withstand radiation damage and maintain their ability to proliferate and form colonies [10]. In this type of experiment, the endpoint is typically set at a specific survival level. That is, the doses of two types of radiation that result in the formation of the same relative number of colonies. A common source of error with this approach is that the number of colonies identified may vary from one observer to another or between automated tools due to the subjectivity of colony identification [84]. Clonogenic cell survival assays allow to study individual cell lines under different and well-defined conditions [8]. Many of the RBE models proposed for PBT and IBT have been derived using data obtained from clonogenic cell survival assays [83, 85–87]. Therefore, despite their limitations, clonogenic cell survival assays are commonly used as a first-line method to benchmark RBE models [88–90].

Another *in-vitro* approach that can be used to assess the RBE of light-ions is the quantification of DNA damage, specifically double-strand breaks (DSBs),[1.i] by immunofluorescence analysis with the γ-H2AX biomarker [91–93]. This marker allows indirect assessment of DSBs by quantifying radiation-induced discrete foci using fluorescence microscopy or flow cytometry [94, 95]. For immunofluorescence assays, common endpoints are the number of foci per cell [91, 92] and the median fluorescence intensity [93], which are considered surrogates for the number of DSBs. An advantage of this technique is that the formation of foci can be studied over time, providing insight into the kinetics of damage and repair processes. However, it should be noted that γ-H2AX foci can arise from other mechanisms and therefore cannot be always uniquely associated with DSBs caused by ionizing radiation [96]. Another technique that can be employed to indirectly assess the number of DSBs is gel electrophoresis by examining migration profiles. This method operates under the assumption that more fragmented DNA will migrate at a faster rate within a gel matrix than undamaged DNA, when subjected to a fixed electric field [97]. The fraction of DNA within a specified range of fragment sizes is extracted from the migration profiles and used as endpoint [98, 99]. However, the sensitivity of this technique is relatively low and requires exposing the samples to doses that exceed those commonly used in clinical settings.

At a higher level of DNA organization, radiation-induced chromosomal damage can be used to assess the RBE through cytogenetic testing techniques. One example is the quantification of the formation of chromosomal defects, such as dicentric aberrations and centric rings [100, 101], which occur when chromosomal segments join or rearrange in a defective manner. Techniques such as fluorescence *in-situ* hybridization can be used to assess the frequency of aberrations [102]. However, it should be noted that the frequency of aberrations is dependent on the cell cycle phase at which cells are analyzed [103]. Since these alterations can be distinct for different types of radiation, the predicted RBE may vary significantly. Other cytogenetic techniques that have been used to assess the RBE of light-ions include micronuclei formation and premature chromosome condensation assays [104–106]. Micronuclei are formed as a result of dissociation of chromosome fragments from the spindle apparatus, indicating chromosome damage. Thus, the frequency of micronuclei induction can be used as an endpoint to determine the RBE [104, 105]. Premature chromosome condensation occurs as a cellular mechanism to repair damaged DNA, aiming to facilitate the identification of such damage. In this case, the endpoint that is used to assess the RBE is the excess of chromosome fragments [106, 107].

In the context of *in-vivo* studies, animal models play a crucial role in determining the RBE of light-ions and can be used to study the RBE in both healthy tissues and tumors [108–111]. The biological similarity of animal models to humans, particularly in the case of mammals, is a clear advantage over *in-vitro* experiments. Additionally, species with a short lifespan allow for the study of long-term effects in a relatively short period of time. However, if the life span of is too short, radiation-induced effects may not be observed. One of the key benefits of experiments in animal models is that the tumor environment can be similar to that found in patients. Particularly, the presence of hypoxic regions and stem cells, which may respond differently depending on the type of radiation and can play a crucial role in treatment outcomes. Moreover, animal models allow for conducting dose escalation experiments to determine dose-response curves and investigate various fractionation schemes [108, 112], which is extremely relevant to the clinical practice. Conducting such experiments in patients would

[1.i] DSBs represent one of the most severe forms of DNA damage. This type of damage poses a greater challenge for the cell to repair compared to single-strand breaks. If not properly repaired, DSBs can lead to mutations, chromosomal aberrations, and cell death [10].

be unfeasible due to ethical concerns. Common clinically relevant endpoints used to evaluate the RBE with animal models include growth delay and local tumor control for tumors [108, 109, 113], as well as acute and late radiation effects for healthy tissues [110–114]. Depending on the site, radiation effects in healthy tissues may manifest as skin reactions, changes in rectal wall, paresis, and lung fibrosis. Histologic and imaging techniques or direct observations and measurements can be used to study tissue changes associated with these endpoints. Although animal models are valuable for studying the RBE, they tend to be more resource-intensive and time-consuming compared to *in-vitro* settings. Furthermore, ethical considerations should also be taken into account.

Given that the ultimate goal of radiotherapy is patient treatment, the RBE should ideally derive from clinical findings in humans. However, obtaining meaningful and robust clinical-RBE values is challenging, requiring considerable efforts while adhering to standards of care and ethical principles. Moreover, clinical-RBE values are based on observations in rather large volumes, where volumetric averaging is unavoidable. In addition, certain symptoms may take extended periods of time to manifest. Therefore, studies must be conducted for a sufficient duration to obtain conclusive data. In some cases, the standard of care indicates that patients should receive a combination of radiotherapy and other therapies. When evaluating the RBE, it is important to consider the synergies between the combined treatments. To assess the RBE from clinical data, both retrospective and prospective studies have been conducted [115, 116]. Examples of endpoints that have been used to estimate the clinical-RBE relative to conventional radiotherapy include tumor control probability at 80 % based on biochemical or clinical failure-free rate [115], the minimum dose received by the hottest 1 % of the irradiated volume (D1%) in the temporal lobe after detection of changes with magnetic resonance imaging (MRI) techniques [116], and tolerance doses for mandibular osteoradionecrosis to an iso-critical volume [117]. Even if scarce, clinical-RBE values can be used to assess the veracity of those obtained from other approaches.

Table 1.2.: Settings and methods used to assess the relative biological effectiveness (RBE).

Setting	Technique / model	Endpoint	Reference
In-vitro	Clonogenic cell survival	Survival fraction at a fixed survival level.	[10]
	Immunofluorescence	Formation of double strand brakes foci.	[91]
		Median fluorescence intensity.	[93]
	Electrophoresis	Fraction of activity released.	[98, 99]
	Fluorescence *in-situ* hybridization	Frequency of chromosomal aberrations.	[102]
	Micronucleus formation	Frequency of micronuclei induction.	[104, 105]
	Premature chromosome condensation	Excess of chromosome fragments.	[106, 107]
In-vivo	Animal	Local tumor control.	[108, 113]
		Delayed tumor growth.	[109]
		Skin reactions.	[110, 113]
		Paresis after spinal cord irradiation.	[110, 112]
		Lung fibrosis.	[111]
		Changes in the rectal wall.	[114]
	Human patients	Tumor control probability at 80 % based on biochemical or clinical failure-free rate.	[115]
		Temporal lobe enhancement on T1-weighted MRI at D1%.	[116]
		Tolerance doses for mandibular osteoradionecrosis to an iso-critical volume.	[117]

Abbreviations: MRI = magnetic resonance imaging, D1% = dose received by the hottest 1 % of the irradiated volume.

1.3. Rationale of the thesis

This thesis focuses on the study of Al_2O_3:C,Mg-based FNTDs and OSLDs. The rationale for studying this type of detectors is that they enable the measurement of LET in a range suitable for applications in PBT and IBT. Additionally, both of these detectors can withstand the fluence rates encountered in the clinical environment and are well-suited for performing measurements in regions characterized by steep LET gradients due to their small size. While FNTDs offer the remarkable advantage of allowing to perform LET spectra measurements, current technologies do not support high sample readout throughput. On the other hand, OSLDs are unable to provide spectral information, but current devices allow for the swift readout of a relatively high number of detectors, which can better fit a clinical pipeline. Whilst FNTDs have been used for LET measurements in PBT and IBT, the challenge posed by variations in sensitivity between individual crystals has yet to be tackled experimentally. These variations have been shown to lead to highly inaccurate LET results. Therefore, a purely experimental approach to correct for the sensitivity of each crystal would represent a substantial step forward in the development of FNTD-related techniques. For OSLDs, the properties and performance of Al_2O_3:C,Mg for LET measurements in PBT and IBT have not been studied so far. Investigating this material is strongly motivated by previous studies regarding its OSL properties and previous observations with Al_2O_3:C-based OSLDs.

Regarding the RBE, it is conceivable to exploit LET measurements to estimate the RBE in PBT and IBT. Particularly, considering the dependence of the RBE with the type of particle, the spectroscopic information that can be obtained from FNTDs appears highly attractive for applications in mixed-ion fields. However, it is also reasonable to simply use the average LET obtained from OSLDs to estimate the RBE, especially in PBT. To estimate the RBE, LET measurements can be used as input in phenomenological RBE models. However, it would be necessary to validate this approach with a biological assay, such as clonogenic cell survival, to establish its reliability.

A detector capable of effectively measuring LET and estimating the RBE can facilitate the validation of TPSs that optimize treatments in terms of these quantities, and simplify the comparison of different RBE models. In addition, such a detector would allow the development and routine application of patient-specific quality assurance protocols.

1.4. Aim of the thesis

The aim of this thesis was to advance the techniques for measuring LET and to develop the methods for assessing RBE using Al_2O_3:C,Mg-based FNTDs and OSLDs. To this end, a fully experimental methodology was developed to derive a detector-specific sensitivity correction factor for FNTDs, leading to more accurate LET measurements and an improved fluorescence intensity-to-LET calibration curve. Once the sensitivity correction methodology was developed and the calibration was established, the accuracy of LET predictions made by FNTDs in unknown ion fields was tested by exposing detectors to proton and ^{4}He-ion clinical beams. These measurements were then compared to LET values obtained from Monte Carlo simulations using two commonly used approaches for its calculation. To predict the RBE of these beams, the LET measurements were used as input in phenomenological RBE models which are suitable, or have been used, for treatment planning. The predicted RBE values were validated through *in-silico* methods (Monte Carlo simulations) and *in-vitro* experiments (clonogenic cell survival assays). For OSLDs, a calibration between the LET and the blue- to UV-signal ratio was established for Al_2O_3:C,Mg-based detectors. In the final step, a compar-

ison study was conducted by exposing both OSLDs and FNTDs to the same clinical proton beams. The latter study was carried out as part of a multi-institutional intercomparison campaign organized by the European Radiation Dosimetry Group (EURADOS). Figure 1.1 shows a diagram outlining the overall workflow of this thesis.

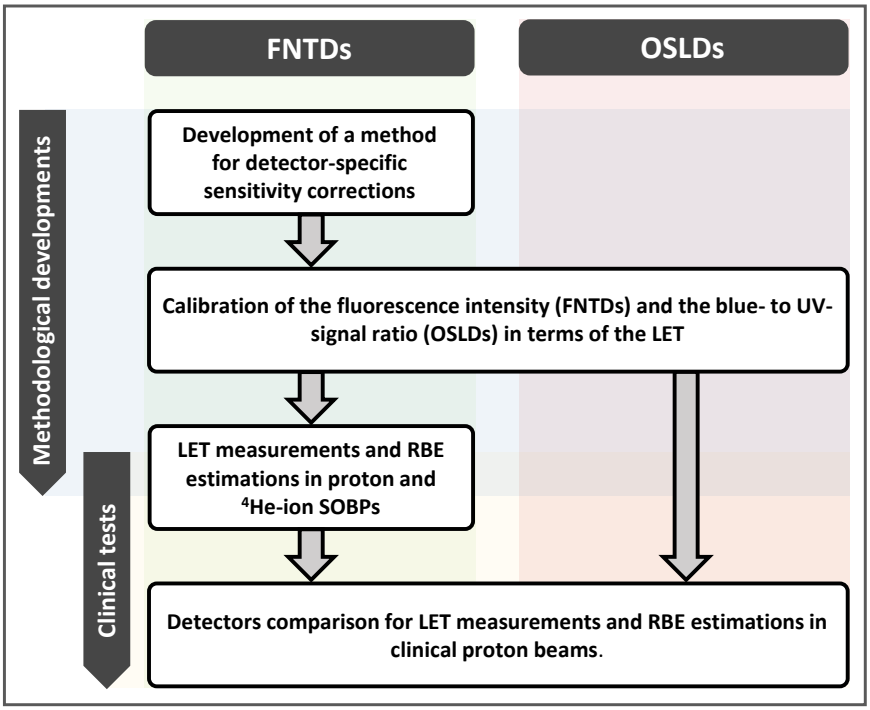

Figure 1.1.: Diagram depicting the main stages of the thesis. Each stage is represented by a single box, with the width of the boxes indicating which type of detector was used. Left arrows indicate whether a stage involves methodological developments or clinical testing. In the first stage, a method for deriving sensitivity corrections for fluorescent nuclear track detectors (FNTDs) was developed. In the second stage, calibration curves for conducting linear energy transfer (LET) measurements in unknown light-ion fields were established for both FNTDs and optically stimulated luminescence detectors (OSLDs). In the third stage, LET and relative biological effectiveness (RBE) measurements were conducted in proton and ^{4}He-ion spread-out Bragg peaks (SOBPs). In the fourth and final stage, various detectors were compared for assessing LET and RBE in clinical proton beams.

Chapter 2 Background

2.1. Cancer

2.1.1. What is cancer?

According to the World Health Organization (WHO; Geneva, Switzerland), the term cancer makes reference to a set of different diseases capable of manifesting in any part of the body [118]; yet, cancer is often used in a manner that suggest a single disease. Labeling a group of diseases as a single entity can be justified by their shared characteristics. It has been suggested that most if not all types of cancer cells share at least the following features [119]:

- Capacity for growth in the absence of external signals.
- Insensitivity to signals that prevent growth.
- Ability to spread to and invade other tissues (metastasize).
- Unlimited replication potential.
- Ability to trigger the production of new vasculature (angiogenesis).
- Capacity for escaping programmed cell death (apoptosis).

While this definition has been embraced by some in the medical and scientific communities, it has also faced criticism. For instance, some argue that benign tumors may also display these hallmarks, with the exception of the ability to metastasize [120]. Apart from the six features listed above, additional ones have been proposed [121], such as:

- Deregulated metabolism.
- Capacity for evading the immune system.

This demonstrates the challenge of giving a general and simple definition that includes all diseases recognized as cancer. For modern society, cancer remains one of the major challenges to overcome and stands as one of the leading causes of death worldwide [1]. Furthermore, cancer poses a substantial economic burden and consumes a significant portion of healthcare resources [122, 123], that could otherwise be allocated to other diseases.

2.1.2. Cancer epidemiology

Based on data from the Global Cancer Observatory (GCO; Lyon, France), just in 2020 approximately 19 million new cancer-patients were diagnosed and 10 million cancer-related deaths occurred worldwide [1]. On top of this scenario, considering that aging is one of the major risk factors for developing cancer and with a growing elderly population [124, 125], along with non-cancer competing causes of death decreasing [126], cancer burden is expected to increase by almost 50 % worldwide in the next two decades [1]. Currently, with a cancer incidence of 22.8 %, Europe constitutes 19.6 % of all cancer deaths, despite the fact that only 9.7 % of the global population resides in the region [1]. Among other factors, these figures are linked to age demographics, but also to availability and accessibility to quality therapeutic options,

screening campaigns and prevention programs or policies [1, 127]. When considering both sexes, female breast cancer is the most prevalent type, accounting for 11.7 % of all diagnosed cancers, followed by lung (11.4 %), and colorectal cancers (10.0 %) (Figure 2.1(a)). The three cancers with the highest mortality rates are lung cancer (18.0 %), colorectal cancer (9.4 %), and liver cancer (8.3 %) (Figure 2.1(b)). It is worth noting that these figures vary across different geographic regions and with the human development index [1].

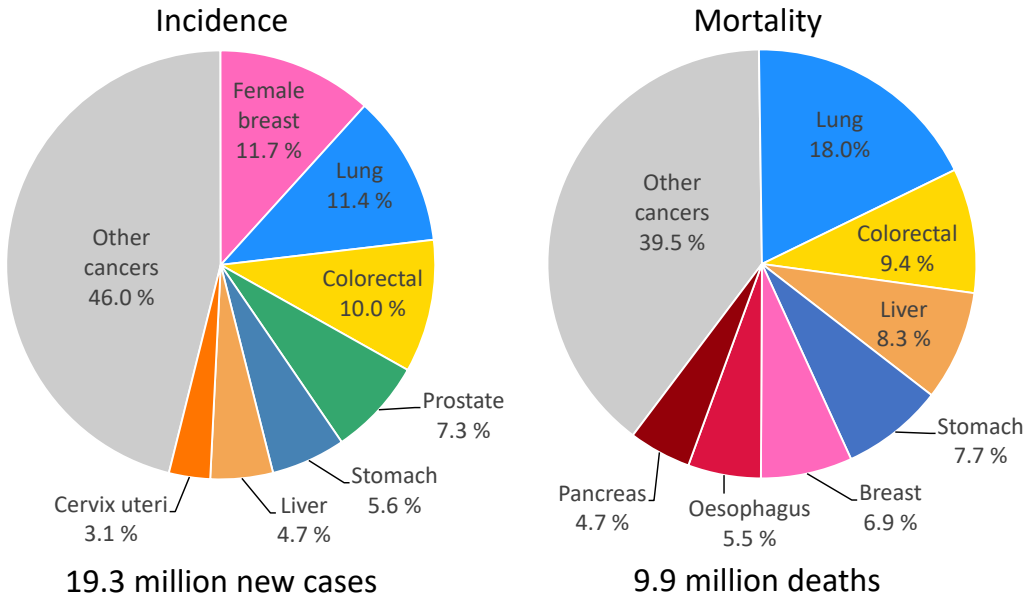

(a) Cancer incidence **(b)** Cancer mortality

Figure 2.1.: Worldwide estimated number of **(a)** new cancer cases and **(b)** deaths for both sexes and all ages in 2020. In **(a)** non-melanoma skin cancers (incidence of 6.2 %) are included in the category of "Other cancers". Adapted from [1] with data from [128].

2.1.3. Cancer treatment and management

There are several treatment options for cancer, and the choice of treatment depends on factors such as the cancer's location, type, and stage [129, 130]. Patients may undergo one or more types of treatment [129, 130]. In the case of multiple treatments, they can be administered as adjuvant, neoadjuvant, or concomitant therapies. Depending on the extent of the disease, the treatment intention can be curative or palliative. For the five most prevalent types of cancer (including non-melanoma skin cancers), which account for almost half of the cases [1], the main therapeutic options for diagnosed patients are surgery, chemotherapy, and radiotherapy, both alone and combined [131–135]. It is estimated that approximately half of cancer patients will require radiotherapy, either for palliative or curative purposes, over the course of their treatment [2, 136]. Radiotherapy utilizes ionizing radiation to damage the DNA of cancerous cells, inhibiting their ability to divide further.

2.2. Ionizing radiation

Ionizing radiation refers to particles – both charged and uncharged – carrying sufficient energy to ionize the atoms and molecules in the matter they interact with, or capable to trigger nuclear reactions or elementary-particle transformations that can in turn result in ionizing

events [137, 138]. Since the binding energy of electrons in the valence band falls within the range from (5 to 25) eV, a limit could be set around this range of values. However, such limit would also include a great portion of the UV-light spectrum, which is commonly excluded [138]. To solve the lack of an accurate threshold, the International Commission on Radiation Units and Measurements (ICRU; Bethesda, MD, USA) introduced the *ad-hoc* energy threshold concept [137]. This concept suggests to set an energy threshold, below which charged particles can be considered as no longer ionizing, without impacting – for all practical purposes – the spatial distribution of energy deposition. The determination of the threshold value should be tailored to each specific application. For instance, an energy threshold of 10 eV is suggested to be appropriate for most radiobiology applications [137]. The following are common types of ionizing particles [138, 139]:

- γ-rays: Electromagnetic radiation produced as a result of nuclear transformations or matter-antimatter annihilation processes.
- X-rays: Electromagnetic radiation produced as a result of transitions between atomic energy levels (characteristic) or by charged particles slowing down in the presence of electrostatic fields (*bremsstrahlung*).
- Electrons: Electrons artificially accelerated, generated or ejected during the decay of radioactive nuclei (β^--rays and internal conversion electrons, respectively), released through collisions by charged particles traversing a medium (δ-rays), released by photons through the photoelectric effect or Compton effect (photoelectrons and recoil electrons, respectively), and generated by photons interacting with the atomic nucleus or orbital electrons (pair production and triplet production electrons, respectively).
- Positrons: Positrons generated during the decay of radioactive nuclei (β^+-rays) and generated by photons interacting with the atomic nucleus or orbital electrons (pair production and triplet production positrons, respectively).
- Heavy charged particles:[2.a] Fully or partially stripped nuclei that are accelerated either naturally or artificially (e.g., protons, ^{12}C-, ^{56}Fe-, and ^{208}Pb-ions), ^{4}He-nuclei emitted through radioactive decay (α-particles),[2.b] muons, and other charged particles generated during high energy collisions (e.g., π^-).
- Neutrons: Neutrons generated as a result of nuclear reactions, either artificially through bombarding materials with neutrons or other particles, or naturally during the disintegration of unstable nuclei.

Ionizing radiation can be divided based on how the energy is transferred and deposited to matter as directly ionizing radiation and indirectly ionizing radiation [140]. Directly ionizing radiation consists of charged particles (electrons, positrons, and heavy charged particles) that deposit their energy into the medium through elastic and inelastic collisions as well as nuclear reactions [139]. Indirectly ionizing radiation consists of uncharged particles (neutrons, γ-, and X-rays) that transfer all or part of their energy to directly ionizing particles, which then deposit the energy into the medium [138]. Typically, directly ionizing particles undergo a large number of interactions before coming to rest. In contrast, indirectly ionizing particles transfer their energy through a few or single catastrophic interactions, after which the primary particles lose a significant amount of energy or cease to exist altogether.

[2.a] Within the context of the present thesis, any charged particle with a mass larger than that of the electron is considered a heavy charged particle.

[2.b] Although ^{4}He-ions and α-particles are identical in nuclear structure, they are distinguished by their origin. α-particles are generated during the radioactive α-decay, while ^{4}He-ions refer to accelerated nuclei or byproducts of nuclear reactions such as nuclear fragmentation in ion-ion collisions.

2.2.1. Interactions of γ- and X-rays with matter

The γ- and X-ray photon[2.c] energies relevant to most medical applications range from tens of keV (e.g., mammography) to tens of MeV (e.g., radiotherapy). Within this energy range, the main processes governing the interaction of photons with matter are the photoelectric effect, Compton effect, and pair production [139, 141]. Rayleigh scattering, triplet production, and photonuclear interactions can also occur at energies relevant to medical applications but are typically considered as less relevant due to their relatively lower probability of occurrence [138]. The relative probability for the photoelectric effect, Compton effect, and pair production to occur depends primarily on the interacting photon energy and atomic number (Z) of the medium with which the photons interact (Figure 2.2) [139].

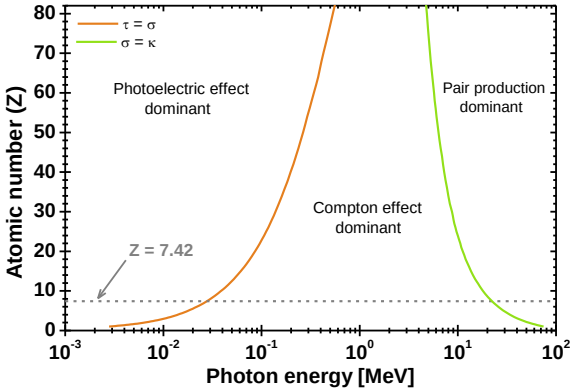

Figure 2.2.: Relative importance of the photoelectric effect, Compton effect and pair production. Solid curves show the photon energy and atomic number (Z) loci where the cross section of two effects are equal. Labels indicate regions where the photoelectric effect cross section (τ), Compton effect cross section (σ) and pair production cross section (κ) are predominant. The dashed line corresponds to the effective Z of water ($Z = 7.42$). Data generated using XCOM: Photon Cross Sections Database of the National Institute of Standards and Technology (NIST; Gaithersburg, MD, USA) [142].

For a monoenergetic parallel photon beam under narrow beam conditions (i.e., without detection of secondary and scattered particles), the rate of change in the number of primary photons per unit of path length ($\mathrm{d}N/\mathrm{d}l$) after traversing a material slab of thickness $\mathrm{d}l$ is directly proportional to the number of incident photons. This relationship can be expressed as follows [138]:

$$\frac{\mathrm{d}N}{\mathrm{d}l} = -\mu N \implies N = N_0 e^{-\mu l}, \tag{2.1}$$

where μ is the proportionality constant and is defined as the linear attenuation coefficient, N_0 is the initial number of incident photons and N is the number of primary photons that pass through a slab of thickness l. The linear attenuation coefficient corresponds to the sum of all macroscopic interaction cross sections of the involved interaction processes:

$$\mu = \tau + \sigma + \kappa, \tag{2.2}$$

where τ, σ, and κ are the partial linear attenuation coefficients for the photoelectric effect, Compton effect, and pair production, respectively.

[2.c] For brevity, from this point onwards, the term photons will be used to refer indistinctly to γ- and X-rays. Distinctions will be made only when strictly necessary.

2.2.2. Interactions of charged particles with matter

High-energy charged particles interact with both the electrons and atomic nuclei of the traversed medium, modifying it in the process through ionizations, excitations, and nuclear reactions. These interactions are primarily governed by Coulomb-force interactions, often referred to as collisions [139, 143]. Since, in most cases, only a small fraction of the particle energy is lost in a single collision, charged particles undergo a large number of interactions before coming to rest. Collisions can be classified as soft or hard, depending on whether the amount of energy lost in a single collision is less than or greater than a cutoff energy (W_c). The electronic stopping power (S_{el}) quantifies the mean rate of energy loss per unit of path length ($\langle dE/dx \rangle$) and is the sum of the energy losses due to soft and hard collisions. S_{el} only accounts for energy losses resulting from interactions with atomic electrons. Energy losses from interactions with the nucleus, not involving changes in the charge and mass of the target and/or projectile, are included in the nuclear stopping power (S_{nucl}), and can be neglected in the energy ranges used in PBT and IBT [143]. In its more general form, the mass electronic stopping power (S_{el}/ρ) for heavy charged particles is given by [144]:

$$\frac{S_{el}}{\rho} = \left\langle \frac{dE}{\rho dx} \right\rangle_{el} = 2K_S \frac{Z}{A} \frac{z^2}{\beta^2} \left[\ln\left(\frac{2m_e c^2 \beta^2}{(1-\beta^2)I} \right) - \beta^2 - \frac{\delta}{2} - \frac{C}{Z} \right], \tag{2.3}$$

where $K_S = 0.153\,5375$ MeV mol^{-1} cm^2 is the coefficient for stopping powers and depends only on fundamental physical constants, ρ, Z, A and I are, respectively, the density, atomic number, atomic mass, and the mean excitation energy of the medium, z is the charge of the interacting particle, m_e is the electron mass, c is the speed of light in vacuum, and $\beta = v/c$ with v the speed of the interacting particle. The terms $\delta/2$ and C/Z are the density-effect and shell corrections, respectively [143]. It should be noted that Equation 2.3 is independent of W_c and therefore a rigorous numerical definition becomes unnecessary.

Equation 2.3 shows that S_{el}/ρ is inversely proportional to β^2, which explains the steep decrease as the energy of the interacting particle increases (Figure 2.3(a)). However, after reaching a minimum value ($\sim 1 \times 10^3$ MeV u^{-1}), S_{el}/ρ starts to slowly increase at higher energies, due to reativistic effects. The dependence on z^2 implies a rapid increase with the charge of the interacting particle (Figure 2.3(a)). Furthermore, this suggests that the stopping power of any other particles can be determined – in a crude manner – by scaling the stopping power of well-studied particles such as protons or ^{4}He-ions. From Equation 2.3 it can also be noticed that S_{el}/ρ is proportional to the number of electrons per unit of mass (Z/A). Thus, in general, it decreases for media containing high-Z elements (Figure 2.3(b)). One additional factor contributing to the decrease of S_{el} with increasing Z is the dependence with I inside the bracket.

Since light-ions release a number of electrons as they pass through matter, electrons play a critical role in describing the spatial pattern of energy deposition associated with light-ions. In fact, the track structure of the electrons emitted by ions is strongly related to the response of biological and physical systems. The mass electronic stopping power for electrons (S_{el}^-/ρ) is given by [144]:

$$\frac{S_{el}^-}{\rho} = \left\langle \frac{dE}{\rho dx} \right\rangle_{el}^- = K_S \frac{Z}{A} \frac{1}{\beta^2} \left[\ln\left(\frac{T}{I} \right)^2 + \ln\left(1 + \frac{\tau}{2} \right) + F^-(\tau) - \delta \right], \tag{2.4}$$

where T is the electron initial kinetic energy, $\tau = T/m_e c^2$, and $F^-(\tau) = (1-\beta^2)[1 + (\tau^2/8) - (2\tau+1)\ln(2)]$.

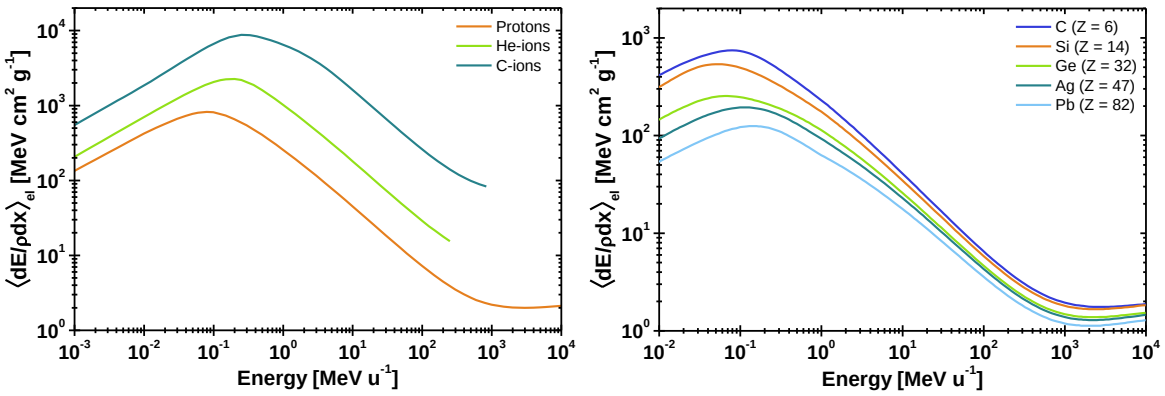

(a) Mass electronic stopping power in water. **(b)** Mass electronic stopping power of protons.

Figure 2.3.: (a) Mass electronic stopping power $\langle \mathrm{d}E/\rho \mathrm{d}x \rangle_{\mathrm{el}}$ for protons, He-, and C-ions in water as a function of the energy per atomic mass. Data from Report 90 of the International Commission on Radiation Units and Measurements (ICRU; Bethesda, MD, USA) [145]. **(b)** $\langle \mathrm{d}E/\rho \mathrm{d}x \rangle_{\mathrm{el}}$ of protons for different elemental-materials (C, Si, Ge, Ag, and Pb). Data generated using the Stopping and Range of Ions in Matter (SRIM) software [146].

Charged particles can lose energy through radiative emissions that result from their deceleration while interacting with the electrostatic field of the atomic nucleus. To take into account this, the radiative stopping power (S_{rad}) is introduced. However, at the energies used in medical applications, this effect is mostly relevant for electrons, and can be neglected for heavier particles. The mass radiative stopping power for electrons ($S^{-}_{\mathrm{rad}}/\rho$) is given by [144]:

$$\frac{S^{-}_{\mathrm{rad}}}{\rho} = \left\langle \frac{\mathrm{d}E}{\rho \mathrm{d}x} \right\rangle^{-}_{\mathrm{rad}} = 4\alpha_{\mathrm{e}} r_{\mathrm{e}}^2 N_{\mathrm{A}} \frac{Z^2}{A} E \left(\ln\left(\frac{E}{m_{\mathrm{e}}c^2} \right) - \frac{1}{3} \right), \tag{2.5}$$

where $E = m_{\mathrm{e}}c^2 + T$ is the electron initial total energy, r_{e} is the classical electron radius, α_{e} is the fine-structure constant, and N_{A} is the Avogadro's number. The total mass stopping power ($S^{-}_{\mathrm{tot}}/\rho$) due to collisional and radiative losses is calculated as the sum of S^{-}_{el}/ρ and $S^{-}_{\mathrm{rad}}/\rho$. For low-$Z$ materials, S^{-}_{el}/ρ dominates the energy loss for electrons with energies below $\sim 5 \times 10^1$ MeV (Figure 2.4).

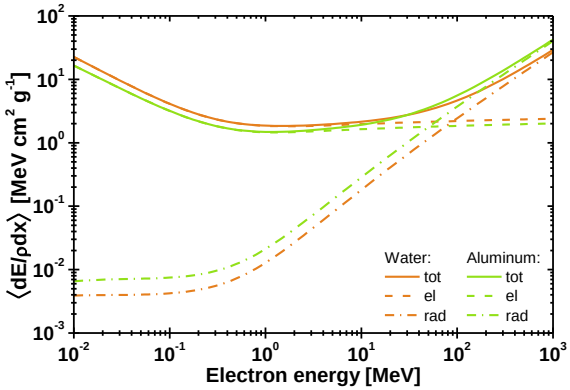

Figure 2.4.: Mass total (tot), electronic (el), and radiative (rad) stopping powers $\langle \mathrm{d}E/\rho \mathrm{d}x \rangle$ of electrons in water and aluminum, as a function of the electron kinetic energy. Data generated using ESTAR: Stopping Powers and Ranges for Electrons of the National Institute of Standards and Technology (NIST; Gaithersburg, MD, USA) [147].

The interactions presented thus far are mediated by the electromagnetic force. However, if the energy of the interacting particles is high enough, the Coulomb barrier can be exceeded, leading to nuclear reactions. In such cases, both the interacting particles and the target nuclei can be fragmented, resulting in modifications to both mass and charge. Furthermore, the fragmentation can be accompanied by the emission of secondary charged particles (protons and heavier ions) and uncharged particles (neutrons and photons) following nuclear relaxation. Several models have been proposed to describe the fragmentation process, mostly relying on semi-empirical relations and geometric assumptions [148]. Tripathi's parametrization has been widely adopted for its ability to accurately describe measured data across a wide range of energies. The nucleus-to-nucleus absorption cross section ($\sigma_{\text{n-n}}$) for the Tripathi parametrization is given by [149]:

$$\sigma_{\text{n-n}} = \pi r_0^2 (A_{\text{p}}^{1/3} + A_{\text{t}}^{1/3} + \delta_{\text{E}})^2 \left(1 - \frac{B}{E_{\text{cm}}}\right), \tag{2.6}$$

where A_{p} and A_{t} are, respectively, the atomic mass numbers of the interacting particle and target nucleus, $r_0 \approx 1.1$ fm, δ_{E} is the transparency parameter, B is the Coulomb barrier, and E_{cm} is the total energy in the center-of-mass frame of reference [149]. Figure 2.5 shows $\sigma_{\text{n-n}}$ for ^{4}He-^{12}C collisions.

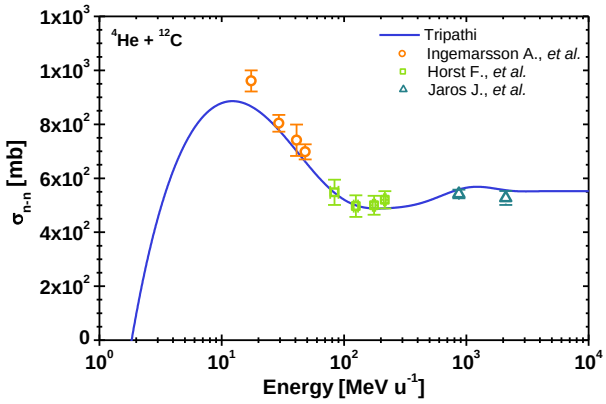

Figure 2.5.: Nucleus-to-nucleus absorption cross section ($\sigma_{\text{n-n}}$) for collisions of ^{4}He-ions in ^{12}C as a function of the projectile kinetic energy. The solid line was calculated using Tripathi's parameterization [149]. Symbols show data from Ingemarsson A., *et al.* [150], Horst F., *et al.* [151], and Jaros J., *et al.* [152].

As light-ions move through a medium, the number of primary particles decreases due to nuclear reactions. The decrease in the number of particles can be modeled as a decaying exponential function, as follows [143, 153]:

$$N_{\text{c}} = N_{\text{c},0} e^{-l/\lambda}, \tag{2.7}$$

where $N_{\text{c},0}$ is the initial number of particles, N_{c} is the remaining number of primary particles after traversing an absorber, l is the thickness of the absorber, and λ is the mean free path. Figure 2.6 depicts the attenuation of ^{12}C-ions in water. Fragmentation plays a crucial role in both proton-beam therapy (PBT) and ion-beam therapy (IBT). Particularly, fragments that are lighter than the primary ions may have ranges greater than that of the primary particles, resulting in dose delivery beyond the Bragg peak, also known as the fragmentation-tail.

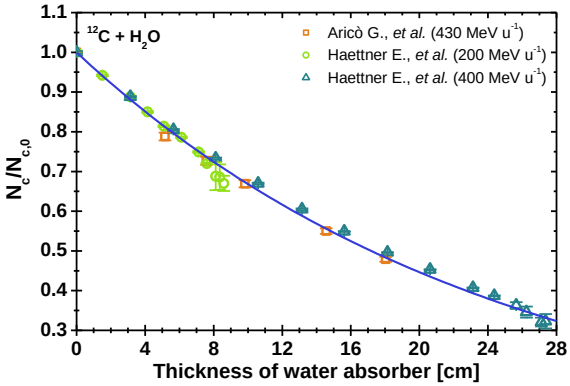

Figure 2.6.: Relative number of transmitted ^{12}C-ions ($N_c/N_{c,0}$) impinging in water as a function of the target thickness. Data from Aricò G., *et al.* [154] and Haettner E., *et al.* [153]. The solid line was generated by fitting an exponential decay function to all data points.

Energy deposition is a discrete stochastic process, and therefore it is not possible to predict the energy loss of a given single collision. The term energy straggling is often used to refer to the stochastic energy deposition. Because the number of interactions decreases with the mass thickness of the traversed material, energy straggling becomes more important for thin or low-density absorbers. Various mathematical formalisms, most notably the Landau and Landau-Vavilov theories, have been developed to model fluctuations in the energy loss (Δ_E) of charged particles [155, 156]. These theories predict that the probability density function is given by a highly skewed distribution (Figure 2.7). The most probable energy loss ($\widehat{\Delta}_\mathrm{E}$) for an absorber with a given mass thickness (x_ρ) is given by [155]:

$$\widehat{\Delta}_\mathrm{E} = \xi\left[\ln\left(\frac{2m_\mathrm{e}c^2\beta^2\gamma^2}{I}\right) + \ln\left(\frac{\xi}{I}\right) + j - \beta^2 - \delta\right], \tag{2.8}$$

where $\xi = K_\mathrm{S}(Z/A)z^2(x_\rho/\beta^2)$, $j = 0.2$, and γ is the so-called Lorentz factor.

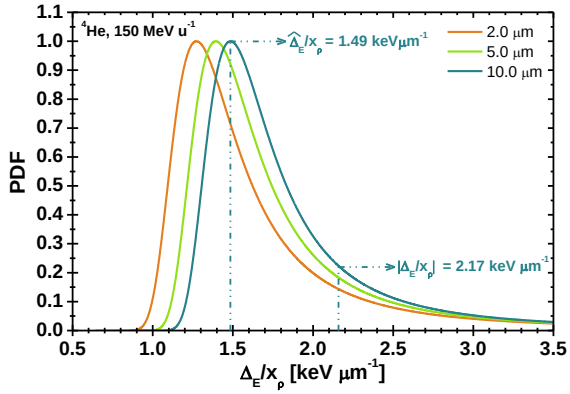

Figure 2.7.: Probability density function (PDF) according to the Landau theory for 150 MeV u^{-1} ^{4}He-ions in water as a function of the energy loss per mass thickness (Δ_E/x_ρ) for absorbers of (2.0, 5.0, and 10.0) µm thickness. The points for the most probable energy loss rate ($\widehat{\Delta}_\mathrm{E}/x_\rho$) and mean energy loss rate ($|\Delta_\mathrm{E}/x_\rho|$) in the 10.0 µm absorber are indicated.

2.2.3. Quantities used to describe the ionizing radiation

2.2.3.1. Absorbed dose

As discussed earlier, the energy deposition at the microscopic level is stochastic in nature. However, in large volumes – where a sufficiently large number of events occur – it is reasonable to define non-stochastic quantities. In such large volumes, the mean energy imparted ($\bar{\epsilon}$) is defined as follows [143]:

$$\bar{\epsilon} = R_{\text{in}} - R_{\text{out}} + \sum Q, \tag{2.9}$$

where R_{in} is the total energy of the ionizing particles the enter the volume, R_{out} is the total energy of the ionizing particles that leave the volume, and $\sum Q$ is the total change in the rest energies of all particles within the volume. With this, the absorbed dose (D) in a given volume is defined as the ratio of $\bar{\epsilon}$ to the mass (m) of the volume in the limit where m tends to zero [157]:

$$D = \lim_{m \to 0} \frac{\Delta \bar{\epsilon}}{\Delta m} = \frac{\mathrm{d}\bar{\epsilon}}{\mathrm{d}m}. \tag{2.10}$$

Nowadays the main device used to measure the absorbed dose in the clinics is the ionization chamber. In an ionization chamber, the charge generated by the ionizing radiation in the chamber's sensitive volume – usually filled with gas – is collected by applying an electric field. Since the quantity measured by ionization chambers is charge or current, extremely robust traceability chains have been established to reference laboratories in which ionization chambers are calibrated in terms of absorbed dose in water [158]. The primary reference instrument to establish the absorbed dose is the water calorimeter. The specific derived-unit used for the aborted dose is the Gray ($\text{Gy} = \text{J}\,\text{kg}^{-1}$) [159].

2.2.3.2. LET

The linear energy transfer (LET) concept was introduced by the first time to take into account the energy lost by ionizing particles while traversing a medium and the energy gained by the medium from both ionizations and excitations [160]. The ICRU formally defines the LET (also known as restricted linear collision stopping power) as follows [161]:[2.d]

$$L_\Delta = \lim_{l \to 0} \left. \frac{\Delta \bar{E}}{\Delta l} \right|_\Delta = \left. \frac{\mathrm{d}\bar{E}}{\mathrm{d}l} \right|_\Delta, \tag{2.11}$$

where $\bar{E}$ is the mean energy-loss due to collisions with energy transfers below the energy cut-off value Δ and l is the distance transited by the particle. The unrestricted LET corresponds to the case when all energy transfers are considered (i.e., $\Delta = \infty$) and is often denoted by L_∞ or, for brevity, by L. For such a limit, L_∞ is numerically equal to S_{el}. As with absorbed dose, the LET is a non-stochastic quantity. For indirectly ionizing radiation, the LET corresponds to that of the released secondary charged particles.

Radiation fields are often characterized by an LET distribution. In such a case, the fraction of particles having an LET within the infinitesimal interval $[L, L + \mathrm{d}L]$ can be written as

[2.d] For the sake of clarity, LET is used in this thesis to refer to the concept of linear energy transfer, while L is used as the mathematical symbol representing LET.

$F(L)\,\mathrm{d}L$, where $F(L)$ is the probability density function in fluence. If $F(L)$ is normalized to the unity, the track average linear energy transfer (L_F) can be calculated as [161]:

$$L_F = \int_0^\infty L\, F(L)\,\mathrm{d}L. \tag{2.12}$$

Analogously, if $D(L)\,\mathrm{d}L$ represents the absorbed dose delivered by the particles within the interval $[L, L+\mathrm{d}L]$, the dose average linear energy transfer (L_D) can be calculated as [161]:

$$L_D = \int_0^\infty L\, D(L)\,\mathrm{d}L, \tag{2.13}$$

where $D(L)$ is the probability density function in dose. Mathematically, L_F is the first moment of $F(L)$ and L_D is the ratio of the second moment of $F(L)$ and L_F. Thus, it can be shown that $D(L) = L\, F(L)/L_F$ and Equation 2.13 can be rewritten as:

$$L_D = \frac{1}{L_F}\int_0^\infty L^2\, F(L)\,\mathrm{d}L. \tag{2.14}$$

From Equations 2.12 and 2.13 it follows that for monoenergetic charged particle beams $L_F = L_D$. The LET is usually reported with water as the reference material and expressed in units of $\mathrm{keV\,\mu m^{-1}}$ or, less commonly, $\mathrm{MeV\,cm^{-1}}$. Unlike absorbed dose, no reference instrument exist to measure the LET.

Making reference to the term ionization density, the LET is commonly used as a quantitative parameter to distinguish between sparsely and densely ionizing radiation. However, arbitrary values are still employed to make this distinction, and certain type of particles are commonly directly referred to as either sparsely or densely ionizing radiation. For example, γ- and X-rays are commonly referred to as sparsely ionizing radiation, despite the fact that the LET associated with low-energy photons can be higher than that of protons, which are sometimes referred to as densely ionizing radiation.

2.3. Radiobiology

Ionizing radiation is characterized by the profound effects it can produce on living organisms. These effects are varied and can occur at all the organizational levels of life. Examples include: cell death, early and late tissue responses (e.g., leukopenia, erythema, fibrosis and carcinogenesis), organ failure, organism death, and hereditary defects, to name a few. Remarkably, the effects of ionizing radiation can take place even when minute amounts of energy are deposited. This derives from the ability that ionizing radiation has to interact with living cells at the molecular level and trigger a cascade of events that can lead to impaired biological functioning [10, 162]. As the DNA molecule encodes the instructions for proper cell functioning, it stands as the primary and most crucial target for ionizing radiation. Therefore, understanding how ionizing radiation interacts and alters the DNA is essential in comprehending its effects. The processes leading to the biological response take place in succession and can be divided into three main phases, namely the physical, chemical and biological phases [10]. These phases take place on radically different – often overlapping – time scales [162].

The physical phase consists of the interaction between ionizing radiation and target atoms or molecules, causing ionizations, excitations or nuclear reactions in the process. This phase goes from the initial interactions of the ionizing radiation with the medium to the thermalization of the primary and secondary ionizing particles. During this phase, ionizing radiation can

directly interact with the DNA, resulting in damage (Figure 2.8(a)). The latter is traditionally referred to as direct action or direct damage. The physical phase takes place in a time-scale going from (1×10^{-18} to 1×10^{-11}) s [162].

The chemical phase is characterized by the formation of reactive chemical species that diffuse to cause damage to the DNA (Figure 2.8(b)). Since this damage is mediated by an intermediary between ionizing radiation and DNA, the process is called indirect action or indirect damage. Because the cell medium is mostly aqueous, the primary molecule involved in the indirect action of radiation is the water molecule, through a process known as water radiolysis. Examples of free radicals produced in water during the chemical phase are the hydroxyl radical (OH·) and the hydrogen radical (H·). Free radicals consist of highly reactive atoms or molecules due to orbital electron imbalances. Free radicals can also combine with each other or other molecules to form non-radical chemical species that are toxic to the cell, such as hydrogen peroxide (H_2O_2). The chemical phase also includes reactions from molecules and enzymes as part of the cellular mechanisms used to cope with oxidative stress [163]. The chemical phase occurs in a time-scale going from (1×10^{-12} to 1×10^{1}) s [162].

The biological phase begins with enzymatic reactions aiming to repair the radiation-induced lesions. The early biological phase is also characterized by inflammatory responses and reactions from the immune system [164]. Depending on the extent of the damage, cells may fully recover, undergo defective repair, or experience cell death.[2.e] The loss of an extended number of functional cells – particularly stem cells – through cell death and consequential tissue remodeling is what gives rise to a number of radiation effects. Some effects can become apparent within hours or days after radiation exposure and may be reversible, while others may take months or even years to manifest and can sometimes be long-lasting and irreversible. Cells carrying a considerable amount of residual DNA damage can lead to carcinogenesis. In addition, changes in the genetic material can skip to next generations and cause heredetary deffects. The biological phase occurs in a time-scale going from (1×10^{-2} to 1×10^{9}) s [162].

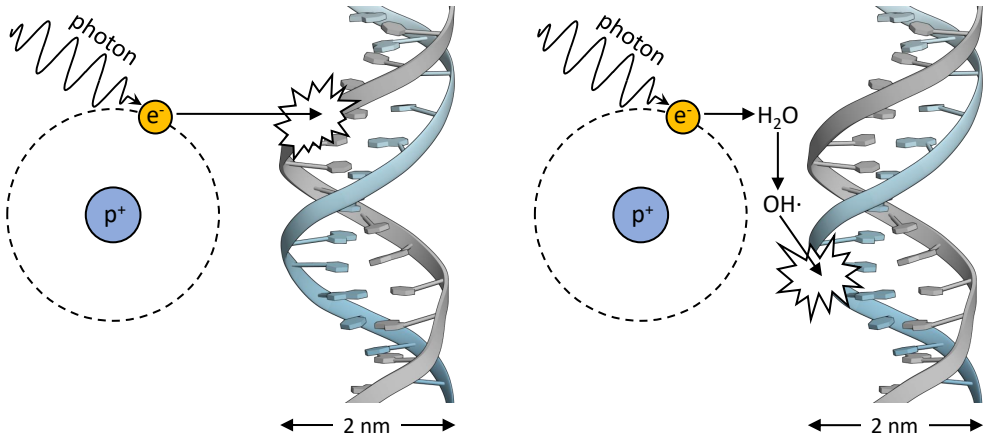

(a) Direct action of radiation **(b)** Indirect action of radiation

Figure 2.8.: A photon releases an electron from the medium which **(a)** interacts with the DNA, producing direct damage, or **(b)** generates an OH· free radical through water radiolysis, causing indirect damage to the DNA. For simplicity, only the cases of a photon-electron interaction and the production of an OH· free radical are shown. Molecule model from the Research Collaboratory for Structural Bioinformatics (RCSB) Protein Data Bank (PDB), protein feature view: 5CBZ [167].

[2.e] Cell death is defined as "*Irreversible degeneration of vital cellular functions culminating in the loss of cellular integrity*" [165]. Cell death can occur through different mechanisms, such as: apoptosis, necrosis, mitotic catastrophe, autophagy and senescence [166]. Cell death includes the loss of clonogenic capacity.

Some radiation effects only manifest after a certain threshold dose is exceeded. Once this threshold is exceeded, the severity of these effects intensifies with increasing dose. These effects are known as deterministic [168]. As an example, the severity of radiation-induced skin reactions increases with the dose, progressing from skin flushing to burn-like reactions. In contrast, the probability for certain effects to occur will increase with the dose, yet their severity will remain constant. These effects are categorized as stochastic [169]. For instance, the probability of developing cancer increases with the absorbed dose, but the severity of the cancer remains unchanged.

As mentioned earlier, the DNA molecule stands as the primary target associated with the biological effect of ionizing radiation. Depending on the proximity between energy transfer events and the local amount of the toxic radiation-induced chemical species, ionizing radiation can cause single-strand breaks (SSBs) and double-strand breaks (DSBs) in the DNA double helical structure [170]. Since densely ionizing radiation is characterized by a high spatial frequency of energy transfer events, it is likely to yield a higher number of DSBs when compared to sparsely ionizing radiation [171]. SSBs tend to be readily repaired by the cell without significant effects. In contrast, the repair of DSBs is more prone to failure and can lead to further biological consequences. Thus, DSBs are considered to be the main lesions of interests for describing radiation effects [10].

2.3.1. Linear-quadratic model

When a group of proliferating cells is exposed to ionizing radiation, some of the cells will maintain their ability to replicate, while others will lose their reproductive integrity [10]. Generally, when the dose to which cells are exposed is increased while maintaining all other variables constant, a higher number of cells will lose their ability to replicate and form colonies (i.e., clonogenic capacity) [162]. This forms the basis of the clonogenic cell survival assay, where cell survival is studied as a function of the dose by quantifying the number of colonies formed after exposure. Semi-empirically, this can be modeled using an exponential function with the following form [172]:

$$SF = e^{-(\alpha D + \beta D^2)}, \tag{2.15}$$

where SF is the survival fraction relative to an unirradiated control sample, α and β are cell- or tissue-specific parameters, and D is the absorbed dose. Equation 2.15 is often referred to as the linear-quadratic model (LQM). The curvature or steepness of the LQM curve can be quantified by the ratio between α and β (α/β-ratio). The value of the α/β-ratio is given in units of Gy and corresponds to the absorbed dose at which the exponential cell-killing components αD and βD^2 are equal (Figure 2.9) [141, 172]. The α/β-ratio is often used to describe the radiosensitivity of a given system. Particularly, cells with lower α/β-ratio values are considered less radiosensitive to single dose exposures.

Although the biological effects of ionizing radiation involve numerous variables and complex processes, the LQM, despite its simplicity, has proven to be a useful tool for interpreting and describing the response of various systems. For instance, in the clinics the LQM is frequently used to compare the effects of different fractionation schemes and predict the benefits of adopting certain ones [173]. In addition, it is often used as the basis to estimate the cell-killing efficiency of different types of radiation, as explained below (Section 2.3.2). However, it is important to note that the applicability of the LQM is limited to a specific range of doses, and reformulations may be necessary to extend its validity [10, 174].

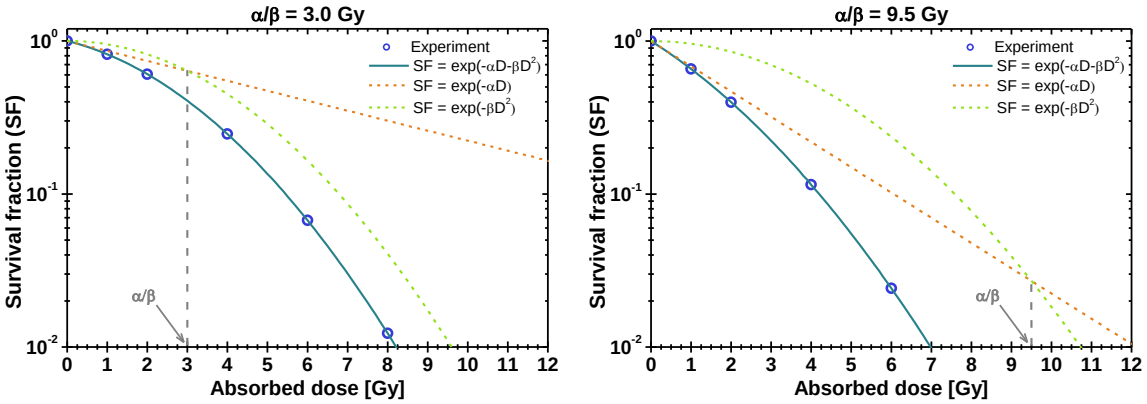

(a) Survival fraction with $\alpha/\beta = 3.0$ Gy. **(b)** Survival fraction with $\alpha/\beta = 9.5$ Gy.

Figure 2.9.: Survival fraction (SF) as a function of the absorbed dose (D) for two cell lines having different α and β parameters for the linear-quadratic model (LQM). Data points were generated assuming hypothetical scenarios, with **(a)** $\alpha/\beta = 3.0$ Gy and **(b)** $\alpha/\beta = 9.5$ Gy. The solid curves correspond to the LQM. Dashed curves show the cell-killing components $SF = e^{-\alpha D}$ and $SF = e^{-\beta D^2}$, with vertical dashed lines indicating their intersection and corresponding α/β-ratio values.

2.3.2. RBE

Cells of the same type may exhibit different survival capacities when exposed under identical conditions to the same absorbed dose but to different types of radiation. To account for this effect, the concept of relative biological effectiveness (RBE) is introduced. According to the ICRU, the RBE is defined as the ratio of two absorbed doses that result in the same biological effect (isoeffect) when all other parameters are kept constant. This can be expressed as [175]:

$$\mathrm{RBE} = \left.\frac{D_\mathrm{r}}{D_\mathrm{t}}\right|_\mathrm{isoeffect}, \tag{2.16}$$

where D_r and D_t are the doses from the reference and test radiation, respectively. Typical reference radiation types are X-rays (e.g., 200 kV or 6 MV X-rays) or γ-rays (e.g., from ^{137}Cs or ^{60}Co radioactive sources). These types of radiation are used because the LET associated with the secondary electrons they produce is considered low ($L_F \sim$ (0.2 to 1.7) keV µm^{-1}) [161]. It should be noted that changes in the reference radiation can modify the value of the RBE, even between photons, and is therefore an important parameter to consider [7]. For applications in PBT and IBT, high-energy X-rays are the preferred reference radiation, as the majority of the available clinical data has been derived from this type of radiation.

It follows from Equation 2.16 that if a lower test radiation dose is required to achieve the same biological effect (e.g., cell survival) as the reference radiation, then the RBE is greater than unity. In this case, the test radiation is said to be more effective, as depicted in Figure 2.10(a) for particles with different LET. In general, the RBE steadily increases with the LET up to a maximum located between (100 and 200) keV µm^{-1}, after which it decreases due to overkilling (Figure 2.10(b)). Overkilling occurs when the absorbed dose from high-LET radiation in a cell exceeds the amount needed to kill the cell. This results in wasted energy that could otherwise have been used to kill other cells. When parameterized in terms of the LET, the RBE also depends on the particle type [176]. This means that two different ion species with the same LET can have different RBE values. According to the LQM, the RBE is also dependent on the absorbed dose and generally increases with decreasing dose.

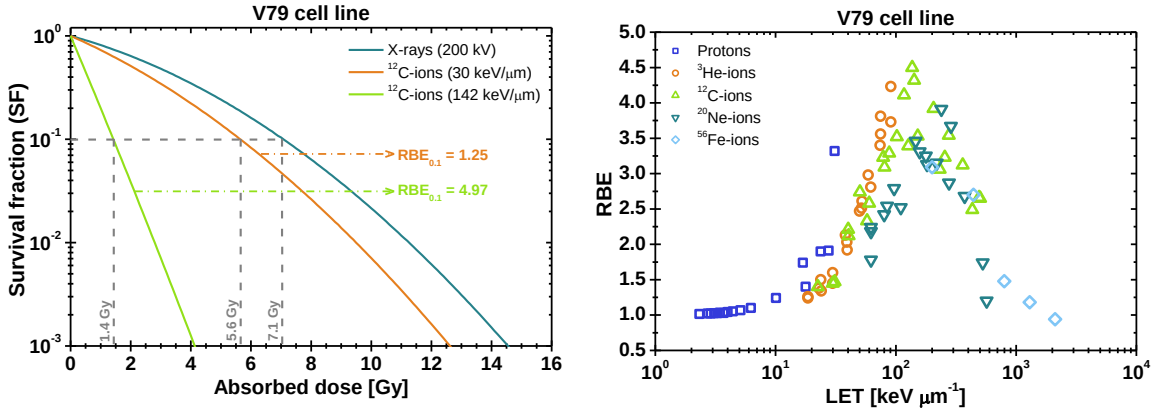

(a) Comparison of survival curves.

(b) RBE as a function of the LET.

Figure 2.10.: (a) Survival fraction (SF) as a function of the absorbed dose (D) after exposure to 200 kV X-rays and ^{12}C-ions. Dashed gray lines show D at 10 % survival. Dashed-dotted color lines mark the curve associated with the displayed relative biological effectiveness (RBE) at 10 % survival ($\mathrm{RBE}_{0.1}$). SF curves generated from reported data [8]. **(b)** RBE as a funtion of the linear energy transfer (LET) in water for protons, ^{3}He-, ^{12}C-, ^{20}Ne-, and ^{56}Fe-ions. RBE values were calculated from data compiled on the Particle Irradiation Data Ensemble (PIDE) version 3.2 [178]. All RBE values were normalized relative to the RBE of 200 kV X-rays and, due to ambiguities in reporting the original data, are presented as a function of LET rather than its averages. Both panels show data for chinese hamster lung fibroblast (V79) cells under aerobic conditions and asynchronous cell division.

The RBE also depends on parameters such as dose rate, dose fractionation, stage of the cell cycle, studied endpoint, biological system and oxygen concentrations, to name some of the most recognized factors [7, 175, 177].

It is worth noting that the RBE concept is not exclusive to the LQM, and other dose-response curves can be used for its study. Notable examples are the tumor control probability (TCP) and normal tissue complication probability (NTCP) models. In these models, doses from two types of radiation resulting in the same probabilities of local tumor control (TCP) or undesirable side effects (NTCP) are used to assess the RBE [108, 112].

2.3.3. RBE models

Several RBE models have been developed to take into account the RBE in PBT and IBT for patient treatment [83, 177, 179]. These models range from mechanistic to phenomenological. All of the models used in this thesis are phenomenological and based on the LQM. According to Equation 2.15, if the cell survival is the same for the reference and test radiation, then:

$$\alpha_\mathrm{r} D_\mathrm{r} + \beta_\mathrm{r} D_\mathrm{r}^2 = \alpha_\mathrm{t} D_\mathrm{t} + \beta_\mathrm{t} D_\mathrm{t}^2. \tag{2.17}$$

By solving for D_r and diving the solution by D_t the following expression is obtained for RBE:

$$\mathrm{RBE} := \frac{D_\mathrm{r}}{D_\mathrm{t}} = -\frac{1}{2D_\mathrm{t}}\left(\frac{\alpha}{\beta}\right)_\mathrm{r} + \frac{1}{D_\mathrm{t}}\sqrt{\frac{1}{4}\left(\frac{\alpha}{\beta}\right)_\mathrm{r}^2 + \frac{\alpha_\mathrm{t}}{\alpha_\mathrm{r}}\left(\frac{\alpha}{\beta}\right)_\mathrm{r} D_\mathrm{t} + \frac{\beta_\mathrm{t}}{\beta_\mathrm{r}} D_\mathrm{t}^2}, \tag{2.18}$$

where $(\alpha/\beta)_\mathrm{r}$ is the α/β-ratio for the reference radiation. Equation 2.18 can be expressed in terms of RBE in the limits $D_\mathrm{r} \to 0$ ($\mathrm{RBE}_\mathrm{max} = \alpha_\mathrm{t}/\alpha_\mathrm{r}$) and $D_\mathrm{r} \to \infty$ ($\mathrm{RBE}_\mathrm{min} = \sqrt{\beta_\mathrm{t}/\beta_\mathrm{r}}$), as follows [86, 180]:

$$\mathrm{RBE} = -\frac{1}{2D_\mathrm{t}}\left(\frac{\alpha}{\beta}\right)_\mathrm{r} + \frac{1}{D_\mathrm{t}}\sqrt{\frac{1}{4}\left(\frac{\alpha}{\beta}\right)_\mathrm{r}^2 + \mathrm{RBE}_\mathrm{max}\left(\frac{\alpha}{\beta}\right)_\mathrm{r} D_\mathrm{t} + \mathrm{RBE}_\mathrm{min}^2 D_\mathrm{t}^2}. \tag{2.19}$$

If expressions for $\mathrm{RBE}_\mathrm{max}$ and $\mathrm{RBE}_\mathrm{min}$ can be established, this representation enables the calculation of the RBE as a function of the absorbed dose and LET for tissues with known $(\alpha/\beta)_\mathrm{r}$ values. This enables to take advantage of the fact that the α/β-ratio for photons is well-documented across a variety of cell lines and tissues, extending clinical observations made in conventional radiotherapy to light-ions. Table 2.1 summarizes the empirical functional forms proposed for $\mathrm{RBE}_\mathrm{max}$ and $\mathrm{RBE}_\mathrm{min}$ for protons and He-ions, which were utilized in this thesis. In all these models, the free parameters were obtained by fitting to data from cell survival clonogenic assays as a function of the LET [83, 85–87].

Other prominent models that have been developed and used for applications in PBT and IBT, especially for C-ions, are the so-called modified microdosimetric kinetic model (mMKM) and the local effect model (LEM) [177]. These models are based on stochastic energy deposition distributions (mMKM) and amorphous track structure models (LEM) [65, 181]. In contrast to the original microdosimetric kinetic model (MKM) [182], the mMKM incorporates non-Poisson distribution effects to account for clustered lethal lesions, describing overkilling in the high-LET regime [65, 183]. For LEM, various versions have been developed. While initial versions (LEM I to LEM III) focus on the local energy distribution, LEM IV also considers the spatial distribution of clustered DSBs within the DNA structure [184].

Table 2.1.: Phenomenological models based on the linear-quadratic model (LQM) for relative biological effectiveness (RBE) calculations. Each model is named after the last name of the first author in the publication where it was first published.

Model	$\mathbf{RBE_{max}}$	$\mathbf{RBE^2_{min}}$	**Reference**
Wedenberg	$1 + \frac{q}{(\alpha/\beta)_\mathrm{r}} L_D$,	1.0	[85]
	$q = 4.34 \times 10^{-1}$ Gy µm keV^{-1}		
McNamara	$p_0 + \frac{p_1}{(\alpha/\beta)_\mathrm{r}} L_D$,	$(p_2 + p_3\sqrt{(\alpha/\beta)_\mathrm{r}} L_D)^2$,	[86]
	$p_0 = 9.91 \times 10^{-1}$,	$p_2 = 1.10$,	
	$p_1 = 3.56 \times 10^{-1}$ Gy µm keV^{-1}	$p_3 = -3.87 \times 10^{-3}$ Gy$^{-1/2}$ µm keV^{-1}	
Mairani*	$1 + \left(k_0 + \frac{1}{(\alpha/\beta)_\mathrm{r}}\right) k_1 L_F e^{-k_2 L_F^2}$,	$b_0 e^{-((L_F - b_1)/b_2)^2}$,	[83]
	$k_0 = 1.40 \times 10^{-1}$ Gy^{-1},	$b_0 = 2.66$,	
	$k_1 = 2.56 \times 10^{-1}$ Gy µm keV^{-1},	$b_1 = 6.26 \times 10^{1}$ keV µm^{-1},	
	$k_2 = 2.36 \times 10^{-5}$ µm^2 keV^{-2}	$b_2 = 4.81 \times 10^{1}$ keV µm^{-1}	
Mairani†	$1 + \left(k_0' + \frac{1}{(\alpha/\beta)_\mathrm{r}}\right) k_1' L_D$,	1.0	[87]
	$k_0' = 2.32 \times 10^{-1}$ Gy^{-1},		
	$k_1' = 1.59 \times 10^{-1}$ Gy µm keV^{-1}		

Abbreviations: $\mathrm{RBE}_\mathrm{max}$ = linear-quadratic model α parameter ratio between the reference and test radiations, $\mathrm{RBE}^2_\mathrm{min}$ = linear-quadratic model β parameter ratio between the reference and test radiations, $(\alpha/\beta)_\mathrm{r}$ = ratio between the linear-quadratic model α and β parameters for the reference radiation, L_D = dose average linear energy transfer, L_F = track average linear energy transfer.

Notes: The Wedenberg and McNamara models, originally developed for protons, are assumed to be also applicable to heavier H-ions. The Mairani models are intended for He-ion beams, including all isotopes.

*Model developed for single-particle applications. Thus, it is assumed that L_F can be used as an input quantity.

†Model developed specifically for using L_D as the input quantity.

2.4. Radiotherapy

Radiotherapy is the medical application of ionizing radiation for the treatment and management of diseases. The primary objective is to induce the death of diseased cells through the targeted application of ionizing radiation. While radiotherapy is predominantly associated with cancer treatment, it is also used to treat non-oncological diseases [185]. In radiotherapy, the radiation source can be positioned at a distance from the patient (teletherapy) or in direct contact – superficial, interstitial, or intracavitary – with the patient (brachytherapy) [186].

In principle, any form of ionizing radiation can be utilized in radiotherapy. However, the preference for a specific type is determined by factors such as localization of the treatment site, medical indication, treatment intention, induced biological effects, and availability. With more than 15 000 teletherapy units and 3 000 brachytherapy units reported worldwide [187], it can be safely stated that photons and electrons are the most commonly used particles in radiotherapy nowadays (Figure 2.11(a)). This preference can be attributed to the fact that accelerating electrons, which can effectively produce X-rays, is technologically less challenging and more economically viable compared to generating beams of heavier particles. Additionally, the availability of radiation sources emitting β^-- and γ-rays with suitable energies further supports the utilization of these particles. Already at the mid-1940s, the idea of using protons and heavier ions for cancer treatment started to flourish [188]. As further explained below (Section 2.4.2), compelling reasons support the utilization of these particles. However, a significant limitation has been the technological challenges and high costs associated with accelerating these particles to the energies required to treat deep-seated tumors, as well as manufacturing the hardware necessary to deliver the radiation beams with the required accuracy and flexibility [189]. Another factor is the high-cost of operation with lower patient throughput compared to other modalities. As a result, the availability of centers offering light-ion treatments remains relatively low. Despite these challenges, the past decade has seen a rapid increase in the number of PBT and IBT centers (Figure 2.11(b)).

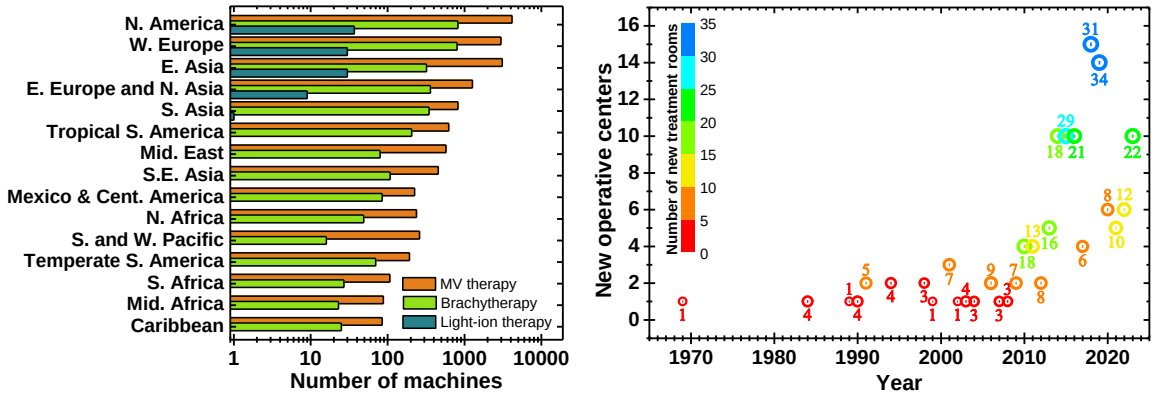

(a) Number of radiotherapy machines per region. **(b)** Proton- and ion-beam therapy centers over time.

Figure 2.11.: (a) Bar chart illustrating the distribution of combined proton-beam therapy (PBT) and ion-beam therapy (IBT) centers (Light-ion therapy), brachytherapy devices (Brachytherapy), and MV machines using either electrons, X-rays, or both (MV therapy). Data per geographic region based on the World Health Organization (WHO; Geneva, Switzerland) subdivision and retrieved from the DIrectory of RAdiotherapy Centers (DIRAC), Status of Radiation Therapy Equipment of the International Atomic Energy Agency (IAEA; Vienna, Austria) [187]. **(b)** Bubble plot depicting the temporal evolution of combined PBT and IBT centers. The bubble size, numbers, and color coding represent the total number of treatment rooms. Data from the Particle Therapy Co-Operative Group (PTCOG) webpage, Particle therapy facilities in clinical operation (update January 2024) [9].

2.4.1. Conventional external radiotherapy

In the context of this thesis, conventional radiotherapy refers to any modality of teletherapy involving photons and electrons having energies on the order of MeV. These particles are obtained by accelerating electrons in dedicated clinical linear accelerators [139]. For therapies using electron beams, quasi-monoenergetic electrons are delivered directly. In the case of X-rays, beams are produced by impinging an electron beam on a high-Z target (usually a tungsten-based alloy). This process produces broad X-ray spectra with energies up to those of the electrons used to generate them (Figure 2.12(a)) [190]. It is worth noting that the same machine is often used to produce electron and X-ray beams by simply removing the high-Z target. In addition to X-rays, some modern machines still use ^{60}Co as a source of γ-rays.

As a consequence of the different processes governing their interactions, electrons and X-rays exhibit distinct depth dose distributions (Figure 2.12(b)). At the energies used clinically, the depth dose of electrons is characterized by a small increase after the patient's surface to a peak or plateau, the width of which depends on the energy of the primary electrons, followed by a marked decrease. Depending on the initial energy of the electrons, the production of *bremsstrahlung* X-rays within the patient can result in a dose tail that extends beyond the range of the electrons. For X-rays, the dose increases rapidly after the patient surface to a maximum, after which the dose decreases almost exponentially. For both electrons and X-rays, the position of the maximum dose is shifted to greater depths with increasing energy. The higher ratio of maximum dose to entrance dose allows for better skin sparing with X-rays. Electrons, due to their short range, can only be used to treat superficial lesions, while X-rays allow the treatment of deep-seated lesions.

Since photons attenuate rather than stop, it is inevitable that a significant amount of dose will be delivered behind the treated volume. In practice, multiple beams are delivered from different angles to place the maximum dose within the treated volume, albeit at the expense of irradiating a larger amount of healthy tissue. To reduce the dose to adjacent healthy tissue and further escalate the dose to the target volume, the beams are shaped to the projection of the tumor at each angle [191]. In addition, the photon fluence can be modulated at each angle to further reduce dose to critical organs [192].

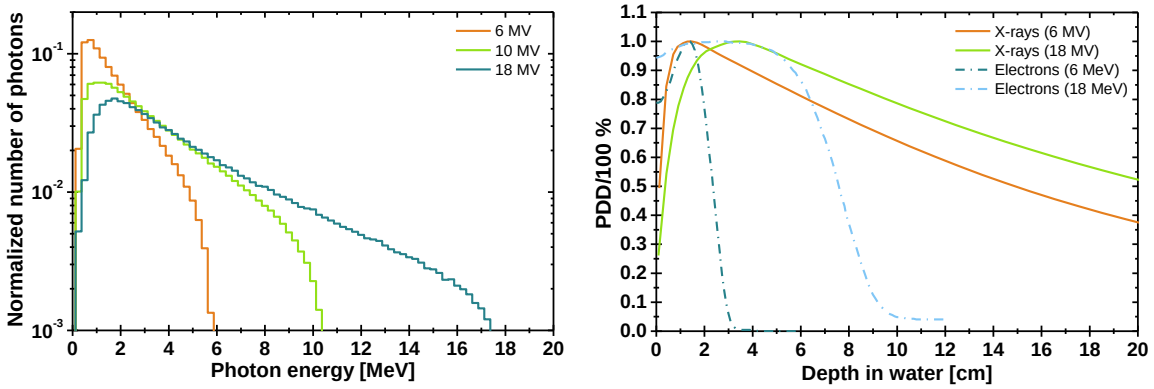

(a) MV X-ray spectra

(b) X-ray and electron depth dose profiles

Figure 2.12.: (a) (6, 10 and 18) MV X-ray spectra normalized with respect to the total number of particles. Data from Sheikh-Bagheri D. and Rogers D. W. O. [190]. **(b)** Normalized percentage depth dose (PDD) for (6 and 18) MV X-rays and (6 and 18) MeV electrons. PDDs are shown normalized to 100 %. X-ray PDDs adapted from Sheikh-Bagheri D. and Rogers D. W. O. [190]. Electron PDDs adapted from Łukomska S., *et al.* [193].

2.4.2. Proton-beam therapy and ion-beam therapy

Several ion species, ranging from protons to Ar-ions, have been proposed and investigated for applications in radiotherapy [194, 195]. However, based on the outcomes during the early era of PBT and IBT, and due to technological advances, protons and C-ions emerged as favored options over time. Consequently, protons and C-ions are now the primary heavy charged particles used clinically, with protons standing as the leading choice [9]. It is worth noting that at the Heidelberg Ion-Beam Therapy Center (HIT; Heidelberg, Germany), there is a renewed interest in reintroducing He-ions, with plans to start treating patients with this particle species on a regular basis; the first patient has already been treated [196].

To be able to reach any location in the human body and treat deep-seated tumors, light-ions with energies in the range of tens to hundreds of MeV u^{-1} are required. These energies are achieved by accelerating the ions using either cyclotrons or synchrotrons [197]. In cyclotrons, degraders are necessary to decrease and adjust the energy in accordance with treatment requirements, as the extraction energy is mostly fixed. In contrast, synchrotrons do not require additional elements to modify the energy, as energy selection occurs within the accelerator. For both types of systems, a transportation line is necessary to reach the treatment room. Delivery can be done using either fixed ports or gantries. However, due to the high costs associated with gantries for C-ions, gantries are far more common for protons [9]. Two types of techniques are used to deliver and shape the beam: passive scattering and active scanning. In passive scattering systems, dose conformation is achieved through patient-specific collimators and compensators [198]. For active scanning systems, the dose is conformed using pencil beams with raster scanning and in-flight energy selection [199]. Currently, active scanning is the standard in clinical systems as it can help reduce the dose received by healthy tissues.

As discussed in the previous subsection, the treatment of deep-seated tumors with X-rays can result in the exposure of a significant amount of healthy tissue laying behind the target volume. In contrast to photons, protons and heavier ions gradually lose their energy while traveling through the tissue and come to rest after losing all of their energy. Therefore, if the energy is precisely selected in a way that the light-ions stop at the target volume, the tissue behind remains unirradiated [200]. Furthermore, in accordance with the stopping power formula (Equation 2.3), the amount of energy deposited increases as the energy decreases, resulting in a sharp increase in the absorbed dose near the maximum range of the light-ions [6]. This results in an advantageous depth dose profile known as Bragg curve (Figure 2.13(a)). The Bragg peak is the region of the Bragg curve where there is a sharp increase in the absorbed dose, just before the ions come to a stop. Given that the width of a single Bragg peak is usually insufficient to cover the entire extent of the target volume, light-ions with multiple energies are delivered, resulting in what is known as a spread-out Bragg peak (SOBP) [201].

In addition to the Bragg peak, the energy loss of light-ions also results in a significant increase in LET near the point where particles come to a stop (Figure 2.13(b)), which, in turn, can lead to an enhanced RBE in the vicinity of the Bragg peak [200]. Since an elevated RBE translates into higher cell-killing efficiency, this can be taken advantage of by placing the higher RBE within the treated volume, further enhancing the therapeutic advantages of light-ions. However, simultaneously, care must be taken to avoid placing high RBE components within healthy tissues. To this end, treatment planning techniques and systems that take into account LET and/or RBE have been developed [12–18]. These systems enable the setting of constraints to avoid critical structures, guarantee a homogeneous RBE-weighted dose (that is RBE times the absorbed dose) delivered to the treatment volume, or even push the high LET to more radioresistant subvolumes of tumors.

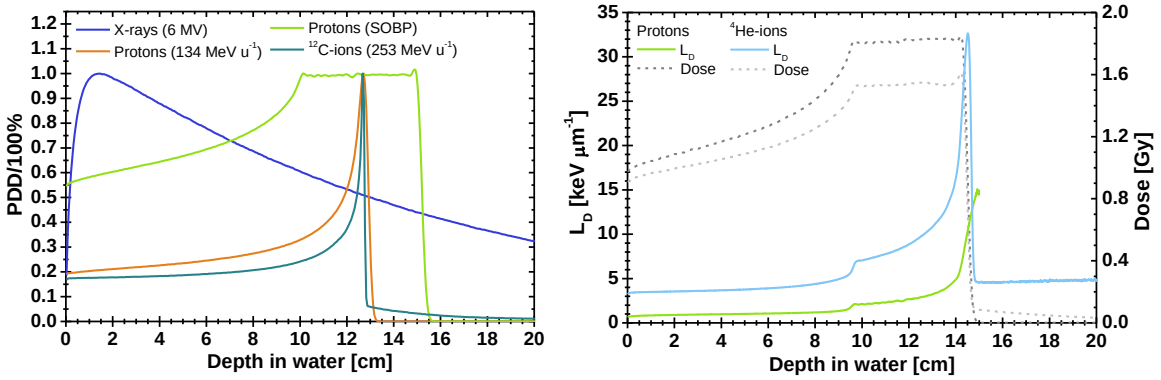

(a) X-ray and light-ion depth dose profiles

(b) Proton and ^{4}He-ion depth L_D profiles

Figure 2.13.: (a) Normalized percentage depth dose (PDD) for 6 MV X-rays, 134 MeV u^{-1} protons, 253 MeV u^{-1} ^{12}C-ions, and a proton spread-out Bragg peak (SOBP) comprising 18 energies between (117 and 147) MeV u^{-1}. PDDs are shown normalized to 100 %. **(b)** In-depth dose average linear energy transfer (L_D) distributions for proton and ^{4}He-ion SOBPs comprising 18 energies between (117 and 147) MeV u^{-1} and 17 energies between (120 and 148) MeV u^{-1}, respectively. Depth dose profiles are shown for reference. These have been optimized to deliver (1.82 and 1.54) Gy at the proton and ^{4}He-ion SOBPs, respectively. In all cases, data were obtained from Monte Carlo simulations for fields of 4 × 4 cm^2 at the water phantom surface and scoring all quantities using a bin size of 0.05 cm in the depth direction and integrating over an area of 2 × 2 cm^2 around the central beam-axis.

The stochastic energy deposition of light-ions in matter leads to energy straggling (Subsection 2.2.2), which causes range straggling and broadening of the Bragg peak [6]. Empirically, if the range distribution is approximated by a Gaussian function, the variance of the distribution is nearly directly proportional to the range and inversely proportional to the square root of the primary-ion atomic number [202]. Consequently, for ions of the same type, the Bragg peak widens at higher energies, while increasing the ion's mass leads to a sharper peak (Figures 2.13(a) and 2.14). For C-ions, passive devices are essential to broaden the Bragg peak and minimize the number of energies required to achieve smooth SOBPs [203].

The numerous Coulomb interactions that light-ions undergo while passing through matter cause them to deviate from their initial trajectory. Generally, at each interaction, the scattering angle is small. However, the accumulation of scattering angles results in beam broadening with depth, increasing the extent of the lateral penumbra and exposing tissue adjacent to the beam [200]. Multiple scattering theories show that scattering angles increase proportionally with the square of the ion charge and decrease proportionally with the square of the ion kinetic energy [143]. Since the difference in energy required to reach the same depth with two ions having different charges is significantly higher than the difference in their charges, heavier ions exhibit sharper lateral penumbras (Figures 2.14(a) and 2.14(b)). This reduction in the dose to adjacent tissues contributes to the physical advantages that motivate the use of ions heavier than protons, such as He- and C-ions. It is worth noting that even X-rays can produce a sharper lateral penumbra than protons (Figures 2.14(a) and 2.14(c)).

At the energies used in PBT and IBT, nucleus-to-nucleus interactions take place, resulting in the presence of a significant number of nuclear fragments [148]. The spectrum of these fragments may include all ion-species with atomic numbers equal to or less than that of the primary particles, including isotopes of each [154]. However, the most common fragments produced in nucleus-to-nucleus interactions are H-ions (i.e., protons, ^{2}H-, and ^{3}H-ions) and He-ions [48, 154]. Short-range ion-species heavier than the primary particles are also produced as a by-product of nuclear reactions. However, these are generally neglected and their effects

are still under debate. Although the energy carried by light-fragments is generally lower than that of the primary-ions, these can have ranges greater than those of the primary particles due to their lower charge [6]. As mentioned previously (Subsection 2.2.2), this results in the fragmentation tail extending beyond the Bragg peak (Figure 2.14(b)). Since the RBE depends on the ion-species, another consequence is that the biological effect of all fragments, weighted relative to the spectral distribution, should be considered when determining the RBE. Considering the above, a detector with spectroscopic capabilities can be highly advantageous for LET measurements and RBE assessment in PBT and IBT.

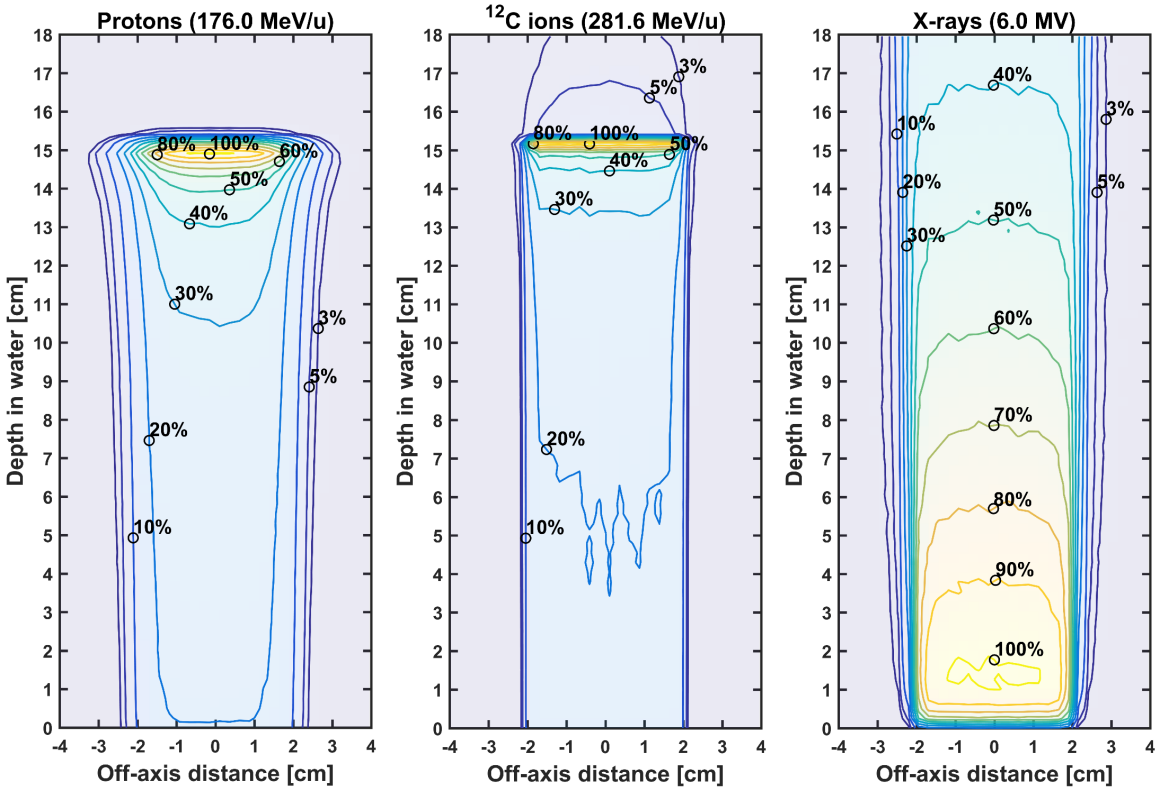

(a) Protons **(b)** ^{12}C-ions **(c)** X-rays

Figure 2.14.: Two-dimensional contour plot of dose distributions in water for **(a)** 176.0 MeV u^{-1} protons, **(b)** 281.6 MeV u^{-1} ^{12}C-ions, and **(c)** 6 MV X-rays. Data obtained from Monte Carlo simulations using a voxel size of 0.05 cm in the depth and off-axis directions and 0.2 cm in the orthogonal direction. Contour lines show the percentage dose at the indicated level relative to the maximum. The color wash in the background is displayed with the same color lookup table as the contour lines for eye guidance. In all cases, the distributions correspond to primary beams arriving at the bottom and moving upward.

2.4.3. Clinical workflow: Importance of LET and RBE measurements

When a patient is diagnosed with cancer and external radiotherapy is prescribed, the treatment intention, technique, and scheme are established. To create treatment plans specific to each patient's anatomy at the time of diagnosis, a three-dimensional model is required. This model is obtained through computed tomography (CT) imaging. During image acquisition, the patient's position is established, and if necessary, immobilization devices are incorporated to ensure a reproducible position while maintaining a degree of comfort for the patient. The acquired images are then exported to a computerized treatment planning system (TPS)

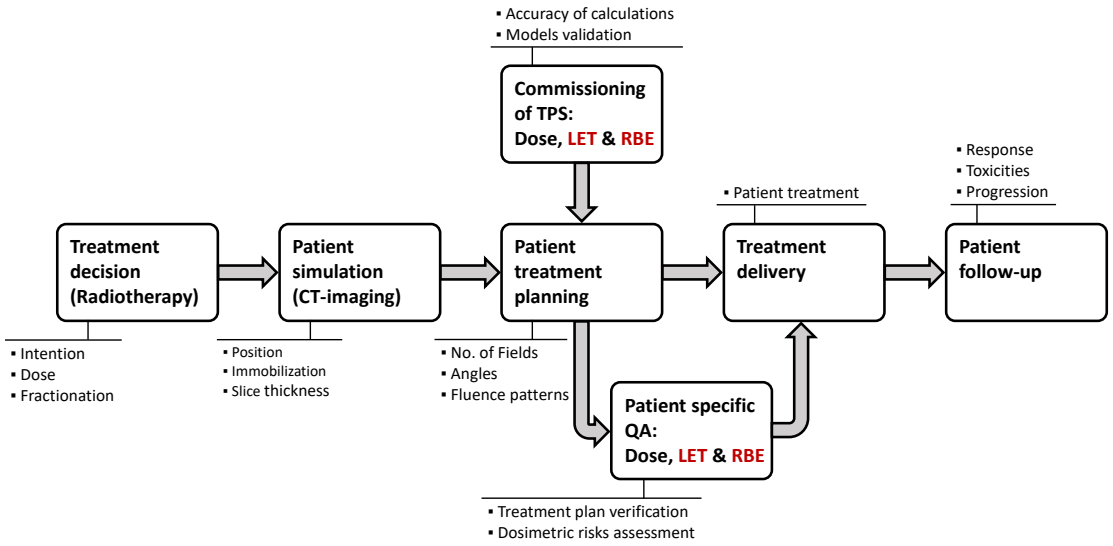

Figure 2.15.: Simplified typical radiotherapy workflow. Once radiotherapy is prescribed, computed tomography (CT) imaging is used to create an anatomical model of the patient. This model is used as input into the treatment planning system (TPS) to design the treatment. Once the treatment has been approved, it is administered to the patient. Patient follow-up takes place during and after treatment to monitor the radiation effects. Prior to clinical use, the TPS must be commissioned. In some cases, as part of quality assurance (QA), the treatment is experimentally verified before administration. Currently, there is no protocol and standard tools for performing linear energy transfer (LET) and relative biological effectiveness (RBE) verification; this is highlighted in red.

where treatment design and optimization take place. Finally, the treatment is delivered to the patient. However, depending on the complexity of the technique or the treatment scheme, patient-specific quality assurance tasks may be conducted prior to treatment to guarantee that the treatment is delivered with sufficient accuracy [204, 205]. Follow-up of the patient is initiated to monitor the response of the tumor and any side effects to the radiation during and after treatment. It is important to note that the workflow described above and shown in Figure 2.15 is of a general scope. Techniques such as image-guided radiotherapy may include additional steps, which can further increase the complexity [206].

TPSs are central to modern radiotherapy, allowing the modeling of the interaction of radiation beams with tissues and the accurate determination of the spatial distribution of the absorbed dose within the patient. Commercial TPSs implement a wide variety of algorithms and models [207]. To ensure accurate dose calculation and model implementation in each TPS, commissioning must be performed prior to clinical use. This process involves comparing TPS predictions with absorbed dose measurements under well-established conditions. Protocols, recommendations, and tools have been developed for this purpose [208–211]. In addition, it is common practice to perform dosimetric testing prior to treatment as part of quality assurance to ensure that the absorbed dose is delivered as intended [204, 205]. This is particularly important for techniques involving steep dose gradients and/or high doses per fraction, where even small deviations between treatment plan and treatment delivery can lead to severe adverse outcomes. As previosly mentioned in this section, TPSs incorporating LET and RBE have been developed for applications in PBT and IBT. However, the lack of instrumentation and standardized procedures prevents experimental validation of these quantities either during TPS commisioning or patient-specific quality assuarnce, as it is routinely done for absorbed dose. Currently, best practices include dose verification and comparison of

treatment plans with secondary calculation engines. To fill this gap, this thesis investigates experimental techniques that could be applied to the assessment of LET and RBE.

2.5. Luminescence dosimetry

Luminescence is the phenomenon in which light is emitted from a material as a result of the de-excitation of atoms or molecules [212]. Of particular interest for radiation dosimetry are those materials that can store some of the energy deposited in the material and re-emit it in the form of luminescence under the influence of controlled stimulation or excitation [213]. It is fundamental that the luminescence yield is proportional to the amount of energy deposited in the material, in such a way that a relation between absorbed dose and the signal in question can be established. In certain crystalline insulators, ionizing radiation produces electron-hole pairs (charge carriers) that are trapped in metastable energy levels located between the valence and conduction bands (Figure 2.16(a)) [214]. This means that some of the energy spent by the ionizing radiation to create the charge carriers is stored within the crystal lattice. The energy levels can be generated by introducing defects in the crystal lattice through the addition of dopants to a host material. These energy levels are often referred to as color centers or optically active centers.

Luminescence can be categorized based on the type of stimulation or excitation that results in the emission of light. If the stimulus is light in the visible spectrum, it is called optically stimulated luminescence (OSL) [215]. Another notable example worth mentioning due to its ubiquity in modern luminescence dosimetry is thermoluminescence (TL), where the source of stimulation is thermal energy [212]. When the previously irradiated material is stimulated in any of these ways, the charge carriers recombine and luminescent light is emitted (Figure 2.16(b)). This recombination leads to the loss of stored information regarding the exposure to the ionizing radiation. Alternatively, trapped electrons can be excited by an external light source, causing them to move to an excited state and emit light with a shifted wavelength upon relaxation (Figure 2.16(c)). This process is known as radiophotoluminescence (RPL) [216]. Detectors based on this phenomenon can be interrogated with no loss of information since electrons return to the ground state within the same center, without recombination.

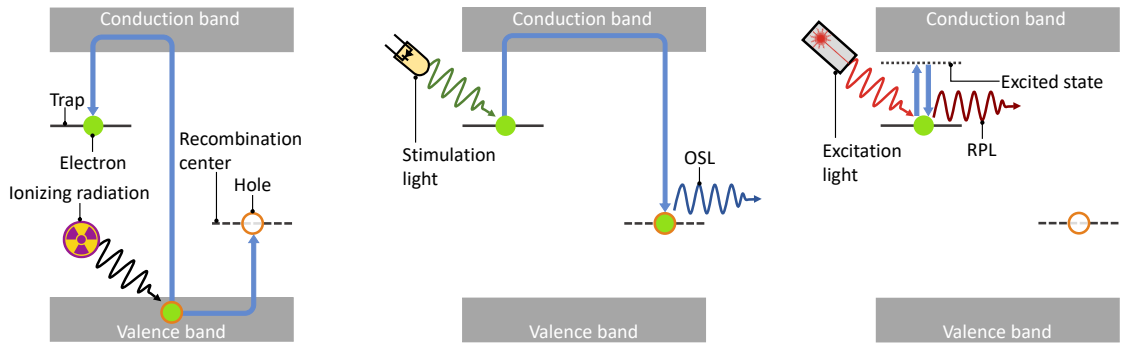

(a) Exposure **(b)** Stimulation and emission **(c)** Excitation and emission

Figure 2.16.: Band diagram illustrating the stages in optically stimulated luminescence (OSL) and radiophotoluminescence (RPL) processes. **(a)** Ionizing radiation generates electron-hole pairs which are trapped between the valence and conduction bands. **(b)** OSL occurs as trapped electrons recombine with holes upon light stimulation. **(c)** RPL takes place as trapped electrons, when excited with light, return to their ground level within the same center.

2.5.1. FNTDs

Electrons released by ionizing radiation and responsible for luminescence are trapped in close proximity to the point where they are liberated. Therefore, by probing individual sets of color centers with known localization within the crystal, the spatial distribution of ionizing events can be inferred. Based on this concept, fluorescent nuclear track detectors (FNTDs) combine the RPL phenomenon with fluorescence microscopy techniques to examine individual micrometer-sized crystal volumes, enabling the visualization of charged particle tracks [39].

Various fluorescence microscopy systems can be employed to image FNTDs [39–42]. However, due to its superior spatial resolution, laser scanning confocal microscopy (LSCM) stands out as the most commonly used technique for this purpose. In this technique, laser light is focused into a small volume of the FNTD to excite the transformed color centers within it. The resulting luminescent light is then transported and focused onto a single-cell detector located at the conjugate plane (Figure 2.17(a)). This process is repeated for a series of contiguous volumes through raster scanning to obtain a full image in a single plane (Figure 2.17(b)). The focal spot can be shifted to different planes to record images at various depths, enabling the acquisition of three-dimensional information. In the post-processing stage, single ion-tracks can be reconstructed by connecting the track spots in different imaging planes [217, 218]. The technical details of the LSCM system used in this thesis are presented in Appendix A.

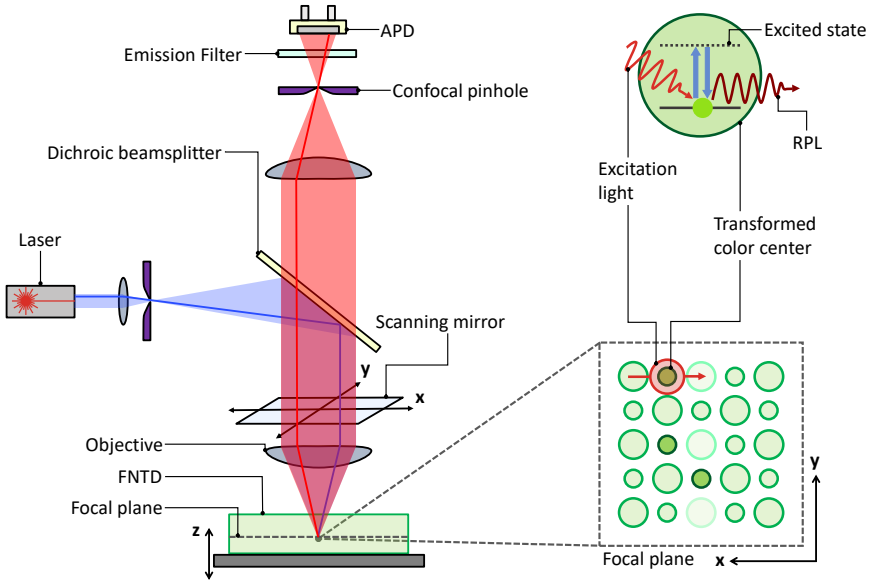

(a) Confocal microscope **(b)** FNTD readout

Figure 2.17.: (a) Diagram illustrating the main components in a confocal microscope and the light path. Excitation light (in blue) is directed by a dichroic beamsplitter and focused by an objective onto the fluorescent nuclear track detector (FNTD) at the focal plane. The luminescent light (in red) is separated from the excitation light using a dichroic beamsplitter before being refocused and collected by an avalanche photodiode (APD). An emission filter may be placed before light detection to distinguish between emission bands. The confocal pinhole is employed to eliminate out-of-focus light. The lateral position (x-y plane) of the focal spot is adjusted using a piezoelectric-controlled scanning mirror, while the transversal position (z-axis) is modified by shifting the sample tray. **(b)** At the bottom is a representation of the FNTD at the microscopic level, viewed from the top at the focal plane. The focal spot is depicted as a red circle with an arrow indicating the direction of the laser scanning. Darker circles represent transformed color centers. At the top is a diagram illustrating a single color center with radiophotoluminescence (RPL) emission taking place.

Since the number of transformed color centers depends on the amount of energy locally absorbed, for a fixed volume traversed by a single particle, the luminescence is expected to increase with LET [43] (Figure 2.18). This forms the basis of LET measurements with FNTDs. In practice, FNTDs are exposed to beams with known LET, and a calibration curve is determined by establishing a relationship between the fluorescence intensity and the LET [45]. It is worth noting that FNTDs stand out among other luminescent techniques because the LET can be determined for each recorded particle track, enabling the derivation of LET spectra. From the LET spectrum L_F and L_D can be calculated using the discrete forms of Equations 2.12 and 2.14 [219].

To date, three materials have been investigated as FNTDs: un-doped lithium fluoride (LiF) [220], silver-activated (Ag^+) phosphate glass [221], and aluminum oxide doped with carbon and magnesium (Al_2O_3:C,Mg) [39]. However, the only one currently commercially available and on which FNTD methods have been predominantly developed is Al_2O_3:C,Mg. One further advantageous feature of Al_2O_3:C,Mg-based FNTDs is that they enable LET measurements in a wide range [43]. Particularly, the lower LET detection limit (~ 0.4 keV µm^{-1}) makes this material suitable for measuring the LET even for the most energetic protons encountered in PBT as primary particles and in IBT as nuclear fragments [44, 222].

Since their introduction, one of the main challenges hindering LET measurements with FNTDs has been the non-homogeneous sensitivity (luminescence yield per unit of absorbed dose) between individual crystals or even within the same crystal [223]. This has been shown to lead to highly inaccurate LET predictions [44, 45, 47]. The varying sensitivities can be attributed to crystals with differing concentrations of color centers. To overcome this problem, a sensitivity correction based on matching the measured LET spectra to that obtained from Monte Carlo simulations has been proposed [47, 48]. However, this requires detailed knowledge of the experimental setup and access to computational resources, which might not always be available. In cases where the desired outcome is to validate simulation results, a purely experimental approach may be necessary. Thus, the development of a fully experimental method to derive a detector-specific correction factor was one of the main objectives of this thesis.

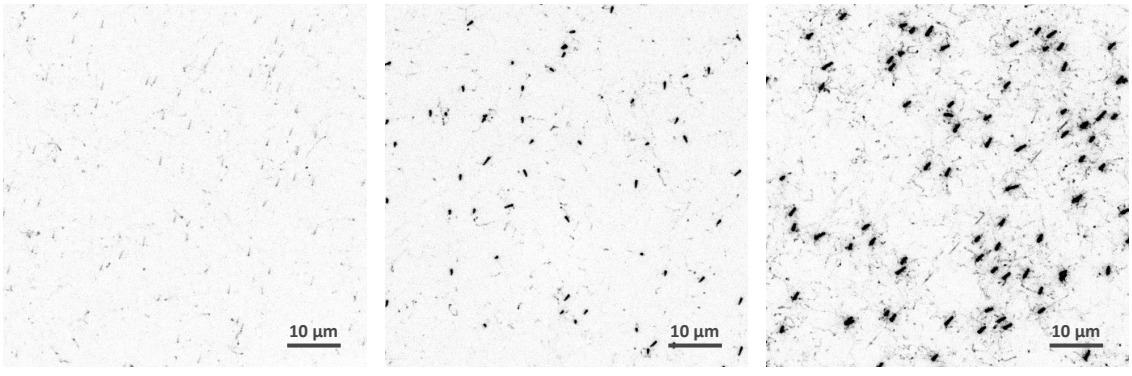

(a) Protons **(b)** ^{4}He-ions **(c)** ^{12}C-ions

Figure 2.18.: Maximum fluorescence intensity projection images (640 pixels × 640 pixels) from fluorescent nuclear track detectors (FNTDs) exposed to **(a)** 221.06 MeV u^{-1} protons, **(b)** 70.79 MeV u^{-1} ^{4}He-ions, and **(c)** 88.83 MeV u^{-1} ^{12}C-ions, each with a track average linear energy transfer (L_F) of (0.42, 3.89, and 30.7) keV µm^{-1}, respectively. The images were acquired from detectors with similar sensitivities. Equal contrast windows were applied to all images for fair comparison. Images are displayed with an inverted lookup table, where darker colors indicate higher fluorescence intensity.

2.5.2. OSLDs

As discussed earlier in this section, when a material with OSL properties that has previously been exposed to ionizing radiation is stimulated with light, luminescence is emitted due to electron-hole recombination. Thus, if the stimulation is prolonged or repeated over time, the number of charge carriers will decrease. In a first-order approximation, assuming that the recombination of charge carriers occurs instantaneously, and in the absence of retrapping, the rate of change of the number of electron-hole pairs available per unit time ($\mathrm{d}N_{\text{e-h}}/\mathrm{d}t$) can be written as directly proportional to the population of electron-hole pairs at a given time. This relationship can be expressed as [215]:

$$\frac{\mathrm{d}N_{\text{e-h}}}{\mathrm{d}t} = -\frac{1}{\tau_{\text{R}}} N_{\text{e-h}} \implies N_{\text{e-h}} = N_{\text{e-h,0}} e^{-t/\tau_{\text{R}}}, \tag{2.20}$$

where $N_{\text{e-h,0}}$ is the initial number of electron-hole pairs, τ_{R} is the lifetime of the optically active centers under stimulation, and t is the duration of the stimulus. Equation 2.20 shows that under a continuous stimulus, the OSL signal decays exponentially with time (Figure 2.19(a)). The total amount of signal, here referred to as intensity, is equal to the integral of the OSL curve. Optically stimulated luminescence detectors (OSLDs) are based on the principle that the OSL intensity (S_{OSL}) is proportional to the energy deposited in the material. This allows for a relationship to be established between the absorbed dose and S_{OSL} [213].

One of the main challenges for the application of OSLDs in PBT and IBT is that S_{OSL} can also strongly depend on the LET of the radiation field. This effect is quantified through the luminescent relative efficiency (η), which is expressed as follows [224]:

$$\eta = \left.\frac{S_{\text{OSL,t}}}{S_{\text{OSL,r}}}\right|_{\text{isodose}}, \tag{2.21}$$

where $S_{\text{OSL,t}}$ and $S_{\text{OSL,r}}$ represent the OSL intensities after exposure to the same doses from test and reference radiations, respectively. In general, η decreases with increasing LET (Figure 2.19(b)). This effect is commonly referred to as quenching and has been shown to lead to an underestimation of the absorbed dose in light-ion beams [37, 225].

As a result of having multiple types of color centers, some OSL materials exhibit emissions in different wavelength bands. In addition, η of each emission band can be distinctive, and it is therefore possible to relate the ratio of two emissions to the LET [35]. This concept is the basis for LET measurements with OSLDs. In the case of Al_2O_3:C, the ratio between blue- and UV-light emissions (blue- to UV-signal ratio) has been used to measure the LET in clinical proton beams [37]. Since η is parameterized in terms of LET, once the LET is determined, η can be calculated to derive a corrected dose. Therefore, both absorbed dose and LET can be determined with a single detector in the same measurement [37, 226]. Moreover, by incorporating the measured LET into RBE models, it becomes possible to estimate the RBE-weighted dose.

One of the limitations of the blue- to UV-signal ratio, when parameterized in terms of LET, is that it also depends on the type of particle [35]. This means that two ions with the same LET can result in a different blue- to UV-signal ratio. Clearly, this creates difficulties for applications in the highly mixed-ion fields found in IBT. However, the choice of LET as the main parameter is somewhat arbitrary, and other quantities related to ionization density can be used in principle. Of particular interest is the so-called Q_{eff}, which is defined as [227]:[2.f]

[2.f] In the literature, no specific name is given to Q_{eff}. The term effective quality factor is preferably avoided to prevent confusion with the quality factor (Q) used in radiation protection.

$$Q_{\text{eff}} = \frac{z^2}{\beta^2}\left(1 - e^{-125\beta/z^{2/3}}\right)^2. \tag{2.22}$$

The main rationale for using Q_{eff} to parameterize the blue- to UV-signal ratio is its suitability as an ionization density descriptor for RBE [227, 228].

In a typical OSL readout system, the stimulation light is directed and/or focused into the OSLDs. The stimulation light can be either continuous or pulsed. Pulsed stimulation allows discrimination between different emission bands by exploiting the different lifetimes of the color centers responsible for the emissions [229]. For Al_2O_3:C, both blue-light (τ_R = 35 ms) and UV-light (τ_R < 7 ns) emissions are detected during stimulation, while only blue-light emission is detected between pulses (quiescence). Assuming negligible decay during a single stimulation pulse ($t \sim 100$ µs), the UV-light emission can be obtained by subtracting the signals detected during stimulation from those detected during quiescence [35]. The emitted luminescence light is detected by a photodetector, most commonly a photomultiplier. To separate the stimulation light from the emission light, a spectral filter is placed in front of the photodetector. The technical specifications of the OSL reader used in this thesis are presented in Appendix A.

Previous studies have demonstrated that Al_2O_3:C can be effectively used for LET measurements in PBT [37]. Al_2O_3:C,Mg has been used for LET measurements as FNTD [47, 48], and has also been investigated for dosimetry as OSLD [230]. The higher UV-emission intensity and the better signal-to-noise ratio for dose measurements of Al_2O_3:C,Mg compared to Al_2O_3:C motivate further studies for potential applications of Al_2O_3:C,Mg in PBT and IBT [231]. Additionally, the relatively shorter lifetime of the color centers in Al_2O_3:C,Mg could be more suitable for OSL film dosimetry than that of Al_2O_3:C, which could enable two-dimensional LET measurements. In light of this, the suitability of Al_2O_3:C,Mg-based OSLDs for LET measurement in PBT and IBT was investigated in this thesis.

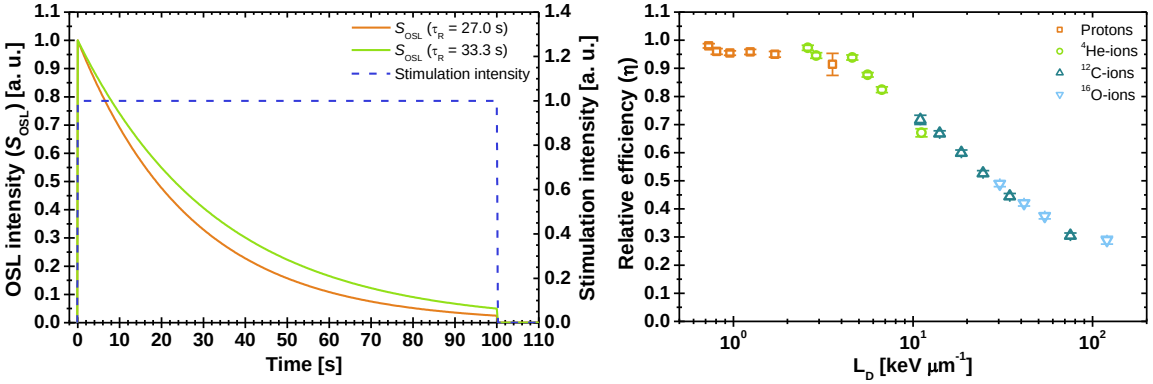

(a) Luminescence decay. **(b)** Luminescence relative efficiency.

Figure 2.19.: (a) Normalized optically stimulated luminescence (OSL) intensity (S_{OSL}) as a function of the time for luminescence center lifetimes (τ_R) of (27.0 and 33.3) s, shown with solid lines. The dashed line indicates a single square stimulation pulse. All data sets have been normalized to their maximum value. **(b)** Relative efficiency (η) for aluminum oxide doped with carbon (Al_2O_3:C) exposed to monoenergetic protons, ^{4}He-, ^{12}C-, and ^{16}O-ions as a function of the dose average linear energy transfer (L_D). Data from Yukihara E. G., *et al.* [35].

Chapter 3 Publications

This thesis is presented in cumulative form according to the regulations of the Department of Physics and Astronomy at the University of Heidelberg. It consists of four research papers that have been submitted to internationally renowned peer-reviewed journals and have either been published or accepted for publication. As stipulated by the rules for cumulative theses, none of the publications have been presented as part of other theses. For the sake of clarity, the publications are numbered using Roman numerals. The author of this thesis is the first author of publications I, III, and IV, and the second author of publication II.

3.1. Overview of the publications

The publications are structured towards the aim of developing suitable experimental tools to measure the linear energy transfer (LET) and relative biological effectiveness (RBE) in proton-beam therapy (PBT) and ion-beam therapy (IBT). Publications I (Section 3.5) and II (Section 3.6) present the methods for accurately measuring LET using fluorescent nuclear track detectors (FNTDs) and optically stimulated luminescence detectors (OSLDs), respectively. Publication III (Section 3.7) presents LET and RBE measurements in proton and ^{4}He-ion spread-out Bragg peaks (SOBPs). Publication IV (Section 3.8) presents a comparative study of FNTDs, OSLDs, and thermoluminescent dosimeters (TLDs) for measuring LET and RBE in clinical proton beams. Following the roadmap presented in the Introduction (Section 1.4, Figure 1.1), the contributions, here in the form of publications, are categorized into methodological developments (Section 3.2) and clinical tests (Section 3.3).

3.2. Methodological developments

3.2.1. FNTDs sensitivity correction

A novel fully experimental method to derive a detector-specific correction factor is presented in Publication I. This correction factor is based on exposing the detectors to α-particles and addresses the variability in sensitivity between individual detectors. The idea is that the fluorescence intensity of the recorded α-particle tracks can be used to probe the concentration of color centers relative to a reference set of detectors. α-particles were chosen due to their short range in aluminum oxide (Al_2O_3). Since confocal microscopy enables scanning the detectors at different focal planes, measurements with light-ions can be performed below the maximum penetration depth of the α-particles. To establish the impact of the sensitivity correction on the accuracy of LET measurements, a blind test was performed. In this test, detectors were exposed to unknown monoenergetic light-ion beams. The measured track average linear energy transfer (L_F) and dose average linear energy transfer (L_D) were compared to theoretical values, which were withheld until the analysis of the experimental data was completed. The sensitivity correction developed in this study was applied to all FNTDs used in subsequent phases of the project (Publications III and IV) to ensure traceability to the calibration set and accurate results.

3.2.2. Calibration curve for LET measurements with FNTDs

The calibration curve, which relates the fluorescence intensity of single ion-tracks to the LET, is presented in Publication I. This curve is central to all LET measurements performed with FNTDs and is fundamental for the next stages of the project. To cover an LET range fitting applications in PBT and IBT, the detectors were irradiated to monoenergetic protons, ^{4}He-, ^{12}C-, and ^{16}O-ions at the Heidelberg Ion-Beam Therapy Center (HIT; Heidelberg, Germany). The calibration data ranged from (0.42 to 48.6) keV µm^{-1}. As an additional test to assess the effectiveness of the sensitivity correction, the calibration curve was established by fitting the same function to both the corrected and uncorrected data. The LET spectra in the unknown proton and ^{4}He-ion fields studied during the clinical tests (Publications III and IV) were determined using data reported in this publication.

3.2.3. Calibration curves for LET measurements with OSLDs

The calibration curves, which relate the blue- to UV-signal ratio with L_F, L_D, and Q_{eff}, are presented in Publication II. These curves were established for both aluminum oxide doped with carbon (Al_2O_3:C) and aluminum oxide doped with carbon and magnesium (Al_2O_3:C,Mg). In this publication, Al_2O_3:C,Mg is presented for the first time as an alternative material for performing LET measurements in optically stimulated luminescence (OSL)-mode. As in the case of FNTDs, the calibration curves are intended to be used for LET measurements in unknown light-ion fields with OSLDs. In addition to the calibration curves, the relative efficiency for Al_2O_3:C and Al_2O_3:C,Mg is presented and the accuracy for the dose assessment through ionization density corrections is evaluated. For this study, the detectors were irradiated to monoenergetic protons at the Center for Proton Therapy (CPT) of the Paul Scherrer Institute (PSI; Villigen, Switzerland) and monoenergetic protons, ^{4}He-, ^{12}C-, and ^{16}O-ions at HIT. The calibration data ranged from (0.45 to 55.2) keV µm^{-1} for L_F, from (0.96 to 62.2) keV µm^{-1} for L_D, and from 3.15 to 425 for Q_{eff}. The geometry implemented in the Monte Carlo simulations used to derive L_F, L_D, and Q_{eff} was validated against measurements of depth dose profiles taken with ionization chambers. This same geometry was also utilized in the work conducted for Publication III. This work was developed as a colaboration with PSI, were all the OSLDs were read and analyzed, and the project was coordinated. The calibration curves developed in this study were used to assess L_F and L_D during the comparisson study (Publication IV).

3.2.4. Integration of RBE models

The approaches used to integrate phenomenological RBE models based on the linear-quadratic model (LQM) into the FNTDs analysis pipeline are described in detail in Publication III. These models are summarized in Subsection 2.3.3 (Table 2.1). For both protons and ^{4}He-ions, two approaches were adopted. The first approach takes full advantage of the spectroscopic capabilities of FNTDs to calculate the LQM α and β parameters associated with each recorded track using the Wedenberg- and/or Mairani-RBE models. From these sets of values, the average α and β values associated with the full LET spectrum were calculated. In the second approach, L_D was calculated from the LET spectrum and then used as input in the McNamara- or Mairani-RBE models to calculate the α and β parameters of the ion-field. Both approaches were employed and validated during the clinical tests, the results of which are also presented in Publication III. The L_D-based approach was used to estimate the RBE in the proton beams studied during the comparison study presented in Publication IV.

3.3. Clinical tests

3.3.1. LET measurements in clinical proton and ^{4}He-ion beams

LET measurements of FNTDs exposed to proton and ^{4}He-ion SOBPs are presented in Publication III. In this study, FNTDs were positioned and irradiated behind a solid water phantom at increasing phantom thicknesses to represent different depths in water. The LET spectra at each studied position were obtained from the exposed detectors using the calibration curve and methods reported in Publication I, including the detector-specific correction factor. To verify and test the fluorescence intensity dependence on the type of particle, a second calibration curve was established using only data for protons and ^{4}He-ions and applied to the FNTD measurements. The L_F and L_D values were calculated from the LET spectra. The LET spectra, L_F, and L_D measurements were compared to Monte Carlo simulations. Two methods were used in the simulations to derive all these quantities. The first method is based on scoring the particle spectra in energy and calculating the corresponding LET spectra using energy-to-electronic stopping power lookup tables. The second method is based on scoring the energy depositions in a volume and dividing them by the step lengths. The geometry and parameters used in the simulations were further validated against ionization chamber measurements of depth dose profiles for the specific studied beams.

3.3.2. RBE measurements in clinical proton and ^{4}He-ion beams

RBE values obtained using FNTD-based LET measurements in combination with RBE models are reported in Publication III. These results were obtained from the FNTDs exposed to proton and ^{4}He-ion SOBPs. To provide *in-vitro* validation of the RBE predicted values, clonogenic cell survival assays were performed with human alveolar adenocarcinoma (A549) cells. Monolayer cell cultures were exposed to RBE-weighted doses ranging from (1.0 to 6.0) Gy at the same positions as the FNTDs. As a reference for the calculation of RBE values, a group of cells was also irradiated at absorbed doses between (1.0 to 6.0) Gy using 6 MV X-rays. To derive the LQM α and β parameters at each studied depth, the survival fractions were parameterized as a function of the absorbed dose, and a function matching the LQM was fitted to the corresponding dataset. The endpoint was set to the survival fraction at the clinically relevant dose. *In-silico* validation was performed by using the LET results from Monte Carlo simulations as input to the same RBE models used with the FNTDs.

3.3.3. Luminescent detectors comparison study

The results of a multi-institutional measurement campaign aimed at investigating the suitability and comparing the performance of FNTDs, OSLDs, and TLDs for L_F and L_D measurements in PBT are presented in Publication IV. This campaign was organized by the European Radiation Dosimetry Group (EURADOS), and the irradiations were performed at the Danish Center for Particle Therapy (DCPT; Aarhus, Denmark). All detectors were irradiated at the same depths in a water-equivalent phantom with a 160 MeV u^{-1} proton beam and a proton SOBP. FNTDs were handled by the German Cancer Research Center (DKFZ; Heidelberg, Germany) group, OSLDs by the PSI group, and TLDs by the Belgian Nuclear Research Center (SCK-CEN; Mol, Belgium) and the Institute of Nuclear Physics, Polish Academy of Sciences (IFJ; Krakow, Poland) groups. The methods and data reported in Publications I and II were applied to FNTDs and OSLDs, respectively. RBE values at the studied positions were calculated from the L_D measurements. The experimental results were compared with dedicated Monte Carlo simulations performed at DCPT.

3.4. Graphical overview

Figure 3.1 summarizes the main results of each publication and the connections among them.

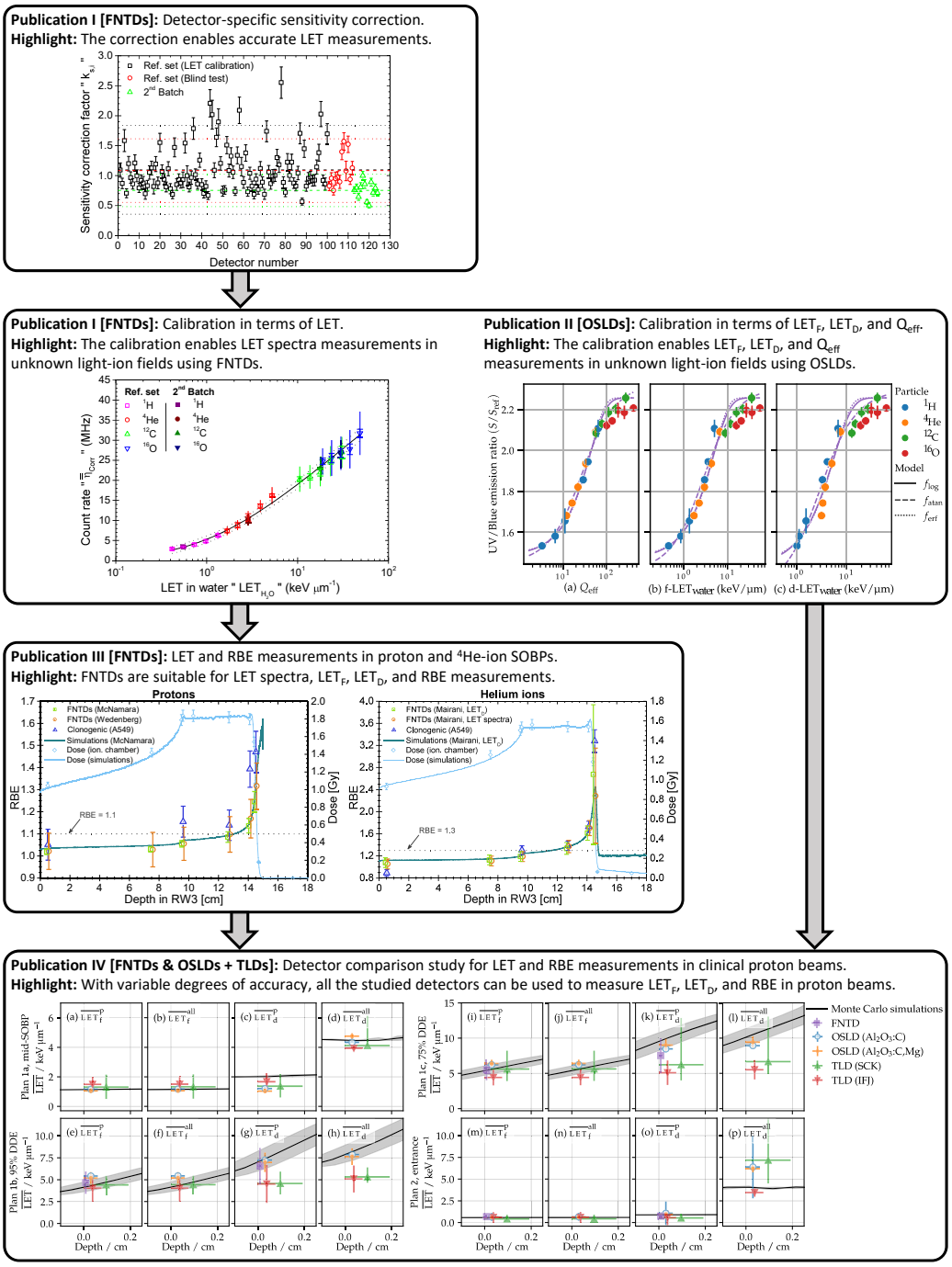

Figure 3.1.: (Top box) Detector-specific correction factor for fluorescent nuclear track detectors (FNTDs). **(Second box from the top)** Calibration curves for linear energy transfer (LET) measurements with FNTDs and Q_{eff}, track average linear energy transfer (L_F), or dose average linear energy transfer (L_D) measurements with optically stimulated luminescence detectors (OSLDs). **(Third box from the top)** In-depth relative biological effectiveness (RBE) distributions in proton and ^{4}He-ion spread-out Bragg peaks (SOBPs) using FNTDs. **(Bottom box)** L_F and L_D measurements in proton beams using FNTDs, OSLDs, and thermoluminescent dosimeters (TLDs).

3.5. Publication I

Sensitivity correction of fluorescent nuclear track detectors using alpha particles: Determining LET spectra of light ions with enhanced accuracy

Authors: I. D. Muñoz, L. N. Burigo, T. Gehrke, S. Brons, S. Greilich, and O. Jäkel
Status: Published
Journal: Medical Physics
DOI: http://doi.org/10.1002/mp.16083

Contributions: IDM was responsible for the execution and optimization of the experiments, including irradiations and detectors readout. TG assisted during the experiments and prepared the plans for the blind test. SB prepared the irradiation plans for the calibration curve and provided technical assistance at all stages. The concept of deriving a detector specific correction factor using α-particles was conceived by SG and IDM, and developed in detail by IDM. OJ and LNB supervised and managed the research. SG provided scientific advice regarding FNTDs. OJ secured and allocated the necessary resources for the project. Data curation and visualization were performed by IDM. IDM drafted and edited the original manuscript. All authors participated in the review of the final version of the manuscript.

Received: 4 August 2022 | Revised: 20 October 2022 | Accepted: 20 October 2022

DOI: 10.1002/mp.16083

RESEARCH ARTICLE

MEDICAL PHYSICS

Sensitivity correction of fluorescent nuclear track detectors using alpha particles: Determining LET spectra of light ions with enhanced accuracy

Iván D. Muñoz[1,2,3] | **Lucas N. Burigo**[2,3] | **Tim Gehrke**[2,3,4] | **Stephan Brons**[3,5] | **Steffen Greilich**[2,3] | **Oliver Jäkel**[2,3,5]

[1]Department of Physics and Astronomy, Ruprecht-Karl University of Heidelberg, Heidelberg, Germany

[2]Division of Medical Physics in Radiation Oncology, German Cancer Research Center (DKFZ), Heidelberg, Germany

[3]Heidelberg Institute for Radiation Oncology (HIRO), National Center for Radiation Research in Oncology (NCRO), Heidelberg, Germany

[4]Department of Radiation Oncology, Heidelberg University Hospital, Heidelberg, Germany

[5]Heidelberg Ion-Beam Therapy Center (HIT), Department of Radiation Oncology, Heidelberg University Hospital, Heidelberg, Germany

Correspondence
Oliver Jäkel, Division of Medical Physics in Radiation Oncology, German Cancer Research Center (DKFZ), Im Neuenheimer Feld 280, D-69120 Heidelberg, Germany.
Email: o.jaekel@dkfz-heidelberg.de

Present address
Steffen Greilich, Berthold Technologies GmbH & Co. KG 75323, Bad Wildbad, Germany

Steffen Greilich and Oliver Jäkel are senior authors.

Funding information
Deutscher Akademischer Austauschdienst, Grant/Award Number: 57440921

Abstract

Background: Radiation fields encountered in proton therapy (PT) and ion-beam therapy (IBT) are characterized by a variable linear energy transfer (LET), which lead to a variation of relative biological effectiveness and also affect the response of certain dosimeters. Therefore, reliable tools to measure LET are advantageous to predict and correct LET effects. Fluorescent nuclear track detectors (FNTDs) are suitable to measure LET spectra within the range of interest for PT and IBT, but so far the accuracy and precision have been challenged by sensitivity variations between individual crystals.

Purpose: To develop a novel methodology to correct changes in the fluorescent intensity due to sensitivity variations among FNTDs. This methodology is based on exposing FNTDs to alpha particles in order to derive a detector-specific correction factor. This will allow us to improve the accuracy and precision of LET spectra measurements with FNTDs.

Methods: FNTDs were exposed to alpha particles. Afterward, the detectors were irradiated to monoenergetic protons, ^{4}He-, ^{12}C-, and ^{16}O-ions. At each step, the detectors were imaged with a confocal laser scanning microscope. The tracks were reconstructed and analyzed using in-house developed tools. Alpha-particle tracks were used to derive a detector-specific sensitivity correction factor ($k_{s,i}$). Proton, ^{4}He-, ^{12}C-, and ^{16}O-ion tracks were used to establish a traceable calibration curve that relates the fluorescence intensity with the LET in water (LET_{H_2O}). FNTDs from a second batch were exposed and analyzed following the same procedures, to test if $k_{s,i}$ can be used to extend the applicability of the calibration curve to detectors from different batches. Finally, a set of blind tests was performed to assess the accuracy of the proposed methodology without user bias. Throughout all stages, the main sources of uncertainty were evaluated.

Results: Based on a sample of 100 FNTDs, our findings show a high sensitivity heterogeneity between FNTDs, with $k_{s,i}$ having values between 0.57 and 2.55. The fitting quality of the calibration curve, characterized by the mean absolute percentage residuals and correlation coefficient, was improved when $k_{s,i}$ was considered. Results for detectors from the second batch show that, if the fluorescence signal is corrected by $k_{s,i}$, the differences in the predicted LET_{H_2O} with respect to the reference set are reduced from 55%, 141%, 41%, and 186% to 4.2%, 6.5%, 5.0%, and 11.0%, for protons, ^{4}He-, ^{12}C-, and ^{16}O-ions, respectively.

The blind tests showed that it is possible to measure the track- and dose-average LET_{H_2O} with an accuracy of 0.3%, 16%, and 9.6% and 1.7%, 28%, and 30% for protons, ^{12}C-ions and mixed beams, respectively. On average, the combined uncertainty of the measured LET_{H_2O} was 11%, 13%, 21%, and 26% for protons, ^{4}He-, ^{12}C-, and ^{16}O-ions, respectively. These values were increased by a mean factor of 2.0 when $k_{s,i}$ was not applied.
Conclusions: We have demonstrated for the first time that alpha particles can be used to derive a detector-specific sensitivity correction factor. The proposed methodology allows us to measure LET spectra using FNTD-technology, with a degree of accuracy and precision unreachable before with sole experimental approaches.

KEYWORDS
fluorescent nuclear track detectors, ion-beam therapy, linear energy transfer (LET), proton therapy

1 | INTRODUCTION

In proton therapy (PT) and ion-beam therapy (IBT) the linear energy transfer (LET) is the main macroscopic physical quantity used to characterize the beam quality in terms of ionization density.[1,2] Partly, this is a consequence of the fact that the relation between relative biological effectiveness (RBE) and ionization density is most commonly expressed, modeled, or parameterized as a function of the LET or its averages.[2–4] Therefore, being able to calculate or measure the LET could be advantageous or necessary to predict the RBE on clinical scenarios.* Knowledge regarding the LET may also be essential for accurate dosimetry in PT and IBT, as the responses of several dosimeters exhibit dependence with the LET.[5–9] For beams commonly used in PT and IBT, the LET increases with penetration depth, but most notably at the distal end, as a result of the slowing down of the ions; thus a single LET value is not sufficient to globally describe the radiation field, and local values are more suitable. Furthermore, due to energy modulation techniques, energy straggling, and production of secondary ions, the LET may exhibit a wide spectrum. In addition, the LET changes abruptly close to the end of the ion tracks, leading to sharp LET gradients. Considering the above, it is desirable to have a compact detector capable of accurately measuring LET for PT and IBT applications.

Over the years, a wide variety of techniques and devices have been explored and developed to measure LET in PT and IBT. For instance, the distinct signal quenching and physical properties of various scintillator materials were studied as means to simultaneously measure the LET and dose of proton beams.[10] For thermoluminescent (TL) dosimeters (TLDs), the high- to low-temperature ratio of the glow curve has been extensively explored as a way to measure LET of proton and heavier ion beams.[11–14] In addition, exploiting the different relative efficiencies (defined as TL-signal per unit of absorbed dose) of two lithium fluoride-based TLDs having different dopants, LET distributions in-depth were measured on a clinical proton spread out Bragg peak.[15] In the case of optically stimulated luminescent (OSL) detectors (OSLDs), both the shape of the OSL decay curve and the ultraviolet- to blue-emission intensity ratio of aluminum oxide doped with carbon have been proposed and applied to measure LET in PT.[16–18] Alternatively, silicon-based detectors have also been tested for LET measurements in PT and IBT.[19] A rather novel and promising type of detectors, which have been used for LET measurements on proton and ion beams, are fluorescent nuclear track detectors (FNTDs).[20–23] Unlike other passive detectors, such as TLDs and OSLDs, which can only provide average values, FNTDs are capable of delivering the full LET spectra in a broad range.[21–23] Additionally, FNTDs, due to their passive-functioning nature, can withstand the fluence rates commonly encountered in PT and IBT, which typically is a limiting factor for active or time-resolved detectors. Moreover, FNTDs are small sized and therefore highly suitable for measuring on regions with sharp LET gradients.

FNTDs combine the photoluminescence of solid state materials with photo-stimulated microscopy techniques to visualize individual tracks** of ionizing charged particles.[24–27] Nowadays, the most prominent material used in FNTD-technology is aluminum oxide doped with carbon and magnesium (Al_2O_3:C,Mg).[28] The purpose of the dopants is to introduce oxygen defects within the crystal lattice and generate aggregate color centers—particularly, F_2^{2+}(Mg) color centers—that are prone to undergo radiochromic changes after exposure to ionizing radiation.[24,28,29] The sensitivity of each detector (defined as emitted fluorescence light per unit

* It should be noticed that, besides the LET, the RBE also depends on the type of particles, cell cycle, oxygenation, type of tissue and dose rate, among other factors.

** For the sake of accuracy, the authors want to point out that what actually is visualized are the traces, in the form of transformed color centers, left behind by the actual tracks. For brevity and clearness, the authors will refer to as tracks to the traces, within the context of FNTDs.

of absorbed dose, with respect to a reference sample or value) depends on the amount of color centers within the crystal, which is also referred to as coloration. Consequently, different color center concentrations could lead to non-negligible changes in the sensitivity of individual crystals.[25,30] In fact, intra- and inter-batch sensitivity variability has been identified as one of the main limitations to accurately measure LET spectra in PT and IBT with FNTDs.[20,21,23,31–34] It is worth mentioning that sensitivity variations have also been shown to restrict the accuracy of dosimetric measurements for photons and neutrons.[35]

Some approaches have been proposed to overcome the limited accuracy and precision that results from sensitivity variations of FNTDs. For instance, by applying detector- or batch-specific rescaling factors derived from Monte Carlo simulations or by interrogating the preexisting population of F_2^{2+} color centers.[31,33–35] The main limitation imposed by rescaling factors based on information derived from Monte Carlo simulations is that detailed and validated models of the irradiation system or experimental setup may be required.[31,33,34] Moreover, these types of rescaling factors are only applicable to specific scenarios and do not correct for different colorations but displace the LET spectra to match some prominent features. In the case of correction factors based on the initial populations of F_2^{2+} color centers, it can be speculated that the sensitivity could not be fully described by the initial crystal coloration, as the migration of charge carriers may not occur exclusively between F_2^{2+} and F_2^{+} color centers. Furthermore, this requires a secondary excitation-detection system, which is not available on all devices.[35] Therefore, a sensitivity correction factor obtained by irradiating the crystals to a reference radiation field—ideally resembling the ones that will be investigated—could be more appropriate. However, choosing the reference radiation should be done bearing on mind that the signal resulting from irradiating the FNTDs to the reference radiation must not interfere with the measurements. In addition, the reference radiation field needs to be highly reproducible and, preferably, the irradiation process should be easily incorporated into any workflow.

Alpha particles, owing to their relatively short range in condensed matter, well-defined energy, and high ionization density, are suitable candidates to characterize the sensitivity of single crystals. In addition, an alpha-emitting radioactive source can provide a controlled and highly reproducible reference radiation field. Most importantly, as alpha particles do not penetrate into the crystal beyond just a few microns, the un-irradiated volume can be used to perform measurements with other particles, without introducing any additional or spurious signal; but with the requisite for the studied particles to have a range larger than the one of the alpha particles.

Aiming to improve the reliability of LET-spectrometric measurements using FNTDs, in this work we established and fully evaluated a robust methodology to derive a detector-specific sensitivity correction factor by exposing FNTDs to alpha particles. The newly developed methodology described here is used to review the relation between the fluorescence intensity of individual tracks and the LET by irradiating FNTDs to monoenergetic protons and light-ion beams (namely, ^{4}He-, ^{12}C-, and ^{16}O-ions).[***] In addition, the feasibility of using the sensitivity correction to extend the applicability of the LET-calibration curve to other batches was studied. We also identified the main sources of uncertainty and quantified the combined uncertainty of the measured LET. Finally, the proposed methodology was tested and verified by performing a set of blind tests.

2 | MATERIALS AND METHODS

2.1 | Irradiations

The irradiations were carried out in two steps. First, brand new Al_2O_3:Mg,C crystals ($8.0 \times 4.0 \times 0.5$ mm^3; one-sided polished) produced by Landauer Inc-Crystal Growth Division (Stillwater, OK, USA.) were exposed to alpha particles. Second, the same detectors were irradiated to different light-ion species. To avoid biased results, the detectors were randomly selected from the same unscreened batch, that is, without any considerations regarding their coloration. Further details of the irradiation sources and experimental setups are given in the following sections.

2.1.1 | Exposure to alpha particles

FNTDs were exposed to alpha particles from an unshielded ^{244}Cm radioactive source type CLRB22299 (S.N.: BA-7779, Eckert & Ziegler Nuclitec; Berlin, Germany). The source consisted of a stainless disk of 5.0 cm diameter and 0.05 cm thickness, with the radioactive material electrodeposited on top of the disk over a circular area of 0.3 cm diameter. The activity of the source was 8.73 ± 0.26 kBq at the date of calibration, with 0.96% and 0.38% coming from ^{239}Pu/^{240}Pu and ^{245}Cm/^{246}Cm impurities, respectively. The source was calibrated by the German Accreditation Body (*Deutsche Akkreditierungsstelle*; Berlin, Germany), which holds traceability to primary laboratories.

For the exposures, the FNTDs were individually placed at 0.3 cm above the source by means of a dedicated 3D-printed holder, with the FNTDs polished surface facing toward the source. The exposures were carried out in air, and variations on the energy of the

[***] From this point onward the authors adopt and keep to the recommendation issued jointly by the International Commission on Radiation Units and Measurements and the International Atomic Energy Agency on the Technical Reports Series No. 461, by referring to as light ions to partially or completely stripped nuclei having an atomic number less or equal to 10, including protons. Therefore, protons will be differentiated explicitly only when necessary.

TABLE 1 Type of particle, nominal energies, residual energies, and associated unrestricted linear energy transfer in water (LET_{H_2O}) of the studied beams

Ion	Nominal energies (MeV/u)	Residual energies (MeV/u)	LET_{H_2O} (keV/μm)
^{1}H	221.06, 145.46, 99.74, 69.06, 48.12	220.23, 144.37, 98.30, 67.15, 45.55	0.42, 0.55, 0.73, 0.98, 1.33
^{4}He	220.51, 148.48, 103.76, 70.79, 50.57	219.08, 146.61, 101.34, 67.52, 46.25	1.68, 2.19, 2.85, 3.89, 5.23
^{12}C	430.10, 264.95, 176.56, 124.25, 88.83	427.09, 261.06, 171.53, 117.78, 80.41	10.6, 13.7, 17.8, 23.1, 30.7
^{16}O	430.32, 278.85, 193.77, 141.39, 103.77	426.29, 273.81, 187.44, 133.50, 93.76	18.9, 23.7, 29.9, 37.6, 48.6

Note: The LET_{H_2O} values correspond to those calculated from the residual energies.

alpha particles due to changes in the pressure and temperature were neglected. No collimation was used between the source and the detectors. The detectors were exposed for 90.0 ± 2.0 s, which corresponded to a particle fluence of approximately 3.9×10^5 cm^{-2} at the central area of the detector surface. The particle fluence was selected to result in a number of tracks large enough to get a statistical representative sample, without saturating the track reconstruction algorithm, even after the irradiations with light ions.

2.1.2 | Irradiations with light ions

FNTDs previously exposed to alpha particles were irradiated separately to protons, ^{4}He-, ^{12}C-, and ^{16}O-ions at the Heidelberg Ion Beam Therapy Center (HIT, Heidelberg, Germany), to the beam qualities—given by the ion-type and nominal energy[†] combination—listed in Table 1. The detectors were placed at the isocenter of the experimental room (100.0 cm upstream from the nozzle window) by attaching them to the surface of a poly-methyl-methacrylate (PMMA) slab, with the FNTDs polished surface pointing toward the nozzle, that is, orthogonal to the beam direction. In all cases, scanned beams with an effective field size of 5×5 cm^2 and particle fluence of 1.8×10^6 cm^{-2} were used. A 3.0 mm PMMA ripple filter (RiFi) was present on the beam path during the irradiations with ^{4}He-, ^{12}C-, and ^{16}O-ion beams. The RiFi is a static modulation device that is clinically used to decrease the number of energies required to achieve smooth extended dose distributions. Five detectors were irradiated per beam quality. The unrestricted LET in water ($LET_{\infty,H_2O} = LET_{H_2O}$)[36] associated with the studied beams was set as the electronic stopping power in liquid water of a monoenergetic beam with an energy equal to the residual energy—with respect to the nominal energies and assuming continuous slowing down approximation (CSDA)—of the light ions after crossing a water slab with a thickness equivalent to the vacuum window, static elements standing within the nozzle, and air gap before the isocenter (Table 1). Based on the information of the vacuum window, beam monitoring system, and RiFi,[37,38] thicknesses of 2.00 and 3.43 mm of water were assumed for protons and all other ions, respectively. As recommended on the Report 90 from the International Commission on Radiation Units and Measurements (ICRU; Bethesda, MD, USA.), for protons, ^{4}He- and ^{12}C-ions the stopping powers were calculated using polynomial interpolation on a log–log scale to the data tabulated on that report.[39] The same methodology was adopted for ^{16}O-ions, however using published data[40] that combines values from the MSTAR and BEST codes.[41,42] For all ion species and within the studied energy ranges, this approach resulted in a percentage difference of less than 0.36% with respect to the tabulated data, which is below the estimated relative uncertainties of the electronic stopping powers. In the case of monoenergetic beams, the track- and dose-average LET_{H_2O} (LET_{F,H_2O} and LET_{D,H_2O}) have identical values, which follows from the mathematical definition of these quantities. Therefore, the difference is explicitly expressed only when required.

[†] The nominal energy corresponds to the energy at which the particles are accelerated and extracted from the synchrotron. As the nominal energy is the parameter that can be selected by the user, and for the sake brevity, we will refer to the nominal energy simply as energy.

2.2 | Detector readout

All FNTDs were imaged twice, first after the exposure to alpha particles and second after the irradiations with light ions. Due to the persistency of the transformed color centers, both alpha-particle and light-ion tracks could be visualized during the second readout. Nevertheless, as the range in Al_2O_3 of the alpha particles emitted by ^{244}Cm is 15.7 μm (under CSDA, after 0.3 cm of dry air and perpendicular incidence), acquiring images below this depth allowed imaging only the light-ion tracks. To avoid systematic effects, the detectors were randomized prior to the readouts.

For the readouts, the FNTDs were placed on top of P35G-1.5-20-C glass-bottom dishes (MatTek; Ashland, Massachusetts, USA). The detectors were imaged with a Zeiss LSM-710 (S.N.: 2502000464, Carl Zeiss Microscopy GmbH; Jena, Germany) confocal laser scanning microscope (CLSM) employing the ConfoCor-3 detection module, which is equipped with avalanche photodiodes (APDs). A 63x/1.40 Oil DIC M27 objective

was used to focus the excitation- and emission-light. Zeiss Immersol 518F immersion oil was used to ensure optical coupling between the objective, glass-bottom dish, and FNTDs. Color centers were excited by means of an HeNe laser (633 nm) having a nominal output power of 5.0 mW (approximately 100 μW at the FNTD surface).[26] An MBS-488/561/633 multi-beam splitter and an LP-655 low-pass emission-filter were placed within the light path for signal selection. The pinhole aperture was set to 1.0 Airy unit, resulting in a slice thickness (t_z) of 0.8 μm. In all cases, images of $135.0 \times 135.0\ \mu m^2$ (1280×1280 pixels) were acquired with a dwelling time (τ) of 40.33 μs per pixel and a depth of 16 bits. It was assumed that using fixed relative—to the nominal output power—laser powers could facilitate future measurements on unknown mixed-radiation fields. Therefore, unlike previous works carried out in our group, a fixed percentage laser power (p) of 20% was used to acquire images of light-ion tracks. This laser power proved to be adequate to detect low-LET particles, while minimizing saturation effects on the APD for high-LET particles. For imaging alpha-particle tracks p was set to 5%, in order to fit the whole range of sensitivities, without noticeable saturation of the APD.

After exposure to alpha particles, each detector was scanned at four positions, with each position centered at $\pm$150.0 μm in both lateral directions, with respect to the center of the traverse plane[††] (coinciding with the center of the polished surface). Scanning different regions of the same detector allowed characterizing the sensitivity over a large area and study variations within single detectors. At each position, a stack of five images was acquired from 3.0 to 7.0 μm below the detector polished surface by changing the focal plane at steps of 1.0 μm. After exposure to light ions, for each detector, one stack of 11 images was acquired at the center of the transverse plane from 15.0 to 65.0 μm below the polished surface at intervals of 5.0 μm. At the same lateral position, an additional stack of five images from 3.0 to 7.0 μm below the polished surface was acquired in 1.0 μm steps. The latter was used to investigate whether it was possible to isolate the alpha-particle tracks, which could allow us to skip the first readout.

As the campaign to expose and scan the FNTDs took place over several months, it was paramount to assess and correct for long-term variations of the CLSM response. To accomplish this, a reference FNTD was imaged at the beginning of each readout session under identical conditions. The reference FNTD was previously exposed to alpha particles and the track spots were used as fiducial markers, to ensure that the same region was always scanned. Owing to the persistency and stability of the color centers interrogated during the imaging process, fluorescence signal decay, due to fading or bleaching resulting from repeated scans, was neglected.[30] The aforementioned persistency is due to the fact that there is no recombination of the charge carriers, unlike the OSL process. To correct the readings for changes in the CLSM response, an inter readout session correction factor (k_d) was introduced and calculated as follows:

$$k_d = \frac{MPI_{baseline}}{MPI_d}, \tag{1}$$

where $MPI_{baseline}$ is the mean pixel intensity baseline value and MPI_d is the mean pixel intensity measured at a given readout session (denoted by the subscript d and standing for date). The mean pixel intensities were calculated as the mean pixel value of the reference FNTD images. The baseline value was established after general service to the CLSM. In general, k_d allows us to compare and correct measurements carried out at different readout sessions, by taking into account changes in the microscope response.

2.3 | Tracking and tracks analysis

From the acquired images, the tracks were reconstructed with an in-house developed plugin for Fiji-ImageJ.[43] This plugin performs routines for background subtraction and corrections for optical aberrations and light attenuation, followed by a segmentation of the track spots based on a threshold level. Individual tracks were reconstructed from the track spots by means of a 3D feature point tracking algorithm, which is also included on the plugin.[44] The tracking resulted in the raw fluorescence intensity (I_{raw}) for each one of the reconstructed tracks. I_{raw} was calculated as the mean value of the fluorescence intensity for all the track spots belonging to the same track. The mean raw count rate ($\bar{\eta}_{raw}$) was calculated as the ratio between the mean value of I_{raw} averaged over all the tracks ($\bar{I}_{raw}$) and τ. From $\bar{\eta}_{raw}$, the mean count rate corrected by the APD saturation, variable laser power, and nonlinearities between the laser power and the fluorescence intensity ($\bar{\eta}$) was calculated as follows[21]:

$$\bar{\eta} = k_p\ (-\eta_{sat} \ln(1 - \bar{\eta}_{raw}/\eta_{sat})), \tag{2}$$

where $\eta_{sat} = 16.2 \pm 1.4$ MHz is the saturation count rate and $k_p = (100\%/p)(p/p_{ref})^{-0.164}$ is the correction factor associated with the laser power.[21] Although a fixed laser power was used for the present work, the correction factor k_p was considered during the analysis for the sake

[††] Defined as the parallel plane going through the polished surface. By definition the traverse plane is perpendicular to the axial direction and parallel to the focal planes.

of consistency and for comparison purposes with previous data obtained in our group. For the same reasons, a value of 10% was used for the reference laser power (p_{ref}) in Equation (2).[21]

2.4 | Sensitivity correction factor

To cope with sensitivity variations among single crystals, a detector-specific sensitivity correction factor (k_s) was introduced into the workflow. This approach is analogous to the one proposed for TLDs and OSLDs.[45] The underlying idea is to rescale the response of each detector to match the average response of a given batch or reference sample. However, unlike TLDs and OSLDs, where the output signal is averaged over the detector volume, for FNTDs the intensity of a statistically representative number of tracks has to be used. Thus, for each detector (denoted by the subscript i), the sensitivity correction factor was calculated as

$$k_{s,i} = \frac{m^{-1}\, n^{-1} \sum_{i=1}^{m} k_{d,\alpha} \sum_{j=1}^{n} \left(\bar{\bar{I}}_{raw,\,\alpha} \right)_{j,i}}{k_{d,\alpha}\, n^{-1} \sum_{j=1}^{n} \left(\bar{\bar{I}}_{raw,\,\alpha} \right)_{j,i}} = \frac{m^{-1} \sum_{i=1}^{m} \left\langle \bar{\bar{I}}_{raw,\,\alpha} \right\rangle_i}{\left\langle \bar{\bar{I}}_{raw,\,\alpha} \right\rangle_i} = \frac{\left\langle \left\langle \bar{\bar{I}}_{raw,\,\alpha} \right\rangle \right\rangle}{\left\langle \bar{\bar{I}}_{raw,\,\alpha} \right\rangle_i}, \quad (3)$$

where $n = 4$ is the number of image stacks acquired on a single FNTD, $m = 100$ is the number of FNTDs on the reference set and $\bar{\bar{I}}_{raw,\alpha}$ is the mean intensity of the reconstructed alpha-particle tracks (hence, the α subscript) in one image stack. On the right side of Equation (3), $\langle \bar{\bar{I}}_{raw,\alpha} \rangle_i$ is the mean fluorescence intensity of all the tracks obtained from a single detector and $\langle\langle \bar{\bar{I}}_{raw,\alpha} \rangle\rangle$ is the mean fluorescence intensity of all the tracks obtained from the entire reference set, which in our case corresponds to the FNTDs used to study the relation between fluorescence intensity and LET_{H_2O}. Clearly, $\langle\langle \bar{\bar{I}}_{raw,\alpha} \rangle\rangle$ characterizes the response of the entire set of FNTDs. Due to the impossibility to scan all the detectors during the same readout session, the signal of each detector was corrected by k_d. However, the subscript α is added to k_d to explicitly show that all the images used to calculate $k_{s,i}$ for a given detector were acquired on the same date.

Similar to $k_{s,i}$, a sensitivity correction factor was calculated from the images containing both alpha-particle and light-ion tracks ($k'_{s,i}$). However, in this case the alpha-particle tracks had to be separated from the light-ion tracks. Assuming, based on previous observations for light and heavy ions,[20,22] that the distribution of I_{raw} for each type of particle can be approximated by a Gaussian distribution, a bi-Gaussian peak function was fitted to the I_{raw} distributions. One peak was associated with the alpha particles, whereas the other with the light ions. Equivalent to $k_{s,i}$, $k'_{s,i}$ was calculated as

$$k'_{s,i} = \frac{m^{-1}\, n^{-1} \sum_{i=1}^{m} k_{d,\alpha} \sum_{j=1}^{n} \left(\bar{\bar{I}}'_{raw,\alpha} \right)_{j,i}}{k_{d,\alpha}\, n^{-1} \sum_{j=1}^{n} \left(\bar{\bar{I}}'_{raw,\alpha} \right)_{j}} = \frac{\left\langle \left\langle \bar{\bar{I}}'_{raw,\alpha} \right\rangle \right\rangle}{\left\langle \bar{\bar{I}}'_{raw,\alpha} \right\rangle_i}, \quad (4)$$

where $\bar{\bar{I}}'_{raw,\alpha}$ is the mean intensity of the Gaussian peak associated with the alpha particles. All other parameters have the same or analogous meaning as in Equation (3).

2.5 | Calibration in terms of LET

For detectors exposed to light ions, the count rate corrected by k_d and $k_{s,i}$ was calculated as

$$\bar{\eta}_{corr,i} = k_{s,i}\, k_d\, \bar{\eta}_{ion,i}, \quad (5)$$

where $\bar{\eta}_{ion,i}$ is the mean count rate of the light-ion tracks (hence, the *ion* subscript) on a single detector. The mean corrected count rate ($\bar{\bar{\eta}}_{corr}$) was calculated as the arithmetic mean of $\bar{\eta}_{corr,i}$ for detectors exposed under the same conditions. In addition, a mean uncorrected count rate ($\bar{\bar{\eta}}_{uncorr}$) was calculated in order to evaluate the effect of the sensitivity correction $k_{s,i}$ on the results by setting $k_{s,i} = 1$ in Equation (5).

As already reported in previous works, the mean fluorescence intensity—or mean count rate in the same extent, due to their proportionality—of individual tracks depends on the ionization density of the ions interacting with the crystals.[20–23] Briefly, a higher ionization density results in the release of more secondary electrons per path length, which translates into a higher number of transformed color centers and, consequently, into a higher fluorescence intensity. To the best of the author's knowledge, currently there is no suitable theoretical framework, based on first principles, to derive a model describing the dependence of the fluorescence intensity with the ionization density. Therefore, the

relation between $\bar{\bar{\eta}}_{corr}$ and LET_{H_2O} was modeled through the following empirical analytical function:

$$\bar{\bar{\eta}}_{corr} = a \log\left(\frac{LET_{H_2O}}{b} + 1\right), \quad (6)$$

where a and b are free fitting parameters and were calculated using standard deviation weighted least squares fitting. The fitting error of a (σ_a) and b (σ_b) were weighted by the reduced chi-squared. The model presented in Equation (6) is based on previous works from our group, but with fewer free fitting parameters.[21] For an unknown radiation field, the LET_{H_2O} can be calculated by solving Equation (6):

$$LET_{H_2O} = b\left(10^{\frac{\bar{\bar{\eta}}_{corr}}{a}} - 1\right). \quad (7)$$

Hereafter, we will refer to Equations (6) and (7) as the response and calibration curves, respectively.

To compute LET_{F,H_2O} and LET_{D,H_2O}, the first and second moments (μ_1 and μ_2) of the count rate were calculated as follows:

$$\mu_R = \frac{1}{\mu_{R-1}} \sum_q^R \bar{\bar{\eta}}_{corr_q} P\left(\bar{\bar{\eta}}_{corr_q}\right) \Delta\bar{\bar{\eta}}_{corr}, \quad (8)$$

where $P(\bar{\bar{\eta}}_{corr_q})$ is the probability mass function of $\bar{\bar{\eta}}_{corr}$ (i.e., the discrete track-spectrum in the $\bar{\bar{\eta}}_{corr}$ space), $\Delta\bar{\bar{\eta}}_{corr}$ is the bin width used to discretize $P(\bar{\bar{\eta}}_{corr_q})$ and $\mu_0 = 1$ by definition. Afterward, μ_1 and μ_2 were used as input quantities in Equation (7) to calculate LET_{F,H_2O} and LET_{D,H_2O}, respectively. This approach showed to reduce the effects on the values of LET_{F,H_2O} and LET_{D,H_2O}, due to the nonlinear relation between $\bar{\bar{\eta}}_{corr}$ and LET_{H_2O}.

2.6 | Batch-to-batch sensitivity variations

Besides intra-batch sensitivity differences, batch-to-batch variations would invalidate applying the same calibration curve (Equation 7) to FNTDs from different batches (i.e., crystals produced on independent runs). In such cases, the free parameters on Equation (7) may have to be rescaled or redetermined. To investigate the viability to use $k_{s,i}$ to apply the same calibration curve to detectors from different batches, FNTDs from a second batch were exposed to protons, ^{4}He-, ^{12}C-, and ^{16}O-ions with energies of 145.46, 103.76, 176.56, and 193.77 MeV/u, respectively. The measured LET_{H_2O} was then compared with the values obtained from FNTDs of the reference set.

2.7 | Blind tests

A set of blind tests was performed to establish the accuracy of the LET_{H_2O} measured with FNTDs by an unbiased observer. Two groups of four FNTDs were exposed to unknown monoenergetic light-ion beams using the same experimental setup as the one described on Section 2.1.2. One further group was exposed, under the same conditions, to a mixed beam for which the type and number of particle species and their relative fluences were unknown. The last was deemed as a challenging scenario and used to mimic—in a controlled manner—those conditions frequently encountered in ^{12}C-ion radiotherapy, where it is common to find secondary light ions covering a broad-LET range. FNTDs from the same batch as the reference set were used for the blind tests. The accuracy was quantified through the absolute percentage difference between measured and theoretical LET_{F,H_2O} and LET_{D,H_2O} values. The latter were analytically calculated from the energies and fluences on the beam-delivery plans used to irradiate the FNTDs, following the same procedure as the one described on Section 2.1.2 and definitions for LET_{F,H_2O} and LET_{D,H_2O}.[36]

2.8 | Uncertainty analysis

The uncertainty analysis was performed according to the recommendations issued by the Joint Committee for Guides in Metrology Working Group 1 and the National Institute of Standards and Technology (NIST) on the NIST Technical Note 1297.[46,47]

The uncertainty on the fluorescence intensity due to the CLSM can mostly be attributed to long-term changes in the light path, variations in the laser intensity, and the accuracy on the position of the focal plane. The uncertainty associated with changes in the light path ($\sigma_{m_{lp}}$) was calculated as the standard deviation of MPI_d measured on three images of the reference FNTD, acquired consecutively at the same position. Regarding the focal plane position, two factors hamper to accurately establish it. First, the slice thickness due to the diffraction limited focus dimension and second the rather ambiguous position of the detector surface, which is also caused by the focus spot size. Therefore, the uncertainty on the position of the focal plane with respect to the FNTD was calculated as $\sigma_z = \sqrt{2}\, t_z$. Tests varying the focal plane by a factor equal to σ_z around depths of 5.0 and 7.0 μm showed an average change of 3.4% in the detected emitted light. Hence, the relative uncertainty on the measured fluorescence intensity due to the limited

precision on the position of the focal plane ($\sigma_{m_{fp}}$) was set equal to that value. The uncertainties of k_d (σ_{k_d}) and $k_{s,i}$ ($\sigma_{k_{s,i}}$) were calculated as follows:

$$\sigma_{k_d} = k_d \sqrt{\left(\frac{\sigma_{m_{lp}}}{MPI_d}\right)^2 + \left(\frac{\sigma_{m_{fp}}}{100\%}\right)^2}, \quad (9)$$

$$\sigma_{k_{s,i}} = k_{s,i} \sqrt{\left(\frac{\sigma_{\overline{\langle I_{raw,\alpha}\rangle}_i}}{\overline{\langle I_{raw,\alpha}\rangle}_i}\right)^2 + \left(\frac{\sigma_{m_{fp}}}{100\%}\right)^2 + \left(\frac{\sigma_{k_{d,\alpha}}}{k_{d,\alpha}}\right)^2}, \quad (10)$$

where $\sigma_{\overline{\langle I_{raw,\alpha}\rangle}_i}$ is the standard deviation of $\overline{\langle I_{raw,\alpha}\rangle}_i$.

The uncertainty of $\bar{\eta}_{corr,i}$ was calculated as follows:

$$\sigma_{\bar{\eta}_{corr,i}} = \bar{\eta}_{corr,i} \sqrt{\left(\frac{\sigma_{k_{s,i}}}{k_{s,i}}\right)^2 + \left(\frac{\sigma_{k_d}}{k_d}\right)^2 + \left(\frac{\sigma_{\bar{\eta}_{ion,i}}}{\bar{\eta}_{ion,i}}\right)^2}, \quad (11)$$

where $\sigma_{\bar{\eta}_{ion,i}}$ is the standard deviation of $\bar{\eta}_{ion,i}$. The uncertainty due to the stochastic energy deposition of the light ions interacting with the crystals is unavoidably included in $\sigma_{\bar{\eta}_{ion,i}}$, as the energy straggling is directly reflected in the statistical variations of $\bar{\eta}_{ion,i}$. The combined uncertainty of $\overline{\bar{\eta}}_{corr}$ ($\sigma_{\overline{\bar{\eta}}_{corr}}$) was calculated as

$$\sigma_{\overline{\bar{\eta}}_{corr}} = \sqrt{\sigma^2_{s,\bar{\eta}_{corr}} + \frac{1}{k}\sum_{i=1}^{k} \sigma^2_{\bar{\eta}_{corr,i}}}, \quad (12)$$

where $\sigma_{s,\bar{\eta}_{corr}}$ is the standard uncertainty of $\bar{\eta}_{corr}$ and k is the number of detectors exposed under the same conditions.

The combined uncertainty of the LET_{H_2O} predicted by Equation (7) ($\sigma_{f,LET_{H_2O}}$) was calculated according to the law of propagation of uncertainty, assuming null correlation between the input quantities:

$$\sigma_{f,LET_{H_2O},corr} = \sqrt{\sum_{I=a,b,\overline{\bar{\eta}}_{corr}} \left(\frac{\partial LET_{H_2O}}{\partial I}\right)^2 \sigma_I{}^2}. \quad (13)$$

Finally, the total combined uncertainty of LET_{H_2O} ($\sigma_{c,\ LET_{H_2O}}$) was calculated as

$$\sigma_{c,\ LET_{H_2O},corr} = \sqrt{\sigma_{f,LET_{H_2O},corr}{}^2 + \sigma_{ICRU}{}^2}, \quad (14)$$

where σ_{ICRU} is the relative standard uncertainty of the electronic stopping powers in water recommended by the ICRU Report 90.[39]

3 | RESULTS

3.1 | Exposure to alpha particles

Examples of fluorescence images are displayed in Figure 1a,b. Particularly, Figure 1a shows a typical image obtained after scanning a detector exposed to alpha particles. The mean number of alpha-particle tracks recorded per stack of images was 84 ± 9. It can be noticed that most of the tracks appear elongated due to the lack of collimation during the exposures, which resulted in tracks having angles with respect to the axial direction ranging from 0° to ±36°. As a result of this broad angular range, $\bar{I}_{raw}$ also exhibited a wide distribution, with a mean relative standard deviation of 29%. Images acquired between 7.0 and 17.0 μm below the detector surface in steps of 1.0 μm in the axial direction showed that the particle fluence decreased rapidly after 11.0 μm and that the maximum range of the alpha particles was 15.0 ± 1.2 μm, which corresponded to particles moving parallel to the axial direction. It is worth noting that the particle fluence remained constant between 3.0 and 7.0 μm, that is, at the depths used to calculate $k_{s,i}$. For the set of detectors used to establish the response curve (i.e., the reference set), $\langle\langle \overline{I}_{raw,\alpha}\rangle\rangle$ = 62.4 ± 17.2 corresponds to the rescaling factor used in Equation (3).

3.2 | Sensitivity correction factors

The values of $k_{s,i}$ for each one of the FNTDs used in the present work and their distributions are shown in Figure 2a,b, respectively. Values of $k_{s,i}$ greater and smaller than 1.0 indicate, respectively, lower and higher sensitivities with respect to the mean sensitivity of the reference set. For the three sets of FNTDs, the maximum, minimum, mean, and standard deviation of $k_{s,i}$ are tabulated in Table 2. For the reference set, $k_{s,i}$ spanned a range from 0.57 up to 2.55, with the values following a right-skewed distribution due to the presence of a relatively large number of detectors with low sensitivity. It can be noticed that a fraction of 6/100 detectors had a $k_{s,i}$ with values lying beyond 1.96 times the standard deviation. The $k_{s,i}$ values for the FNTDs used during the blind tests were consistent with those from the reference set. Regarding the second batch, the distribution of $k_{s,i}$ was narrower than the one for the reference set, with $k_{s,i}$ having values between 0.51 and 1.00. In general, the results showed that the lower the sensitivity of a particular FNTD, the higher the sensitivity variations within that detector, which ultimately translated into a higher uncertainty of $k_{s,i}$.

Examples of I_{raw} distributions obtained from FNTDs exposed to both alpha particles and light ions are depicted in Figure 3. The position of the peak associated with the alpha particles appears at different positions

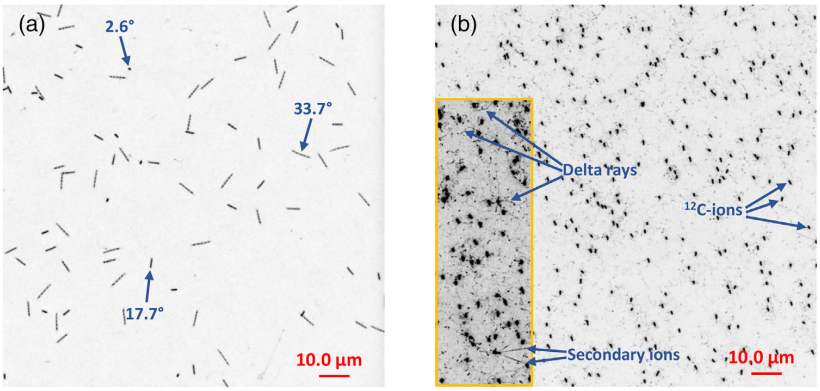

FIGURE 1 Gray scale maximum intensity projection images for detectors exposed to (a) alpha particles and (b) 124.25 MeV/u ^{12}C-ions. (a) The angle with respect to the axial direction is indicated for a selection of alpha-particle tracks. (b) A selection of primary ^{12}C-ions, delta rays, and secondary light-ions produced during a fragmentation nuclear reaction are indicated. (b) The enclosed region has a narrower contrast window, in order to enhance the visualization of low contrast objects. The lookup table is shown inverted; thus, a darker color corresponds to higher fluorescence intensity.

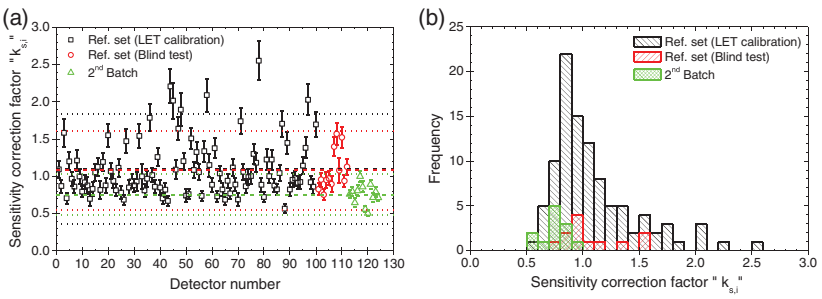

FIGURE 2 (a) Sensitivity correction factors ($k_{s,i}$) for all the detectors used in this work. With same colors as the data points, dashed and dotted lines indicate the mean values and 95% confidence intervals, respectively. The error bars correspond to the combined uncertainty of $k_{s,i}$ with a coverage factor equal to one. (b) Distributions of the sensitivity correction factors with a bin-width of 0.1

TABLE 2 Statistical figures of the sensitivity correction factors

Group	Maximum	Minimum	Mean	Standard deviation
Reference set (LET calibration)	2.55	0.57	1.10	0.38
Reference set (blind test)	1.57	0.75	1.08	0.27
Second batch	1.00	0.51	0.75	0.14

Note: The datasets are categorized according to their corresponding groups.
Abbreviation: LET, linear energy transfer.

($I_{raw,\alpha}$ = 56 and 34 on Figure 3a,b, respectively) due to different sensitivities. In fact, the idea behind the sensitivity correction proposed in this work relies on displacing the distributions so that the position of the alpha-particle peaks match a reference value (in our case the numerators in Equations 3 and 4). For FNTDs irradiated with both alpha particles and light ions other than protons, the I_{raw} distributions were adequately described by the fitted bi-Gaussian peak function. In the case of FNTDs irradiated with alpha particles and protons, the relatively low laser power used during the imaging process resulted in a low fluorescence intensity of the proton track spots and, therefore, only the alpha-particle tracks were reconstructed during the image analysis. In the latter, for consistency with the adopted methodology, a single Gaussian peak function was fitted to the I_{raw} distributions. For FNTDs irradiated with alpha particles and ^{4}He-ions, the I_{raw} distributions exhibited one prominent

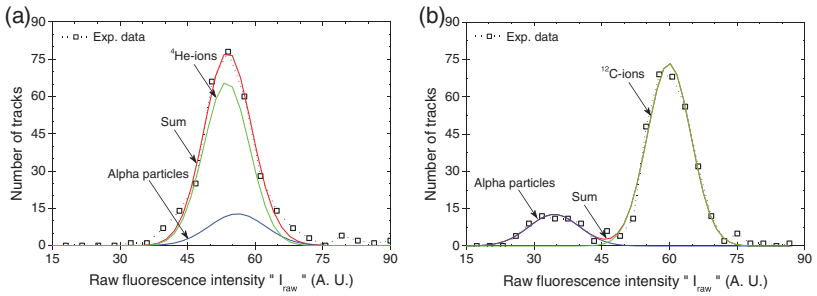

FIGURE 3 Number of tracks as a function of the raw fluorescence intensity (I_{raw}), for detectors exposed to (a) alpha particles and 70.79 MeV/u ^{4}He-ions and (b) alpha particles and 264.95 MeV/u ^{12}C-ions. The experimental data are shown with symbols connected with dotted lines. The solid lines correspond to the results from the fitted bi-Gaussian peak function.

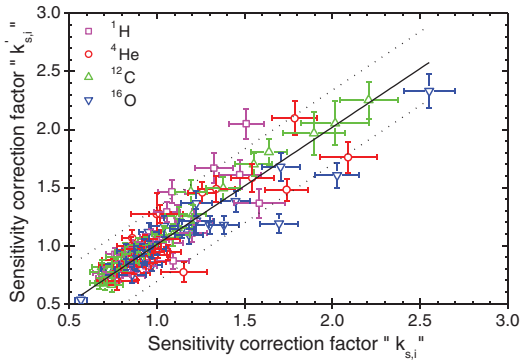

FIGURE 4 Sensitivity correction factors obtained after the exposure to both alpha particles and light ions ($k'_{s,i}$) against the sensitivity correction factor obtained from detectors exposed solely to alpha particles ($k_{s,i}$). The solid and dashed lines correspond, respectively, to a linear fit ($r^2 = 0.823$) and prediction bands at 95%. The error bars represent the uncertainty of $k_{s,i}$ and $k'_{s,i}$ with a coverage factor equal to 1.

peak due to alpha-particle and ^{4}He-ion peaks being completely overlapped. This made it challenging to isolate the signals and to accurately establish the position of the alpha-particle peak, requiring to set the height of the alpha-particle peak as a fixed parameter. Contrarily, for FNTDs irradiated with alpha particles and ^{12}C-ions, the I_{raw} distributions displayed two well-defined peaks. Similar to the latter, for FNTDs irradiated with alpha particles and ^{16}O-ions, the I_{raw} distributions presented two separate peaks.

Figure 4 displays $k'_{s,i}$ against $k_{s,i}$. A linear fit to the data resulted in a slope equal to 1.01 ± 0.01 ($r^2 = 0.823$), which is consistent with the identity. The mean absolute percentage residual after the fitting was 10.3%. Congruent with the observations for $k_{s,i}$, detectors with a higher under-response tend to deviate more from the linear fit due to larger sensitivity variations within the crystal.

3.3 | Exposure to light ions and LET calibration

Figure 1b shows a typical fluorescence image obtained after scanning an FNTD exposed to ^{12}C-ions. Equivalent images were obtained for all other ion species, except for track-spot intensities and number of observable delta rays increased or decreased according to the LET of the primary ions. In general, the higher the LET, the higher the fluorescence intensity and the number of delta rays. Unlike the case for the alpha-particle tracks, the projection of the light-ion tracks appeared as spots due to the ions moving parallel to the axial direction and low scattering in the material.

To visualize the effect of $k_{s,i}$ on the response curve, $\bar{\eta}_{uncorr}$ and $\bar{\eta}_{corr}$ are shown as a function of LET_{H_2O} in Figure 5a,b, respectively. The fitting parameters for the response curve were found to be $a = 19.00 \pm 0.67$ MHz and $b = 1.11 \pm 0.07$ keV/μm when sensitivity corrections were applied and $a = 18.22 \pm 1.21$ MHz and $b = 1.02 \pm 0.12$ keV/μm when sensitivity corrections were not taken into account. The sensitivity correction resulted in a better correlation between the data points and the fitted model, with a reduction of the mean absolute percentage residuals from 8.3% to 4.4% and an increase of r^2 from 0.973 to 0.993. For comparison, the same fitting process and model were applied to previously published data,[21] but parametrized in terms of LET_{H_2O}, which resulted in $a = 16.62 \pm 0.69$ MHz and $b = 1.12 \pm 0.09$ keV/μm. Using the latter fitting parameters and those obtained from the data corrected by $k_{s,i}$, the LET_{H_2O} was calculated using the same $\bar{\eta}_{corr}$ values as input (Table 3). These results show that, depending on the measured $\bar{\eta}_{corr}$, the change of the calibration curve parameters lead to differences between 19% and 77%, for protons and ^{16}O-ions, respectively.

Results for the second batch are shown in Figure 5 along with data from the reference set and response

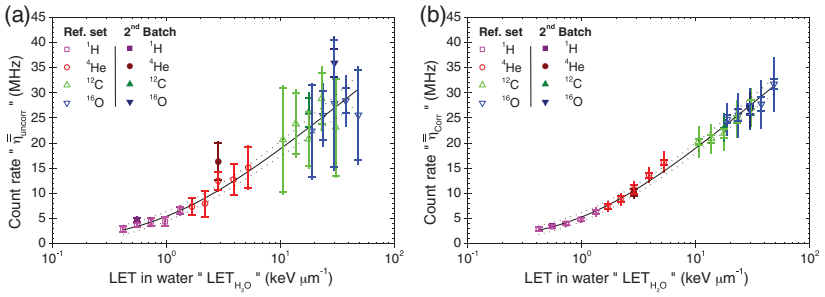

FIGURE 5 Mean count rate (a) uncorrected ($\bar{\eta}_{uncorr}$) and (b) corrected ($\bar{\eta}_{corr}$) by the sensitivity of each detector. Hollow and filled symbols correspond to detectors from the reference set (Ref. set) and from the second batch (2nd Batch), respectively. Solid and dashed lines show the response curves and prediction bands at 95%, respectively. Error bars with and without caps represent, respectively, the standard ($\sigma_{\bar{\eta}}$) and combined uncertainties ($\sigma_{\bar{\eta}}$) of the mean corrected count rates with coverage factors equal to 1.

TABLE 3 Linear energy transfer in water (LET_{H_2O}) calculated using different sets of parameters for the calibration curve

Ion	Nominal energy (MeV/u)	$\bar{\eta}_{corr}$ (MHz)	LET_{H_2O} (keV/μm) Theoretical[a]	This work (corrected by $k_{s,i}$)	Klimpki et al.[21]
^{1}H	221.06	2.9 ± 0.5	0.42	0.47 ± 0.05	0.55 ± 0.07
^{4}He	103.76	10.8 ± 1.6	2.9	3.0 ± 0.4	3.9 ± 0.6
^{12}C	176.56	22.0 ± 3.4	17.8	14.8 ± 3.1	22.5 ± 5.4
^{16}O	103.77	31.7 ± 5.4	48.6	50.8 ± 15.3	89.8 ± 13.1

Note: Uncertainties correspond to the combined uncertainty with a coverage factor equal to one.
[a]Calculated from the residual energy of the primary ion beams.

curves. In the absence of sensitivity corrections, the differences in the predicted LET_{H_2O}, between the reference set and the second batch, were 55%, 141%, 41%, and 186% for protons, ^{4}He-, ^{12}C-, and ^{16}O-ions, respectively, which is a direct consequence of the FNTDs from the second batch having a higher sensitivity with respect to the reference set. When the sensitivity correction was considered, the corresponding differences were reduced to 4.2%, 6.5%, 5.0%, and 11.0% for protons, ^{4}He-, ^{12}C-, and ^{16}O-ions, respectively.

3.4 | Blind tests

The LET_{H_2O} spectra obtained from the blind tests are summarized on Figure 6. Figure 6a,c,e shows the LET_{H_2O} spectra obtained without sensitivity corrections, whereas Figure 6b,d,f shows the respective LET_{H_2O} spectra after correcting by $k_{s,i}$. When the sensitivity correction is not taken into account, the spectra appear displaced toward lower and higher LET_{H_2O}, depending on the sensitivity of each detector. Contrarily, if $k_{s,i}$ is considered, the spectra tend to align around the same value. Based on the LET_{H_2O} range (available ranges can be seen in Table 1), for the two sets of FNTDs irradiated with monoenergetic light ions, it was concluded that the particle species were protons (Figure 6a,b) and ^{12}C-ions (Figure 6c,d). For the detectors exposed to the mixed beam (Figure 6e,f), four distinct peaks were identified and each peak was associated with a monoenergetic beam. Similar to the other two tests, based on the LET_{H_2O} range, the peak at the low-LET_{H_2O} region (LET_{H_2O} < 1.5 keV/μm), the two intermediate peaks (1.5 keV/μm < LET_{H_2O} < 10.0 keV/μm), and the peak at the high-LET_{H_2O} range (LET_{H_2O} > 10.0 keV/μm) were associated with protons, ^{4}He-ions, and ^{12}C-ions, respectively. It should be noticed that, in order to increase the track count, each FNTD exposed to the mixed beam required to be scanned at four lateral positions.

The mean LET_{F,H_2O} and LET_{D,H_2O} values obtained from the measured $\bar{\eta}_{corr}$ spectra are listed in Table 4, along with the theoretical values calculated from the beam-delivery plans. Without sensitivity correction, the differences between measured and the theoretical LET_{F,H_2O} were 20%, 7.4%, and 27% for protons, ^{12}C-ions and the mixed beam, respectively. When the sensitivity correction was considered, the same differences were 0.3%, 16% and 9.6% for protons, ^{12}C-ions and the mixed

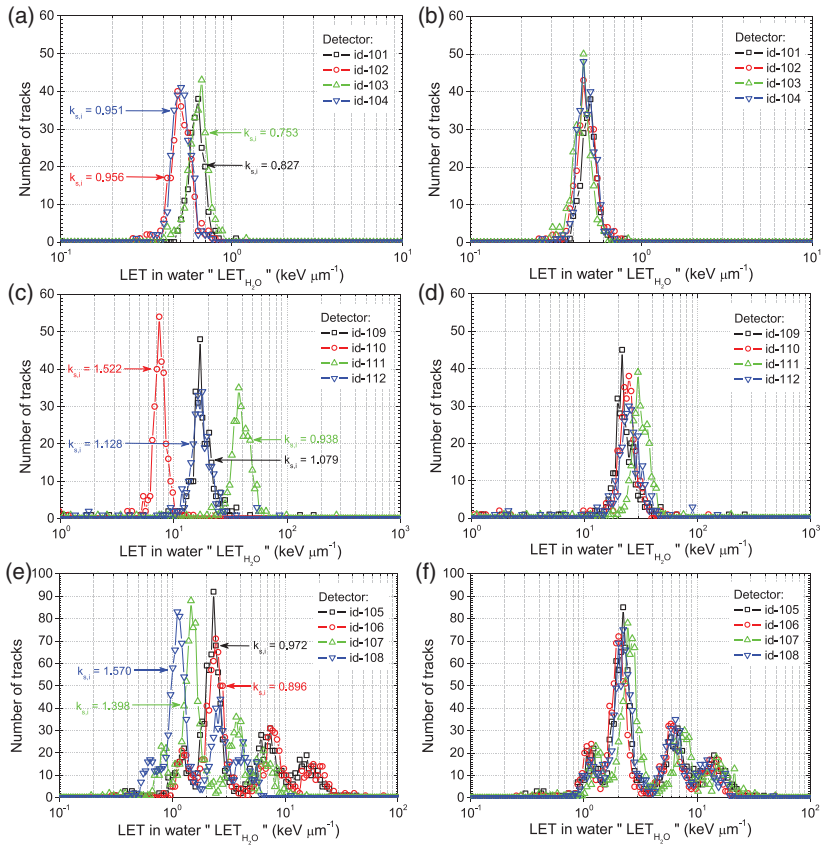

FIGURE 6 Measured spectra of linear energy transfer (LET) in water (LET_{H_2O}) for the blind tests, (a, c, and e, i.e., left column) without and (b, d, and f, i.e., right column) with sensitivity corrections. (a, c, and e) The sensitivity correction factors ($k_{s,i}$) used to obtain the corrected spectra are indicated with arrows for each detector. A pair of graphs in the same row correspond to the same test. The spectra were generated using a logarithmic binning with 200 bins between 0.1 and 1000 keV/μm.

TABLE 4 Measured and theoretical track- and dose-average linear energy transfer (LET) in water (LET_{F,H_2O} and LET_{D,H_2O}) for the blind tests

	LET_{F,H_2O} (keV/μm)			LET_{D,H_2O} (keV/μm)		
	Measured		Theoretical	Measured		
Ion	Uncor.	Cor.		Uncor.	Cor.	Theoretical
^{1}H	0.57 ± 0.07	0.48 ± 0.02	0.48 ± 0.01	0.58 ± 0.07	0.48 ± 0.02	0.48 ± 0.01
^{12}C	18.5 ± 12.3	23.1 ± 3.8	20.0 ± 0.5	20.2 ± 13.0	25.5 ± 3.5	20.0 ± 0.5
Mixed	3.0 ± 1.1	3.6 ± 0.3	4.0 ± 0.1	4.0 ± 1.8	5.0 ± 0.4	7.2 ± 0.2

Note: For the measurements, values for both corrected and uncorrected by the sensitivity are included. The uncertainty of the measured data corresponds to the standard uncertainty for detectors exposed under the same conditions. For the theoretical values, the uncertainty corresponds to the standard uncertainty of the electronic stopping powers in water. In all cases the uncertainties are reported with a coverage factor equal to one.

beam, respectively. For the LET_{D,H_2O}, the differences between measured and theoretical values were 21%, 1.0%, and 44% without sensitivity corrections and 1.7%, 28%, and 30% with sensitivity correction, for protons, ^{12}C-ions, and the mixed beam, respectively. In all cases, the standard uncertainty of the measured quantities was reduced—by a mean factor of 3.7—when the sensitivity correction was applied. For the detectors exposed to ^{12}C-ions, the fact that LET_{F,H_2O} and LET_{D,H_2O} are in better agreement with the theoretical values follows the coincidental fact that the mean value of $k_{s,i}$ is close to 1 for that set of detectors.

TABLE 5 Mean position of the peaks for the detectors exposed to the mixed beam

Ion	Peak position (keV/μm) Measured Uncor.	Cor.	Theoretical
^{1}H	0.98 ± 0.31	1.20 ± 0.05	1.12
^{4}He	1.8 ± 0.7	2.2 ± 0.2	2.1
^{4}He	5.0 ± 2.2	6.7 ± 0.8	5.0
^{12}C	11.0 ± 6.7	13.6 ± 1.1	12.7

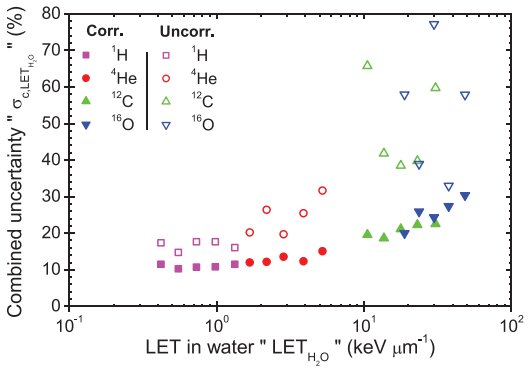

FIGURE 7 Combined uncertainty of the linear energy transfer (LET) in water (LET_{H_2O}) with ($\sigma_{c,\ LET_{H_2O},corr}$, solid symbols) and without ($\sigma_{c,\ LET_{H_2O},uncorr}$, hollow symbols) sensitivity corrections

The positions of the peaks on the LET_{H_2O} spectra for the mixed beam are listed in Table 5. In general, when the sensitivity correction is applied, the position of the peaks better agrees with the theoretical values, with the peak at 5.0 keV/μm as the only exception. Similar to previous results, the standard uncertainty is decreased as a result of the sensitivity correction.

3.5 | Uncertainty on the predicted LET

Figure 7 presents $\sigma_{c,\ LET_{H_2O},corr}$ and $\sigma_{c,\ LET_{H_2O},uncorr}$ as a function of LET_{H_2O}. In general, the combined uncertainty increases with LET_{H_2O}. This trend can mainly be attributed to the increase of the energy straggling, and thus $\sigma_{\bar{\eta}_{ion,i}}$, with LET_{H_2O}. On average, $\sigma_{c,\ LET_{H_2O},corr}$ is 11%, 13%, 21%, and 26% for protons, ^{4}He-, ^{12}C-, and ^{16}O-ions, respectively. These values increased for the most part by a factor of 2.0 when the sensitivity correction was not considered. In this case, the dominant source of uncertainty was $\sigma_{s,\bar{\eta}_{uncorr}}$, with an average value of 28%, which by itself is higher than $\sigma_{c,\ LET_{H_2O},corr}$. Contrarily, $\sigma_{s,\bar{\eta}_{corr}}$ had an average value of 5.2%, that is, there was a reduction by a factor of 5.0 in the standard uncertainty of $\bar{\eta}_{corr}$. Regarding $k_{s,i}$, the mean value of $\sigma_{k_{s,i}}$ was 8.5%, with values ranging from 4.9% up to 14%. Typically, the relative standard uncertainty of $\langle \bar{\bar{I}}_{raw,\alpha} \rangle_i$ and σ_{k_d} contributed by 4.4% and 3.5% to $\sigma_{k_{s,i}}$, respectively. Almost independent of LET_{H_2O}, the error of the fitting parameters introduced an uncertainty of 2.0% and 3.4% with and without the sensitivity correction, respectively.

4 | DISCUSSION

4.1 | Exposure to alpha particles

Our experimental setup resulted in wide angular and $\bar{I}_{raw}$ distributions. In principle, the width of these distributions can be reduced by introducing a collimation device between the source and the FNTDs, as previously shown in other works.[48] However, this would require to increase the source activity or exposure time. Moreover, our results suggest that, as long as the same experimental setup is used, the lack of collimation should not have an impact on the values of $k_{s,i}$, as it is a relative quantity. Clearly, for the last to be true, a sufficiently large number of tracks have to be analyzed.

4.2 | Sensitivity correction factor

Despite the observed large sensitivity variations, the results show that alpha particles can be effectively used to derive a detector-specific sensitivity correction factor. Particularly, their short range, high ionization density and straight line tracks make alpha particles highly convenient to characterize the sensitivity of single FNTDs, while exploiting the tools already available for the analysis of ion tracks. Furthermore, alpha-particle sources are relatively common, readily accessible, of low cost and can provide a highly reproducible radiation field. In addition, by utilizing an alpha-particle source, FNTDs can be exposed with a simple and compact tabletop experimental setup that allows a high exposure throughput.

In principle, besides alpha particles, other particle types could be used to assess the sensitivity of single crystals. Similar to alpha particles, low-energy (with a maximum energy less than 70 keV) beta particles are good candidates due to their finite and short range in condensed matter. However, due to the tortuous trajectory and relatively low LET of electrons, tracking is unviable with current tools. In such case, it might be feasible to use the mean pixel intensity after the exposure to adequately large particle fluence, instead of the intensity of individual tracks. Alternatively, reference ion beams might be used to derive $k_{s,i}$. One option is ions with energy sufficiently low for them to stop within a few microns below the detector surface. However, ions with such low energies (e.g., protons with an energy of

1 MeV/u have a range of approximately 25 μm in Al_2O_3) might require to expose the FNTDs under complicated experimental conditions, such as vacuum chambers with ultrathin windows, to avoid perturbations of the ion beam. Another further option are ions having an LET markedly different to the radiation fields under study; however, this would require to develop a robust methodology to isolate the reference ion tracks from those of the radiation field that is being investigated. Moreover, for both cases, it is necessary to have access to suitable particle accelerators, circumstance mostly reserved for a group of specialized research centers.

The previous discussion assumes that the state of the transformed color centers remains unaltered after the exposure to the reference radiation. For this reason, it is necessary to develop suitable strategies to characterize the sensitivity without interfering with actual measurements. Being able to erase the radiation induced signal in order to restore the initial state of the FNTDs—e.g., by optical bleaching—could allow to use a reference radiation field having less restrictive characteristics. Clearly, the sensitivity of the FNTDs should not be altered by the erasing process and the time required to erase the signal should be considered. It is worth noting that, even if possible to erase the radiation induced signal to avoid disturbing the measurements, the properties of alpha particles remain appealing.

A major drawback with the proposed methodology is that imaging alpha-particle tracks with confocal microscopy techniques is time-consuming. With the instruments and settings used for this work, it took approximately 15 min to acquire a single stack of images containing alpha-particle tracks. Widefield microscopy has shown promising results at reducing the time required to image FNTDs, without compromising the detection efficiency of light-ion tracks.[27] As $k_{s,i}$ is based on relative measurements, it appears plausible to image the FNTDs after the exposure to alpha particles by means of a widefield microscope to reduce the time invested on characterizing the sensitivity of each detector. In addition, dedicated FNTD readers can also be advantageous at reducing the time to image alpha-particle tracks, albeit not with the same magnitude as widefield microscopy.

Although our results show the efficacy of applying a detector-specific correction factor, a single value may only describe locally the sensitivity of a given crystal. Therefore, using a single value is reasonable for measurements that involve regions close to the one used to assess the sensitivity. However, applications that require scanning larger portions of the crystal would require more than one correction factor, depending on the desired level of accuracy. In-depth crystal inhomogeneities may also be a concern, and it is advised to perform measurements in the vicinity below the volume used to evaluate the sensitivity. In the present study, the volume used to derive $k_{s,i}$ and the one used to perform the ion-track measurements were adjacent and, thus, sensitivity changes were neglected.

The results regarding $k'_{s,i}$ show that it is possible to avoid imaging the FNTDs after the exposure to alpha particles and prior to the irradiations with light ions. From the perspective of reducing the time, there is no advantage as it is still necessary to image regions exposed to alpha particles. Moreover, this method can be deemed as more challenging and time-consuming as it requires to separate the alpha-particle and light-ion signals. However, this approach can mostly be useful for detectors exposed in the past and for which it is necessary to know the sensitivity or to perform measurements close to the FNTD surface that could be perturbed by the presence of the alpha-particle tracks. In the latter, it might also be convenient to use two-sided polished FNTDs. Particularly, one side can be exposed to alpha particles and used to assess the sensitivity, whereas the second side can be irradiated with another type of radiation and used to perform the measurements of interest. Another further option is to expose only a small region of the FNTDs to alpha particles, instead of the whole face. For the last two options, the uncertainty due to sensitivity inhomogeneities within the detector should be considered.

In previous works on which FNTDs were used for LET spectrometry of light ions, the sensitivity variations were managed by applying rescaling factors based on Monte Carlo simulations.[31,33,34] As explained earlier, this approach might entail some limitations, as it requires validated codes, detailed knowledge regarding the experimental components, and computational resources. Moreover, this type of rescaling factors can be applied only to the specific situations implemented on the simulations. To our best knowledge, in the present work, we have presented for the first time an entirely experimental approach to cope with the sensitivity variations of FNTDs aiming to LET spectrometry applications in PT and IBT.

4.3 | Exposure to light ions and LET calibration

The existence of dependence between the fluorescence intensity of single tracks and the LET, for both light and heavy ions, has been extensively studied and reported.[20–23] Our results showed good quantitative agreement with previous studies performed within our group and elsewhere.[21,22] Nevertheless, by comparing the fitting parameters presented in the results for the calibration curve, it is clear that the relation between fluorescence intensity and LET_{H_2O} depends on the batch, due to differences in the sensitivities. Less obvious, still not negligible, is that the fitting parameters might also depend on the microscope response at the moment of establishing the calibration curve and its temporal drift.

Clearly, reliable calibration parameters are essential for accurate LET-spectra measurements. This is especially true for ^{12}C-ions, as small changes in the measured fluorescence intensity can lead to largely inaccurate results due to the flatness of the response curve on the high-LET range. As $k_{s,i}$ and k_d introduce traceability to a specific batch and to the point in time when the calibration curve was established, we anticipate that the methodology presented in this work will allow in future works to appropriately handle sensitivity variations of the FNTDs (both within the same batch and from one batch to another) and changes in the microscope response.

Other studies reported or implicitly assumed that the fluorescence intensity is uniquely described by the LET.[21–23,31–34] However, our results, by virtue of their superior accuracy, suggest the existence of a dependence with the type of particle. More specifically, it appears (Figure 5b) to be a noncontinuous change in the slope of the data between 70.79 and 50.57 MeV/u (3.89 and 5.23 keV/μm) ^{4}He-ions and 430.10 and 264.95 MeV/u ^{12}C-ions (10.6 and 13.7 keV/μm). This hypothesis is further supported by the fact that, for detectors exposed to both alpha particles and light ions, the alpha-particle peak appears at lower intensities than the peaks of ^{12}C- and ^{16}O-ions, despite alpha particles having a higher LET (LET_{H_2O} of approximately 190 keV/μm at 5.0 μm below the detector surface). For the latter, a fall in the efficiency at high LET could be argued, but this argument contradicts observations for ^{56}Fe-ions (LET_{H_2O} = 147–431 keV/μm) with respect to ^{12}C-ions (LET_{H_2O} = 12.6–257 keV/μm).[23] The dependence of the response with the ion type is common for luminescent detectors and can be explained on the basis of track-structure theories.[49–51] Briefly, different particles having the same LET result in nonidentical secondary electron spectra and, in consequence, a different spatial energy deposition around the track core. To experimentally prove the suggested existence of a dependence between the fluorescence intensity of single tracks measured with FNTDs and the type of ion, data for different ion species within overlapping LET ranges would be necessary. If our hypothesis holds true, the magnitude of this dependence and its implications within the frame of PT and IBT will have to be evaluated and fully deserve further investigations.

4.4 | Blind test

The results from the blind tests allowed us to assess the robustness of the proposed protocol and further demonstrate that the sensitivity correction improves the accuracy of the LET spectra measured with FNTDs in unknown-mixed-radiation fields composed of light ions having energies relevant to PT and IBT. Although monoenergetic ^{4}He- and ^{16}O-ions were not included as part of the blind tests, we expect that a similar degree of accuracy can be achieved as for protons and ^{12}C-ions, respectively. As mentioned earlier, the lower accuracy for ^{12}C-ions, if compared with protons, results from the exponential increase of the calibration curve derivative with $\bar{\bar{\eta}}_{corr}$. To further illustrate, at $\bar{\bar{\eta}}_{corr}$ = 4.0 MHz ($dLET_{H_2O}/d\bar{\bar{\eta}}_{corr}$ = 0.22 keV/μm MHz), which is within the expected values for protons, a perturbation of 5.0% would lead to a change of 6.4% in the LET_{H_2O} predicted by Equation (7). In contrast, a perturbation of the same magnitude at $\bar{\bar{\eta}}_{corr}$ = 22.0 MHz ($dLET_{H_2O}/d\bar{\bar{\eta}}_{corr}$ = 1.93 keV/μm MHz), which is within the typical range for ^{12}C-ions, will result in a change of 15% on the LET_{H_2O}.

4.5 | Uncertainty on the predicted LET

Our approach to correct for sensitivity variations introduces the additional factor $k_{s,i}$, and therefore one further component of uncertainty that propagates to $\sigma_{c,\,LET_{H_2O}}$. Despite this, using $k_{s,i}$ to correct the sensitivity of each detector results in a decrease of $\sigma_{c,\,LET_{H_2O}}$, as it counters the statistical dispersion of $\bar{\eta}_{ion,i}$.

Taking into account the sources of uncertainty, different strategies can be proposed to reduce their relative values. For instance, as the higher contribution to $\sigma_{k_{s,i}}$ comes from $\sigma_{\bar{\bar{\langle I_{raw,\alpha}\rangle}}_i}$, the uncertainty of $k_{s,i}$ can be decreased by using crystals having a more homogeneous sensitivity. The uncertainty due to the lack of accuracy in the position of the focal plane can be lowered by decreasing the pinhole aperture, as a lower pinhole diameter reduces the value of t_z. However, to keep the count of fluorescence photons constant, it would be necessary to increase the dwelling time accordingly, and therefore the scanning time. Moreover, the slice thickness is subject to the diffraction limit. To reduce the uncertainty due to fluctuations in the laser power rescanning, techniques can be easily implemented, but at the expense of increasing the imaging time. Finally, increasing the number of analyzed tracks should decrease, to some extent, the relative value of $\sigma_{\bar{\eta}_{ion,i}}$, which is a major component of uncertainty. Clearly, scanning different positions of the same detector would increase the track count while escalating the scanning time. An alternative approach is to image a larger area by using an objective with a lower magnification, with the disadvantage of having a reduced spatial resolution. In summary, if necessary, alternatives can be explored to decrease the uncertainty of LET_{H_2O} and, for each application, cost-effective strategies for its reduction and their implications should be carefully evaluated.

5 | CONCLUSIONS

We have demonstrated for the first time that alpha particles can be effectively used to derive a detector-specific sensitivity correction factor that enhances the accuracy and precision of LET spectra measured with FNTDs. Furthermore, this type of sensitivity correction factor allows us to apply the calibration curve established with one batch to FNTDs from other batches. The robustness and accuracy of the proposed methodology was verified by means of a series of blind tests and the main sources of uncertainty were identified and quantified. FNTD technology represents a valuable and powerful tool to measure LET spectra on therapeutic light-ion radiation fields. We envision that our proposal can be applied to accurately measure LET spectra both on clinically relevant scenarios and radiobiology experiments related to PT and IBT.

ACKNOWLEDGMENTS

The authors are deeply indebted to Dr. Felix Bestvater and Manuela Brom from the Light Microscopy Core Facility at DKFZ for their help and support to operate the CLSM and ensuring optimal working conditions. From the Division of Medical Physics in Radiation Oncology at DKFZ, the authors would like to thank Armin Runz and Kathrin Panow for designing and printing the holder used to irradiate with alpha particles, Dr. Renato Felix for support during the irradiations at HIT and Dr. José Vedelago and Anna Becker for fruitful discussions about FNTDs. From the Division of Biomedical Physics in Radiation Oncology at DKFZ, we thank Daniel García for useful advice regarding the CLSM. We also thank Dr. Eduardo Yukihara from the Paul Scherrer Institute for reviewing the manuscript and valuable comments. I.D.M. acknowledges the German Academic Exchange Service for funding through the "Research Grants—Doctoral Programmes in Germany" program (program number: 57440921).

CONFLICTS OF INTEREST

The authors declare that there are no conflicts of interest.

DATA AVAILABILITY STATEMENT

Data available on request from the authors.

REFERENCES

1. ICRU. Prescribing, recording, and reporting light ion beam therapy. *ICRU Report 93. International Commission of Radiological Units*. ICRU; 2020. https://doi.org/10.1093/jicru/ndy025
2. Paganetti H. Relative biological effectiveness (RBE) values for proton beam therapy. Variations as a function of biological endpoint, dose, and linear energy transfer. *Phys Med Biol*. 2014;59:R419. https://doi.org/10.1088/0031-9155/59/22/R419
3. Mairani A, Magro G, Dokic I, et al. Data-driven RBE parameterization for helium ion beams. *Phys Med Biol*. 2016;61:888. https://doi.org/10.1088/0031-9155/61/2/888
4. IAEA ICRU. Relative biological effectiveness in ion beam therapy. *IAEA Technical Reports Series 461*. International Atomic Energy Agency; 2008.
5. Rossomme S, Marinelli M, Verona-Rinati G, et al. Response of synthetic diamond detectors in proton, carbon, and oxygen ion beams. *Med Phys*. 2017;44:5445. https://doi.org/10.1002/mp.12473
6. Sawakuchi GO, Yukihara EG, McKeever SWS, Benton ER. Optically stimulated luminescence fluence response of Al_2O_3:C dosimeters exposed to different types of radiation. *Radiat Meas*. 2008;43:450. https://doi.org/10.1016/j.radmeas.2007.08.003
7. Grusell E, Medin J. General characteristics of the use of silicon diode detectors for clinical dosimetry in proton beams. *Phys Med Biol*. 2000;45:2573. https://doi.org/10.1088/0031-9155/45/9/310
8. Massillon-JL G, Gamboa-deBuen I, Brandan ME. TL response of LiF:Mg,Ti exposed to intermediate energy ^{1}H, ^{3}He, ^{12}C, ^{16}O and ^{20}Ne ions. *J Phys D: Appl Phys*. 2007;40:2584. https://doi.org/10.1088/0022-3727/40/8/025
9. Castriconi R, Ciocca M, Mirandola A, et al. Dose–response of EBT3 radiochromic films to proton and carbon ion clinical beams. *Phys Med Biol*. 2016;62:377. https://doi.org/10.1088/1361-6560/aa5078
10. Alsanea F, Therriault-Proulx F, Sawakuchi G, Beddar S. A real-time method to simultaneously measure linear energy transfer and dose for proton therapy using organic scintillators. *Med Phys*. 2018;45:1782. https://doi.org/10.1002/mp.12815
11. Schöner W, Vana N, Fugger M. The LET dependence of LiF:Mg,Ti dosemeters and its application for LET measurements in mixed radiation fields. *Radiat Prot Dosim*. 1999;85:263. https://doi.org/10.1093/oxfordjournals.rpd.a032847
12. Loncol T, Hamal M, Denis JM, Vynckier S, Wambersie A, Scalliet P. Response analysis of TLD-300 dosimeters in heavy-particle beams. *Phys Med Biol*. 1996;41:1665. https://doi.org/10.1088/0031-9155/41/9/007
13. Puchalska M, Bilski P. An improved method of estimating ionisation density using TLDs. *Radiat Meas*. 2008;43:679. https://doi.org/10.1016/j.radmeas.2007.11.049
14. Reft C, Pankuch M, Ramirez H. Thermoluminescent detectors to measure let in proton beams. *Austin J Med Oncol*. 2017;4:1.
15. Parisi A, Chiriotti S, De Saint-Hubert M, et al. A novel methodology to assess linear energy transfer and relative biological effectiveness in proton therapy using pairs of differently doped thermoluminescent detectors. *Phys Med Biol*. 2019;64:085005. https://doi.org/10.1088/1361-6560/aaff20
16. Sawakuchi GO, Saho N, Gasparian PB, et al. Determination of average LET of therapeutic proton beams using Al_2O_3:C optically stimulated luminescence (OSL) detectors. *Phys Med Biol*. 2010;55:4963. https://doi.org/10.1088/0031-9155/55/17/006
17. Granville DA, Sahoo N, Sawakuchi GO. Simultaneous measurements of absorbed dose and linear energy transfer in therapeutic proton beams. *Phys Med Biol*. 2016;61:1765. https://doi.org/10.1088/0031-9155/61/4/1765
18. Christensen JB, Togno M, Bossin L, Pakari OV, Safai S, Yukihara EG. Improved simultaneous LET and dose measurements in proton therapy. *Sci Rep*. 2022;12:8262. https://doi.org/10.1038/s41598-022-10575-4
19. Granja C, Jakubek J, Polansky S, et al. Resolving power of pixel detector Timepix for wide-range electron, proton and ion detection. *Nucl Instrum Methods Phys Res. Sect A*. 2018;908:60. https://doi.org/10.1016/j.nima.2018.08.014
20. Sawakuchi GO, Ferreira FA, McFadden CH, et al. Nanoscale measurements of proton tracks using fluorescent nuclear track detectors. *Med Phys*. 2016;43:2485. https://doi.org/10.1118/1.4947128
21. Klimpki G, Mescher H, Akselrod MS, Jäkel O, Greilich S. Fluence-based dosimetry of proton and heavier ion beams using single track detectors. *Phys Med Biol*. 2016;61:1021. https://doi.org/10.1088/0031-9155/61/3/1021

22. Sykora GJ, Akselrod MS, Benton ER, Yasuda N. Spectroscopic properties of novel fluorescent nuclear track detectors for high and low LET charged particles. *Radiat Meas*. 2008;43:422. https://doi.org/10.1016/j.radmeas.2007.11.009
23. Bartz JA, Kodaira S, Kurano M, Yasuda N, Akselrod MS. High resolution charge spectroscopy of heavy ions with FNTD technology. *Nucl Instrum Methods Phys Res Sect B*. 2014;335:24. https://doi.org/10.1016/j.nimb.2014.05.019
24. Akselrod MS, Yoder RC, Akselrod GM. Confocal fluorescent imaging of tracks from heavy charged particles utilising new Al_2O_3:C,Mg crystals. *Radiat Prot Dosim*. 2006;119:357. https://doi.org/10.1093/rpd/nci664
25. Akselrod GM, Akselrod MS, Benton ER, Yasuda N. A novel Al_2O_3 fluorescent nuclear track detector for heavy charged particles and neutrons. *Nucl Instrum Methods Phys Res Sect B*. 2006;247:295. https://doi.org/10.1016/j.nimb.2006.01.056
26. Greilich S, Osinga JM, Niklas M, et al. Fluorescent nuclear track detectors as a tool for ion-beam therapy research. *Radiat Meas*. 2013;56:267. https://doi.org/10.1016/j.radmeas.2013.01.033
27. Walsh DW, Liew H, Schlegel J, Mairani A, Abdollahi A, Niklas M. Carbon ion dosimetry on a fluorescent nuclear track detector using widefield microscopy. *Phys Med Biol*. 2020;65:21NT02. https://doi.org/10.1088/1361-6560/abb7c5
28. Akselrod M, Kouwenberg J. Fluorescent nuclear track detectors–review of past, present and future of the technology. *Radiat Meas*. 2018;117:35. https://doi.org/10.1016/j.radmeas.2018.07.005
29. Akselrod MS, Akselrod AE, Orlov SS, Sanyal S, Underwood TH. Fluorescent aluminum oxide crystals for volumetric optical data storage and imaging applications. *J Fluoresc*. 2003;13:503. https://doi.org/10.1023/B:JOFL.0000008061.71099.55
30. Akselrod MS, Akselrod AE. New Al_2O_3:C,Mg crystals for radiophotoluminescent dosimetry and optical imaging. *Radiat Prot Dosim*. 2006;119:218. https://doi.org/10.1093/rpd/nci663
31. Rahmanian S, Niklas M, Abdollahi A, Jäkel O, Greilich S. Application of fluorescent nuclear track detectors for cellular dosimetry. *Phys Med Biol*. 2017;62:2719. https://doi.org/10.1088/1361-6560/aa56b4
32. Greilich S, Jansen J, Neuholz A, Stadler A, Mescher H, Klimpki G. Evaluation of additional track parameters from fluorescent nuclear track detectors to determine the LET of individual ions. *Radiat Prot Dosim*. 2018;180:206. https://doi.org/10.1093/rpd/ncx228
33. Verkhovtsev A, Zimmer L, Greilich S. Calibration of intensity spectra from fluorescent nuclear track detectors in clinical ion beams. *Radiat Meas*. 2019;121:37. https://doi.org/10.1016/j.radmeas.2018.12.006
34. McFadden CH, Rahmanian S, Flint DB, et al. Isolation of time-dependent DNA damage induced by energetic carbon ions and their fragments using fluorescent nuclear track detectors. *Med Phys*. 2020;47:272. https://doi.org/10.1002/mp.13897
35. Akselrod MS, Fomenko VV, Bartz JA, Ding F. FNTD radiation dosimetry system enhanced with dual-color wide-field imaging. *Radiat Meas*. 2014;71:166. https://doi.org/10.1016/j.radmeas.2014.05.026
36. ICRU. Linear energy transfer. *ICRU Report 16. International Commission of Radiological Units*. ICRU; 1970. https://doi.org/10.1093/jicru/os9.1.Report16
37. Parodi K, Mairani A, Brons S, et al. Monte Carlo simulations to support start-up and treatment planning of scanned proton and carbon ion therapy at a synchrotron-based facility. *Phys Med Biol*. 2012;57:3759. https://doi.org/10.1088/0031-9155/57/12/3759
38. Weber U, Kraft G. Design and construction of a ripple filter for a smoothed depth dose distribution in conformal particle therapy. *Phys Med Biol*. 1999;44:2765. https://doi.org/10.1088/0031-9155/44/11/306
39. ICRU. Key data for ionizing-radiation dosimetry: measurements standards and applications. *ICRU Report 90. International Commission on Radiation Units and Measurements*. ICRU; 2016. https://doi.org/10.1093/jicru/ndw043
40. Burigo LN, Greilich S. Impact of new ICRU 90 key data on stopping-power ratios and beam quality correction factors for carbon ion beams. *Phys Med Biol*. 2019;64:195005. https://doi.org/10.1088/1361-6560/ab376e
41. Paul H, Schinner A. An empirical approach to the stopping power of solids and gases for ions from $_3$Li to $_{18}$Ar. *Nucl Instrum Methods Phys Res Sect B*. 2001;179:299. https://doi.org/10.1016/S0168-583X(01)00576-6
42. Paul H, Schinner A. An empirical approach to the stopping power of solids and gases for ions from $_3$Li to $_{18}$Ar – Part II. *Nucl Instrum Methods Phys Res Sect B*. 2002;195:166. https://doi.org/10.1016/S0168-583X(02)01027-3
43. Schindelin J, Arganda-Carreras I, Frise E, et al. Fiji: an open-source platform for biological-image analysis. *Nat Methods*. 2012;9:676. https://doi.org/10.1038/nmeth.2019
44. Kouwenberg JJM, Ulrich L, Jäkel O, Greilich S. A 3D feature point tracking method for ion radiation. *Phys Med Biol*. 2016;61:4088. https://doi.org/10.1088/0031-9155/61/11/4088
45. Kry SF, Alvarez P, Cygler JE, et al. AAPM TG 191: clinical use of luminescent dosimeters: TLDs and OSLDs. *Med Phys*. 2020;47:e19. https://doi.org/10.1002/mp.13839
46. JCGM Working Group 1 (100:2008). Evaluation of measurement data – guide to the expression of uncertainty in measurement (corrected version 2010). *International Organization for Standardization (ISO)*. Joint Committee for Guides in Metrology; 2010.
47. Taylor BN, Kuyatt CE. Guidelines for evaluating and expressing the uncertainty of NIST measurement results. *NIST Technical Note 1297*. National Institute of Standards and Technology; 1994.
48. Thompson JM, Elliott A, D'Abrantes S, Sawakuchi GO, Hill MA. Tracking down alpha-particles: the design, characterisation and testing of a shallow-angled alpha-particle irradiator. *Radiat Prot Dosim*. 2019;183:264. https://doi.org/10.1093/rpd/ncy300
49. Berger T, Hajek M, Summerer L, Fugger M, Vana N. The efficiency of various thermoluminescence dosemeter types to heavy ions. *Radiat Prot Dosim*. 2006;120:365. https://doi.org/10.1093/rpd/nci582
50. Yukihara EG, Doull BA, Ahmed M, et al. Time-resolved optically stimulated luminescence of Al_2O_3:C for ion beam therapy dosimetry. *Phys Med Biol*. 2015;60:6613. https://doi.org/10.1088/0031-9155/60/17/6613
51. Parisi A, Sawakuchi G, Granville D, Yukihara EG. Microdosimetric modeling of the relative efficiency of Al_2O_3:C (Luxel, blue emission) optically stimulated luminescent detectors exposed to ions from ^{1}H to ^{132}Xe. *Radiat Meas*. 2022;150:106678. https://doi.org/10.1016/j.radmeas.2021.106678

How to cite this article: Muñoz ID, Burigo LN, Gehrke T, Brons S, Greilich S, Jäkel O. Sensitivity correction of fluorescent nuclear track detectors using alpha particles: Determining LET spectra of light ions with enhanced accuracy. *Med Phys*. 2023;50:2385–2401. https://doi.org/10.1002/mp.16083

3.6. Publication II

Optically stimulated luminescence detectors for dosimetry and LET measurements in light ion beams

Authors: J. B. Christensen, I. D. Muñoz, N. Bassler, C. Stengl, L. Bossin, M. Togno, S. Safai, O. Jäkel, and E. G. Yukihara

Status: Published
Journal: Physics in Medicine & Biology
DOI: http://doi.org/10.1088/1361-6560/acdfb0

Contributions: JBC was responsible for the readout of the OSLDs and analyzing the resulting data. IDM was responsible for performing and optimizing the irradiations at HIT. IDM performed the dosimetric characterization of all the beams used at HIT. JBC supported the optimization of the irradiation conditions and assisted during the irradiations at HIT. CS assisted during the irradiations at HIT and secured the beam time. JBC, MT, and SS were responsible for performing and optimizing the irradiations at PSI. LB assisted during the irradiations and data analysis at PSI. IDM implemented the experimental setup at HIT in the Monte Carlo simulations. JBC and IDM validated the simulated geometry. NB assisted in the validation of the simulations and implementation of the scorers, and provided scientific advice on the simulations. The concept of studying Al_2O_3:C,Mg for LET measurements was conceived by EGY and JBC. JBC, EGY and OJ supervised and managed the research. OJ and EGY secured and allocated the necessary resources for the project. Data curation and visualization were performed by JBC. JBC, IDM, and NB drafted and edited the original manuscript. All authors participated in the review of the final version of the manuscript.

IOP Publishing Phys. Med. Biol. 68 (2023) 155001 https://doi.org/10.1088/1361-6560/acdfb0

Physics in Medicine & Biology

IPEM Institute of Physics and Engineering in Medicine

OPEN ACCESS

RECEIVED
22 March 2023

REVISED
25 May 2023

ACCEPTED FOR PUBLICATION
19 June 2023

PUBLISHED
19 July 2023

PAPER

Optically stimulated luminescence detectors for dosimetry and LET measurements in light ion beams

Jeppe Brage Christensen[1], **Iván Domingo Muñoz**[2,3,4], **Niels Bassler**[5,6], **Christina Stengl**[3,4,7], **Lily Bossin**[1], **Michele Togno**[8], **Sairos Safai**[8], **Oliver Jäkel**[3,4,9] and **Eduardo Gardenali Yukihara**[1]

[1] Department of Radiation Safety and Security, Paul Scherrer Institute, Villigen PSI, Switzerland
[2] Department of Physics and Astronomy, University of Heidelberg, Heidelberg, Germany
[3] Division of Medical Physics in Radiation Oncology, German Cancer Research Center (DKFZ), Heidelberg, Germany
[4] Heidelberg Institute for Radiation Oncology (HIRO), National Center for Radiation Research in Oncology, Heidelberg, Germany
[5] Department of Clinical Medicine, Aarhus University, Aarhus, Denmark
[6] Danish Centre for Particle Therapy, Aarhus University Hospital, Aarhus, Denmark
[7] Faculty of Medicine, University of Heidelberg, Heidelberg, Germany
[8] Center for Proton Therapy, Paul Scherrer Institute, Villigen PSI, Switzerland
[9] Heidelberg Ion-Beam Therapy Center (HIT), Department of Radiation Oncology, Heidelberg University Hospital, Heidelberg, Germany

E-mail: jeppe.christensen@psi.ch

Keywords: particle dosimetry, linear energy transfer (LET), ionization quenching, optically stimulated luminescence (OSL), particle therapy

Abstract

Objective. This work investigates the use of Al_2O_3:C and Al_2O_3:C,Mg optically stimulated luminescence (OSL) detectors to determine both the dose and the radiation quality in light ion beams. The radiation quality is here expressed through either the linear energy transfer (LET) or the closely related metric Q_{eff}, which depends on the particle's speed and effective charge. The derived LET and Q_{eff} values are applied to improve the dosimetry in light ion beams. *Approach.* OSL detectors were irradiated in mono-energetic ^{1}H-, ^{4}He-, ^{12}C-, and ^{16}O-ion beams. The OSL signal is associated with two emission bands that were separated using a pulsed stimulation technique and subjected to automatic corrections based on reference irradiations. Each emission band was investigated independently for dosimetry, and the ratio of the two emission intensities was parameterized as a function of fluence- and dose-averaged LET, as well as Q_{eff}. The determined radiation quality was subsequently applied to correct the dose for ionization quenching. *Main results.* For both materials, the Q_{eff} determinations in ^{1}H- and ^{4}He-ion beams are within 5 % of the Monte Carlo simulated values. Using the determined radiation quality metrics to correct the nonlinear (ionization quenched) detector response leads to doses within 2 % of the reference doses. *Significance.* Al_2O_3:C and Al_2O_3:C,Mg OSL detectors are applicable for dosimetry and radiation quality estimations in ^{1}H- and ^{4}He-ions. Only Al_2O_3:C,Mg shows promising results for dosimetry in ^{12}C-ions. Across both materials and the investigated ions, the estimated Q_{eff} values were less sensitive to the ion types than the estimated LET values were. The reduced uncertainties suggest new possibilities for simultaneously estimating the physical and biological dose in particle therapy with OSL detectors.

1 Introduction

The use of protons and heavier ions for radiotherapy treatments is increasing (Grau *et al* 2020), but the variation of the relative biological effectiveness (RBE) with the local ionization density remains a challenge (McNamara *et al* 2015, Hahn *et al* 2022). To predict the biological effect in ion beams, RBE-models are applied, where the linear energy transfer (LET) is a central parameter. For a more complete reporting of ion beam therapy, Report 93 (ICRU 2016) suggests to report LET-related quantities for treatment plans, e.g. dose-weighted LET distributions. For proton therapy, where a constant RBE is still clinical practice, a direct scaling of RBE with LET may be implemented in treatment planning systems. Methods such as LET painting have been developed to best handle and account for LET distributions for RBE calculations (Bassler *et al* 2010). Nevertheless, LET is defined

for a single ion type and energy in Report 16 (ICRU 1970). For a mixed radiation field, various definitions of averaged LET have been developed.

Due to the lack of a general or reference LET detector, however, the measurement and experimental validation of such LET-optimized plans is challenging. Active detectors may be capable to resolve either the microdosimetric spectrum (Conte *et al* 2020) or lead to a derivation of the particle spectrum using e.g. time-resolved silicon detectors (Nabha *et al* 2022). Active detectors are nonetheless limited by their fluence saturation in raster scanning delivering systems, or by a physical size that hinders their use inside anthropomorphic phantoms. Volumetric detectors have been suggested for LET measurements (Maeyama *et al* 2022, Nielsen *et al* 2022), but they exhibit an ionization quenched response (Hoye *et al* 2017). Passive detectors like fluorescent nuclear track detectors are also capable of estimating both LET and dose (Klimpki *et al* 2016, Muñoz *et al* 2022), but are challenging to use for clinically relevant doses due to track overlapping.

Alternatives for LET measurements with passive detectors are based on thermoluminescence detectors (TLDs) (Vana *et al* 1996) or, in recent years, optically stimulated luminescence detectors (OSLDs) (Sawakuchi *et al* 2010, Yukihara *et al* 2022). Particularly, the Al_2O_3:C OSLD was shown to be able to simultaneously determine the LET and dose at a point of interest (Granville *et al* 2016). Further work demonstrated its capability for LET determinations in clinically relevant proton beams (Granville *et al* 2014a, 2014b, Christensen *et al* 2022), with indications of possible LET measurements in ions heavier than protons (Yukihara *et al* 2015). Also shown to be dose-rate independent, Al_2O_3:C OSLDs can be used for dosimetry and to derive the LET under ultra-high dose rate conditions (Christensen *et al* 2021). Finally, its high sensitivity and small size means that it could be utilized as a point-like object and fitted into phantoms to derive the radiation quality at the point of interest.

Another candidate for LET determinations is Al_2O_3:C,Mg, which is a material with similar properties to Al_2O_3:C (Rodriguez *et al* 2011). Al_2O_3:C,Mg was initially developed as fluorescent nuclear track detector (Akselrod *et al* 2006), but both its radiophotoluminescence and optically stimulated luminescence (OSL) properties can be correlated to the LET in light ions (Denis *et al* 2011, De Saint-Hubert *et al* 2021). Al_2O_3:C and Al_2O_3:C,Mg are characterized by OSL emission bands in the blue and UV regions upon green light stimulation (Denis *et al* 2011).

Sawakuchi *et al* (2010) demonstrated that the ratio of the two emission bands correlates well with the dose- or fluence-averaged LET in protons. Given an LET calibration, the ratio of the UV and blue emission bands can then be used to estimate the average LET in the OSLD, whereupon the estimated LET can be applied to correct the ionization quenched dose derived from the blue emission band (Granville *et al* 2016). Yukihara *et al* (2015) demonstrated that LET measurements of light ions using Al_2O_3:C OSLDs is problematic due to saturation effects, and that the response correlates poorly with dose-averaged LET.

A broader challenge in LET determination is caused by the varying track structure of ions, where the radial dose distribution spans several orders of magnitude in light ion beams. The distinct radial energy distributions of two different ions with the same LET will thus result in two different detector responses, i.e. a single LET value is insufficient to accurately predict the detector response when measured with an OSLD (Yukihara *et al* 2015) or TLD (Olko *et al* 2002). This motivates the search for other radiation quality metrics which are less sensitive to the specific ion type.

Within this study, we propose the use of Q_{eff} to act as a radiation quality metric for ionization quenching corrections. Q_{eff} is related to the LET and depends on the ion's effective charge and speed. Initially used for particle emulsions (Barkas 1963) and amorphous track structure models (Katz 1978), Q_{eff} was recently demonstrated to correlate better with the RBE than LET (Lühr *et al* 2017, Kalholm *et al* 2022).

Therefore, this study aims at investigating the use of Al_2O_3:C and Al_2O_3:C,Mg OSLDs under irradiation with mono-energetic ^{1}H-, ^{4}He-, ^{12}C-, and ^{16}O-ion beams for dosimetry, and Q_{eff}, and LET determinations. To improve the accuracy of previous OSL studies in light ions (Yukihara *et al* 2015), the measured OSL signals were here corrected using automatic reference irradiations of each detector in line with Christensen *et al* (2022). Furthermore, we investigated whether Q_{eff} provides a better prediction of the detector response than LET does, and, ultimately, improves the dosimetry.

2 Materials and methods

2.1 Radiation quality metrics

The radiation quality Q_{eff} is independent of the material density and given as a function of the relativistic speed $\beta = v/c$ as

$$Q_{\text{eff}} = \frac{z^{*2}}{\beta^2}, \qquad \text{where} \quad z^*(\beta) = z\left(1 - \exp\left(-\frac{125\beta}{z^{2/3}}\right)\right) \tag{1}$$

is the effective charge of a particle with charge z and speed v (Barkas 1963). To calculate an averaged LET, a distinction is made between the LET calculated by weighting it by the dose (d-LET) or fluence (f-LET), where the

latter also is referred to as track-averaged LET. The Monte Carlo scoring of the averaged values follows the implementation defined in Cortés-Giraldo and Carabe (2015) as method C. In this work, Q_{eff} is exclusively used in its fluence-averaged definition. Q_{eff}, f-LET, and d-LET are henceforth collectively referred to as the radiation quality metrics.

2.2 Optically stimulated luminescence detectors

2.2.1 Detector preparation

The Al_2O_3:C and Al_2O_3:C,Mg OSLDs consist of a $(50 \pm 3)\mu$m Al_2O_3 layer mixed with a binder on a 75 μm polyester substrate as described in Ahmed *et al* (2014). The detectors were cut to ø4.5 mm and optically bleached with a green LED prior to irradiation to erase previous signal caused by background irradiation. For each irradiation, the OSLDs were placed in custom made opaque polylactide (PLA) containers (5 cm × 5 cm × 0.3 mm), each accommodating five detectors of both OSL materials in a centered 2 cm × 2 cm grid. The thickness of the PLA cover shielding the OSLDs from external light was measured to be 1.0 mm with a density of 1.15 g cm^{-3}.

2.2.2 OSL readout and reference irradiation

The blue and UV emission bands of the Al_2O_3:C and Al_2O_3:C,Mg detectors were measured using a time-resolved OSL readout technique (Yukihara and McKeever 2006). The OSLDs were stimulated with 100 μs pulses and the two components were separated using the stimulation parameters detailed in Christensen *et al* (2022). Due to the build-up rate of the UV emission band, the OSLDs were read out between (14–19) days after the irradiation to minimize the variation of the OSL intensities during the course of the readouts. The fading rate of the blue emission band is approximately constant after a week (Christensen *et al* 2022). Both signals from the blue and UV emission bands were normalized to the signal 14 days after irradiation with fading or build-up corrections <1 %.

Each OSLD was subject to the same automated readout sequence in a Risø reader (TL/OSL-DA-20, DTU Nutech, Denmark). The sequence is detailed in Christensen *et al* (2022) and consists of (i) a 300 s readout of an irradiated OSL using green light stimulation giving the integral signal S, (ii) a 30 s irradiation with the build-in $^{90}Sr/^{90}Y$ beta source corresponding to ≈1 Gy, followed by (iii) a second 300 s readout of the reference irradiation giving the integral signal S_{ref}.

The OSL intensity after ∼250 s stimulation is generally 3–4 orders of magnitude lower than the initial OSL intensity. This allows for an estimation of the background OSL signal from the last 10 s readout, which subsequently is subtracted from the OSL curve. Here, the signal S describes the integral luminescence of either the blue or UV emission band from the irradiation in an ion beam, whereas the ratio S/S_{ref} represents the ratio between the luminescence signal after the unknown dose and the luminescence signal after the irradiation using the built-in beta source, both signals defined and calculated in the same way. Although the quantity S/S_{ref} is sensitive to the irradiation history of the OSLD, it normalizes the OSL signal to the detector size and sensitivity when all OSLDs are subject to the same dose.

Whilst this work models the OSL response based on the integral OSL signal, Sawakuchi *et al* (2010) demonstrated that the shape of the OSL curve also can be used to infer the radiation quality. Relating the shape of the OSL curve to the radiation quality has the advantage that a constant background signal is irrelevant. On the other hand, the OSL curve shape is more sensitive to data fluctuations at low doses than an integral OSL signal is (Sawakuchi *et al* 2010). The use of the OSL shape to determine the radiation quality is not pursued in this work.

2.3 Irradiations

All OSLDs used for this work were irradiated at ≈0.25 Gy at the Center for Proton Therapy (CPT) at the Paul Scherrer Institute (PSI) or the Heidelberg Ion-Beam Therapy Center (HIT). At each facility, the OSLDs were contained within a 2 cm × 2 cm grid and the dose at the OSLD position was measured with an ionization chamber with its effective measurement point coinciding with the OSLDs. For irradiations at both centers, the ionization chamber measurements were corrected by as described in the TRS-398 (IAEA 2000).

The effect of overlapping ion tracks may affect the OSL emission intensities but requires further studies. To exclude such an effect from this study, the dose was chosen to be sufficiently low for the effect of track overlap to be negligible (Granville 2015), while still providing a luminescence signal equivalent to at least 100 mGy for the heavily ionization quenched ^{16}O-ions.

2.3.1 PSI irradiations

The irradiations with protons at the CPT were performed with the OSLDs positioned below 2 cm solid water (RW3 Water Slab, PTW Freiburg, Germany) in (70, 100, 230) MeV beams. The dose to each OSLD measurement point was measured with an ionization chamber (Advanced Markus TM34045, PTW Freiburg, Germany).

Table 1. Al_2O_3:C and Al_2O_3:C,Mg OSLD irradiation conditions used for the measurements at PSI and HIT, as well as the Monte Carlo simulated derived quantities. The given water-equivalent depth includes the RW3 slabs and the PLA container in front of the OSLDs in the irradiation with particles of initial energy $E_{initial}$. The Monte Carlo simulated energy in the OSLD (E_{OSLD}) only includes contributions from the primary particles. The Q_{eff} defined in equation (1), as well as the fluence- and dose-averaged LETs, include the contributions from primary and secondary particles. The LET values are given for water.

Irradiation conditions				Monte Carlo simulated results			
Center	Ion	Depth (mm)	$E_{initial}$ (MeV u^{-1})	E_{OSLD} (MeV u^{-1})	Q_{eff}	f-LET (keV µm^{-1})	d-LET (keV µm^{-1})
PSI	^{1}H	20.5	70.0	42.5	11.1	1.35	1.57
PSI	^{1}H	35.5	70.0	15.0	29.3	3.00	3.32
PSI	^{1}H	36.5	70.0	11.9	37.7	3.62	4.16
PSI	^{1}H	37.5	70.0	8.36	64.9	5.04	6.78
PSI	^{1}H	20.5	100	78.8	6.61	0.860	1.15
PSI	^{1}H	20.5	230	212	3.28	0.453	1.07
HIT	^{1}H[a]	6.4	221	212	3.15	0.447	0.958
HIT	^{4}He	6.4	50.6	32.2	56.8	6.71	7.74
HIT	^{4}He	6.4	70.8	56.3	33.7	4.29	5.13
HIT	^{4}He	6.4	103	91.0	22.3	2.99	4.01
HIT	^{4}He	6.4	148	136	16.2	2.25	3.53
HIT	^{4}He	6.4	221	206	12.0	1.72	3.21
HIT	^{12}C	6.4	88.8	51.3	280	35.5	41.3
HIT	^{12}C	6.4	124	95.1	167	22.8	26.9
HIT	^{12}C	6.4	177	144	114	16.3	19.6
HIT	^{12}C	6.4	265	218	80.2	11.8	14.9
HIT	^{12}C	6.4	430	364	58.9	9.06	12.0
HIT	^{16}O	6.4	104	59.0	425	55.2	62.2
HIT	^{16}O	6.4	141	101	264	36.5	41.6
HIT	^{16}O	6.4	194	151	186	26.9	31.2
HIT	^{16}O	6.4	279	231	138	20.8	23.6
HIT	^{16}O	6.4	430	361	103	16.0	19.6

[a] This radiation quality was not measured with Al_2O_3:C,Mg.

Measurements at lower energies were obtained by varying the upstream solid water thickness in the 70 MeV field as detailed in table 1, while scaling the fluence to achieve a 0.25 Gy dose at the OSLD location.

The dose calibration used for all readouts were obtained by delivering the 230 MeV protons at different doses to the OSLDs placed below 2 cm solid water, as detailed in Christensen *et al* (2022).

2.3.2 HIT irradiations

The irradiations with ^{1}H-, ^{4}He-, ^{12}C-, and ^{16}O-ions at HIT were conducted with the OSLDs placed behind 0.5 cm of the same type of solid water slabs used at PSI. This thickness was used to ensure charge particle equilibrium, even for the highest energies, at the point of interest. The dose was measured for each ion and energy using an ionization chamber (Farmer 001714, PTW Freiburg, Germany). For protons, an energy-dependent radiation quality-correction factor was used, which is parameterized in terms of the residual energy (IAEA 2000). For ^{4}He- and ^{12}C-ions a constant radiation quality-correction was applied, which is based on calorimetry measurements (Holm *et al* 2021).

Each ion/energy combination is detailed in table 1. A 3.0 mm PMMA ripple filter was used during the measurements with the ^{4}He-, ^{12}C-, ^{16}O-ions (Weber and Kraft 1999). The ripple filter is used in clinical setups to increase the the Bragg peak's width and was included to facilitate the validation of the simulations by comparing the measurements to HIT's reference data (Parodi *et al* 2012).

2.4 Monte Carlo simulations

The experimental setups used at PSI and HIT were simulated using Monte Carlo particle transport methods to calculate the radiation quality parameters at the OSLD positions. The grid resolution in the Monte Carlo scoring with `TOPAS` was set to 0.5 mm to approximate the detector thickness. For the scoring of Q_{eff}, f-LET, and d-LET, secondary particles heavier than the primary particle were excluded to avoid biasing the d-LET for ^{1}H-and ^{4}He-ions. The kinetic energy of the primary particles was scored at the OSLD position. The LET was scored for water at density 1.0 g cm^{-3}. Delta-particle equilibrium was assumed, so unrestricted LET was used, i.e. secondary electrons in the LET averaging were excluded to avoid double counting their contribution. The software and

Table 2. Summary of the Monte Carlo simulation parameters as proposed by Sechopoulos *et al* (2018). The models are used to calculate the dose, Q_{eff}, fluence-, and dose-averaged LET distributions during the experiments at PSI and HIT.

Item name	Description	References
Code, version	`TOPAS`, version 3.9.1	Perl *et al* (2012)
Validation	Depth-dose measurements against simulations	
Timing	16 CPUs, CPU time 1×10^5 s	
Geometry	Detectors placed in a 2 cm $\times$ 2 cm grid at the isocenter with solid slabs (RW3) upstream.	Schoenfeld *et al* (2015)
Physics	A modular list consisting of `g4decay`, `g4h-elastic_HP`, `g4em-standard_opt4`, `g4h-phy_QGSP_BIC_HP`, `g4stopping`, `g4ion-binarycascade`.	
Scoring	Dose to water, Q_{eff}, fluence- and dose-averaged LET in water; Excluding secondaries heavier than the primary particle.	
# Histories	10^8 primaries for each radiation quality	

most relevant simulation parameters are provided in table 2 following the recommendations by Sechopoulos *et al* (2018). The composition and density of the RW3 solid water follows Schoenfeld *et al* (2015).

To validate the Monte Carlo simulations, depth-dose curves were measured with ionization chambers in ^{1}H-ions at CPT and in ^{1}H-, ^{4}He-, ^{12}C-ions at HIT.

2.5 Q_{eff} and LET calibrations

The ratios of the UV and blue emission bands from Al_2O_3:C and Al_2O_3:C,Mg were parameterized as a function of each of the Monte Carlo derived radiation quality metrics Q_{eff}, f-LET, d-LET. To model the data and establish a relationship between the OSL response and each of the three metrics, empirical functions were fitted to the data. The three models, described through an arc-tan, an error-function, and a logistic function are defined as

$$f_{\text{atan}}(\alpha) = A\left(\frac{1}{2} + \frac{\text{atan}\alpha}{\pi}\right), \tag{2}$$

$$f_{\text{erf}}(\alpha) = A\left(\frac{1 + \text{erf}\,\alpha}{2}\right), \tag{3}$$

$$f_{\log}(\alpha) = A\left(1 - \frac{1}{1 + \exp\,\alpha}\right), \tag{4}$$

for $\alpha = (x - \mu)/\sigma$, where A is the amplitude with μ and σ the mean and spread, respectively. The `python` module `LMFIT` (Newville *et al* 2016) version 1.1.0 was used to estimate the fit quality of each function.

2.6 Relative effectiveness

To describe the detector response in the different radiation qualities, the relative effectiveness is introduced to relate the relative response of the OSL detector to the reference ionization chamber.

The relative detector efficiency is here defined using the iso-dose definition

$$\eta = \frac{D_{\text{OSLD}}}{D_{\text{ref}}}\bigg|_{\text{iso-dose}}, \tag{5}$$

where D_{ref} is the dose measured with an ionization chamber at the OSLD position, and D_{OSLD} the measured dose with the OSLD without any ionization quenching corrections. To avoid measurements near steep dose gradients, only the OSLDs irradiated at the entrance region are used to map the relative detector efficiency to reduce the uncertainty.

The dose calibrations for both emission bands in Al_2O_3:C and Al_2O_3:C,Mg were obtained for OSLDs irradiated at doses (0.050–1.0) Gy in the 230 MeV proton beam and is detailed in Christensen *et al* (2022). The relative detector efficiency for both the UV and blue emission bands was parameterized as a function of Q_{eff}, f-LET, and d-LET.

3 Results and discussion

3.1 Monte Carlo simulations

The simulated depth-dose curves for ^{1}H-ions at PSI and ^{1}H-, ^{4}He-, and ^{12}C-ions at HIT are shown in figure 1, along with the ionization chamber measurements. The overall agreement between the measurements and simulations validates the use of the Monte Carlo models to simulate the Q_{eff} and LET at the OSLD positions.

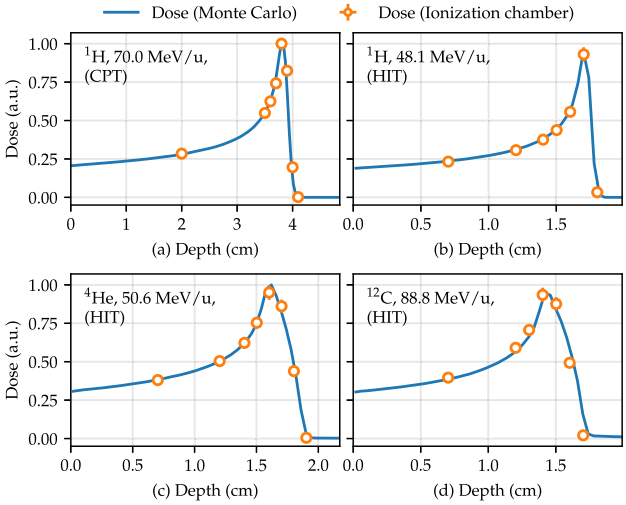

Figure 1. Depth-dose distributions in solid water (RW3) simulated with the Monte Carlo particle transport code (solid line) and ionization chamber measurements (markers) for (a) ^{1}H at CPT, and at HIT for (b) ^{1}H, (c) ^{4}He, and (d) ^{12}C.

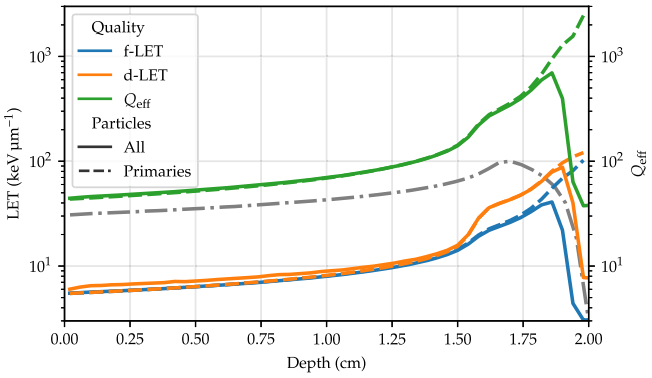

Figure 2. Example of the simulated in-depth distributions of the fluence-averaged LET (f-LET), dose-averaged LET (d-LET), and Q_{eff} for 50.6 MeV u^{-1} ^{4}He-ions along the central beam axis. The distributions are plotted for both the primary particle fields (dashed lines) and including both primaries and secondaries (solid lines). The dose distribution is plotted with dotted–dashed lines for reference.

3.1.1 LET and Q_{eff} distributions

A comparison between the simulated Q_{eff} and LET distributions in He-ions at HIT is shown in figure 2. As a particle slows down, Q_{eff} and f-LET are generally monotonically increasing functions along the central beam axis until the Bragg peak region. For d-LET, however, the heavy dose-weighted fragments released at high particle speeds results in a slightly lower d-LET gradient along the central axis. Along with the higher weight of heavy fragments, it indicates that it will be difficult to establish a unique relation between the OSLD response and d-LET. For each irradiation, the simulated values of the energy, Q_{eff}, f-LET, and d-LET at the OSLD position are given in table 1.

3.2 OSL curves

Examples of OSL curves for Al_2O_3:C and Al_2O_3:C,Mg, where the blue and UV emissions are separated, are shown in figure 3 for ^{1}H-, ^{4}He-, and ^{12}C-ions measured at HIT. For each irradiation, between four and five OSLDs were read out, as shown in each sub-figure. The OSLDs may differ slightly in size and sensitivity, which is

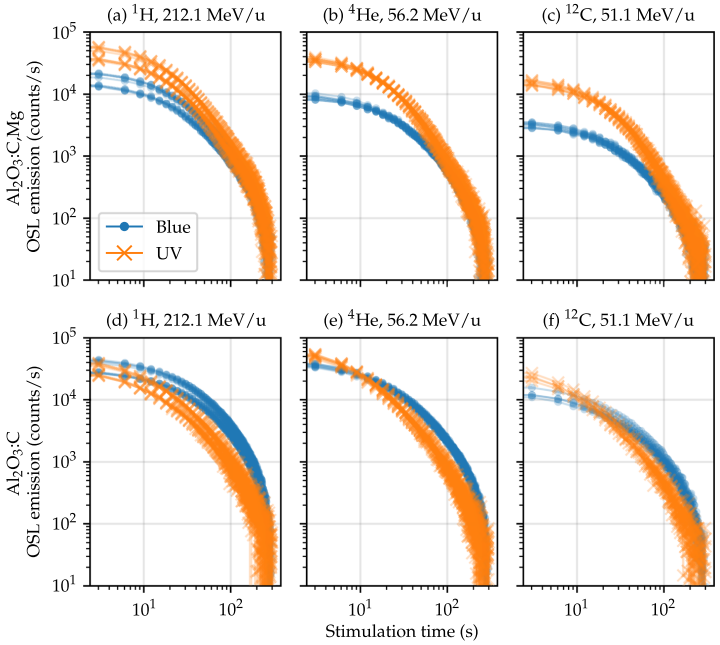

Figure 3. Example of the OSL curves for Al_2O_3:C,Mg for in (a)–(c) and Al_2O_3:C in (d)–(f) for ^{1}H- , ^{4}He- , and ^{12}C-ions, respectively. The UV and blue emissions are separated using the pulsed OSL technique outlined in section 2.2.2. The integral of each OSL curves gives the signal S, which, after a background subtraction, is normalized with respect to the reference signal intensity S_{ref} for either emission band. All OSL detectors were irradiated with a dose near 0.25 Gy.

evident from the OSL curves in figure 3(a). Nonetheless, the integral signal of each curve S is eventually normalized by the signal S_{ref} from the reference irradiation in the reader, which cancels out the differences (Yukihara *et al* 2006).

3.3 Detector efficiencies in ion beams

The relative detector efficiency defined in equation (5) is plotted in figure 4 for ^{1}H-, ^{4}He-, ^{12}C-, and ^{16}O-ions for both Al_2O_3:C and Al_2O_3:C,Mg as a function of Q_{eff}. The relative detector efficiencies as a function of f-LET and d-LET are included in the supplementary materials figure A.1 for reference.

As also observed in figure 3(e), the intensity of the UV emission for Al_2O_3:C increases for particles near the Q_{eff} or LET range relevant to ^{4}He-ions, and exceeds the efficiency relative to fast ^{1}H-ions in figure 3(d). The UV efficiency of Al_2O_3:C,Mg exceeds unity but is lower than the increase of Al_2O_3:C. Indeed, the relative efficiency close to unity for the Al_2O_3:C,Mg UV emission band for ^{1}H- and ^{4}He-ions indicates its relevance for dosimetry in ^{4}He-ions with smaller correction factors for ionization quenching than e.g. for Al_2O_3:C.

Whilst the relative detector efficiency for the blue emission band in figure 4(a) is relatively similar for Al_2O_3:C and Al_2O_3:C,Mg ions, the relative efficiencies for the UV emission band between the two materials differ. Thus, the ratio of the UV/blue emission band as a function of Q_{eff} or LET will differ for the two OSL materials Al_2O_3:C and Al_2O_3:C,Mg.

Interestingly, the relative detector efficiency of two different ions at the same value of Q_{eff} is almost similar for each emission band, e.g. for the slow ^{4}He-ions and fast ^{12}C-ions in figure 4(b). This indicates that Q_{eff} is less sensitive to the ion type than e.g. f-LET, where the relative detector efficiency for two different ions at the same LET value differs, as demonstrated in previous studies (Yukihara *et al* 2015, Christensen and Andersen 2018) or in supplementary material figure A.1.

Due to the non-monotonic behavior of the UV emission band in both materials, shown in figure 4(b), the relative detector efficiency as a function of Q_{eff} or LET is modeled with cubic splines shown in figure 4 as solid lines.

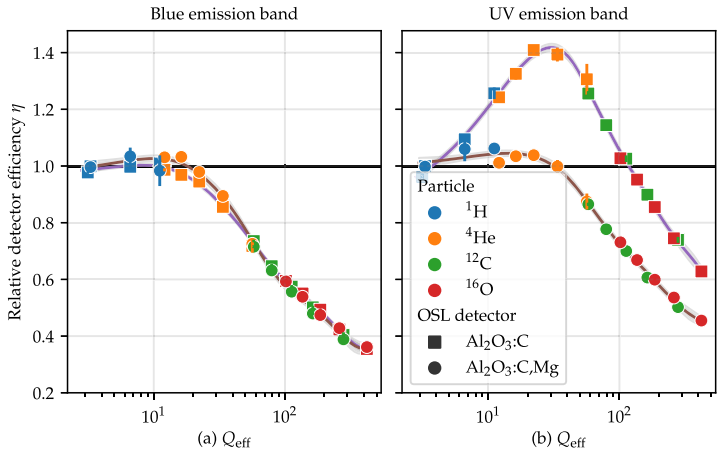

Figure 4. The relative detector efficiencies in equation (5) for the (a) blue and (b) UV emission bands, respectively, for Al_2O_3:C and Al_2O_3:C, Mg exemplified as a function of Q_{eff}. Each data set was fitted with cubic splines (solid lines). The legend in (b) applies to both figures.

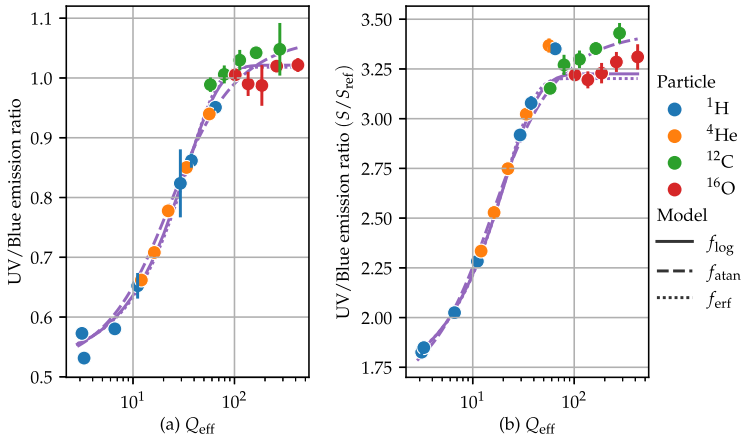

Figure 5. Example of the difference between the ratio of the UV and blue emission bands for Al_2O_3:C for (a) the uncorrected signal S and (b) where the signal S from both emission bands is corrected with respect to the reference irradiation S_{ref}. The test functions defined in equations (2)–(4) are fitted to the data and plotted with lines. No models were found able to describe the saturating signal for ^{16}O-ions.

3.4 Detector response

The ratio of the two emission bands as a function of Q_{eff} is exemplified for Al_2O_3:C in figure 5. The figure highlights the two cases where the uncorrected UV/blue emission ratio is shown in figure 5(a). The reference-corrected UV/blue emission ratio in figure 5(b), where the latter is corrected using the reference irradiation signals S_{ref} as described in section 2.2.2.

In each case, the three models in equations (2)–(4) are fitted to the data as given in the figure legend. Although the figure only shows the relationship for Al_2O_3:C as a function of Q_{eff}, similar results were obtained for Al_2O_3:C,Mg and parameterized as a function of f-LET or d-LET.

The use of the reference irradiation S/S_{ref} serves both to reduce the variation in the group of OSLDs irradiated in the same radiation quality (Christensen *et al* 2022), but also provides a different response between ion types. Henceforth, only the reference-corrected OSLD readouts are used for dosimetry and to estimate the radiation quality metric.

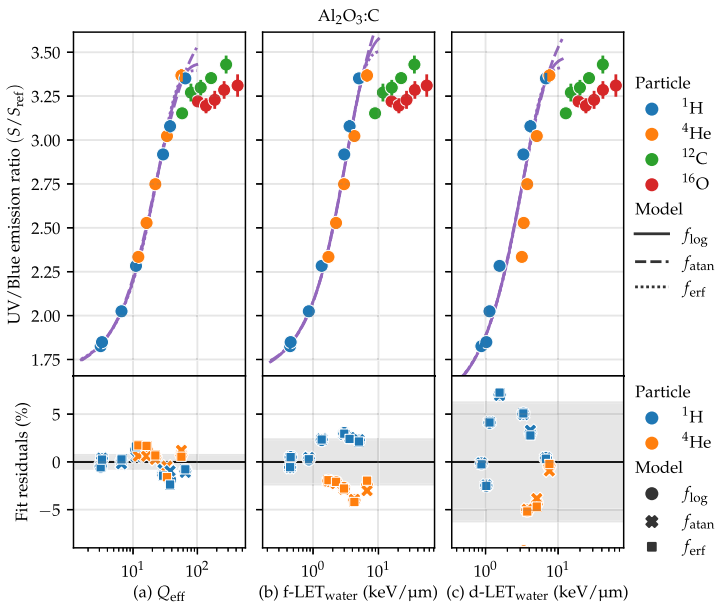

Figure 6. The S/S_{ref} ratio of the UV and blue emission bands for Al_2O_3:C as a function of Q_{eff}, f-LET, and d-LET, where only ^{1}H- and ^{4}He-ions are considered for the model fits. The ^{12}C- and ^{16}O-ions are only shown for reference. The residuals are shown in percentage in the lower figures, where the shaded band illustrates the standard deviation of the residuals. For Q_{eff}, all three models describe the data well, whereas the ion type are split into two for f-LET. For d-LET, only a single ion type can be fitted to the data at a time.

In both figures 5(a), (b), the ^{16}O-ions appear to show saturation with a UV/blue emission ratio lower than those for ^{12}C-ions. This is in agreement with the results observed in Yukihara *et al* (2015). The constant UV/blue ratio for ^{16}O-ions can also be inferred from figure 4, where the slopes of the UV and blue efficiencies are similar for high values of Q_{eff} or LET. This renders the OSLDs inapplicable for Q_{eff} or LET estimations in ^{16}O-ions.

Furthermore, the use of the reference corrections in figure 5(b) appears to give a well-defined relationship for ^{1}H- and ^{4}He-ions across all energies, which indicates a possible common calibration for ions with charge $Z \leqslant 2$. The latter could be particularly advantageous for dosimetry applications in clinical ^{4}He-ion beams, where the mixed fields are mostly composed of He- and H-ion species.

3.5 OSLD determination of the radiation quality

The following investigates the ability to determine the radiation quality for both OSLD materials. This prediction is a challenge due to the effect of track structures, which causes the OSL response to vary for two different ion types at the same radiation quality, and further complicated by the apparent saturation at high ionization densities as observed in figure 4. The section is divided into four parts: one for each of the two OSL materials, which then is subdivided depending on the investigated ions for (i) ^{1}H- and ^{4}He-ions, and for (ii) ^{1}H- , ^{4}He- , and ^{12}C-ions. Due to its saturation, ^{16}O-ions are omitted in the following analysis but included in the figures for reference. Although other functions than the ones described in equations (2)–(4) may describe the data slightly better, it is not expected to change the overall conclusions.

3.5.1 Al_2O_3:C response in ^{4}He-ions

To establish the best relationship between the OSLD response and the radiation quality metrics, the three models are fitted to the Al_2O_3:C data for ^{1}H- and ^{4}He-ions in figure 6. The ^{1}H- and ^{4}He-ion data are well-defined as a function of Q_{eff} but splits slightly up for f-LET depending on the ion type, as seen in the residual plots. For d-LET, in particular, a unique calibration to each ion type is needed to model the data. Hence, d-LET cannot be determined in a mixed particle field with Al_2O_3:C, which is in agreement with the conclusions in Yukihara *et al* (2015).

As evident from figures 6(a)–(c), the UV/blue ratio of slow ^{1}H- and ^{4}He-ions is too different from that of fast ^{12}C-ions to be modeled with a single curve. Thus, the use of Al_2O_3:C to determine the radiation quality metrics in ^{12}C-ions is challenging, as the ^{1}H- and ^{4}He-fragments will deviate from the ^{12}C-ion calibration curve, and will

IOP Publishing Phys. Med. Biol. 68 (2023) 155001 J B Christensen et al

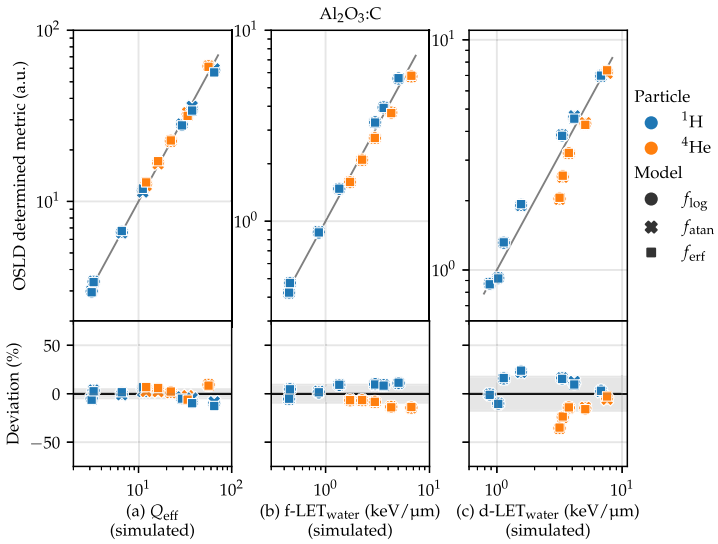

Figure 7. The OSLD derived radiation quality for the metrics Q_{eff}, f-LET, and d-LET for Al_2O_3:C and the fits to ^{1}H- and ^{4}He-ions in figure 6 plotted as a function of the Monte Carlo simulated values. The shaded band illustrates the standard deviation of the data for the model that describes the data the best, in each case the f_{atan} function in equation (2). Again, a single function is unable to describe the mixed ion data for d-LET.

not be pursued further here. For reference, the results of fitting the empirical models to the ^{1}H-, ^{4}He-, and ^{12}C-ion data for Al_2O_3:C are shown in the supplementary material figure A.3.

3.5.2 Radiation quality metrics in ^{4}He-ions for Al_2O_3:C

To assess how well the Al_2O_3:C OSLDs can be used to determine each radiation quality metric in ^{4}He-ions, the empirical models fitted to the data in figure 6 are used to evaluate the radiation quality metrics as shown in figure 7.

The lower subfigures show the deviation from the OSLD-derived metric relative to the Monte Carlo-simulated one. For each radiation quality metric, the standard deviation of the data for the empirical function providing the best agreement is shown with a shaded area. The OSLD determinations of Q_{eff} using the f_{atan} model gives a standard deviation of 5 %, whereas that of the f-LET determinations was 10 %. This indicates, that Al_2O_3:C OSLDs can be used to determine the radiation quality in ^{4}He-beams.

3.5.3 Al_2O_3:C,Mg response in ^{4}He-ions

Unlike the results for Al_2O_3:C, the UV/blue ratio for Al_2O_3:C,Mg is well-approximated with a single model across ^{1}H-, ^{4}He-, and ^{12}C-ions in figure 8 for Q_{eff}. Again, the data are better described with Q_{eff} than LET, where each ion type follows a unique relationship. This indicates that Al_2O_3:C,Mg can be applied for dosimetry in ^{12}C-ions.

Following from the fit in figure 8, also a ^{4}He-beam can be described through Q_{eff}. For consistency, the results where the empirical models only are fitted to ^{1}H- and ^{4}He-ions for Al_2O_3:C,Mg, are shown in the supplementary material figure A.3.

3.5.4 Radiation quality metrics in ^{12}C-ions for Al_2O_3:C,Mg

The determination of the radiation quality metric with Al_2O_3:C,Mg for ions lighter than ^{16}O-ions is displayed in figure 9. As for Al_2O_3:C in figure 7, the lowest standard deviation between the OSLD derived and the Monte Carlo simulated values are found for Q_{eff}. When averaged LET is used as the radiation quality metric, the data are splitting up depending on the ion type.

However, in each case, the addition of the ^{12}C-ions gives a poorer fit to the data, than when only ^{1}H- and ^{4}He-ions are considered. The slowest ^{12}C-ions, which have the highest ionization densities, deviate the most from the fits, which could indicate a trend towards saturation.

The results for Al_2O_3:C,Mg for a ^{4}He-beam are included in the supplementary figure A.4 with the same conclusion.

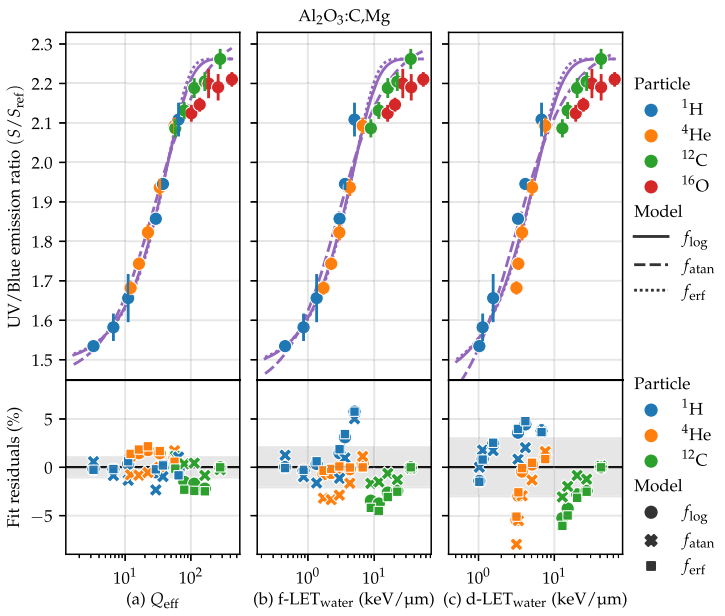

Figure 8. The S/S_{ref} ratio of the UV and blue emission bands for Al_2O_3:C,Mg for ^{1}H-, ^{4}He- , and ^{12}C-ions as a function of Q_{eff}, f-LET, and d-LET. ^{16}O-ions are omitted from the fits. The residuals are shown in percentage in the lower figures, where the shaded area denotes the standard deviation of the data. For Q_{eff}, the three models all describe the data well, whereas the data as a function of f-LET are split into distributions for each ion type. For d-LET, only a single ion type can be fitted to the data at once.

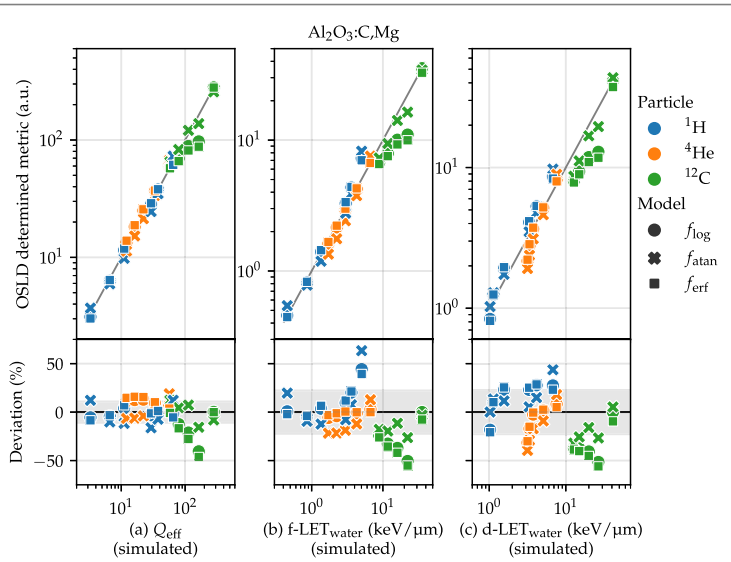

Figure 9. The OSLD derived radiation quality for the metrics Q_{eff}, f-LET, and d-LET for Al_2O_3:C,Mg and the three fits to the ^{1}H-, ^{4}He-, and ^{12}C-ions in figure 8. The shaded band illustrates the standard deviation of the data for the model that best describes the data, in each case the f_{atan} function in equation (2).

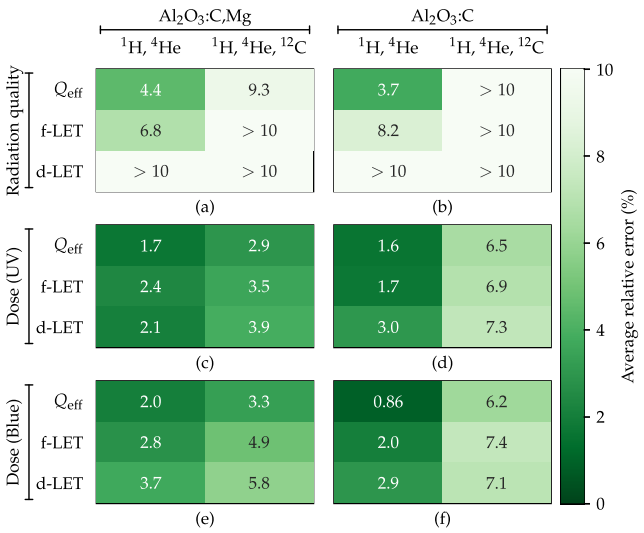

Figure 10. The OSLD determined radiation quality metrics for both (a) Al_2O_3:C,Mg and (b) Al_2O_3:C using either ^{1}H- and ^{4}He-ions or ^{1}H-, ^{4}He-, and ^{12}C-ions. The results are shown as the average relative error between the OSLD determined quantity relative to the Monte Carlo determined one across the investigated ions. The OSLD estimate of the radiation quality in (a) and (b) are used to derive correction factors for the dose derived from the UV (c), (d) and blue (e), (f) emission bands for both materials. (c)–(f) Show the average relative error of the OSLD determined doses relative to the measured ones.

3.6 OSLD measurements in light ions

The ability of the Al_2O_3:C and Al_2O_3:C,Mg OSLDs to determine the radiation quality is now used to correct the ionization density dependent response. The estimates of the radiation quality metrics are used to determine the relative detector efficiency, as shown in figure 4 for Q_{eff}. The dose is subsequently calculated for the intensities of both the blue and UV emission bands and corrected by the determined relative efficiency for each band.

The OSLD estimates of the radiation quality metrics and quenching-corrected doses are compiled in figure 10 for both materials. The results are presented as the relative error between the OSLD determined value and the true value, where the latter is taken to be either the dose measured with an ionization chamber or the radiation quality determined through the Monte Carlo simulations

3.6.1 Dosimetry in ^{4}He-beams

For both the Al_2O_3:C and Al_2O_3:C,Mg OSL measurements in ^{1}H- and ^{4}He-ions in figures 10(a), (b), the determinations of Q_{eff} are closer to the reference values than the LET determinations. This in turn gives a better dose correction and ultimately an improved dosimetry when Q_{eff} is used to predict the radiation quality.

The doses in the mono-energetic ^{1}H- and ^{4}He-ions were determined with an average relative error on a 1.5 % level for both materials when Q_{eff} is used as the radiation quality metric. The relative error increases to 2% when f-LET or d-LET is used.

3.6.2 Dosimetry in ^{12}C-beams

When all ^{1}H-, ^{4}He-, and ^{12}C-ions are considered, only Al_2O_3:C,Mg is found able to predict the radiation quality with a relative error lower than 10 % relative to the simulated values.

Across all ions, Q_{eff} was found to be the best describing radiation quality metric with a 9 % average relative error. The relative detector efficiency for Al_2O_3:C,Mg for the UV emission band in figure 4(b) is closer to unity for ^{4}He-ions than that of Al_2O_3:C, which means that the ionization quenching correction factors for Al_2O_3:C,Mg are smaller and vary less than those of Al_2O_3:C. Hence, the dose corrections using the Al_2O_3:C,Mg UV emission band are insensitive to small deviations in the radiation quality determinations, and the determined doses are all of similar quality with a relative around 3%. The dose determinations relying on the Q_{eff} determinations are closer to the reference values than the ones relying on the LET determinations.

As Q_{eff} was demonstrated to correlate better with the RBE than LET does (Kalholm *et al* 2022), these results suggest that not only the physical dose in light ion beams can be estimated with OSLDs but also the

RBE-weighted dose. A detector with such capability might be helpful for ^{4}He-and ^{12}C-ion beam radiotherapy, as a variable RBE is used clinically.

These results are, however, based on measurements in mono-energetic beams at shallow depths, which limits variations due to energy spread and the nuclear fragmentation spectrum. Further studies in mixed particles are needed.

4 Conclusions

Both Al_2O_3:C and Al_2O_3:C,Mg OSLDs are applicable for dosimetry and determination of the radiation quality metrics in ^{1}H- and ^{4}He-ion beams. The radiation quality Q_{eff} was determined with a relative error of 4 % relative to the reference values. This enables determinations of corrections for ionization quenching which resulted in dose determinations within 2 % of the reference values.

Due to the differences in the relative detector efficiencies, only Al_2O_3:C,Mg was found suitable for radiation quality estimations and dosimetry in ^{12}C-ions. Q_{eff} is here estimated across three orders of magnitude within 9 %, which leads to doses within 3 % of the reference values.

Overall, the radiation quality metric Q_{eff} was found to be less sensitive to the response variations caused by different ion types than fluence- or dose-averaged LET was. Q_{eff} provided the best determinations of the radiation quality and the dose. This opens an avenue towards the use of Q_{eff}—rather than LET—to not only calculate the physical dose with OSLD detectors, but also the RBE.

Acknowledgments

The Risø TL/OSL-DA-20 reader (DTU Nutech, Denmark) was acquired with partial support from the Swiss National Science Foundation (R'Equip project 206021_177028). This research was supported in part by PL-Grid Infrastructure. IDM acknowledges the German Academic Exchange Service for funding through the *Research Grants—Doctoral Programmes in Germany* program (program number: 57440921). NB acknowledges support by the Novo Nordisk Foundation (grant number NNF195A0059372), DCCC Radiotherapy—The Danish National Research Center for Radiotherapy, Danish Cancer Society (grant no. R191-A11526) and Danish Comprehensive Cancer Center.

The authors would like to thank the staff from PSI and HIT for technical support during the experiments and providing the irradiation conditions.

Data availability statement

The data that support the findings of this study are openly available at the following URL/DOI: https://doi.org/10.17632/h9w68wdy3b.1.

ORCID iDs

Jeppe Brage Christensen https://orcid.org/0000-0002-6894-381X
Iván Domingo Muñoz https://orcid.org/0000-0001-5183-3705
Niels Bassler https://orcid.org/0000-0002-4160-1078
Christina Stengl https://orcid.org/0000-0003-0273-0878
Oliver Jäkel https://orcid.org/0000-0002-6056-9747
Eduardo Gardenali Yukihara https://orcid.org/0000-0002-4615-6698

References

Ahmed M F, Eller S A, Schnell E, Ahmad S, Akselrod M S, Hanson O D and Yukihara E G 2014 Development of a 2D dosimetry system based on the optically stimulated luminescence of Al_2O_3 *Radiat. Meas.* **71** 187–92

Akselrod G M, Akselrod M S, Benton E R and Yasuda N 2006 A novel Al_2O_3 fluorescent nuclear track detector for heavy charged charged *Nucl. Instrum. Methods Phys. Res. B* **247** 295–306

Barkas H W 1963 *Nuclear Research Emulsions* vol 1 (New York and London: Academic Press)

Bassler N, Jäkel O, Søndergaard C S and Petersen J B 2010 Dose-and LET-painting with particle therapy *Acta Oncol.* **49** 1170–6

Christensen J B and Andersen C E 2018 Relating ionization quenching in organic plastic scintillators to basic material properties by modelling excitation density transport and amorphous track structure during proton irradiation *Phys. Med. Biol.* **63** 195010

Christensen J B, Togno M, Bossin L, Pakari O V, Safai S and Yukihara E G 2022 Improved simultaneous LET and dose measurements in proton therapy *Sci. Rep.* **12** 1–10

Christensen J B, Togno M, Nesteruk K P, Psoroulas S, Meer D, Weber D C, Lomax T, Yukihara E G and Safai S 2021 Al_2O_3:C optically stimulated luminescence dosimeters (OSLDs) for ultra-high dose rate proton dosimetry *Phys. Med. Biol.* **66** 085003

Conte V *et al* 2020 Microdosimetry of a therapeutic proton beam with a mini-TEPC and a MicroPlus-Bridge detector for RBE assessment *Phys. Med. Biol.* **65** 245018

Cortés-Giraldo M A and Carabe A 2015 A critical study of different Monte Carlo scoring methods of dose average linear-energy-transfer maps calculated in voxelized geometries irradiated with clinical proton beams *Phys. Med. Biol.* **60** 2645–69

De Saint-Hubert M, Castellano F, Leblans P, Sterckx P, Kodaira S, Swakoń J and de Freitas Nascimento L 2021 Characterization of 2D Al_2O_3:C, Mg radiophotoluminescence films in charged particle beams *Radiat. Meas.* **141** 106518

Denis G, Rodriguez M G, Akselrod M S, Underwood T H and Yukihara E G 2011 Time-resolved measurements of optically stimulated luminescence of Al_2O_3:C and Al_2O_3:C, Mg *Radiat. Meas.* **46** 1457–61

Granville D A 2015 Development of a technique to simultaneously verify linear energy transfer and absorbed dose in therapeutic proton beams *PhD Thesis* Carleton University, Ottawa, Canada

Granville D A, Sahoo N and Sawakuchi G O 2014a Calibration of the Al_2O_3:C optically stimulated luminescence (OSL) signal for linear energy transfer (LET) measurements in therapeutic proton beams *Phys. Med. Biol.* **59** 4295–310

Granville D A, Sahoo N and Sawakuchi G O 2014b Linear energy transfer dependence of Al_2O_3:C optically stimulated luminescence detectors exposed to therapeutic proton beams *Radiat. Meas.* **71** 69–73

Granville D A, Sahoo N and Sawakuchi G O 2016 Simultaneous measurements of absorbed dose and linear energy transfer in therapeutic proton beams *Phys. Med. Biol.* **61** 1765–79

Grau C, Durante M, Georg D, Langendijk J A and Weber D C 2020 Particle therapy in europe *Mol. Oncol.* **14** 1492–9

Hahn C *et al* 2022 Towards harmonizing clinical linear energy transfer (LET) reporting in proton radiotherapy: a European multi-centric study *Acta Oncol.* **61** 206–14

Holm K M, Jäkel O and Krauss A 2021 Water calorimetry-based k Qfactors for Farmer-type ionization chambers in the SOBP of a carbon-ion beam *Phys. Med. Biol.* **66** 145012

Hoye E M, Skyt P S, Balling P, Muren L P, Taasti V T, Swakoń J, Mierzwińska G, Rydygier M, Bassler N and Petersen J B 2017 Chemically tuned linear energy transfer dependent quenching in a deformable, radiochromic 3D dosimeter *Phys. Med. Biol.* **62** N73–89

International Atomic Energy Agency 2000 *Absorbed dose determination in external beam radiotherapy: An International Code of Practice for dosimetry based on standards of absorbed dose to water*.Technical Reports Series No. 398

ICRU 1970 *Linear Energy Transfer* Report 16 Washington DC, USA

ICRU 2016 *Prescribing, recording, and reporting light ion beam therapy* Report 93 Washington DC, USA

Kalholm F, Grzanka L, Toma-Dasu I and Bassler N 2022 Modeling RBE with other quantities than LET significantly improves prediction of in vitro cell survival for proton therapy *Med. Phys.* **50** 651–9

Katz R 1978 Track structure theory in radiobiology and in radiation detection *Nucl. Track Detect.* **2** 1–28

Klimpki G, Mescher H, Akselrod M S, Jakel O and Greilich S 2016 Fluence-based dosimetry of proton and heavier ion beams using single track detectors *Phys. Med. Biol.* **61** 1021–40

Lühr A, von Neubeck C, Helmbrecht S, Baumann M, Enghardt W and Krause M 2017 Modeling in vivo relative biological effectiveness in particle therapy for clinically relevant endpoints *Acta Oncol.* **56** 1392–8

Maeyama T, Mochizuki A, Yoshida K, Fukunishi N, Ishikawa K L and Fukuda S 2022 Radio-fluorogenic nanoclay gel dosimeters with reduced linear energy transfer dependence for carbon-ion beam radiotherapy *Med. Phys.* **50** 1073–85

McNamara A L, Schuemann J and Paganetti H 2015 A phenomenological relative biological effectiveness (RBE) model for proton therapy based on all published in vitro cell survival data *Phys. Med. Biol.* **60** 8399–416

Muñoz I D, Burigo L N, Gehrke T, Brons S, Greilich S and Jäkel O 2022 Sensitivity correction of Fluorescent Nuclear Track Detectors using alpha particles: determining LET spectra of light ions with enhanced accuracy *Med. Phys.* **50** 2385–401

Nabha R *et al* 2022 A novel method to assess the incident angle and the LET of protons using a compact single-layer Timepix detector *Radiat. Phys. Chem.* **199** 110349

Newville M, Stensitzki T, Allen D B, Rawlik M, Ingargiola A and Nelson A 2016 LMFIT: Non-linear least-square minimization and curve-fitting for Python *Astrophys. Source Code Libr.* **1606**

Nielsen C L, Turtos R M, Bondesgaard M, Nyemann J S, Jensen M L, Iversen B B, Muren L P, Julsgaard B and Balling P 2022 A novel nanocomposite material for optically stimulated luminescence dosimetry *Nano Lett.* **22** 1566–72

Olko P, Bilski P, Budzanowski M, Patrick M, Waligórski R and Reitz G 2002 Modeling the response of thermoluminescence detectors exposed to low- and high-let radiation fields *J. Radiat. Res.* **43** 59–62

Parodi K, Mairani A, Brons S, Hasch B G, Sommerer F, Naumann J, Jäkel O, Haberer T and Debus J 2012 Monte Carlo simulations to support start-up and treatment planning of scanned proton and carbon ion therapy at a synchrotron-based facility *Phys. Med. Biol.* **57** 3759–84

Perl J, Shin J, Schümann J, Faddegon B and Paganetti H 2012 TOPAS: an innovative proton Monte Carlo platform for research and clinical applications *Med. Phys.* **39** 6818–37

Rodriguez M G, Denis G, Akselrod M S, Underwood T H and Yukihara E G 2011 Thermoluminescence, optically stimulated luminescence and radioluminescence properties of Al_2O_3:C, Mg *Radiat. Meas.* **46** 1469–73

Sawakuchi G, Sahoo N, Gasparian P, Rodriguez M, Archambault L, Titt U and Yukihara E 2010 Determination of average LET of therapeutic proton beams using Al_2O_3:C optically stimulated luminescence (OSL) detectors *Med. Phys.* **37** 3453

Schoenfeld A A, Harder D, Poppe B and Chofor N 2015 Water equivalent phantom materials for ^{192}Ir brachytherapy *Phys. Med. Biol.* **60** 9403–20

Sechopoulos I, Rogers D W, Bazalova-Carter M, Bolch W E, Heath E C, McNitt-Gray M F, Sempau J and Williamson J F 2018 RECORDS: improved reporting of monte carlo radiation transport studies: report of the aapm research committee task group 268 *Med. Phys.* **45** e1–5

Vana N, Schöne W, Fugger M and Akatov Y 1996 Absorbed dose measurement and LET determination with TLDs in space *Radiat. Prot. Dosim.* **66** 145–52

Weber U and Kraft G 1999 Design and construction of a ripple filter for a smoothed depth dose distribution in conformal particle therapy *Phys. Med. Biol.* **44** 2765–75

Yukihara E G, Doull B A, Ahmed M, Brons S, Tessonnier T, Jäkel O and Greilich S 2015 Time-resolved optically stimulated luminescence of Al_2O_3:C for ion beam therapy dosimetry *Phys. Med. Biol.* **60** 6613–38

Yukihara E G and McKeever S W 2006 Spectroscopy and optically stimulated luminescence of Al_2O_3:C using time-resolved measurements *J. Appl. Phys.* **100** 083512

Yukihara E G, McKeever S W, Andersen C E, Bos A J, Bailiff I K, Yoshimura E M, Sawakuchi G O, Bossin L and Christensen J B 2022 Luminescence dosimetry *Nat. Rev. Methods Primers* **2** 26

Yukihara E G, Sawakuchi G O, Guduru S, McKeever S W, Gaza R, Benton E R, Yasuda N, Uchihori Y and Kitamura H 2006 Application of the optically stimulated luminescence (OSL) technique in space dosimetry *Radiat. Meas.* **41** 1126–35

3.7. Publication III

Linear Energy Transfer Measurements and Estimation of Relative Biological Effectiveness in Proton and Helium-Ion Beams Using Fluorescent Nuclear Track Detectors

Authors: I. D. Muñoz, D. García-Calderón, R. Felix-Bautista, L. N. Burigo, J. B. Christensen, S. Brons, A. Runz, P. Häring, S. Greilich, J. Seco, and O. Jäkel

Status: Accepted (In Press)
Journal: International Journal of Radiation Oncology · Biology · Physics
DOI: https://doi.org/10.1016/j.ijrobp.2024.02.047

Contributions: IDM was responsible for preparing, irradiating, and reading the FNTDs and analyzing the resulting data. IDM integrated the RBE models into the FNTDs analysis workflow. IDM was responsible for optimizing the irradiation plans according to the requirements of each experiment with proton and ^{4}He-ion SOBPs. IDM was responsible for performing the proton and ^{4}He-ion irradiations. IDM performed the experimental dosimetric characterization of the proton and ^{4}He-ion SOBPs. DGC and RFB assisted in all proton and ^{4}He-ion irradiations. SB prepared the base irradiation plans for the proton and ^{4}He-ion SOBPs and provided technical assistance at all stages during the irradiations. IDM was responsible for performing the cell irradiations and dosimetric verifications with 6 MV X-rays. DGC assisted in the 6 MV X-ray irradiations. PH designed the irradiation plans and assisted in the 6 MV X-ray irradiations. AR designed all the holders necessary to ensure reproducible irradiation conditions and the phantom for 6 MV X-ray irradiation of cells. DGC was responsible for the clonogenic cell survival assays. IDM assisted with cell fixation and cell colony counting. IDM analyzed the data to derive LQM α and β parameters and experimental RBE values for all the studied beams. IDM designed, performed, and validated the simulations. JBC assisted in the implementation of the scorers in the simulations. SG provided scientific advice regarding FNTDs. OJ, LNB, and IDM conceived the concept of integrating the RBE models for the RBE assessment in PBT and IBT. OJ, DG, and IDM conceived the idea of using clonogenic cell survival assays to validate the results. OJ, JS, and LNB supervised and managed the research. OJ and JS secured and allocated the necessary resources for the project. Data curation and visualization was performed by IDM. IDM drafted and edited the original manuscript. All authors participated in the review of the final version of the manuscript.

ARTICLE IN PRESS

INTERNATIONAL JOURNAL OF
RADIATION ONCOLOGY • BIOLOGY • PHYSICS
www.redjournal.org

PHYSICS CONTRIBUTION

Linear Energy Transfer Measurements and Estimation of Relative Biological Effectiveness in Proton and Helium Ion Beams Using Fluorescent Nuclear Track Detectors

Iván D. Muñoz, MSc,[*,†,‡] Daniel García-Calderón, MSc,[*,‡,§] Renato Felix-Bautista, PhD,[†,‡] Lucas N. Burigo, PhD,[†,‡] Jeppe Brage Christensen, PhD,[‖] Stephan Brons, PhD,[‡,¶] Armin Runz,[†,‡] Peter Häring, PhD,[†,‡] Steffen Greilich, PhD,[#] Joao Seco, PhD,[‡,§] and Oliver Jäkel, PhD[†,‡,¶]

[*]*Department of Physics and Astronomy, University of Heidelberg, Heidelberg, Germany;* [†]*Division of Medical Physics in Radiation Oncology, German Cancer Research Center (DKFZ), Heidelberg, Germany;* [‡]*Heidelberg Institute for Radiation Oncology (HIRO), National Center for Radiation Research in Oncology (NCRO), Heidelberg, Germany;* [§]*Division of Biomedical Physics in Radiation Oncology, German Cancer Research Center (DKFZ), Heidelberg, Germany;* [‖]*Department of Radiation Safety and Security, Paul Scherrer Institute (PSI), Villigen, Switzerland;* [¶]*Heidelberg Ion-Beam Therapy Center (HIT), Department of Radiation Oncology, Heidelberg University Hospital, Heidelberg, Germany; and* [#]*Berthold Technologies GmbH & Co KG, Units of Radiation Protection and Bioanalytics, Bad Wildbad, Germany*

Received Oct 3, 2023; Accepted for publication Feb 22, 2024

Purpose: Our objective was to develop a methodology for assessing the linear energy transfer (LET) and relative biological effectiveness (RBE) in clinical proton and helium ion beams using fluorescent nuclear track detectors (FNTDs).

Methods and Materials: FNTDs were exposed behind solid water to proton and helium (^{4}He) ion spread-out Bragg peaks. Detectors were imaged with a confocal microscope, and the LET spectra were derived from the fluorescence intensity. The track- and dose-averaged LET (LET_F and LET_D, respectively) were calculated from the LET spectra. LET measurements were used as input on RBE models to estimate the RBE. Human alveolar adenocarcinoma cells (A549) were exposed at the same positions as the FNTDs. The RBE was calculated from the resulting survival curves. All measurements were compared with Monte Carlo simulations.

Results: For protons, average relative differences between measurements and simulations were 6% and 19% for LET_F and LET_D, respectively. For helium ions, the same differences were 11% for both quantities. The position of the experimental LET spectra primary peaks agreed with the simulations within 9% and 14% for protons and helium ions, respectively. For the RBE

Corresponding author: Iván D. Muñoz, MSc; E-mail: i.munoz@dkfz-heidelberg.de

Joao Seco and Oliver Jäkel made equal contributions to this study.

Disclosures: The authors declare that they have no known competing financial interests or personal relationships that could have influenced the work reported in this paper. I.D.M. and D.G. report funding from the German Academic Exchange Service (program numbers: 57440921 and 57450037, respectively). Funding organizations had no role in study design, data collection and analysis, publishing, or manuscript preparation.

Data Sharing Statement: Data are available upon reasonable request from the authors.

Acknowledgments—The authors thank Dr Felix Bestvater and Manuela Brom from DKFZ for invaluable support performing experiments with the confocal microscope. The authors thank the staff from HIT and Mona Lifferth and Clemens Lang from DKFZ for granting optimal irradiation conditions and support during the experiments. The authors thank Dr Ina Kurth from DKFZ for providing the cell line used in this work. I.D.M. thanks Dr Eduardo Yukihara from PSI for fruitful discussions regarding solid state dosimetry.

Declaration of generative artificial intelligence and artificial intelligence–assisted technologies in the writing process: During the preparation of this work, the authors used ChatGPT version 3.5 to improve language and readability of a limited number of specific and isolated sentences. After using this service, the authors thoroughly reviewed and edited the content as needed and take full responsibility for the content of the publication.

Supplementary material associated with this article can be found in the online version at doi:10.1016/j.ijrobp.2024.02.047.

Int J Radiation Oncol Biol Phys, Vol. 000, No. 00, pp. 1–11, 2024
0360-3016/$ - see front matter
https://doi.org/10.1016/j.ijrobp.2024.02.047

models using LET_D as input, FNTD-based RBE values ranged from 1.02 ± 0.01 to 1.25 ± 0.04 and from 1.08 ± 0.09 to 2.68 ± 1.26 for protons and helium ions, respectively. The average relative differences between these values and simulations were 2% and 4%. For A549 cells, the RBE ranged from 1.05 ± 0.07 to 1.47 ± 0.09 and from 0.89 ± 0.06 to 3.28 ± 0.20 for protons and helium ions, respectively. Regarding the RBE-weighted dose (2.0 Gy at the spread-out Bragg peak), the differences between simulations and measurements were below 0.10 Gy.

Conclusions: This study demonstrates for the first time that FNTDs can be used to perform direct LET measurements and to estimate the RBE in clinical proton and helium ion beams.

Introduction

Owing to their physical characteristics and induced biological response, proton and helium ion beams constitute a powerful tool for cancer treatment. Presently, proton beam therapy (PBT) is an already well-established clinical option. Although helium ions have only been used to a limited extent for cancer treatment,[1,2] this particle species offers promising characteristics, with the potential to bridge the gap between protons and carbon ions.[3,4] Currently, at the Heidelberg Ion-Beam Therapy Center in Germany, there is an ongoing effort to initiate treatments with helium ions on a regular basis, with the first patient already having received treatment.[5]

Current practice in PBT is to assume a constant relative biological effectiveness (RBE) of 1.1,[6,7] although there is evidence suggesting an RBE increase toward the end of the proton range.[6-8] For helium ion beam therapy (HeBT), both constant and variable RBE approaches have been proposed.[4,9,10] Intending to readily predict the RBE for clinical settings, empirical RBE models based on in vitro cell survival data have been developed for both protons and helium ions.[9,11-13] These models are parameterized in terms of the linear energy transfer (LET), which has traditionally been the quantity of choice to relate RBE and ionization density. Thus, in principle, the ability to measure the LET would enable the experimental measurement of the RBE for clinical scenarios. However, the RBE also depends—among other factors such as absorbed dose, cell line, and oxygenation—on the type of ion, that is, 2 ions with the same LET can have different RBEs.[14] Because of nuclear reactions, the mixed ion fields in HeBT are primarily composed of hydrogen and helium ions.[1] Therefore, the full LET spectrum might be necessary to apply adequate models to calculate the RBE for each ion component.[9]

Fluorescent nuclear track detectors (FNTDs) enable the measurement of the LET spectra of protons and heavier ions, within the energy range relevant to PBT and HeBT.[15-17] However, the accuracy of such measurements is limited because of nonuniform sensitivities between individual detectors.[16,17] Recently, an experimental approach was developed to correct for the sensitivity of each detector, allowing for the direct measurement of LET for unknown ion fields.[17] Given these tools, it appears plausible to use FNTD-based LET measurements in combination with phenomenological RBE models to estimate the RBE for PBT and HeBT. Thus, the present study aimed to develop a novel approach to estimate the RBE for PBT and HeBT by using the LET spectra measured with FNTDs as input on phenomenological RBE models. To assess the accuracy of the proposed methods, clonogenic cell survival assays and Monte Carlo simulations were performed.

[1] Hydrogen ions refer to all ions with an atomic number equal to 1, including protons, deuterons, tritons, and heavier isotopes. Helium ions refer to all ions with an atomic number equal to 2, including, for instance, ^{3}He, ^{4}He, and ^{5}He ions.

Methods and Materials

Treatment plans and dosimetry

Experiments were carried out at Heidelberg Ion-Beam Therapy Center with scanned pencil beams. Treatment plans for protons and helium (^{4}He) ions were generated using TRiP version 1310.[18] The plans were optimized in terms of absorbed dose to deliver 1.0 Gy on a 5.0 cm spread-out Bragg peak (SOBP), at a depth from 10 to 15 cm in water. This resulted in 18 and 17 energies, ranging from 117.50 to 146.56 MeV/u and from 119.78 to 147.93 MeV/u for protons and helium ions, respectively. For each energy, 961 scanned spots were used to generate 9.0 × 9.0 cm fields. These plans were used as references for all experiments and will be referred to as "base plans" hereafter. The number of particles per spot was scaled to adapt the base plans according to the requirements of different experiments, without modifying the dose profiles and particle spectra.

The relative depth dose ($D_{rel}(z)$) distributions were measured within a PTW RW3 solid water phantom with an Advanced Markus type 34045 ionization chamber (S.N.: 000378). $D_{rel}(z)$ was calculated as the ratio between the charge measured at a given depth (z) and at the reference depth (z_{ref}) of 12.7 cm. In the latter case, variations due to in-depth changes in the beam quality were neglected. The absolute doses ($D(z)$) were determined by measuring with a Farmer type 30013 ionization chamber (S.N.: 0001714) at z_{ref} and scaling $D_{rel}(z)$ to this value. The absorbed dose was calculated according to international protocols.[19] In particular, the measurements were corrected for influence quantities and changes in the beam quality relative to the reference beam.[19] A fixed beam quality correction factor (k_{Q,Q_0}) of

1.031 ± 0.018 was used for both protons and helium ions. This value was calculated from the practical range of the proton beam.[19] Both chambers were calibrated in terms of absorbed dose in water using ^{60}Co γ rays at the Physikalisch-Technische Bundesanstalt in Brunswick, Germany.

FNTDs

FNTDs (4.0 × 8.0 × 0.5 mm^3) produced by Landauer Inc Crystal Growth Division were used. For each crystal, a sensitivity correction factor was obtained by exposing the FNTDs to ^{244}Cm α particles.[17] Briefly, FNTDs were positioned 3 mm from an unshielded disk source with the polished surface facing the source. The source material consisted of ^{244}Cm electrodeposited on a circular area with a diameter of 3 mm. Afterward, the detectors were exposed behind RW3 solid water at depths of 0.5, 7.5, 9.6, 12.7, 14.1, and 14.5 cm to the proton and helium ion beams. For helium ions, an additional irradiation was conducted at a depth of 17.0 cm to investigate the RBE of hydrogen ions in the fragmentation tail. At each depth, 3 FNTDs were exposed side-by-side around the beam axis. To irradiate all detectors with approximately the same fluence (1.5 × 10^6 cm^{-2}), the base plans were scaled for each depth, based on Monte Carlo simulations. FNTDs were imaged with a Carl Zeiss LSM-710 confocal microscope employing the same setup and parameters as in previous works.[16,17] For each detector, 3 stacks of 11 images were acquired from 15 to 65 μm below the detector surface. For detectors exposed at 14.5 cm to helium ions, 5 stacks were used to reduce the statistical noise due to the broad LET range.

After track reconstruction, the raw count rate of each track (η_{raw}) was calculated as the ratio between the mean intensity of all the track spots belonging to the same track and the pixel dwelling time τ = 40.33 μs, where τ is the time spent by the microscope laser in each scanned position during image acquisition. The count rate corrected for variable laser power, avalanche photodiode saturation, and nonlinearity between laser power and fluorescence intensity was calculated as: $\eta_{sat,p} = \left(-\eta_s \ln(1-\eta_{raw}/\eta_s)\right)(100\%/p)(p/p_{ref})^{-0.164}$, where η_s = 16.2 ± 1.4 MHz is the saturation count rate, p = 20% is the laser power used for image acquisition, and p_{ref} = 10% is the reference laser power.[16,17] The count rate corrected by the FNTD sensitivity, in which a given track was recorded ($k_{s,i}$), and by the microscope response at the scanning time (k_d) was calculated as: $\eta = k_{s,i}k_d\eta_{sat,p}$.[17] For each track, the LET in water was calculated using the following calibration curve:

$$LET = b_i\left(10^{\frac{\eta}{a_i}} - 1\right) \quad (1)$$

where a_i and b_i are fitting parameters. Two parameter sets were tested. One set was obtained by fitting to data for monoenergetic protons, helium (^{4}He), carbon (^{12}C), and oxygen (^{16}O) ions (a_1 = 19.0 ± 0.7 MHz and b_1 = 1.11 ± 0.07 keV/μm).[17] The second set of parameters was obtained by fitting to the same data for protons and helium ions, as well as data for FNTDs exposed behind RW3 slabs to 50.57 MeV/u helium (^{4}He) ions (a_2 = 24.6 ± 1.8 MHz and b_2 = 1.58 ± 0.17 keV/μm; Appendix E1). The track- and dose-averaged LET (LET_F and LET_D, respectively) were calculated from the LET spectra (Appendix E2) according to their definitions.[20] Throughout this work, the LET is reported in water.

RBE calculations

From LET measurements, the RBE was calculated using the McNamara and Wedenberg models for protons[11,12] and the Mairani model for helium ions.[9,13] These models require the LET, absorbed dose, the linear quadratic model (LQM) α and β parameters for x-rays (α_X and β_X, respectively), and their ratio ($[\alpha/\beta]_X$). For the McNamara model, LET_D and $D(z)$ were used directly as input. For the Wedenberg and Mairani models, the LQM α for the kth recorded track ($\alpha_{j,k}$, where $j = H$ for hydrogen ions and $j = He$ for helium ions), with LET equal to LET_k, was calculated as[9,12,13]

$$\alpha_{j,k} = \alpha_X\left[1 + G_j([\alpha/\beta]_X)g_j(LET_k)\right] \quad (2)$$

where $G_H([\alpha/\beta]_X) = k_{0,H}([\alpha/\beta]_X)^{-1}$ with $k_{0,H}$ = 0.434 Gy μm keV^{-1}, $G_{He}([\alpha/\beta]_X) = k_{0,He} + ([\alpha/\beta]_X)^{-1}$ with $k_{0,He}$ = 1.40 × 10^{-1} Gy^{-1}, $g_H(LET_k) = LET_k$ and $g_{He}(LET_k) = (k_{1,He}LET_k)\exp(-k_{2,He}LET_k^2)$ with $k_{1,He}$ = 2.56 × 10^{-1} Gy keV^{-1} μm and $k_{2,He}$ = 2.36 × 10^{-5} keV^{-2} μm^2.[9,13] Similarly, $\beta_{j,k}$ was calculated as

$$\beta_{j,k} = \beta_X h_j(LET_k) \quad (3)$$

where $h_H(LET_k) = 1$ and $h_{He}(LET_k) = b_0\exp\left(-[(LET_k - b_1)/b_2]^2\right)$ with b_0 = 2.66, b_1 = 62.61 keV μm^{-1}, and b_2 = 48.12 keV μm^{-1}[9]. This resulted in one $\alpha_{j,k}$ and $\beta_{j,k}$ value per recorded track. The average α and β for the full spectrum (α_{ion} and β_{ion}, respectively) were calculated as[21]

$$\alpha_{ion} = \frac{\sum_k^n LET_k\alpha_{j,k}}{\sum_k^n LET_k} \quad (4)$$

$$\sqrt{\beta_{ion}} = \frac{\sum_k^n LET_k\sqrt{\beta_{j,k}}}{\sum_k^n LET_k} \quad (5)$$

From α_{ion} and β_{ion}, the RBE was calculated as[12]

$$RBE = -\frac{1}{2D}\left[\frac{\alpha}{\beta}\right]_X + \frac{1}{D}\sqrt{\frac{1}{4}\left[\frac{\alpha}{\beta}\right]_X^2 + \frac{\alpha_{ion}}{\alpha_X}\left[\frac{\alpha}{\beta}\right]_X D + \frac{\beta_{ion}}{\beta_X}D^2} \quad (6)$$

where $D = D(z)$ is the dose per fraction at the studied position. For the mixed ion fields generated by helium ions, the hydrogen and helium ion components were isolated by applying an LET cutoff value (LET_{cut}) to the LET spectra. LET_{cut} was set as the local minimum between the hydrogen and

helium ion peaks. Tracks with LET $\leq$ LET_{cut} were treated as hydrogen ions and tracks with LET $>$ LET_{cut} as helium ions. For the hydrogen and helium ion components, the Wedenberg and Mairani models were applied, respectively.

Additionally, the LET_D approach for the Mairani model was examined for helium ions. In this case, α_{ion} was calculated from Equation 2 with $k_{0,He} = 2.32 \times 10^{-1}$ Gy^{-1} for $G_{He}([\alpha/\beta]_X) = k_{0,He} + ([\alpha/\beta]_X)^{-1}$, $k_{1,He} = 1.59 \times 10^{-1}$ Gy keV^{-1} μm for $g_{He,k}(LET_D) = k_{1,He}LET_D$, and it was assumed that $\beta_{ion} = \beta_X$[9].

The α_X and β_X values obtained in this study for human alveolar adenocarcinoma cells (A549) exposed to 6 MV x-rays (Appendix E2) were applied to all models.

Simulations

The simulations were conducted using TOPAS version 3.7.[22] The nozzle was modeled with a simplified geometry, consisting of a water slab representing the beam application and monitoring system, a 3.0 mm PMMA ripple filter, and a 0.2 mm-thick vacuum window.[23] The phantom was modeled as a 30 $\times$ 30 $\times$ 20 cm^3 box filled with RW3 solid water, with its proximal surface located 1.0 m from the nozzle window. The RW3 material was defined using the density and chemical composition reported in the literature.[24] The source was modeled as a series of 9.0 $\times$ 9.0 cm^2 parallel beams that impinged perpendicularly upon the phantom surface. The energy and relative fluence weight of each beam were retrieved from the treatment plans. The geometry and beam parameters were validated by comparing the depth dose distributions against ionization chamber measurements carried out in this and previous works.[25]

LET_F and LET_D values were obtained using two approaches: one deriving the LET from energy spectra and the other directly scoring energy depositions per track length.[26] For the energy spectrum approach, the energy of each particle was recorded on 4.0 $\times$ 4.0 cm^2 surfaces located at the depths of interest using phase space scorers. The LET of each particle was set equal to the electronic stopping power in water.[20] The electronic stopping powers were calculated from the energy through lookup tables.[27] LET_F and LET_D were calculated from the LET spectra (Appendix E2). For the energy deposition approach, LET_F and LET_D were calculated using in-built and custom scorers. These scorers tally the energy losses on a volume, which are then divided by the step lengths.[26]

The RBE for protons was calculated using the McNamara model in the proton RBE scorer available for TOPAS as an extension.[28] For helium ions, the RBE was calculated from the simulated in-depth dose and LET_D distributions, using the LET_D approach of the Mairani model[9] in a postprocessing stage. For consistency, the α_X and β_X obtained in this work were used for both protons and helium ions (Appendix E3).

In all cases, only particles—from all generations—with atomic numbers equal to or less than the atomic number of the primary ions were considered to calculate LET_F and LET_D, as suggested for protons.[29] The overall parameters of the simulations are summarized in Appendix E4.[30]

Cell survival clonogenic assays

A549 cells were seeded 12 hours before the irradiations on Greiner Bio-One 50-mL cell culture flasks containing 5 mL of Ham's F-12 K (Kaighn's) medium, supplemented with 10% fetal bovine serum and 1% Pen-Strep (both from Thermo Fisher Scientific). The cells were kept at 37 °C under 5% CO_2 for attachment.[31] Before use, the cells were tested for mycoplasma contamination and authenticated by single nucleotide polymorphism profiling.[32]

For the irradiations, flasks were placed behind RW3 plates, with the cell monolayer at the same position as the FNTDs. To account for the water equivalent thickness of the flask attachment wall (1.2 mm), 1.0 mm less of RW3 was placed on the beam path for all depths. At each position and for each replicate, three flasks were irradiated to doses of 1.0, 2.0, 4.0, and 6.0 Gy RBE-weighted dose, where the RBE was estimated from the FNTD measurements. This enabled a comparable number of colonies, independent of the beam quality. To irradiate three flasks under identical conditions, we irradiated one pair of flasks and a single flask separately because of field size constraints. The flasks were positioned upright during irradiation, partially exposing the cell monolayer to air. Because protons and helium ions are scattered mainly at small angles and secondary ions produced by nuclear reactions are emitted predominantly in the forward direction, it was assumed that the dose due to backscattered radiation could be neglected in this experimental setup. To account for any additional stress associated with cell exposure to air, nonirradiated control flasks were also placed in an upright position during the experiments for the same duration as the irradiations. After the irradiations, cells were grown for 11 days at 37 °C under 5% CO_2. Afterward, cell colonies were fixed with 100% ethanol, stained with crystal violet, and counted under a microscope. Colonies containing more than 50 cells were labeled as viable. All experiments were performed in triplicate.

The mean survival fraction was calculated by applying inverse-variance weighting. A curve corresponding to the LQM was fitted to the survival fraction as a function of the absorbed dose using the Levenberg-Marquardt method and applying inverse variance weighting. The survival fraction at each depth was calculated based on the resulting fitting parameters for the clinical absorbed dose at that depth ($D_c(z)$, with $D_c(z_{ref}) = 2.0$ Gy/RBE, assuming RBE values of 1.1 and 1.3 for protons and helium ions, respectively). To serve as low LET reference, cells from the same line were exposed to 6-MV x-rays (Appendix E3). The RBE at each depth was calculated as the ratio between $D_c(z)$ and the dose of 6-MV x-rays that would result in the same survival fraction.

Results

Fluorescent images obtained from FNTDs exposed to the proton and helium ion SOBPs at z_{ref} are depicted in

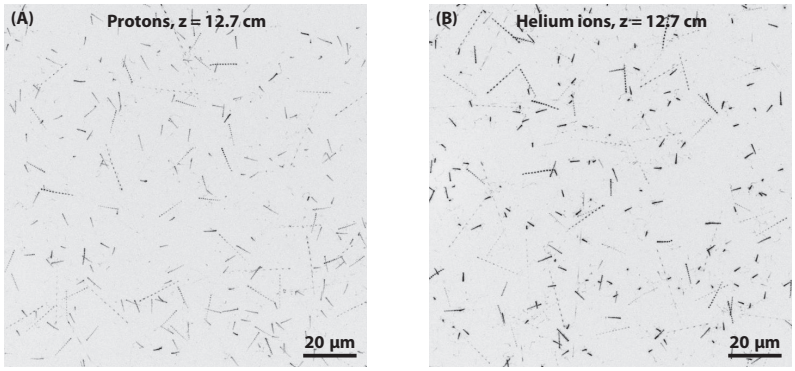

Fig. 1. Maximum fluorescence intensity projection images from fluorescent nuclear track detectors exposed at 12.7 cm in RW3 solid water to (a) protons and (b) helium ions. A darker color indicates a higher fluorescence intensity. Image size: 1280 × 1280 pixels (135 × 135 μm). The same contrast window was applied to both subfigures.

Figure 1. Equivalent images for all irradiation positions can be found in Appendix E5. In general, the fluorescence intensity of recorded tracks increased with depth because of increasing ionization density. Additionally, track projections (ie, lengths) relative to the detector's surface increased with depth because of scattering within the phantom. For FNTDs exposed to helium ions, two well-defined sets of low- and high-intensity tracks were observed, corresponding to hydrogen and helium ions, respectively. In comparison, detectors exposed to protons showed single peaked and narrower fluorescence intensity distributions. On average, 260 ± 27 tracks were recorded per imaged frame.

Figure 2 shows the in-depth distributions of dose, LET_F, and LET_D obtained from measurements and simulations. The consistency between ionization chamber measurements and simulations validates the geometry and parameters implemented in the simulations. The energy spectrum and energy deposition methods employed in the simulations to obtain LET_F agreed within 2%. For LET_D, these 2 methods resulted in average differences of 8%, except for the distal dose falloff ($z = 14.5$ cm), where the differences reached 14% and 26% for protons and helium ions, respectively. Overall, the energy deposition approach resulted in higher values at the entrance channel and lower values toward the distal SOBP compared with the energy spectrum approach. Because of methodology similarities, in the following, LET measurements are compared against simulation results using the energy spectrum approach. Using a_1 and b_1 in Equation 1, for protons the average differences between simulations and measurements were 6% and 19% for LET_F and LET_D, respectively. These differences increased to 8% and 28% by using a_2 and b_2. In contrast, FNTDs and simulations showed better agreement for a_2 and b_2 than for a_1 and b_1 in the case of helium ions, with average differences of 11% for both LET_F and LET_D. However, the values at the distal dose falloff for LET_F and fragmentation tail ($z = 17.0$ cm) for LET_D were not considered in calculating these differences. At these positions, the differences reached 46% and 67%, respectively. Similarly, without considering these two cases, for a_1 and b_1 the average differences between measurements and simulations increased to 31% and 41% for LET_F and LET_D, respectively. The LET_D at the distal dose falloff was overestimated by a factor of 2.2 when using a_1 and b_1 compared with the simulations. Considering these observations, the mixed fields generated by helium ions, using a_1 and b_1 for the low LET component (ie, hydrogen ions) and a_2 and b_2 for the high LET component (ie, helium ions), were also tested. However, this approach resulted in an increase of LET_F and LET_D by less than 1%, which was deemed negligible. In view of these results, a_1 and b_1 were used for protons and a_2 and b_2 for helium ions in subsequent analysis. Thus, according to the measurements, for protons, LET_F ranged from 0.55 ± 0.06 to 6.78 ± 0.59 keV/μm and LET_D from 0.55 ± 0.06 to 8.61 ± 0.53 keV/μm (Table 1). For helium ions, LET_F ranged from 2.48 ± 0.17 to 9.47 ± 1.36 keV/μm and LET_D from 2.53 ± 0.19 to 40.4 ± 23.0 keV/μm (Table 1).

The LET spectra at z_{ref} obtained from both FNTDs and simulations are shown in Figure 3. LET spectra graphs for all depths are provided in Appendix E6. For protons, the LET spectra showed one peak at all depths. Except for the entrance channel ($z = 0.5$ cm), where only one peak was present, the spectra for helium ions were characterized by the presence of two peaks, with the low- and high-LET peaks corresponding to hydrogen and helium ions, respectively. It can be noticed that, in all cases, the measured LET spectra are broader compared with simulations. However, on average, the position of the primary peaks agreed within 9% and 14% for protons and helium ions, respectively. For helium ions, the number of secondary hydrogen ions relative to the total number of ions increased from 13% at 7.5 cm to 32% at 14.1 cm for the measurements and from 22% at 7.5 cm to 39% at 14.1 cm for the simulations. Contrarily, at the distal dose falloff, the relative number of hydrogen ions was 79% and 72% according to the measured and simulated data, respectively.

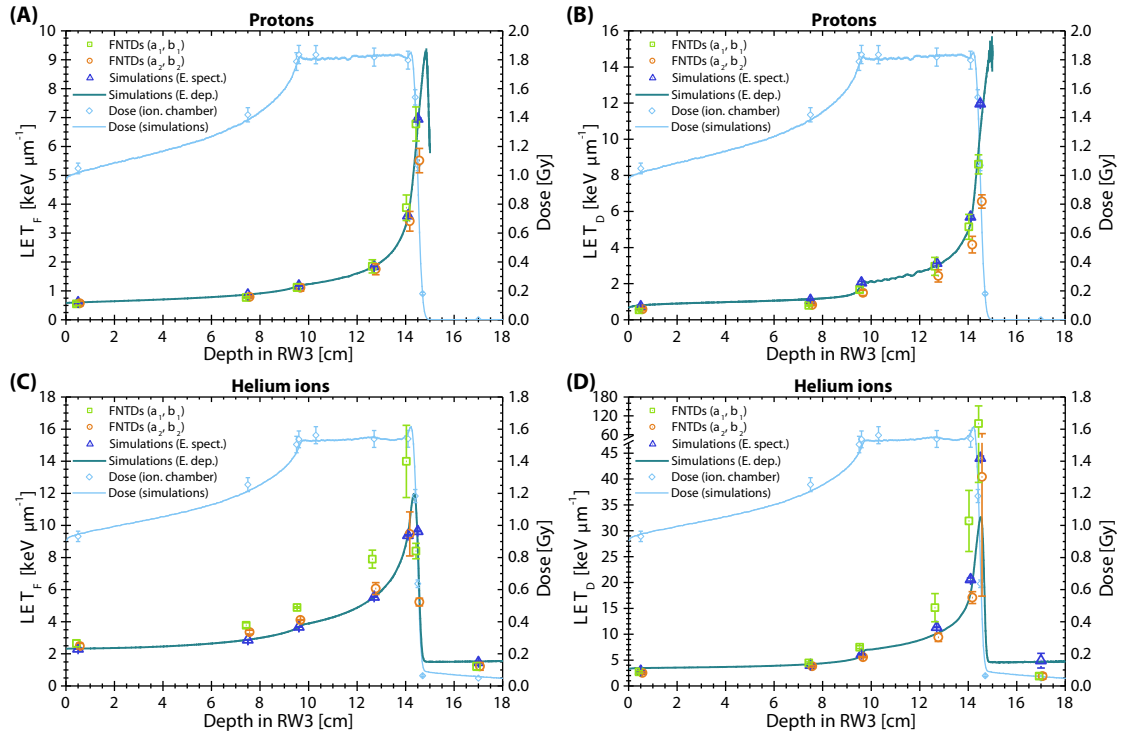

Fig. 2. LET_F and LET_D as a function of the depth in RW3 for the studied proton and helium ion SOBPs. (a) LET_F and (b) LET_D for the proton SOBP. (c) LET_F and (d) LET_D for the helium ion SOBP. Measured and simulated depth-dose (right axes labels) profiles are shown as reference. For FNTDs, error bars indicate the standard uncertainty from detectors exposed under the same conditions. For simulations, error bars correspond to the statistical uncertainty from independent runs. Uncertainties are reported with a coverage factor $k = 1$. *Abbreviations:* FNTD = fluorescent nuclear track detector; LET_D = dose-average linear energy transfer; LET_F = track-average linear energy transfer; SOBPs = spread-out Bragg peaks.

RBE distributions obtained from clonogenic assays, FNTDs, and simulations are shown in Figure 4. In all cases, the RBE sharply increases toward the end of the beam ranges. The McNamara and Wedenberg models showed an average percentage difference of 10% and 8%, respectively, between RBE values obtained from clonogenic assays and those predicted using FNTDs. For both models, the maximum discrepancies relative to the clonogenic assays were observed at the distal SOBP ($z = 14.1$ cm), where differences reached 18% and 16% for the McNamara and Wedenberg models, respectively. Using the measured LET_D as input on the McNamara model resulted in an underestimation of the RBE of 2% on average compared with simulations, with a maximum difference of 5% at the distal dose falloff. For helium ions, both the LET spectra and LET_D approaches used to calculate the RBE resulted in average differences of 12% with respect to the clonogenic assays. For both methods, the greatest differences were found at the distal dose falloff, with underestimations of 30% and 18% for the LET spectra and LET_D approaches, respectively. Compared with simulations, FNTDs yielded RBE values that were 4% lower on average, with a maximum difference of 13% at the distal dose falloff. Regardless of the model, FNTDs predicted average RBE values of 1.1 and 1.4 at the SOBP ($z = 9.6$, 12.7, and 14.1 cm) for protons and helium ions, respectively. Similarly, the clonogenic assays predicted average RBE values of 1.2 and 1.5 for protons and helium ions, respectively. The obtained RBE values are summarized in Table 1.

The in-depth RBE-weighted dose distributions obtained from measurements (ionization chamber and FNTDs) and simulations for the proton and helium ion SOBPs are shown in Figure 5. The average difference between simulations and experiments for protons was 0.02 Gy, with a maximum difference of 0.07 Gy located at the distal dose falloff. For helium ions, the average difference between simulations and measurements was 0.05 Gy, with the highest deviation of 0.10 Gy situated at the distal SOBP. A close-up of the RBE-weighted dose distributions at the SOBP can be found in Appendix E7.

Table 1 Experimental and simulated LET_F, LET_D, and RBE values at the studied depths for experiments with 5.0-cm wide proton (^1H) and helium ion (^4He) spread-out Bragg peaks

Ion	Depth [cm]	LET_F [keV/μm]		LET_D [keV/μm]		RBE			
		FNTDs*	Sims†	FNTDs*	Sims†	FNTDs‡	FNTDs§	Sims‡	Cells
^1H	0.5	0.55 ± 0.06	0.593 ± < 0.001	0.55 ± 0.06	0.73 ± 0.02	1.02 ± 0.01	1.02 ± 0.08	1.034 ± <0.001	1.05 ± 0.07
	7.5	0.77 ± 0.03	0.861 ± <0.001	0.80 ± 0.04	1.08 ± 0.02	1.03 ± 0.01	1.03 ± 0.08	1.047 ± <0.001	
	9.6	1.12 ± 0.13	1.177 ± 0.003	1.67 ± 0.16	2.05 ± 0.08	1.06 ± 0.01	1.06 ± 0.08	1.070 ± <0.001	1.15 ± 0.07
	12.7	1.85 ± 0.23	1.846 ± <0.001	2.96 ± 0.50	3.14 ± 0.03	1.09 ± 0.02	1.10 ± 0.08	1.094 ± <0.001	1.14 ± 0.07
	14.1	3.88 ± 0.44	3.603 ± 0.007	5.15 ± 0.69	5.70 ± 0.10	1.14 ± 0.03	1.17 ± 0.09	1.147 ± <0.001	1.39 ± 0.08
	14.5	6.78 ± 0.59	6.955 ± 0.031	8.61 ± 0.53	11.96 ± 0.07	1.25 ± 0.04	1.32 ± 0.10	1.308 ± <0.001	1.47 ± 0.09
^4He	0.5	2.48 ± 0.17	2.312 ± 0.002	2.53 ± 0.19	2.86 ± 0.07	1.08 ± 0.09	1.06 ± 0.09	1.115 ± 0.001	0.89 ± 0.06
	7.5	3.35 ± 0.12	2.872 ± <0.001	3.81 ± 0.16	4.00 ± 0.10	1.13 ± 0.09	1.11 ± 0.09	1.142 ± 0.001	
	9.6	4.11 ± 0.02	3.674 ± 0.005	5.57 ± 0.11	6.12 ± 0.09	1.19 ± 0.09	1.19 ± 0.09	1.210 ± 0.001	1.30 ± 0.08
	12.7	6.07 ± 0.37	5.542 ± 0.015	9.40 ± 0.81	11.35 ± 0.07	1.34 ± 0.11	1.37 ± 0.11	1.362 ± 0.001	1.38 ± 0.08
	14.1	9.47 ± 1.36	9.382 ± 0.036	17.1 ± 1.2	20.57 ± 0.29	1.61 ± 0.13	1.71 ± 0.14	1.643 ± 0.001	1.73 ± 0.10
	14.5	5.23 ± 0.24	9.635 ± 0.018	40.4 ± 23.0	44.04 ± 0.40	2.68 ± 1.26	2.29 ± 0.86	2.320 ± 0.002	3.28 ± 0.20
	17.0	1.20 ± 0.22	1.464 ± 0.014	1.66 ± 0.41	4.89 ± 1.42				

Depths are reported in RW3 solid water. For FNTD-based LET measurements, the uncertainties indicate the standard uncertainty from detectors exposed under the same conditions. For RBE values derived from FNTD data, the uncertainties correspond to the combined uncertainty taking into account the uncertainties on the LET, α and β parameters, and statistical variations. For RBE values obtained from cell experiments, the uncertainty indicates the combined uncertainty of the dose ratio, considering the uncertainty associated with the α and β parameters. For simulations, the uncertainty corresponds to the statistical variations from independent runs.

Abbreviations: FNTDs = fluorescent nuclear track detectors; LET_D = dose-average linear energy transfer; LET_F = track-average linear energy transfer; RBE = relative biological effectiveness; Sims = simulations.

* a_1 and b_1 for protons and a_2 and b_2 for helium ions.

† Energy spectra method.

‡ McNamara and Mairani (LET_D) models for protons and helium ions, respectively.

§ Wedenberg and Mairani (LET spectra) models for protons and helium ions, respectively.

Discussion

As the availability of PBT continues to expand and algorithms emerge to optimize treatments based on both absorbed dose and LET,[33] there is an increasing need for experimental tools capable of measuring LET in clinical environments. For HeBT, such tools are also relevant, especially considering the higher RBE of helium ions compared with protons and because the LET-based treatment optimization can be equally implemented as in PBT. However, to

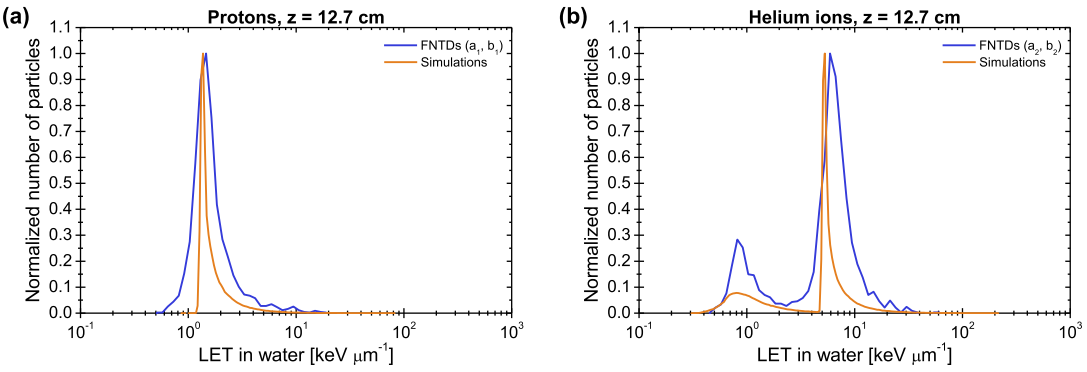

Fig. 3. Measured and simulated LET spectra in water at 12.7 cm in RW3 for the (a) proton and (b) helium ion beams. The spectra are shown normalized to the maximum value. A logarithmic binning from 0.1 to 1000 keV/μm was applied, with 80 and 240 bins to the experimental and simulated data, respectively. *Abbreviations:* LET = linear energy transfer.

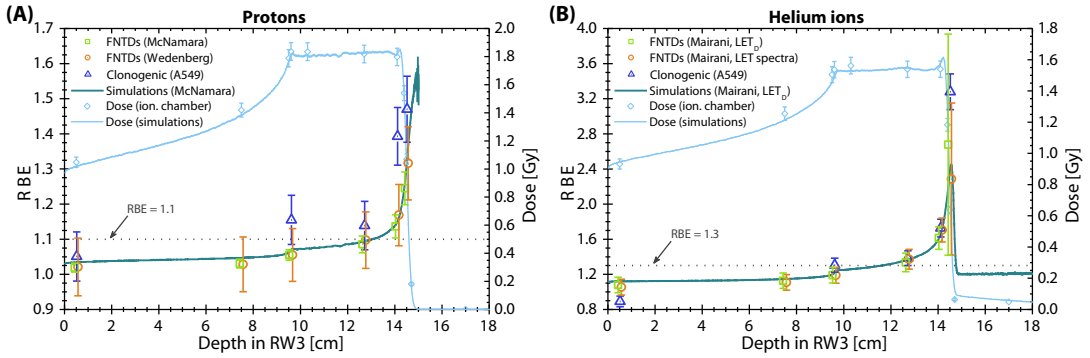

Fig. 4. RBE as a function of the depth in RW3 for (a) protons and (b) helium ions. Measured and simulated depth-dose (right axes labels) profiles are shown as a reference. For experimental data, error bars indicate the combined uncertainty, taking into account the linear energy transfer, α and β parameters, and statistical fluctuations. For simulations, error bars correspond to the standard uncertainty from independent runs. Uncertainties are reported with a coverage factor $k = 1$. *Abbreviations:* RBE = Relative biological effectiveness.

this date, no standard devices or methods exist to cope with this need. In this work, we showed that FNTDs can be used in a clinical setting to measure LET spectra of proton and helium ion beams. These measurements enable the calculation of LET_F and LET_D and can distinguish between components resulting from different ion species in mixed ion fields, such as those encountered in HeBT.

In previous studies, LET spectra in clinical proton, helium, and carbon ion beams measured with FNTDs were presented.[34] However, in this work, we reported for the first time direct LET spectra measurements in proton and helium ion SOBPs, in the sense that no previous knowledge, additional information—such as Monte Carlo simulations—or a priori assumptions were required to obtain accurate results. The latter was possible by merit of the applied sensitivity correction factor to the FNTDs.[17] The proposed method uses knowledge about the beam energy solely during the calibration process. This calibration allows for LET measurements in unknown light-ion fields without requiring information about the energy.[17] The authors foresee that this will allow us to explore even more challenging experimental scenarios in future works, such as additional beams, anthropomorphic phantoms exposed to multiple fields, out-of-field measurements, and intracenter comparisons. However, additional investigations are required to further increase the accuracy of LET measurements, particularly in regions with the highest LET. For instance, the fact that different parameters for the calibration curve (Equation 1) were required supports the hypothesis that the fluorescence intensity depends both on the LET and type of particle because of track structure effects. In particular, different ion species with the same LET produce different energy transfer distributions around the track core, leading to the same amount of energy being deposited in different spatial

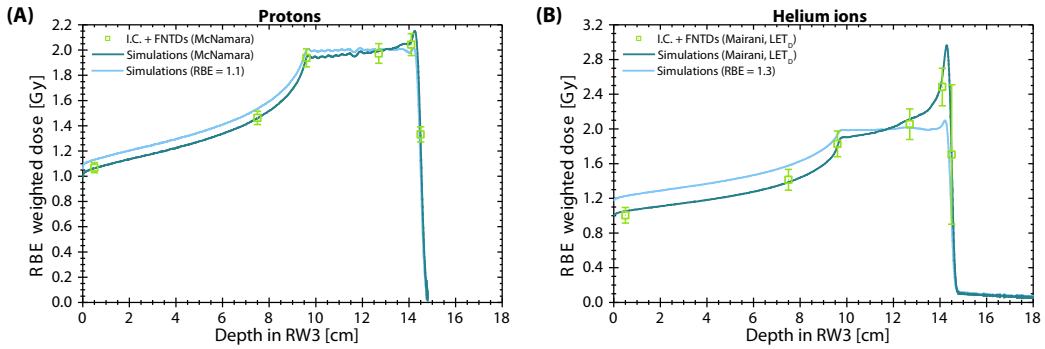

Fig. 5. RBE−weighted dose as a function of the depth in RW3 for (a) protons and (b) helium ions. For measurements performed with ionization chamber and fluorescent nuclear track detectors, error bars indicate the combined uncertainty of both systems. For simulations, error bars correspond to the standard uncertainty from independent runs. Uncertainties are reported with a coverage factor $k = 1$. *Abbreviations:* RBE = Relative biological effectiveness.

patterns within the crystal and consequently modifying the fluorescence of the track spots. Discrepancies between simulations and measurements at the distal dose falloff can be attributed to an increased energy dependence of the fluorescence intensity on the particle type outside the LET range covered by the calibration data, particularly for low-energy protons and helium ions. According to the calibration curve (Equation 1), the fluorescence intensity increases monotonically with the LET. However, it is reasonable to expect that the fluorescence intensity will eventually saturate or decrease for each ion type, deviating as LET increases from the trend set by the calibration. Therefore, improved and independent calibration curves for protons and helium ions, spanning the range of clinically relevant LET values, are required to avoid relying on ions heavier than the ones under study to extend the calibration curves to the highest LET levels that might be encountered. Such calibration curves would require the exposure of FNTDs to low-energy (<50 MeV/u) monoenergetic protons and helium ions. In this work, low-energy helium ion beams were achieved by lowering the energy through absorbers of different thicknesses. However, this approach might not be optimal, as it leads to energy broadening and contamination from particles generated by nuclear reactions.

Apart from inaccuracies caused by the fluorescence intensity-to-LET calibration, differences between simulations and measurements can be ascribed to additional factors, for instance, the broadening of the measured LET spectra with respect to the simulations. In this case, the response of the experimental system (both microscope and FNTDs) to a monoenergetic beam is characterized by a broad LET distribution because of inherent fluctuations in the fluorescence excitation-emission detection process and stochastic energy deposition.[17] In contrast, for the energy spectra approach used in the simulations, the response to a monoenergetic beam in the LET space is a δ function. Clearly, this extends to mixed broad-energy beams and is the primary cause of the observed broadening of the LET spectra. This effect can be partially mitigated by averaging over more slices to compensate for energy straggling and by repeatedly imaging the same regions to reduce variations from fluorescence and detection efficiencies. Another factor is that the high-LET tail of the LET spectra is not entirely represented by the measurements, owing to the low likelihood of high-LET events coupled with the relatively low number of imaged tracks. The latter causes higher discrepancies between measurements and simulations for LET_D than for LET_F. This issue can be addressed by scanning larger areas, albeit at the expense of longer imaging times. Another option is to use lower magnification objectives to cover larger areas faster, but this may compromise the detectability of low-LET events. Clearly, the number of tracks per frame can be increased by increasing the experimental fluences, but more robust tracking parameters would be necessary. One additional consideration is the high inherent uncertainty when measuring close to the distal dose falloff, due to steep dose, LET, and RBE gradients, which might further explain the observed larger deviations in that region. Still, FNTDs are well-suited for high-gradient measurements because of their small measurement volume. Regarding simulations, some limitations should also be recognized, for instance, inaccurate fragmentation cross sections and stopping power data,[35,36] as well as discrepancies due to different scoring techniques.[26,29] The latter highlights the importance of experimental techniques for LET measurements to perform independent verifications.

Conceptually similar to this work, measurements of lineal energy (y) spectra have been performed in clinical proton and helium ion beams and used as input on RBE models to estimate cell survival or RBE through a measured physical beam quality descriptor. These studies have been performed both with tissue equivalent proportional counters and silicon-on-insulator detectors.[37-40] However, it should be noticed that y and LET are distinct quantities, differing in how they are defined and measured.[41,42] In view of these differences, RBE models specifically based both on y and LET have been developed, each requiring the use of the appropriate input quantities. Determining which model and physical quantity is more suitable is beyond the scope of this study.

To better judge the effect of the accuracy of LET measurements on the RBE calculations, the results were compared against in silico and in vitro RBE values. The differences from both simulations and FNTD-based RBE values with respect to the clonogenic assays can be attributed to biological variabilities and to the fact that the RBE models used in this work were based on best fitting to sets of clonogenic data, which were characterized by a high dispersion. The latter supports future attempts to employ FNTDs as a tool for RBE verification of computational tools. The systematic deviation of simulated and FNTD-based RBE values from the cell-based RBE results, despite differences in LET, supports the idea that these deviations are linked to the models and biological variability in our experiments. Future studies, focused on the cell experiments and in vitro RBE validation, should assess to what extent a more realistic simulated geometry would decrease the differences between simulations and experiments. It is noteworthy that the RBE's low sensitivity to variations in LET allows for a certain degree of variability in the measured LET while still yielding relatively accurate RBE results. A dedicated study investigating the sensitivity of the RBE to changes in the LET could shed light on the required accuracy for LET measurements. The differences from both simulations and FNTD-based RBE values with respect to the clonogenic assays can be attributed to biological variabilities and to the fact that the RBE models used in this work are based on best fitting to sets of clonogenic data, which are characterized by a high dispersion. It is worth noting that these are early results, as only 1 cell line has been investigated. Further experiments involving more cell lines and additional beams are required. Data from such experiments could enhance the agreement and provide insights into the observed differences between model predictions and cell experiments. The

results obtained from the clonogenic assays were consistent with those reported in previous studies for the same cell line after exposure to x-rays,[43] protons,[44] and helium ions.[9]

In the last step, the RBE-weighted dose distributions obtained from measurements and simulations were compared. The excellent agreement further demonstrated that FNTDs can provide results comparable to those from simulations. In principle, FNTD-based LET measurements can be used with any model parameterized in terms of the LET and not exclusively with those used in the present study. The proposed method can also be applied to ions other than those studied in this work. For this, it is essential to have LET-based RBE models for all the involved particle species, including secondary ions. Moreover, the accuracy of LET and RBE measurements and the requirements for the calibration curve should be evaluated. Another aspect to consider is that the extraction of single peaks from the LET spectra is expected to become increasingly challenging in the highly mixed particle fields generated by heavier ions, such as carbon ions. To incorporate the proposed technique into clinical routine, it is necessary to automate and increase the sample imaging throughput, which can be achieved by dedicated FNTD readers and faster readout systems.[45,46] In addition, the analysis and modeling tools should be integrated and further automated.

Conclusion

The developed methodology allows for direct measurement of LET spectra, LET_F, and LET_D in clinical proton and helium ion beams using FNTDs. Furthermore, these measurements can be integrated into LET-based RBE models to predict the RBE and, consequently, calculate RBE-weighted doses for both proton and helium ion beams. Although the measured LET values exhibited nonnegligible differences compared with the simulations, we identified possible approaches to enhance the accuracy. Regarding the RBE, results indicate that the accuracy of FNTD-based LET measurements is already adequate for achieving results quantitatively comparable to simulations. The remaining differences with respect to in vitro RBE values can be attributed to the fact that the applied RBE models are based on fitting to data that are characterized by a large dispersion. Nevertheless, the observed differences are within the expected range of uncertainties.

References

1. Castro JR, Chen GTY, Blakely EA. Current considerations in heavy charged-particle radiotherapy: A clinical research trial of the University of California Lawrence Berkeley Laboratory, Northern California Oncology Group, and Radiation Therapy Oncology Group. *Radiat Res Suppl* 1985;104:S263-S271.
2. Jermann M. Particle therapy statistics in 2014. *Int J Part Ther* 2015;2:50.
3. Krämer M, Scifoni E, Schuy C, et al. Helium ions for radiotherapy? Physical and biological verifications of a novel treatment modality. *Med Phys* 2016;43:1995.
4. Mairani A, Mein S, Blakely E, et al. Roadmap: Helium ion therapy. *Phys Med Biol* 2022;67:15TR02.
5. Tessonnier T, Ecker S, Besuglow J, et al. Commissioning of helium ion therapy and the first patient treatment with active beam delivery. *Int J Radiat Oncol Biol Phys* 2023;116:935-948.
6. ICRU. Radiation biology considerations in prescribing, recording, and reporting proton-beam therapy. ICRU Report 78 *J ICRU* 2007;7:21.
7. Paganetti H, Blakely E, Carabe-Fernandez A, et al. Report of the AAPM TG-256 on the relative biological effectiveness of proton beams in radiation therapy. *Med Phys* 2019;46:e53-e78.
8. Paganetti H. Relative biological effectiveness (RBE) values for proton beam therapy. Variations as a function of biological endpoint, dose, and linear energy transfer. *Phys Med Biol* 2014;59:R419-R472.
9. Mairani A, Dokic I, Magro G, et al. Biologically optimized helium ion plans: Calculation approach and its in vitro validation. *Phys Med Biol* 2016;61:4283-4299.
10. Castro JR, Quivey JM. Clinical experience and expectations with helium and heavy ion irradiation. *Int J Radiat Oncol Biol Phys* 1977;3:127-131.
11. McNamara AL, Schuemann J, Paganetti H. A phenomenological relative biological effectiveness (RBE) model for proton therapy based on all published in vitro cell survival data. *Phys Med Biol* 2015;60:8399-8416.
12. Wedenberg M, Lind BK, Hårdemark B. A model for the relative biological effectiveness of protons: The tissue specific parameter α/β of photons is a predictor for the sensitivity to LET changes. *Acta Oncol* 2013;52:580-588.
13. Mairani A, Magro G, Dokic I, et al. Data-driven RBE parameterization for helium ion beams. *Phys Med Biol* 2016;61:888-905.
14. Weyrather WK, Kraft G. RBE of carbon ions: Experimental data and the strategy of RBE calculation for treatment planning. *Radiother Oncol* 2004;73:S161-S169.
15. Sykora GJ, Akselrod MS, Benton ER, Yasuda N. Spectroscopic properties of novel fluorescent nuclear track detectors for high and low LET charged particles. *Radiat Meas* 2008;43:422.
16. Klimpki G, Mescher H, Akselrod MS, Jäkel O, Greilich S. Fluence-based dosimetry of proton and heavier ion beams using single track detectors. *Phys Med Biol* 2016;61:1021-1040.
17. Muñoz ID, Burigo LN, Gehrke T, et al. Sensitivity correction of fluorescent nuclear track detectors using alpha particles: Determining LET spectra of light ions with enhanced accuracy. *Med Phys* 2023;50:2385-2401.
18. Krämer M, Jäkel O, Haberer T, et al. Treatment planning for heavy-ion radiotherapy: Physical beam model and dose optimization. *Phys Med Biol* 2000;45:3299-3317.
19. IAEA. Absorbed dose determination in external beam radiotherapy: An international code of practice for dosimetry based on standards of absorbed dose to water. IAEA TRS-398. Available at: https://www-pub.iaea.org/MTCD/Publications/PDF/TRS398_scr.pdf. Accessed July 20, 2023.
20. *Linear Energy Transfer. ICRU Report 16.* International Commission on Radiation Units and Measurements; 1970.
21. Kanai T, Furusawa Y, Fukutsu K, et al. Irradiation of mixed beam and design of spread-out Bragg peak for heavy-ion radiotherapy. *Radiat Res* 1997;147:78-85.
22. Perl J, Shin J, Schümann J, Faddegon B, Paganetti H. TOPAS: An innovative proton Monte Carlo platform for research and clinical applications. *Med Phys* 2012;39:6818-6837.
23. Parodi K, Mairani A, Brons S, et al. Monte Carlo simulations to support start-up and treatment planning of scanned proton and carbon ion therapy at a synchrotron-based facility. *Phys Med Biol* 2012;57:3759-3784.
24. Schoenfeld AA, Harder D, Poppe B, Chofor N. Water equivalent phantom materials for ^{192}Ir brachytherapy. *Phys Med Biol* 2015;60:9403-9420.

25. Christensen JB, Muñoz ID, Bassler N, et al. Optically stimulated luminescence detectors for dosimetry and LET measurements in light ion beams. *Phys Med Biol* 2023;68.
26. Granville DA, Sawakuchi GO. Comparison of linear energy transfer scoring techniques in Monte Carlo simulations of proton beams. *Phys Med Biol* 2015;60:N283N291.
27. *Key Data for Ionizing-Radiation Dosimetry: Measurements, Standards, and Applications. ICRU Report 90*. International Commission on Radiation Units and Measurements; 2016.
28. Polster L, Schuemann J, Rinaldi I, et al. Extension of TOPAS for the simulation of proton radiation effects considering molecular and cellular endpoints. *Phys Med Biol* 2015;60:5053-5070.
29. Hahn C, Ödén J, Dasu A, et al. Towards harmonizing clinical linear energy transfer (LET) reporting in proton radiotherapy: A European multi-centric study. *Acta Oncol* 2022;61:206-214.
30. Sechopoulos I, Rogers DW, Bazalova-Carter M, et al. RECORDS: Improved reporting of Monte Carlo radiation transport studies: Report of the AAPM Research Committee Task Group 268. *Med Phys* 2018;45:e1-e5.
31. Hanley R, Pagliari F, Garcia-Calderón D, et al. Radio-resistance of hypoxic tumors: Exploring the effects of oxygen and x-ray radiation on non-small lung cancer cell lines. *Radiat Oncol* 2023;18:81.
32. Castro F, Dirks WG, Fähnrich S, et al. High-throughput SNP-based authentication of human cell lines. *Int J Cancer* 2013;132:308-314.
33. Cao W, Khabazian A, Yepes PP, et al. Linear energy transfer incorporated intensity modulated proton therapy optimization. *Phys Med Biol* 2017;63 015013.
34. Verkhovtsev A, Zimmer L, Greilich S. Calibration of intensity spectra from fluorescent nuclear track detectors in clinical ion beams. *Radiat Meas* 2019;121:37.
35. Böhlen TT, Cerutti F, Dosanjh M, et al. Benchmarking nuclear models of FLUKA and GEANT4 for carbon ion therapy. *Phys Med Biol* 2010;55:5833-5847.
36. Burigo LN, Greilich S. Impact of new ICRU 90 key data on stopping-power ratios and beam quality correction factors for carbon ion beams. *Phys Med Biol* 2019;64 195005.
37. Kase Y, Kanai T, Matsumoto Y, et al. Microdosimetric measurements and estimation of human cell survival for heavy-ion beams. *Radiat Res* 2006;166:629-638.
38. Kase Y, Yamashita W, Matsufuji N, et al. Microdosimetric calculation of relative biological effectiveness for design of therapeutic proton beams. *J Radiat Res* 2013;54:485-493.
39. Lee SH, Mizushima K, Yonai S, et al. Predicting the biological effects of human salivary gland tumour cells for scanned ^{4}He-, ^{12}C-, ^{16}O-, and ^{20}Ne-ion beams using an SOI microdosimeter. *Appl Sci* 2022;12:6148.
40. Missiaggia M, Cartechini G, Tommasino F, Scifoni E, La Tessa C. Investigation of in-field and out-of-field radiation quality with microdosimetry and its impact on relative biological effectiveness in proton therapy. *Int J Radiat Oncol Biol Phys* 2023;115:1269-1282.
41. Definitions and concepts of LET. In: *Linear Energy Transfer. ICRU Report 16*. International Commission on Radiation Units and Measurements; 1970.
42. Microdosimetric quantities and distributions. In: *Microdosimetry. ICRU Report 36*. International Commission on Radiation Units and Measurements; 1983.
43. Bromley R, Oliver L, Davey R, Harvie R, Baldock C. Predicting the clonogenic survival of A549 cells after modulated x-ray irradiation using the linear quadratic model. *Phys Med Biol* 2009;54:187-206.
44. Liu Q, Ghosh P, Magpayo N, et al. Lung cancer cell line screen links Fanconi anemia/BRCA pathway defects to increased relative biological effectiveness of proton radiation. *Int J Radiat Oncol Biol Phys* 2015;91:1081-1089.
45. Akselrod MS, Fomenko VV, Bartz JA, Haslett TL. Automatic neutron dosimetry system based on fluorescent nuclear track detector technology. *Radiat Prot Dosim* 2014;161:86-91.
46. Walsh DW, Liew H, Schlegel J, Mairani A, Abdollahi A, Niklas M. Carbon ion dosimetry on a fluorescent nuclear track detector using wide-field microscopy. *Phys Med Biol* 2020;65:21NT02.

3.8. Publication IV

Assessment of fluence- and dose-averaged linear energy transfer with passive luminescence detectors in clinical proton beams

Authors: I. D. Muñoz, O. Van Hoey, A. Parisi, N. Bassler, L. Grzanka, M. De Saint-Hubert, A. Vaniqui, P. Olko, M. Sądel, L. Stolarczyk, A. Vestergaard, O. Jäkel, E. G. Yukihara, and J. B. Christensen
Status: Accepted
Journal: Physics in Medicine & Biology
DOI: https://doi.org/10.1088/1361-6560/ad4e8e

Contributions: IDM was responsible for preparing, irradiating, and reading the FNTDs and analyzing the resulting data. JBC was responsible for preparing, irradiating, and reading the OSLDs and analyzing the resulting data. OVH, AP, MDSH, and AV were responsible for preparing, irradiating, and reading the SCK-CEN TLDs and analyzing the resulting data. LG, PO, and MS were responsible for preparing, irradiating, and reading the IFJ TLDs and analyzing the resulting data. NB, LS, and AV organized the irradiation campaign and prepared the experiments at DCPT. LS and AV performed the experimental dosimetric characterization of the proton beams. MDSH, PO, OJ, and EGY served as coordinators and/or principal investigators at SCK-CEN, IFJ, DKFZ, and PSI, respectively. NB and LG performed all work related to Monte Carlo simulations. IDM, AP and JBC performed the RBE calculations. Data curation and visualization was performed by JBC. IDM, OVH, and JBC compiled all the results for publication and drafted the preliminary manuscript. IDM, OVH, AP, NB, LG, MS, and JBC drafted and edited the manuscript. All authors participated in the review of the final version of the manuscript.

Assessment of fluence- and dose-averaged linear energy transfer with passive luminescence detectors in clinical proton beams

Iván Domingo Muñoz[1,2,3], Olivier Van Hoey[4], Alessio Parisi[5], Niels Bassler[6,7], Leszek Grzanka[8], Marijke De Saint-Hubert[4], Ana Vaniqui[4], Paweł Olko[8], Michał Sądel[8], Liliana Stolarczyk[7], Anne Vestergaard[7], Oliver Jäkel[2,3,9], Eduardo Gardenali Yukihara[10], and Jeppe Brage Christensen*[10]

[1]Department of Physics and Astronomy, University of Heidelberg, Heidelberg, Germany
[2]Division of Medical Physics in Radiation Oncology, German Cancer Research Center (DKFZ), Heidelberg, Germany
[3]Heidelberg Institute for Radiation Oncology (HIRO), National Center for Radiation Research in Oncology (NCRO), Heidelberg, Germany
[4]Belgian Nuclear Research Center (SCK CEN), Mol, Belgium
[5]Department of Radiation Oncology, Mayo Clinic, Jacksonville, Florida, United States of America
[6]Department of Clinical Medicine, Aarhus University, Aarhus, Denmark
[7]Danish Centre for Particle Therapy, Aarhus University Hospital, Aarhus, Denmark
[8]Institute of Nuclear Physics, Polish Academy of Sciences (IFJ PAN), Kraków, Poland
[9]Heidelberg Ion-Beam Therapy Center (HIT), Department of Radiation Oncology, Heidelberg University Hospital, Heidelberg, Germany
[10]Department of Radiation Safety and Security, Paul Scherrer Institute (PSI), Villigen PSI, Switzerland

April 17, 2024

*jeppe.christensen@psi.ch

Abstract

Objective: This work investigates the use of passive luminescence detectors to determine different types of averaged linear energy transfer ($\overline{\text{LET}}$) for the energies relevant to proton therapy. The experimental results are compared to reference values obtained from Monte Carlo simulations.

Approach: Optically stimulated luminescence detectors (OSLDs), fluorescent nuclear track detectors (FNTDs), and two different groups of thermoluminescence detectors (TLDs) were irradiated at four different radiation qualities. For each irradiation, the fluence- ($\overline{\text{LET}}_{\text{f}}$) and dose-averaged LET ($\overline{\text{LET}}_{\text{d}}$) were determined. For both quantities, two sub-types of averages were calculated, either considering the contributions from primary and secondary protons or from all protons and heavier, charged particles. Both simulated and experimental data were used in combination with a phenomenological model to estimate the relative biological effectiveness (RBE).

Main results: All types of $\overline{\text{LET}}$ could be assessed with the luminescence detectors. The experimental determination of $\overline{\text{LET}}_{\text{f}}$ is in agreement with reference data obtained from simulations across all measurement techniques and types of averaging. On the other hand, $\overline{\text{LET}}_{\text{d}}$ can present challenges as a radiation quality metric to describe the detector response in mixed particle fields. However, excluding secondaries heavier than protons from the $\overline{\text{LET}}_{\text{d}}$ calculation, as their contribution to the luminescence is suppressed by ionization quenching, leads to equal accuracy between $\overline{\text{LET}}_{\text{f}}$ and $\overline{\text{LET}}_{\text{d}}$. Assessment of RBE through the experimentally determined $\overline{\text{LET}}_{\text{d}}$ values agrees with independently acquired reference values, indicating that the investigated detectors can determine $\overline{\text{LET}}$ with sufficient accuracy for proton therapy.

Significance: OSLDs, TLDs, and FNTDs can be used to determine $\overline{\text{LET}}$ and RBE in proton therapy. With the capability to determine dose through ionization quenching corrections derived from $\overline{\text{LET}}$, OSLDs and TLDs can simultaneously ascertain dose, $\overline{\text{LET}}$, and RBE. This makes passive detectors appealing for measurements in phantoms to facilitate validation of clinical treatment plans or experiments related to proton therapy.

1 Introduction

Proton therapy offers the advantage of highly conformal dose distributions, minimizing exposure of healthy tissue to ionizing radiation. Compared to high-energy photons, protons generally exhibit higher biological effectiveness (Paganetti, 2014). To leverage the substantial clinical data available for photons, and extend this knowledge to protons, the proton dose is scaled by the relative biological effectiveness (RBE; ICRU (2007)). Presently, a constant and generic RBE of 1.1 is used in the clinics (Paganetti et al., 2019). However, decades of *in vitro* experiments have accumulated a body of evidence indicating an increase in RBE with decreasing proton energy (Paganetti, 2014; Mohan, 2022). This observation has also been validated in *in vivo* systems (Gueulette et al., 2005; Saager et al., 2018; Bahn et al., 2020). The enhanced RBE of protons is tied to the ionization density,

which is typically quantified through the linear energy transfer (LET). Consequently, the LET has become an additional physical dimension in treatment planning, leading to the development of concepts such as LET painting (Bassler et al., 2014) or using averaged LET ($\overline{\text{LET}}$) as input for RBE parameterization (Unkelbach et al., 2016; Bertolet and Carabe, 2020; McIntyre et al., 2023).

While LET is a well-defined physical quantity (ICRU, 1970), currently no standard devices exist for its measurement. To estimate $\overline{\text{LET}}$ in a volume, the particle spectrum is typically averaged with respect to either the fluence ($\overline{\text{LET}}_\text{f}$) or dose ($\overline{\text{LET}}_\text{d}$). In mixed particle fields, the calculation of $\overline{\text{LET}}_\text{d}$ is strongly dependent of the included secondary ions, which may cause very different $\overline{\text{LET}}_\text{d}$ values for the same same radiation field (Kalholm et al., 2021). This contrasts $\overline{\text{LET}}_\text{f}$ which is little sensitive to the omission of certain secondaries in proton beams (Petringa et al., 2020). In proton therapy, however, the RBE is generally parameterized based on $\overline{\text{LET}}_\text{d}$ with contributions from primary and secondary protons only (Hahn et al., 2022).

This lack of standardization is in contrast to absorbed dose, for which standard devices and protocols are in place to ensure traceability and facilitate the comparison of clinical findings (Almond et al., 1999; IAEA, 2000). The absence of a standardized $\overline{\text{LET}}$ definition and assessment device presents a challenge in establishing common practices for routine clinical applications. With the growing interest in incorporating $\overline{\text{LET}}$ as a clinical metric, there is an increased need for a device capable of accurately assessing $\overline{\text{LET}}$. Such a device can facilitate the development and implementation of procedures for experimental $\overline{\text{LET}}$ verification and the comparison of different models or treatment planning algorithms.

Owing to their capabilities, solid-state detectors, including optically stimulated luminescence detectors (OSLDs), thermoluminescent detectors (TLDs), and fluorescent nuclear track detectors (FNTDs), are well-suited for assessing $\overline{\text{LET}}$ in proton therapy.

For Al_2O_3:C OSLDs, both the shape of the emission intensity time profile as well as the ratio between UV and blue emissions have been correlated with the $\overline{\text{LET}}$ in clinically relevant proton beams (Sawakuchi et al., 2010; Granville et al., 2014). Recently, the $\overline{\text{LET}}$ determination with OSLDs relevant to protons was improved by incorporating corrections based on reference irradiation (Christensen et al., 2022). That approach was used to simultaneously determine $\overline{\text{LET}}$ and dose with OSLD measurements in an anthropomorphic head phantom to validate a treatment plan for adaptive proton therapy (Bobić et al., 2024). The measurement technique has been extended to helium and carbon ions with both Al_2O_3:C and Al_2O_3:C,Mg OSLDs (Christensen et al., 2023).

For TLDs, it has been shown that the dose ratio measured with two different TLD materials having distinct relative efficiencies can be correlated with the $\overline{\text{LET}}$ of light and heavy ions (Bilski, 2006; Parisi et al., 2019). By utilizing a microdosimetric formalism, based on dose probability distributions of the specific energy and specific energy response functions for different detector types, it is possible to model the relative efficiency of LiF:Mg,Ti and LiF:Mg,Cu,P TLDs in a wide $\overline{\text{LET}}$ range (Parisi et al., 2019). This approach has been exploited to determine the $\overline{\text{LET}}$ and

assess the RBE for a clinical proton spread-out Bragg peak (Parisi et al., 2019, 2020b).

Unlike OSLDs and TLDs, which rely on the integral signal from all particle interactions, FNTDs enable a single-track analysis. The technique is based on establishing a relationship between the fluorescence intensity of individual track spots and the ionization density of the particles passing through the crystal (Sykora et al., 2008). Hence, FNTDs enable the measurement of LET spectra (Klimpki et al., 2016). FNTDs based on Al_2O_3:C,Mg have been employed to measure the LET spectra of proton and light ion beams (Sawakuchi et al., 2016; Verkhovtsev et al., 2019; Muñoz et al., 2023, 2024). However, to measure LET spectra and $\overline{\text{LET}}$ with FNTDs, the particle fluence needs to be reduced below clinically relevant levels, typically to tens of mGy.

As the calculation of $\overline{\text{LET}}$ depends strongly on the type of averaging and the particle types included, this work aims at identifying the type of $\overline{\text{LET}}$ which can be most accurately assessed with OSLDs, TLDs, and FNTDs. Additionally, a phenomenological RBE model is used to assess the RBE through the $\overline{\text{LET}}$ determined with the luminescence detectors. As the employed RBE model is parameterized in terms of $\overline{\text{LET}}_\text{d}$ for protons, only this type of $\overline{\text{LET}}$ is used to assess the RBE. These results would present a significant step towards a passive detector for simultaneous determination of dose, $\overline{\text{LET}}$, and RBE.

2 Materials and methods

2.1 Experimental design

All proton irradiations were undertaken at the Danish Centre for Particle Therapy (DCPT) in Aarhus, Denmark, organised by the EURADOS WG9. The detectors were irradiated in four positions in two irradiation plans; one 160 MeV quasi-monoenergetic beam and one spread-out Bragg peak (SOBP) consisting of 24 energy layers ranging from 78 MeV to 154 MeV providing a 10 cm × 10 cm × 10 cm box, both by lateral scanning. The experimental setup and each measurement configuration details are available at Bassler et al. (2024) and outlined in table 1. The positions and fields were chosen such that they cover the conditions relevant to proton therapy, ranging from a relatively mono-energetic condition, over the middle of the SOBP to the distal edge of the SOBP with a highly mixed particle field and high LET. The positions in table 1 refer to the interface between the PMMA slab and the detector surface. The depth is provided in terms of water equivalent depth.

The absorbed dose to water was in the range 0.5 Gy to 1.0 Gy for all OSLD and TLD irradiations with a 10 cm × 10 cm field size. A dose below 2 Gy ensures that the effect of overlapping tracks in the OSLDs and TLDs can be neglected, which otherwise would affect the detector response used to determine $\overline{\text{LET}}$ (Flint et al., 2016). FNTDs were irradiated at doses around 30 mGy to minimize track overlaps.

Table 1: The two irradiation plans and four measurement positions used for the experiments. All positions are detailed in Bassler et al. (2024). The SOBP consists of 24 energy layers ranging from 78 MeV to 154 MeV. The $\overline{\text{LET}}$ values obtained from Monte Carlo simulations at each position, where the particles included in the averaging are given in the superscripts.

Plan	Position	Depth /cm	Description	$\overline{\text{LET}}_\text{f}$/ keV µm^{-1}		$\overline{\text{LET}}_\text{d}$/ keV µm^{-1}	
				$\overline{\text{LET}}_\text{f}^\text{p}$	$\overline{\text{LET}}_\text{f}^\text{all}$	$\overline{\text{LET}}_\text{d}^\text{p}$	$\overline{\text{LET}}_\text{d}^\text{all}$
SOBP	1a	10.25	SOBP center	1.14	1.15	2.02	4.46
SOBP	1b	15.25	Distal 95 % dose	4.18	4.19	7.13	7.94
SOBP	1c	15.45	Distal 75 % dose	5.38	5.39	9.56	10.1
160 MeV	2	2.25	Entrance plateau	0.58	0.59	0.90	3.99

2.1.1 Monte Carlo simulations

To compare the experimentally obtained results with OSLDs, TLDs, and FNTDs with independent reference values, the dose and $\overline{\text{LET}}$ at the four measurement positions were calculated with Monte Carlo radiation transport methods. The absorbed dose and $\overline{\text{LET}}$ values in water were simulated with `SHIELD-HIT12A` (Hansen et al., 2012) based on the geometry detailed at Bassler et al. (2024). The $\overline{\text{LET}}$ scoring in `SHIELD-HIT12A` relies on the averaging method defined as method 'C' in Cortés-Giraldo and Carabe (2015). Contributions from delta-electrons are not included in the $\overline{\text{LET}}$ scoring, and all $\overline{\text{LET}}$ values are given for water.

Both $\overline{\text{LET}}_\text{f}$ and $\overline{\text{LET}}_\text{d}$ were calculated in two ways, giving a total of four different types of $\overline{\text{LET}}$: One method includes contributions from protons and all heavier charged particles, which is denoted with superscript 'all'. This average is used to reflect all particles that may interact with the luminescence detectors. The second type of $\overline{\text{LET}}$ considers only the contributions from primary and secondary protons, referred to with superscript 'p'. This type of $\overline{\text{LET}}$ is in line with recommendations for proton therapy for $\overline{\text{LET}}_\text{d}$ given in Hahn et al. (2022).

The simulated field was 10 cm × 10 cm, where dose and $\overline{\text{LET}}$ quantities were scored in water in bins of 1 mm thickness along the central beam axis within an area of 2 cm × 2 cm to match the extend where the detectors were placed. The simulated dose and $\overline{\text{LET}}$ distributions in the two irradiation fields are shown in figure 1, where the four measurement positions outlined in table 1 are highlighted.

For position 2 in table 1, the calculated $\overline{\text{LET}}_\text{d}^\text{p}$ for primary and secondary protons is around 4 times lower than $\overline{\text{LET}}_\text{d}^\text{all}$ which includes contributions from all particles. This large difference emphasizes the effect of particles heavier than protons for dose-averaging and is in agreement with similar simulations with other particle transport code as `Geant4` (Petringa et al., 2020) and `PHITS` (Parisi et al., 2023). A discussion pertaining to the differences between $\overline{\text{LET}}_\text{d}^\text{p}$ and $\overline{\text{LET}}_\text{d}^\text{all}$ can be found in Petringa et al. (2020) or Kalholm et al. (2021).

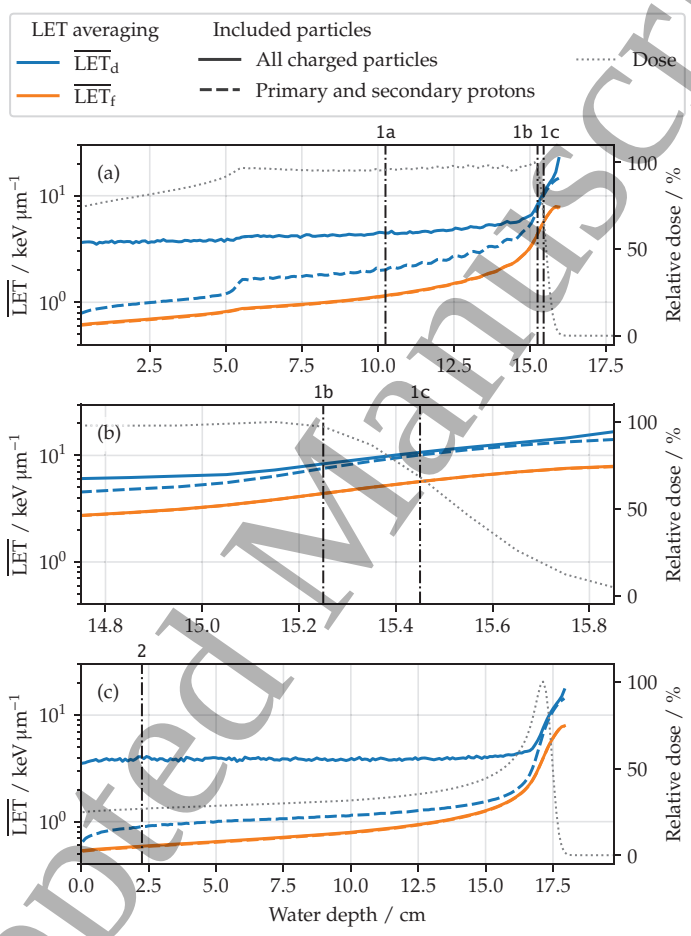

Figure 1: Monte Carlo simulations (`SHIELD-HIT12A`) of the absorbed dose, $\overline{\mathrm{LET}}_\mathrm{f}$ and $\overline{\mathrm{LET}}_\mathrm{d}$ distributions along the beam axes with the measurement positions indicated with vertical, dashed lines. (a) shows the SOBP with measurement positions `1a`, `1b`, and `1c`. (b) shows a close-up of positions `1b` and `1c` at the distal dose falloff in (a). (c) shows the mono-energetic 160 MeV beam with position `2`. The $\overline{\mathrm{LET}}_\mathrm{f}$ lines overlap with $\overline{\mathrm{LET}}$ values given for water.

2.2 Luminescence detectors

The luminescence detectors used to determine the $\overline{\text{LET}}$ are listed in table 2. Each detector type was irradiated in an independent session, where custom made holders were used to accommodate each detector type and ensure a reproducible positioning. The $\overline{\text{LET}}$ determination with TLDs was conducted utilizing different protocols and $\overline{\text{LET}}$ calibrations by SCK CEN (Belgium) and IFJ PAN Krakow (Poland), referred to herein as SCK and IFJ, respectively. The detector preparation and readout is detailed for all detector types in the supplementary material A.1.

Table 2: Overview of the detector types used for $\overline{\text{LET}}$ determination. The $\overline{\text{LET}}$ was either determined through a single detector with OSLDs and FNTDs or through the response differences between two detectors with TLDs. The last column specifies the number of detectors used per irradiation.

Institute	Detector	Name	Material	Density / g cm^{-3}	Dimensions / mm	Detectors
PSI	OSLD	Mipox	Al_2O_3:C	4.0	$\varnothing\, 4 \times 0.1$	$7-10$
PSI	OSLD		Al_2O_3:C,Mg	4.0	$\varnothing\, 4 \times 0.1$	$7-10$
SCK	TLD	MCP-7	^{7}LiF:Mg,Cu,P	2.5	$\varnothing\, 4.5 \times 0.9$	$12-13$
SCK	TLD	MTS-7	^{7}LiF:Mg,Ti	2.5	$\varnothing\, 4.5 \times 0.9$	$12-13$
IFJ	TLD	MCP-N	LiF:Mg,Cu,P	2.5	$\varnothing\, 3.2 \times 0.3$	$7-8$
IFJ	TLD	MTS-N	LiF:Mg,Ti	2.5	$\varnothing\, 3.2 \times 0.3$	$7-8$
DKFZ	FNTD		Al_2O_3:C,Mg	4.0	$4.0 \times 8.0 \times 0.5$	3

2.3 $\overline{\text{LET}}$ determination techniques

The calibrations that relate the OSLD, TLD, and FNTD response to $\overline{\text{LET}}$ are acquired independently from the measurements at DCPT presented in section 2.1. As detailed below, the $\overline{\text{LET}}$ calibrations with OSLD and TLDs from IFJ are based on experimentally acquired data, whereas both the $\overline{\text{LET}}$ determination with FNTDs and the TLDs from SCK are based on calculations.

2.3.1 $\overline{\text{LET}}$ determination with OSLDs

The OSLDs were prepared from a thin, flexible film as given in supplementary material A.1.1. The $\overline{\text{LET}}$ determination with OSLDs herein rely on the use of the intensity ratio of the two emission bands, namely those in the UV and blue bands of Al_2O_3:C and Al_2O_3:C,Mg. For both OSLD materials, the $\overline{\text{LET}}$ calibration curves are obtained by irradiating the OSLDs at known radiation conditions, where the $\overline{\text{LET}}$ at the detector position is assessed with the Monte Carlo particle transport code `TOPAS` (Perl et al., 2012) based on `Geant4` (Agostinelli et al., 2003). The relationship between the OSLD emission ratios and different types of $\overline{\text{LET}}$ is shown in figure 2a–b for Al_2O_3:C,Mg OSLDs. The relationships serve as the $\overline{\text{LET}}$-calibrations. The $\overline{\text{LET}}$ calibration data in figure 2a–b are acquired at different beam lines. The scatter in the data is partly due to differences in the Monte Carlo models of the experiments.

To determine the $\overline{\text{LET}}$, the intensity ratio of the UV and blue emission bands is used to look up the corresponding $\overline{\text{LET}}$ value from a fit to the data. Similar $\overline{\text{LET}}$-calibration curves for proton,

helium, and carbon ions are given in Christensen et al. (2023) for both Al_2O_3:C and Al_2O_3:C,Mg OSLDs.

For dosimetry, the assessed $\overline{\text{LET}}_\text{f}$ values are used to determine the relative detector efficiency caused by the ionization quenching, and accordingly to correct the quenched dose. Hence, the dose-rate independent OSLDs (Christensen et al., 2021) enable a simultaneous determination of the different types of $\overline{\text{LET}}$ as well as dose

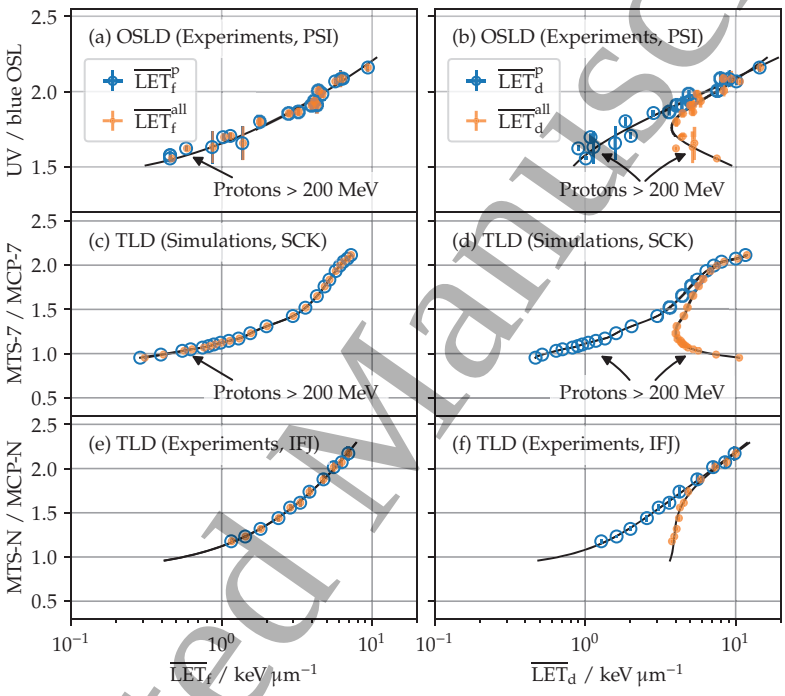

Figure 2: (a-b) The $\overline{\text{LET}}$ calibrations for Al_2O_3:C,Mg OSLDs are experimentally obtained and compiled from different beam lines, which causes some scatter in the data. (c-d) The TLD $\overline{\text{LET}}$-calibrations used by SCK are obtained with theoretical and numerical methods. (e-f) The TLD $\overline{\text{LET}}$-calibrations from IFJ are experimentally determined from the same beam line. Open markers illustrate the contributions to the $\overline{\text{LET}}$ from primary and secondary protons, whereas closed markers include contributions from all charged ions. The left and right columns show $\overline{\text{LET}}_\text{f}$ and $\overline{\text{LET}}_\text{d}$ calibration curves, respectively. The calibrations are independent from the measurements discussed herein.

2.3.2 $\overline{\text{LET}}$ determination with TLDs: The SCK approach

The MTS-7 glow curve exhibits distinct high-temperature peaks, each with a unique dose and LET response, while the MCP-7 glow curve shows a less pronounced variation (Parisi et al., 2017). Therefore, the TLD types were analysed differently. The MCP-7 signal was quantified through

integration across the entire glow curve, whereas for MTS-7, integration focused specifically on the main peak area spanning from 150 °C to 248 °C.

The TLD measurements were quantified in terms of absorbed dose to water through a ^{60}Co calibration. The ratio of the average doses measured by the MTS-7 and MCP-7 detectors is used to assess the $\overline{\text{LET}}$ as illustrated in figure 2c–d. The relative detector efficiencies of the MTS-7 and MCP-7 TLDs were determined by using a lookup table with the relative luminescence efficiencies of MTS-7 and MCP-7 as predicted by the Microdosimetric $d(z)$ Model based on `PHITS` simulations, as detailed in Parisi et al. (2019, 2020b).

The determined TLD efficiencies enable corrections for the TLD efficiency in measured doses, allowing simultaneous assessment of $\overline{\text{LET}}$ and dose in water by combining MTS-7 and MCP-7 TLDs.

2.3.3 $\overline{\text{LET}}$ determination with TLDs: The IFJ approach

The glow curve for IFJ TLDs was analyzed using the GlowView software (Gieszczyk and Bilski, 2017). For both detector types, the main peak position was aligned to a temperature of 220 °C and the glow curve integrated over the main peak area from 100 °C to 240 °C (for MCP-N) and from 150 °C to 250 °C (for MTS-N). Similar to the TLD detectors in section 2.3.2, these TLD detectors were subject to a dose-to-water calibration derived from ^{60}Co irradiations.

The $\overline{\text{LET}}$-calibration is based on experiments performed on the AIC-144 cyclotron at IFJ (Swakon et al., 2010). The TLD detectors were irradiated in a 58.8 MeV proton beam, where a PMMA degrader of variable thickness was used to vary the kinetic energy at the detector position. The ratio of average detector doses were linked to the $\overline{\text{LET}}$ through particle transport simulations with `SHIELD-HIT12A` as illustrated in figure 2e–f.

2.3.4 $\overline{\text{LET}}$ determination with FNTDs

Single proton tracks were reconstructed using in-house developed tools based on track spot segmentation and 3D feature point tracking (Kouwenberg et al., 2016). Background subtraction and optical aberration corrections were applied to the images. This process resulted in the fluorescence intensity of each reconstructed track. The fluorescence intensity is related to the $\overline{\text{LET}}$ through a calibration curve, as shown in figure 3. The reference LET values were estimated analytically from the residual energy at the detector surface as detailed in (Muñoz et al., 2023). Hence, the calibration curve does not represent an average quantity, as it is associated to single particles from mono-energetic beams For consistency, the calibration curve used in this work was determined from data obtained after re-scanning detectors exposed in a previous work to mono-energetic protons, ^{4}He- and ^{12}C-ions (Muñoz et al., 2023), but following the scanning protocol used in this work. From the fluorescence intensity, the LET in water of each track was calculated through the calibration curve.

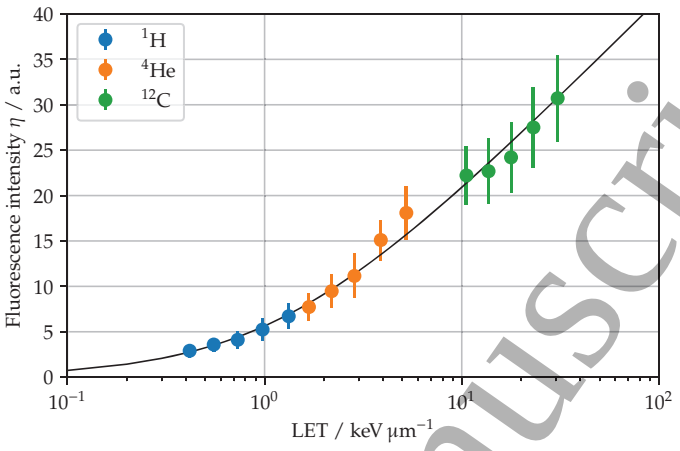

Figure 3: Fluorescence intensity as a function of analytically determined LET in water. The fitted calibration curve is depicted with a solid line. This curve was used to calculate the LET of each reconstructed track. Markers show data obtained after exposure to protons, ^{4}He-, and ^{12}C-ions (Muñoz et al., 2023).

The LET spectra were obtained by binning the LET data from 0.1 keV µm^{-1} to 1000 keV µm^{-1} and counting the track frequencies with a bin size of 0.5 keV µm^{-1}. $\overline{\mathrm{LET}}_{\mathrm{f}}$ and $\overline{\mathrm{LET}}_{\mathrm{d}}$ were calculated from the LET spectra following the definitions established by the ICRU (1970).

2.3.5 RBE model

To assess how the spread of the $\overline{\mathrm{LET}}_{\mathrm{d}}^{\mathrm{p}}$ measurements affects the RBE predicted values, the RBE was calculated with a phenomenological model (McNamara et al., 2015). This model was chosen because it is parameterized in terms of the quantities of interest to this work, and since it is the phenomenological proton RBE model based on the largest *in vitro* data set (Rørvik et al., 2018). The RBE was calculated as

$$\mathrm{RBE} = \frac{1}{2D_p}\left[\sqrt{\left(\frac{\alpha}{\beta}\right)_x^2 + 4\,D_p\left(\frac{\alpha}{\beta}\right)_x \mathrm{RBE}_{\max} + 4\,D_p^2\,\mathrm{RBE}_{\min}^2} - \left(\frac{\alpha}{\beta}\right)_x\right], \tag{1}$$

for

$$\mathrm{RBE}_{\max} = p_0 + \frac{p_1}{(\alpha/\beta)_x}\left(\overline{\mathrm{LET}}_{\mathrm{d}}^{\mathrm{p}} - \overline{\mathrm{LET}}_{\mathrm{D},x}\right), \tag{2}$$

$$\mathrm{RBE}_{\min} = p_2 + p_3\sqrt{\left(\frac{\alpha}{\beta}\right)_x}\left(\overline{\mathrm{LET}}_{\mathrm{d}}^{\mathrm{p}} - \overline{\mathrm{LET}}_{\mathrm{D},x}\right) \tag{3}$$

where p_1, p_2, p_3 and p_4 are fitting parameters given in McNamara et al. (2015) and $(\alpha/\beta)_x$ is the alpha-beta ratio for X-rays. $\overline{\mathrm{LET}}_{\mathrm{D},x} \simeq 0.3$ keV µm^{-1} denotes the dose-averaged LET from photons, which is subtracted from the $\overline{\mathrm{LET}}_{\mathrm{d}}$ from protons for the RBE calculations only. For D_p,

the simulated dose profiles were scaled to 1.82 Gy at the SOPB (plans 1a, 1b and 1c) and at the maximum of the Bragg peak for the 160 MeV proton beam (plan 2) and the absorbed dose at the measuring positions was assumed. The RBE was studied for $(\alpha/\beta)_x$ values of 2 Gy and 10 Gy, representing radiosensitive and radioresistant tissues, respectively.

2.4 LET determination uncertainties

The uncertainty interval of the assessed $\overline{\mathrm{LET}}_{\mathrm{f}}$ and $\overline{\mathrm{LET}}_{\mathrm{d}}$ was determined for a 95 % confidence level (coverage factor $k = 2$). For both OSLDs and TLDs, the absorbed doses ≤ 1 Gy mean that no correction factors are needed to account for non-linearity effects of signal intensity as function of dose that come into play only for higher doses. The application of such correction factors would otherwise contribute to the total uncertainty. For each detector type, the uncertainty components were combined by means of propagation of uncertainties.

2.4.1 OSLD uncertainties

The $\overline{\mathrm{LET}}$ uncertainties from the OSLDs are here caused by two contributions, one being related to the estimation of the ratio of the two OSL emissions, whereas the other is derived from the uncertainty of the $\overline{\mathrm{LET}}$ calibration fit. Although variations between OSLD sensitivities as well as the photomultiplier efficiency between readouts may vary, the use of reference irradiations and readouts enable determination of the UV/blue emission ratio with a standard deviation of the data better than 1 % (Christensen et al., 2022). With more than seven OSLDs of each type per irradiation session, a standard deviation of the mean of the UV/blue emission ratio lower than 0.5 % is achieved for each measurement.

As the $\overline{\mathrm{LET}}$ calibration curves in figure 2a–b are obtained through measurements, the $\overline{\mathrm{LET}}$-calibration is the largest contribution to the total uncertainty. The confidence interval is estimated from the fitting parameters.

2.4.2 TLD uncertainties

The uncertainty of the ratio of the average doses measured with the both TLD detector types (MTS and MCP) was assessed for both detector types used by SCK and IFJ. This uncertainty represents the contributions from the calibration and the background TLDs, as well as the uncertainty on the delivered calibration dose. The uncertainty intervals for $\overline{\mathrm{LET}}$ were determined from the TLD dose ratio and includes the uncertainty on the ratio. For the $\overline{\mathrm{LET}}$ determinations from SCK relying on the Microdosimetric $d(z)$ Model, the uncertainty of the $\overline{\mathrm{LET}}$ assessment is detailed in (Parisi et al., 2019) and is around 10 %. For consistency between the two TLD methods for LET determination from SCK and IFJ, the uncertainty from the $\overline{\mathrm{LET}}$ calibration was omitted. This, however, is in line with previous studies that demonstrate an excellent agreement with experimental data, both for mono-energetic protons (Parisi et al., 2020b) and SOBPs (Parisi et al., 2019).

2.4.3 FNTD uncertainties

The uncertainties due to the calibration and statistical variations between detectors were combined. To estimate the uncertainty of $\overline{\mathrm{LET}}_{\mathrm{f}}$ and $\overline{\mathrm{LET}}_{\mathrm{d}}$, the track- and dose-averaged LET spectra were weighted by the uncertainty obtained from the LET calibration curve. This was done under the assumption that the uncertainty is proportional to the probability density for each bin and inversely proportional to the integral probability. The uncertainty due to the statistical spread from different detectors was calculated as the standard deviation between the predicted $\overline{\mathrm{LET}}_{\mathrm{f}}$ and $\overline{\mathrm{LET}}_{\mathrm{d}}$ values.

3 Results and discussion

3.1 Dose limitations for passive luminescence detectors

The OSLD and TLD responses are affected by the local ionization densities, which is the effect exploited to assess the different types of $\overline{\mathrm{LET}}$. This means that overlapping ion tracks, which increases the local doses, may cause a signal change which cannot be distinguished from that of a higher $\overline{\mathrm{LET}}$ radiation field, i.e. overlapping ion tracks distort the $\overline{\mathrm{LET}}$ assessment above a certain fluence threshold. In a 230 MeV proton beam, the track overlap starts to affect the $\overline{\mathrm{LET}}$ assessment above 2.0 Gy (Flint et al., 2016). As the $\overline{\mathrm{LET}}$ increases towards the end of the range of the primary particles, the corresponding dose limitation is at a $(3-4)$ Gy level in an SOBP, but is complexly depending on the particle field and ion track structures. For FNTDs, trap overlap can lead to erroneous track reconstruction. The FNTDs in this work were irradiated at 30 mGy to avoid track overlap and are unsuitable for clinically relevant doses.

The local dose distributions in mixed particle fields can be estimated numerically with compound Poisson processes (Greilich et al., 2014), which can be used to calculate dose correction factors for a given particle field and dose. To avoid employing such corrections, clinical treatment plans may under certain conditions be scaled down accordingly without modifying the LET spectra. However, dose corrections may be needed if the radiation field dose cannot be downscaled to a suitable fluence level.

3.2 OSLD results

An example of the OSLD readouts is shown in figure 4. The OSLD holder with 7 Al_2O_3:C and 10 Al_2O_3:C,Mg_aOSLDs was irradiated in the position `1a`. Figure 4a–b show the reference-corrected blue and UV emissions, respectively. The ratio of the two was used to determine the $\overline{\mathrm{LET}}_{\mathrm{f}}^{\mathrm{p}}$ in figure 4c using the calibration curve in figure 2a. Similar approaches are used to determine other radiation quality metrics and other types of $\overline{\mathrm{LET}}$.

The determination of the radiation quality enables an estimate of the average ionization quenching to each detector and determining an ionization quenching correction factor through the relative

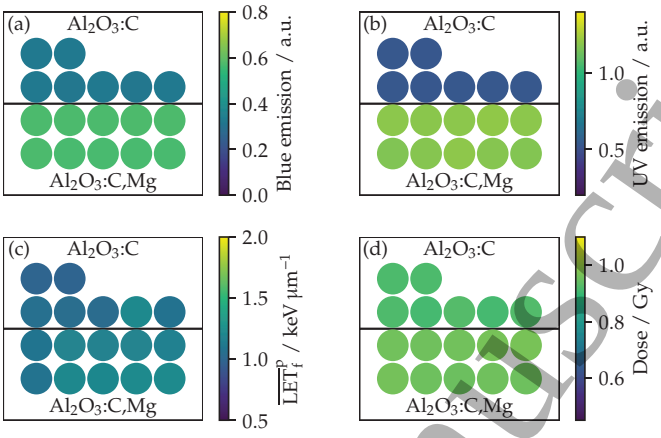

Figure 4: Example of a single irradiation of OSLDs in the 1a position, where the holder contained 7 Al_2O_3:C and 10 Al_2O_3:C,Mg detectors. (a) shows the reference-corrected blue emissions, and (b) the reference-corrected UV emissions for all detectors. (c) shows the determined $\overline{LET}_f^p$ and (d) the dose to each OSLD after quenching corrections.

detector efficiency of the detector given in Christensen et al. (2023). Applying the quenching corrections to the measured doses leads to the correct doses. Figure 4d shows the dose to each OSLD after these quenching corrections.

3.3 TLD results

For the TLDs, the spread on the doses measured in the proton fields and for the calibration TLDs had a standard deviation of the data ranging between 1 % and 7 % for the SCK and between 1 % and 5 % for the IFJ TLDs. No systematic trends for TLD dose variations are observed, which confirms the homogeneity of the proton field over the detector grid, and is in agreement with the OSLD results in figure 4.

The TLD doses and dose ratios are provided in the supplementary table A.1 for both MTS-N and MCP-N TLDs from IFJ as well as the MTS-7 and MCP-7 TLDs from SCK. The delivered doses varied between the sessions, particularly for position 2, which means that the SCK and IFJ doses cannot be directly compared. The dose ratios are used to determined the different types of $\overline{LET}$ through the calibrations in figure 2.

3.4 FNTD results

A typical maximum fluorescence intensity projection of an FNTD is illustrated in figure 5a. For all FNTD images acquired, approximately 9 600, 6 900, and 15 700 tracks were analyzed at positions

1b, 1c, and 2, respectively. Notably, this track count is around one order of magnitude larger than the typical number studied with this technique.

The resulting LET spectra at the studied positions are presented in figure 5b with peaks located at (3.3, 3.7, 0.65) keV µm^{-1} for detectors exposed at positions 1b, 1c, and 2, respectively. In addition to the shifting of the maximum, it can noticed that the LET spectra broaden with increasing depth due to the upstream energy straggling. It should be noted that no FNTDs were irradiated at position 1a due to the high fluences expected during the experiments, which could result in track overlapping, thus hindering the accuracy of the results.

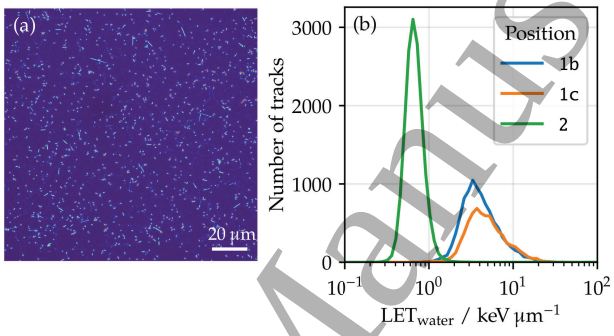

Figure 5: (a) Example of a maximum fluorescence intensity projection image from a Al_2O_3:C,Mg FNTD irradiated in plan 1b. (b) LET spectra measured with FNTDs for the studied fields. The plan 1a was not measured with the FNTDs.

Additionally, it is worth noting that due to their high detection efficiency, FNTDs record all charged particles interacting with the crystal, not just protons. However, given the low experimental fluences and short range of the secondaries, the likelihood of detecting a sufficient number of charged particles heavier than protons in the scanned volumes is low enough to assume that the assessed LET corresponds primarily to contributions from protons.

3.5 $\overline{\text{LET}}$ assessment

All $\overline{\text{LET}}$ determination results are compiled in figure 6a–p for the four types of $\overline{\text{LET}}$ investigated. The $\overline{\text{LET}}$ obtained through simulations is illustrated with a solid line in each subplot of figure 6. The shaded band around the simulation results corresponds to the $\overline{\text{LET}}$ variation for a 1 mm offset to reflect the positioning uncertainty. The detector position is taken as the water equivalent thickness (WET) of half the detector thickness for OSLDs and TLDs, and half the WET of the maximum scanned depth for FNTDs. The horizontal error bars illustrate the WET of each detector, whereas the vertical error bars represent the 95 % confidence interval. The four types of $\overline{\text{LET}}$ were experimentally determined with the two TLD methods and two OSLD types, whereas the FNTDs were used to determine $\overline{\text{LET}}^{\text{p}}_{\text{f}}$ and $\overline{\text{LET}}^{\text{p}}_{\text{d}}$ only.

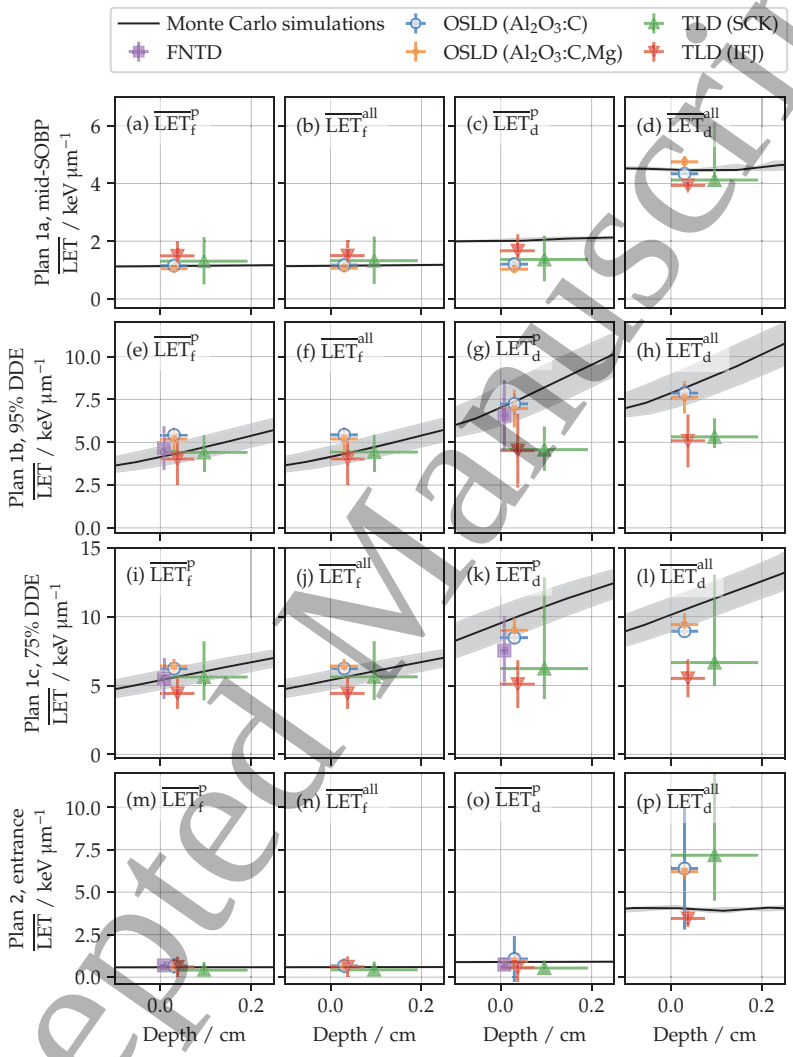

Figure 6: Determination of the four types of $\overline{LET}$ with the luminescence detectors for the four positions `1a` (middle of the SOBP), `1b` (95 % distal dose edge (DDE)), `1c` (75 % DDE), and `2` (entrance region) defined in table 1. Each column shows the results for a given kind of $\overline{LET}$. The depth is relative to the interface between the PMMA-plate and detector holder, where each detector is positioned at a depth that corresponds to its center. The FNTDs were not irradiated in plan `1a` and only used to determine $\overline{LET}_f$ and $\overline{LET}_d$ for protons.

Particularly the determination of the $\overline{\mathrm{LET}}_{\mathrm{f}}$ is accurate across all detector types and field complexity, where all measurements agree with the simulations within the ($k = 2$) uncertainties. This also applies to position 1c at the very distal edge of the SOBP, where a slight misalignment would largely affect the results due to the sharp dose and $\overline{\mathrm{LET}}$ gradients. That agreement for $\overline{\mathrm{LET}}_{\mathrm{f}}$ contrasts that of $\overline{\mathrm{LET}}_{\mathrm{d}}$, where all detectors exhibit larger deviations—both among themselves and relative to the $\overline{\mathrm{LET}}_{\mathrm{d}}$ values obtained from simulations.

The deviation of the determined $\overline{\mathrm{LET}}$ with respect to the values obtained from Monte Carlo simulations is summarised in table 3. Each entry in the table denotes the mean numerical value of the relative deviation between the experimentally and numerically determined $\overline{\mathrm{LET}}$ for all four measurement positions. The deviation at a 15 %-level is mainly a result of the steep $\overline{\mathrm{LET}}$ gradients at the distal edge, where a 1 mm misalignment causes an $\overline{\mathrm{LET}}$ variation of that order of magnitude. All experimental $\overline{\mathrm{LET}}_{\mathrm{f}}$ values are within the uncertainties of the reference Monte Carlo derived $\overline{\mathrm{LET}}_{\mathrm{f}}$ values. One shared advantage of all the studied detectors is that they are small-sized and, therefore, suitable for measurements in steep dose and LET gradients.

Table 3: The mean absolute deviation of the $\overline{\mathrm{LET}}$ determination with passive luminescence detectors relative to the values derived from Monte Carlo simulations across the four irradiation positions in table 1. All experimental $\overline{\mathrm{LET}}_{\mathrm{f}}$ determinations are in agreement with the ones from simulations within the uncertainties.

	Deviation from reference values / %			
Detector	$\overline{\mathrm{LET}}_{\mathrm{f}}^{\mathrm{p}}$	$\overline{\mathrm{LET}}_{\mathrm{f}}^{\mathrm{all}}$	$\overline{\mathrm{LET}}_{\mathrm{d}}^{\mathrm{p}}$	$\overline{\mathrm{LET}}_{\mathrm{d}}^{\mathrm{all}}$
OSLD (Al_2O_3:C)	15	16	18	18
OSLD (Al_2O_3:C,Mg)	15	15	15	17
TLD (SCK)	14	14	40	43
TLD (IFJ)	16	16	36	28
FNTD	11	–	16	–
Mean deviation	14	15	25	26

Whilst the OSLDs and FNTDs determine $\overline{\mathrm{LET}}_{\mathrm{f}}$ and $\overline{\mathrm{LET}}_{\mathrm{d}}$ equally accurate as summarised in table 3 the two TLD groups determine $\overline{\mathrm{LET}}_{\mathrm{f}}$ more accurately than $\overline{\mathrm{LET}}_{\mathrm{d}}$. For FNTDs, it is in principle also possible to measure the fragments. However, the low likelihood of these events to occur in proton beams would require to increase the scanned area several orders of magnitude, increasing the post-processing time significantly.

3.6 RBE estimations

The RBE was calculated using the phenomenological model defined in section 2.3.5 and the experimentally determined $\overline{\mathrm{LET}}_{\mathrm{d}}^{\mathrm{p}}$ values. The results are listed in table 4, where the uncertainty values represent only the effect of propagating the $\overline{\mathrm{LET}}_{\mathrm{d}}^{\mathrm{p}}$ uncertainty in the calculation of the RBE. The RBE determinations from the positions 1a and 2 agree well between the detectors and simulations within the experimental uncertainties propagated through the RBE model.

Table 4: Determination of the RBE for each detector and irradiation position for $(\alpha/\beta)_x$ equal to 2.0 Gy and 10 Gy. The dose D_p was for each position scaled such that the dose to the SOBP region or the maximum of the single energy layer was 1.8 Gy. The RBE was estimated with the $\overline{\text{LET}}_\text{d}$ from protons determined from each detector, and the phenomenological model described in McNamara et al. (2015). The RBE was estimated from the Monte Carlo (MC) simulated values, where the uncertainty is assessed through a 1 mm variation of the position along the central beam axis. The uncertainties represent a coverage factor of $k = 1$.

Plan	$(\alpha/\beta)_x$ / Gy	D_p / Gy	RBE MC	RBE OSLD (Al_2O_3:C)	RBE OSLD (Al_2O_3:C,Mg)	RBE TLD (SCK)	RBE TLD (IFJ)	RBE FNTD
1a	2.0	1.82	1.16 ± 0.01	1.12 ± 0.02	1.11 ± 0.02	1.13 ± 0.04	1.14 ± 0.02	—
1b	2.0	1.73	1.43 ± 0.05	1.43 ± 0.03	1.42 ± 0.05	1.30 ± 0.12	1.30 ± 0.06	1.40 ± 0.05
1c	2.0	1.36	1.62 ± 0.07	1.56 ± 0.02	1.59 ± 0.05	1.43 ± 0.24	1.37 ± 0.05	1.51 ± 0.07
2	2.0	0.55	1.10 ± 0.01	1.12 ± 0.15	1.11 ± 0.01	1.06 ± 0.04	1.07 ± 0.05	1.09 ± 0.01
1a	10.0	1.82	1.07 ± 0.01	1.05 ± 0.01	1.04 ± 0.01	1.05 ± 0.02	1.06 ± 0.01	—
1b	10.0	1.73	1.18 ± 0.02	1.18 ± 0.01	1.18 ± 0.02	1.12 ± 0.05	1.12 ± 0.02	1.17 ± 0.02
1c	10.0	1.36	1.25 ± 0.03	1.22 ± 0.01	1.24 ± 0.02	1.17 ± 0.10	1.14 ± 0.02	1.20 ± 0.03
2	10.0	0.55	1.03 ± 0.00	1.03 ± 0.04	1.03 ± 0.00	1.02 ± 0.01	1.02 ± 0.01	1.02 ± 0.00

The deviation increases for the two points at the distal edge, 1b and 1c, where not only the positioning of the detector is important but also the signal averaging across the detector volume. At the sharp $\overline{\text{LET}}^\text{p}_\text{d}$ gradients relevant to positions 1b and 1c, in particular the FNTDs and thin OSLDs, where the surface was analysed, are in good agreement with the simulations. These results align with a recent study, where FNTDs were demonstrated to be able to assess $\overline{\text{LET}}$ and RBE in clinically relevant helium ion beams (Muñoz et al., 2024).

The agreement between the RBE values derived from the experimentally determined $\overline{\text{LET}}^\text{p}_\text{d}$ values and the ones derived from the independent simulation of the radiation field, confirms that the luminescence detectors can determine $\overline{\text{LET}}$ with sufficient accuracy in proton beams.

3.7 LET averaging challenges

The definition of $\overline{\text{LET}}$ with respect to fluence or dose weighting presents fundamental distinctions. Generally, equivalent values of $\overline{\text{LET}}^\text{all}_\text{f}$ and $\overline{\text{LET}}^\text{p}_\text{f}$ typically yield comparable detector responses. This trend is depicted in figure 2a,c,e for OSLDs and TLDs, where both types of $\overline{\text{LET}}_\text{f}$ are similar across all energies and detector types. This agreement is mainly due to the low fluence of secondary particles heavier than protons combined with low luminescence efficiency for the high-LET secondaries. Specifically, the luminescence efficiency of OSLDs and TLDs generally diminishes with increasing ionization density, here parameterized through $\overline{\text{LET}}$ (Vana et al., 1996; Christensen et al., 2023). Consequently, high-LET secondaries contribute minimally to both the luminescence signal, due to their low luminescence efficiency, and to $\overline{\text{LET}}^\text{all}_\text{f}$ due to their low fluence and thus low weighting in its calculation. This provides the monotonic relationship between the OSLD and TLD responses and both $\overline{\text{LET}}^\text{p}_\text{f}$ and $\overline{\text{LET}}^\text{p}_\text{f}$.

Unlike the case for $\overline{\text{LET}}_\text{f}$, different types of $\overline{\text{LET}}_\text{d}$ may result in very different $\overline{\text{LET}}_\text{d}$ values as illustrated in figure 2b,d. Particularly for proton beams above 200 MeV, the contribution of

high-LET secondaries to $\overline{\mathrm{LET}}_{\mathrm{d}}^{\mathrm{all}}$ becomes significant due to the dose-weighting. However, their contribution to the detector luminescence contrasts the relatively large contribution to $\overline{\mathrm{LET}}_{\mathrm{d}}$ sharply: Instead of proportionally increasing the luminescence signal, the high-LET secondaries exhibit a lower efficiency due to the elevated ionization densities. This phenomenon leads to the separation of the $\overline{\mathrm{LET}}_{\mathrm{d}}$ observable in figure 2b,d, where $\overline{\mathrm{LET}}_{\mathrm{d}}^{\mathrm{all}}$ can take on values up to ten times that of $\overline{\mathrm{LET}}_{\mathrm{d}}^{\mathrm{p}}$ in the entrance region of proton beams above 200 MeV.

Moreover, the $\overline{\mathrm{LET}}_{\mathrm{d}}^{\mathrm{all}}$ calibrations for OSLDs and TLDs in figure 2b,d highlight how the $\overline{\mathrm{LET}}_{\mathrm{d}}^{\mathrm{all}}$ in proton beams above 200 MeV may equal the $\overline{\mathrm{LET}}_{\mathrm{d}}^{\mathrm{all}}$ close to the Bragg peak region, although the detector response is very different. Consequently, the detector response of OSLDs and TLDs cannot be uniquely correlated with $\overline{\mathrm{LET}}_{\mathrm{d}}^{\mathrm{all}}$ in calibration functions, as e.g. an $\overline{\mathrm{LET}}_{\mathrm{d}}^{\mathrm{all}}$ value of 4 keV µm^{-1} is linked to two very different OSLD or TLD responses. Using $\overline{\mathrm{LET}}_{\mathrm{d}}^{\mathrm{all}}$ to describe the radiation quality of a mixed particle field to determine dose corrections for ionization quenching can thus pose challenges: Two distinct detector responses can be associated with the same $\overline{\mathrm{LET}}_{\mathrm{d}}^{\mathrm{all}}$ value, i.e. with the same ionization quenching correction factor, which can result in wrong quenching corrections for dosimetry.

The low contribution to the luminescence from high-LET secondaries, due to their low luminescence efficiency caused by ionization quenching, indicates that the heavy secondaries can be neglected from the calculation of $\overline{\mathrm{LET}}_{\mathrm{d}}$. This indicates that $\overline{\mathrm{LET}}_{\mathrm{d}}^{\mathrm{p}}$ is a better radiation quality metric for the OSLDs and TLDs than $\overline{\mathrm{LET}}_{\mathrm{d}}^{\mathrm{all}}$, which aligns with recommendations for harmonizing $\overline{\mathrm{LET}}_{\mathrm{d}}$ in proton therapy in (Hahn et al., 2022). This observation is consistent with findings from Grün et al. (2019), where $\overline{\mathrm{LET}}_{\mathrm{d}}$ was deemed insufficient as a predictor of RBE in mixed particle fields. Conversely, Resch et al. (2020) concluded, for different definitions of $\overline{\mathrm{LET}}_{\mathrm{d}}$ and $\overline{\mathrm{LET}}_{\mathrm{f}}$ than those investigated here, that the response of radiochromic film is better described through dose-weighting.

However, the necessity of employing an artificial particle filtering, by excluding particles heavier than the primary, for $\overline{\mathrm{LET}}_{\mathrm{d}}$ to effectively describe the luminescence detector response highlights a limitation of $\overline{\mathrm{LET}}_{\mathrm{d}}$, as the heavier secondaries do interact with the detector and contribute to the luminescence.

Furthermore, Kalholm et al. (2023) demonstrated that *in vitro* cell survival in proton therapy was better modeled using radiation quality metrics other than $\overline{\mathrm{LET}}$. Similarly, for the response of OSLDs to light ion beams, neither $\overline{\mathrm{LET}}_{\mathrm{f}}$ nor $\overline{\mathrm{LET}}_{\mathrm{d}}$ were found to provide the most accurate description of the radiation fields (Christensen et al., 2023). These findings collectively suggest that alternative radiation quality metrics or LET-weighting schemes beyond dose or fluence may offer a more precise characterization of mixed particle fields relevant to proton therapy.

Conclusions

This study highlights the potential of passive luminescence detectors for simultaneously assessing dose, $\overline{\text{LET}}$ and RBE in proton therapy. OSLDs and FNTDs were capable of evaluating the four investigated types of $\overline{\text{LET}}$ using a single detector, whereas $\overline{\text{LET}}$ for TLDs was determined through the dose ratio of two TLD types.

Experimental determination of $\overline{\text{LET}}_{\text{f}}$ were in agreement with reference values obtained via Monte Carlo simulations, both for contributions from primary and secondary protons ($\overline{\text{LET}}_{\text{f}}^{\text{p}}$) or considering all charged ions ($\overline{\text{LET}}_{\text{f}}^{\text{all}}$). However, for mixed particle fields, $\overline{\text{LET}}_{\text{d}}$ presents challenges as a radiation quality metric due to the influence of high-LET secondaries. While high-LET secondaries heavily influence $\overline{\text{LET}}_{\text{d}}^{\text{all}}$, their contribution to the luminescence signal is conversely suppressed due to elevated ionization quenching.

For the assessment of radiation quality for dosimetric corrections of ionization quenching in mixed particle fields, corrections are more accurately estimated through $\overline{\text{LET}}_{\text{f}}$ than $\overline{\text{LET}}_{\text{d}}$, unless contributions from secondaries heavier than protons are neglected.

Given their compact size and passive nature, luminescence detectors are well-suited for embedded measurements in phantoms, and in particular anthropomorphic phantoms. This makes them suitable for supporting research in proton therapy dosimetry, or for postal audits, as well as facilitating assessment of $\overline{\text{LET}}$ and RBE,

Data availability

Data repository to be published after acceptance.

CRediT authorship contribution statement

Conceptualization: IDM, OVH, AP, NB, LS, AV, JBC. *Data curation*: All authors. *Formal Analysis*: IDM, OVH, AP, NB, LG, AV, JBC. *Investigation*: All authors. *Methodology*: IDM, OVH, AP, NB, LG, JBC. *Project administration*: NB, LS, AV, JBC. *Resources*: All authors. *Funding acquisition:* IDM, NB, LG, MS, EGY, OJ. *Software*: IDM, OVH, AP, NB, LG, LS, AV, JBC. *Validation*: All authors. *Visualization*: JBC. *Writing—original draft*: IDM, OVH, AP, NB, LG, MS, JBC. *Writing—review and editing*: All authors.

Acknowledgements

The Risø TL/OSL-DA-20 reader (DTU Nutech, Denmark) was acquired with partial support from the Swiss National Science Foundation (R'Equip project 206021_177028). IDM acknowledges funding from the German Academic Exchange Service (DAAD, program number: 57440921). This work was partly supported by the Polish National Science Centre project No. 2021/43/D/ST5/03042. NB acknowledges support of the Novo Nordisk Foundation (grant number NNF195A0059372). We

gratefully acknowledge Poland's high-performance Infrastructure PLGrid ACK Cyfronet AGH for providing computer facilities and support within computational grant no plgccbmc12. The particle transport simulation platfotm yaptide was used to visualise the geometry, handle calculation and presenting the results. The authors would like to thank the staff at the Danish Center for Particle Therapy (DCPT), Aarhus, Denmark, for support throughout the measurements as well as the EURADOS WG9 for organising the measurement campaign.

Bibliography

Agostinelli, S., J. Allison, K. a. Amako, J. Apostolakis, H. Araujo, P. Arce, M. Asai, D. Axen, S. Banerjee, G. Barrand, et al. (2003). GEANT4—a simulation toolkit. *Nuclear instruments and methods in physics research section A: Accelerators, Spectrometers, Detectors and Associated Equipment 506*(3), 250–303.

Ahmed, M. F., S. A. Eller, E. Schnell, S. Ahmad, M. S. Akselrod, O. D. Hanson, and E. G. Yukihara (2014). Development of a 2D dosimetry system based on the optically stimulated luminescence of Al_2O_3. *Radiation Measurements 71*, 187–192.

Almond, P. R., P. J. Biggs, B. M. Coursey, W. F. Hanson, M. Saiful Huq, R. Nath, and D. W. O. Rogers (1999). Report of the AAPM TG-51 oprotocol for clinical reference dosimetry of high-energy photon and electron beams. *Medical physics 26*, 1847–1870.

Bahn, E., J. Bauer, S. Harrabi, K. Herfarth, J. Debus, and M. Alber (2020). Late contrast enhancing brain lesions in proton-treated patients with low-grade glioma: clinical evidence for increased periventricular sensitivity and variable RBE. *International Journal of Radiation Oncology Biology Physics 107*(3), 571–578.

Bassler, N., L. Grzanka, J. B. Christensen, and V. J (2024). Monte Carlo particle transport simulations for the 2022 LET-measurements at DCPT: v1.0.0, .

Bassler, N., J. Toftegaard, A. Lühr, B. S. Sørensen, E. Scifoni, M. Krämer, O. Jäkel, L. S. Mortensen, J. Overgaard, and J. B. Petersen (2014). LET-painting increases tumour control probability in hypoxic tumours. *Acta oncologica 53*(1), 25–32.

Bertolet, A. and A. Carabe (2020). Proton monoenergetic arc therapy (PMAT) to enhance LETd within the target. *Physics in Medicine and Biology 65*(16), 165006.

Bilski, P. (2002). Lithium Fluoride: From LiF:Mg,Ti to LiF:Mg,Cu,P. *Radiation Protection Dosimetry 100*(1-4), 199–205.

Bilski, P. (2006). Dosimetry of densely ionising radiation with three LiF phosphors for space applications. *Radiation Protection Dosimetry 120*(1-4), 397–400.

Bobić, M., J. B. Christensen, H. Lee, E. Choulilitsa, K. Czerska, M. Togno, S. Safai, E. G. Yukihara, B. Winey, A. J. Lomax, H. Paganetti, F. Albertini, and P. Nesteruk (2024). Optically stimulated luminescence dosimeters for simultaneous measurement of point dose and dose-weighted LET in an adaptive proton therapy workflow. *Frontiers in Oncology 13*, 1333039.

Christensen, J. B., I. D. Muñoz, N. Bassler, C. Stengl, L. Bossin, M. Togno, S. Safai, O. Jäkel, and E. G. Yukihara (2023). Optically stimulated luminescence detectors for dosimetry and LET measurements in light ion beams. *Physics in Medicine and Biology 68*(15), 155001.

Christensen, J. B., M. Togno, L. Bossin, O. V. Pakari, S. Safai, and E. G. Yukihara (2022). Improved simultaneous LET and dose measurements in proton therapy. *Scientific Reports 12*(1), 8262.

Christensen, J. B., M. Togno, K. P. Nesteruk, S. Psoroulas, D. Meer, D. C. Weber, T. Lomax, E. G. Yukihara, and S. Safai (2021). Al_2O_3:C optically stimulated luminescence dosimeters (OSLDs) for ultra-high dose rate proton dosimetry. *Physics in Medicine and Biology 66*(8), 085003.

Cortés-Giraldo, M. and A. Carabe (2015). A critical study of different Monte Carlo scoring methods of dose average linear-energy-transfer maps calculated in voxelized geometries irradiated with clinical proton beams. *Physics in Medicine & Biology 60*(7), 2645.

Flint, D. B., D. A. Granville, N. Sahoo, M. McEwen, and G. O. Sawakuchi (2016). Ionization density dependence of the curve shape and ratio of blue to UV emissions of Al_2O_3:C optically stimulated luminescence detectors exposed to 6-MV photon and therapeutic proton beams. *Rad. Meas. 89*, 35–43.

Gieszczyk, W. and P. Bilski (2017). A simplified numerical approach to non-radiation induced high-temperature signals in thermoluminescence. glowview–a useful tool for a multiple glow-curve analysis. *Radiation Measurements 107*, 102–110.

Granville, D. A., N. Sahoo, and G. O. Sawakuchi (2014). Calibration of the Al_2O_3: C optically stimulated luminescence (OSL) signal for linear energy transfer (LET) measurements in therapeutic proton beams. *Physics in Medicine and Biology 59*(15), 4295–4310.

Greilich, S., U. Hahn, M. Kiderlen, C. E. Andersen, and N. Bassler (2014). Efficient calculation of local dose distributions for response modeling in proton and heavier ion beams. *European Physical Journal D 68*(10), 0–4.

Grün, R., T. Friedrich, E. Traneus, and M. Scholz (2019). Is the dose-averaged LET a reliable predictor for the relative biological effectiveness? *Medical physics 46*(2), 1064–1074.

Gueulette, J., H. Blattmann, E. Pedroni, A. Coray, B. M. De Coster, P. Mahy, A. Wambersie, and G. Goitein (2005). Relative biologic effectiveness determination in mouse intestine for scanning

proton beam at Paul Scherrer Institute, Switzerland. Influence of motion. *International Journal of Radiation Oncology Biology Physics 62*(3), 838–845.

Hahn, C., J. Ödén, A. Dasu, A. Vestergaard, M. Fuglsang Jensen, O. Sokol, C. Pardi, F. Bourhaleb, A. Leite, L. de Marzi, et al. (2022). Towards harmonizing clinical linear energy transfer (LET) reporting in proton radiotherapy: a European multi-centric study. *Acta Oncologica 61*(2), 206–214.

Hansen, D. C., A. Lühr, R. Herrmann, N. Sobolevsky, and N. Bassler (2012). Recent improvements in the SHIELD-HIT code. *International Journal of Radiation Biology 88*(1-2), 195–199.

IAEA (2000). *Technical Reports Series No. 398: Absorbed Dose Determination in External Beam Radiotherapy. An International Code of Practice for Dosimetry Based on Standards of Absorbed Dose to Water* . Vienna, Austria: International Atomic Energy Agency.

ICRU (1970). *International Commission on Radiation Units and Measurements Report 16: Linear Energy Transfer*. Bethesda, MD, USA: International Commission on Radiation Units and Measurements.

ICRU (2007). Radiation biology considerations. In International Commission on Radiation Units & Measurements Report 78: Prescribing, recording, and reporting proton-beam therapy. *Journal of ICRU 7*(2), 29–48.

Kalholm, F., L. Grzanka, I. Toma-Dasu, and N. Bassler (2023). Modeling RBE with other quantities than LET significantly improves prediction of in vitro cell survival for proton therapy. *Medical Physics 50*(1), 651–659.

Kalholm, F., L. Grzanka, E. Traneus, and N. Bassler (2021). A systematic review on the usage of averaged LET in radiation biology for particle therapy. *Radiotherapy and Oncology 161*, 211–221.

Klimpki, G., H. Mescher, M. S. Akselrod, O. Jäkel, and S. Greilich (2016). Fluence-based dosimetry of proton and heavier ion beams using single track detectors. *Physics in Medicine and Biology 61*(3), 1021.

Kouwenberg, J. J., L. Ulrich, O. Jäkel, and S. Greilich (2016). A 3d feature point tracking method for ion radiation. *Physics in Medicine and Biology 61*(11), 4088.

McIntyre, M., P. Wilson, P. Gorayski, and E. Bezak (2023). A systematic review of let-guided treatment plan optimisation in proton therapy: Identifying the current state and future needs. *Cancers 15*(17), 4268.

McKeever, S. W. S., M. Moscovitch, and M. P. D. Townsend (1995). *Thermoluminescence dosimetry materials : properties and uses.* Nuclear Technology Pub.

McNamara, A. L., J. Schuemann, and H. Paganetti (2015). A phenomenological relative biological effectiveness (rbe) model for proton therapy based on all published in vitro cell survival data. *Physics in Medicine and Biology 60*(21), 8399.

Mohan, R. (2022). A review of proton therapy–Current status and future directions. *Precision Radiation Oncology 6*(2), 164–176.

Muñoz, I. D., L. N. Burigo, T. Gehrke, S. Brons, S. Greilich, and O. Jäkel (2023). Sensitivity correction of fluorescent nuclear track detectors using alpha particles: Determining let spectra of light ions with enhanced accuracy. *Medical Physics 50*(4), 2385–2401.

Muñoz, I. D., G. D. Calderón, R. F. Bautista, L. N. Burigo, J. B. Christensen, S. Brons, A. Runz, F. Häring, S. Greilich, J. Seco, and O. Jäkel (2024). Linear energy transfer measurements and estimation of relative biological effectiveness in proton and helium-ion beams using fluorescent nuclear track detectors. *Int J Radiat Oncol Biol Phys in press*.

Paganetti, H. (2014). Relative biological effectiveness (RBE) values for proton beam therapy. Variations as a function of biological endpoint, dose, and linear energy transfer. *Physics in Medicine and Biology 59*(22), R419.

Paganetti, H., E. Blakely, A. Carabe-Fernandez, D. J. Carlson, I. J. Das, L. Dong, D. Grosshans, K. D. Held, R. Mohan, V. Moiseenko, et al. (2019). Report of the AAPM TG-256 on the relative biological effectiveness of proton beams in radiation therapy. *Medical physics 46*(3), e53–e78.

Parisi, A., C. J. Beltran, and K. M. Furutani (2023). Variable RBE in proton radiotherapy: a comparative study with the predictive Mayo Clinic Florida microdosimetric kinetic model and phenomenological models of cell survival. *Physics in Medicine & Biology 68*(18), 185020.

Parisi, A., S. Chiriotti, M. De Saint-Hubert, O. Van Hoey, C. Vandevoorde, P. Beukes, E. A. de Kock, J. Symons, J. N. Camero, J. Slabbert, et al. (2019). A novel methodology to assess linear energy transfer and relative biological effectiveness in proton therapy using pairs of differently doped thermoluminescent detectors. *Physics in Medicine and Biology 64*(8), 085005.

Parisi, A., L. de Freitas Nascimento, O. Van Hoey, P. Mégret, H. Kitamura, S. Kodaira, and F. Vanhavere (2018). Low temperature thermoluminescence anomaly of LiF:Mg,Cu,P radiation detectors exposed to ^{1}H and ^{4}He ions. *Radiation Measurements 119*, 155–165.

Parisi, A., P. Olko, J. Swakoń, T. Horwacik, H. Jabłoński, L. Malinowski, T. Nowak, L. Struelens, and F. Vanhavere (2020a). Mitigation of the proton-induced low temperature anomaly of lif:mg,cu,p detectors using a post-irradiation pre-readout thermal protocol. *Radiation Measurements 132*, 106233.

Parisi, A., P. Olko, J. Swakoń, T. Horwacik, H. Jabłoński, L. Malinowski, T. Nowak, L. Struelens, and F. Vanhavere (2020b). Modeling the radiation-induced cell death in a therapeutic

proton beam using thermoluminescent detectors and radiation transport simulations. *Physics in Medicine and Biology 65*(1), 015008.

Parisi, A., O. Van Hoey, P. Mégret, and F. Vanhavere (2017). The influence of the dose assessment method on the LET dependence of the relative luminescence efficiency of LiF:Mg,Ti and LiF:Mg,Cu,P. *Radiation Measurements 98*, 34–40.

Parisi, A., O. Van Hoey, P. Mégret, and F. Vanhavere (2019). Microdosimetric specific energy probability distribution in nanometric targets and its correlation with the efficiency of thermoluminescent detectors exposed to charged particles. *Radiation Measurements 123*, 1–12.

Perl, J., J. Shin, J. Schümann, B. Faddegon, and H. Paganetti (2012). TOPAS: an innovative proton Monte Carlo platform for research and clinical applications. *Med. Phys. 39*(11), 6818–6837.

Petringa, G., L. Pandola, S. Agosteo, R. Catalano, P. Colautti, V. Conte, G. Cuttone, K. Fan, Z. Mei, A. Rosenfeld, et al. (2020). Monte carlo implementation of new algorithms for the evaluation of averaged-dose and-track linear energy transfers in 62 MeV clinical proton beams. *Physics in Medicine and Biology 65*(23), 235043.

Resch, A. F., P. D. Heyes, H. Fuchs, N. Bassler, D. Georg, and H. Palmans (2020). Dose-rather than fluence-averaged LET should be used as a single-parameter descriptor of proton beam quality for radiochromic film dosimetry. *Medical Physics 47*(5), 2289–2299.

Rørvik, E., L. F. Fjæra, T. J. Dahle, J. E. Dale, G. M. Engeseth, C. H. Stokkevåg, S. Thörnqvist, and K. S. Ytre-Hauge (2018). Exploration and application of phenomenological RBE models for proton therapy. *Physics in Medicine and Biology 63*(18), 185013.

Saager, M., P. Peschke, S. Brons, J. Debus, and C. P. Karger (2018). Determination of the proton RBE in the rat spinal cord: Is there an increase towards the end of the spread-out Bragg peak? *Radiotherapy and Oncology 128*(1), 115–120.

Sądel, M., P. Bilski, J. Swakoń, M. Rydygier, T. Horwacik, and A. Weber (2015). Comparative investigations of the relative thermoluminescent efficiency of lif detectors to protons at different proton therapy facilities. *Radiation Measurements 82*, 8–13.

Sawakuchi, G. O., F. A. Ferreira, C. H. McFadden, T. M. Hallacy, D. A. Granville, N. Sahoo, and M. S. Akselrod (2016). Nanoscale measurements of proton tracks using fluorescent nuclear track detectors. *Medical physics 43*(5), 2485–2490.

Sawakuchi, G. O., N. Sahoo, P. B. Gasparian, M. G. Rodriguez, L. Archambault, U. Titt, and E. G. Yukihara (2010). Determination of average LET of therapeutic proton beams using Al_2O_3:C optically stimulated luminescence (OSL) detectors. *Physics in Medicine and Biology 55*(17), 4963.

Swakon, J., P. Olko, D. Adamczyk, T. Cywicka-Jakiel, J. Dabrowska, B. Dulny, L. Grzanka, T. Horwacik, T. Kajdrowicz, B. Michalec, et al. (2010). Facility for proton radiotherapy of eye cancer at IFJ PAN in Krakow. *Radiation Measurements 45*(10), 1469–1471.

Sykora, G., M. Akselrod, E. Benton, and N. Yasuda (2008). Spectroscopic properties of novel fluorescent nuclear track detectors for high and low LET charged particles. *Radiation Measurements 43*(2-6), 422–426.

Unkelbach, J., P. Botas, D. Giantsoudi, B. L. Gorissen, and H. Paganetti (2016). Reoptimization of intensity modulated proton therapy plans based on linear energy transfer. *International Journal of Radiation Oncology* Biology* Physics 96*(5), 1097–1106.

Vana, N., W. Schöner, M. Fugger, and Y. Akatov (1996). Absorbed dose measurement and LET determination with TLDs in space. *Radiation protection dosimetry 66*(1-4), 145–152.

Verkhovtsev, A., L. Zimmer, and S. Greilich (2019). Calibration of intensity spectra from fluorescent nuclear track detectors in clinical ion beams. *Radiation Measurements 121*, 37–41.

Chapter 4 Discussion

With the growing availability of proton-beam therapy (PBT) and ion-beam therapy (IBT), as well as techniques for treatment planning involving linear energy transfer (LET) and relative biological effectiveness (RBE), tools capable of measuring LET and RBE are becoming increasingly relevant. In this thesis, novel methods and techniques for measuring LET and assessing RBE using aluminum oxide doped with carbon and magnesium (Al_2O_3:C,Mg)-based fluorescent nuclear track detectors (FNTDs) and optically stimulated luminescence detectors (OSLDs) have been developed. These tools are intended to be used in the commissioning of computational algorithms such as treatment planning systems (TPSs), to perform quality assurance tasks, or to conduct measurements in research settings.

4.1. Methodological developments

4.1.1. FNTDs sensitivity correction

Since the introduction of Al_2O_3:C,Mg-based FNTDs for dosimetry applications, one of the main challenges in achieving accurate and reproducible measurements has been the variable sensitivity between crystals. One of the major advances resulting from the work performed in this thesis was the development of an experimental approach to determine the sensitivity of single crystals and derive a detector-specific sensitivity correction factor. This correction not only improves the accuracy of LET measurements with FNTDs, but also introduces traceability to a reference set of detectors and readout device. Thus, through a series of cross calibrations, it is possible to relate measurements with FNTDs of different batches and other imaging systems to the reference set of FNTDs and microscope used during the calibration.

Consistent with independent previous works [44, 47, 48], the results presented in Publication I show that FNTDs exhibit large variations in sensitivity between single crystals, with differences of up to a factor of four between the least and most sensitive elements in the studied sets. The results in Publication I also show that, due to their short range in aluminum oxide (Al_2O_3), α-particles can be effectively used to derive a detector-specific sensitivity correction factor without affecting LET measurements in light-ion beams. Additional advantages of using α-particle sources for sensitivity determination are that they are compact, inexpensive, readily available, and highly reproducible.

Sensitivity variations are not exclusive to FNTDs and are also observed with thermoluminescent dosimeters (TLDs) and OSLDs. In fact, the practice of exposing a reference set of detectors to a standard radiation field to determine the sensitivity of individual detectors relative to the reference set has long been used with TLDs and OSLDs [214]. However, returning TLDs and OSLDs to their original unirradiated state is relatively easy through thermal or optical treatment. In contrast, FNTDs require special, high-cost instrumentation, with no guarantee that the crystal response will return to its original state [232]. The use of α-particles and confocal microscopy allows probing of the detector's response in a small subvolume, leaving the rest for the actual measurements without the need to erase the signal from the reference radiation field.

Since radiophotoluminescence (RPL) does not require the crystal to be exposed to ionizing radiation, it is also possible to probe the unexposed FNTDs to determine the concentration of color centers and derive a sensitivity correction. This approach has already been applied to detectors exposed to photon beams by excitation with blue light and detection of the green emission [46]. However, the same color centers can transform differently, so the initial state cannot fully describe the kinematics of the charge carriers within the crystal lattice upon exposure to ionizing radiation. In contrast, the interrogation of transformed color centers after α-particle exposure can better describe the migration of charge carriers and the transformation of color centers induced by heavy charged particles.

The results from the blind test showed that the sensitivity correction increases the accuracy of the predicted track average linear energy transfer (L_F) and dose average linear energy transfer (L_D) for both single- and mixed-ion beams. The better agreement between measurements and theoretical values for L_F than for L_D can be attributed to the asymmetric weight inherent to dose averaging, where a higher weight is given to high-LET tracks. These high-LET tracks are the result of energy straggling and luminescent emission fluctuations causing an apparent higher LET. In all cases, the results show that the sensitivity correction improves the precision and reduces the combined uncertainty of the measured L_F and L_D by a factor of approximately three.

4.1.2. Calibration curve for LET measurements with FNTDs

The results of the FNTDs exposed to monoenergetic protons, ^{4}He-, ^{12}C-, and ^{16}O-ions presented in Publication I are qualitatively consistent with previous studies [43, 44], particularly with those from the same working group in which this thesis was conducted [45, 48]. However, a larger FNTD sample size per energy/ion combination and the use of the sensitivity correction allowed for a better correlation between the fluorescence intensity and LET. At a quantitative level, non-negligible differences were observed between previously published calibration curve fitting parameters and those obtained in this work, even when using the same model and fitting procedure [45]. This change can be attributed in part to FNTD batches having different average sensitivities. However, changes in the response of the confocal microscope cannot be disregarded.

To ensure accurate and reproducible results, potential changes in the readout system were investigated. These changes may occur due to the unavoidable degradation of components or unintended damage. To monitor changes in the response of the laser scanning confocal microscopy (LSCM) system used throughout this thesis, a simple but robust protocol was developed and implemented in the workflow (Appendix B). The protocol involved imaging the same reference FNTD under identical conditions at the beginning of each readout session. This revealed significant changes in the response and, at the same time, enabled the correction of these changes by introducing an intersession correction factor. In fact, this protocol enabled to readily overcome significant changes that occurred during the timeframe of the thesis, such as the replacement of the sample-focusing objective and the laser light source. While the sensitivity correction provides traceability to a reference FNTD set, the intersession correction factor provides temporal traceability to the LSCM system at the time of calibration.

In previous works where the fluorescence intensity was studied as a function of LET, a one-to-one relation between these quantities and across multiple ion species has been assumed [43, 45]. However, this assumption can be attributed to a lack of accurate results masking more subtle effects. The accuracy of the results in Publication I enabled to observe, for the first time, that the fluorescence intensity not only depends on LET but also on the type of particle. This means that using a single calibration curve to model the fluorescence intensity as a

function of LET for multiple ion species is an oversimplification. Such behavior can have significant repercussions on the LET spectra and, consequently, on the values of L_F and L_D if a single calibration curve is applied. However, due to the lack of data in overlapping LET ranges between different ion species, no definitive conclusions could be drawn. This effect was further investigated during the clinical tests with proton and ^{4}He-ion spread-out Bragg peaks (SOBPs).

4.1.3. Calibration curves for LET measurements with OSLDs

The results of OSLDs exposed to monoenergetic protons, ^{4}He-, ^{12}C-, and ^{16}O-ions show differences in the relative efficiency of the UV emission between aluminum oxide doped with carbon (Al_2O_3:C) and Al_2O_3:C,Mg. Contrarily, the relative efficiency of the blue emission is almost identical for both materials. For Al_2O_3:C, the measured relative efficiency as a function of L_D is consistent with previous studies on this material [35]. These results suggest that the blue emission of both Al_2O_3:C and Al_2O_3:C,Mg can only be used for absorbed dose measurements without corrections for optically stimulated luminescence (OSL) quenching in light-ion beams with L_D not exceeding 10 keV µm^{-1}. Corrections are necessary above this value to avoid underestimating the measured absorbed dose.

For both Al_2O_3:C and Al_2O_3:C,Mg, the results show that the blue- to UV-signal ratio is dependent not only on the ionization density metrics Q_{eff}, L_F, and L_D, but also on the type of particle. This type of dependence imposes limitations on the application of the blue- to UV-signal ratio for measuring Q_{eff}, L_F, and L_D in mixed light-ion fields. It is worth noting that the blue- to UV-signal ratio shows less dependence on the particle type when parameterized in terms of Q_{eff} compared to L_F and L_D. The difference in OSL response observed between different types of light-ions with the same LET can be attributed to track structure effects. These effects cause variations in how energy is deposited within the crystal at a microscopic level [233].

In PBT, ions heavier than protons, which can exhibit a high-LET, are generated as a result of nuclear reactions. However, their number relative to that of primary and secondary protons may be sufficiently small to be disregarded, allowing the blue- to UV-signal ratio to be used for assessing the LET in PBT. This assumption finds support in previous studies where Al_2O_3:C was employed to measure L_F and L_D in clinically relevant proton beams [37], as well as in results reported in Publication IV. It should be noted that, in the context of PBT, the impact of secondary ions heavier than protons on the response of solid-state detectors and biological systems is commonly neglected but remains a subject of debate [234, 235].

In IBT, the number of secondary ions resulting from nuclear reactions is often comparable to that of the primary ions [48]. However, the majority of secondary ions have a lower atomic number than the primary ions. In He-ion therapy, most secondary ions correspond to protons and heavier H-ion species [87]. Therefore, it is reasonable to speculate that the blue- to UV-signal ratio can be used to measure the LET in He-ion radiotherapy, as it shows a smaller dependence on the ion type between protons and He-ions compared to heavier ions. In C-ion radiotherapy, mixed ion fields consist mainly of H-ions (including protons) and He-ions, but also a non-negligible proportion of all ions between He and C can be present. Therefore, accurately deriving LET results through the blue-to-UV signal ratio appears to be more challenging due to its strong dependence on the ion type within the range of expected ion species. Further studies are required to establish the reliability of the blue- to UV-signal ratio for LET measurements in IBT.

4.1.4. Integration of RBE models

The primary advantage of FNTDs is their ability to evaluate both the LET spectra and L_D. As a result, FNTDs allow for the calculation of RBE using either a track-by-track approach or directly from L_D. While the track-by-track approach may be considered more complex, as it requires calculation of linear-quadratic model (LQM) α and β parameters before calculating the RBE, it provides the possibility to analyze components associated with different ion species independently and apply specific RBE models for each type of particle. However, in this case, LET-based RBE models for all particle species that could be encountered in the mixed-ion field are required. In contrast, the L_D approach only requires plugging the values directly into the appropriate RBE model. However, because the RBE depends on the type of ion, this approach can lead to inaccurate results. In the case of PBT, the L_D approach may be sufficient if the effect of secondary ions is excluded.

The methods developed in this thesis were applied to four specific RBE models (Table 2.1). However, in principle, any RBE model parameterized in terms of the LET can be used in conjunction with FNTDs. The McNamara- and Wedenberg-RBE models were preferred over others due to their widespread use in TPSs and Monte Carlo simulation analysis routines [236–238]. Additionally, the McNamara model was selected because it is based on a relatively large clonogenic cell survival dataset [86]. The Mairani-RBE models were chosen as they are the only models tailored for He-ions and parameterized in terms of LET [83, 87]. Moreover, all the applied models are based on the LQM formalism, facilitating their simultaneous implementation into the workflow. It is worth noting that the modified microdosimetric kinetic model (mMKM) is also often used in TPSs [196, 239]. Therefore, calculating microdosimetric quantities from FNTD-based LET measurements would be advantageous.

For OSLDs, the absence of spectroscopic LET information implies that only RBE models based on L_F and L_D can be used. As L_D-based methods are frequently employed in computational engines for calculating RBE in PBT [236–238], an experimental approach relying solely on L_D seems appropriate for evaluating the RBE in clinical proton beams. In He-ion therapy, it is preferable to use approaches that rely on spectroscopic information of the ion field due to the contribution of H-ions to the particle fluence. However, previous studies have shown that L_D-based RBE models are capable of accurately predicting the RBE in clinically relevant ^{4}He-ion SOBPs, despite the presence of secondary H-ions [87]. Therefore, if L_D can be assessed with sufficient accuracy with OSLDs, these detectors can be used to predict RBE in He-ion radiotherapy. In C-ion radiotherapy, knowledge of the particle composition of the radiation field is essential for RBE calculations due to the complexity of mixed ion fields [240]. Consequently, the absence of spectroscopic information, combined with the challenge of accurately determining the LET, poses significant obstacles to utilizing the blue- to UV-signal ratio for determining RBE with OSLDs in C-ion radiotherapy. However, dedicated studies are required to determine the applicability of OSLDs for RBE measurements in IBT.

4.2. Clinical tests

4.2.1. LET measurements in clinical proton and ^{4}He-ion beams

In previous studies from the same group where this thesis was conducted, LET spectra for protons, ^{4}He-, and ^{12}C-ions were measured using FNTDs [47, 48]. These studies addressed variations in the sensitivity of FNTDs by employing Monte Carlo simulations. With this approach, a scaling factor is calculated to shift the measured LET spectra so that the position of the peak associated with the primary particles matches that obtained from simulations.

However, this approach has its limitations, as it relies on precise knowledge of the experimental setup and the accuracy of the measurements is inherently dependent on the accuracy of the simulations. Moreover, such corrections are applicable only to specific scenarios, and any alteration in the experimental geometry – whether intentional or unintentional – would render the correction invalid. The accuracy of the LET results presented in Publication III was achieved by using the detector-specific sensitivity correction factor method developed in earlier stages of this thesis (Subsection 4.1.1). One advantage of this methodology for addressing sensitivity variability is that it enables unbiased comparisons between experiments and simulations. Furthermore, this approach has the potential to facilitate the experimental study of LET in more challenging scenarios in future work, such as full treatment plans in anthropomorphic phantoms.

The need for two specific calibration curves to accurately measure the LET in proton and ^{4}He-ion SOBPs strongly supports the hypothesis that the fluorescence intensity depends not only on the LET but also on the type of particle. For the studied beams, this effect increases with the LET of the particles and, therefore, is particularly pronounced at the distal dose-falloff. However, it is possible to take advantage of the FNTDs spectroscopic information to mitigate potential effects due to particle type dependence. Concretely, in a typical LET spectrum the components of each particle type are somewhat isolated due to the rapid increase in the electronic stopping power with the charge of the particles (Figure 2.3(a)). This is in turn reflected in the fluorescence intensity spectra, where clearly defined peaks are observed, each associated with a specific ion type [48]. Therefore, applying the appropriate calibration curve to each component becomes feasible. In fact, such approach was applied to the mixed H/He-ion fields in the studied ^{4}He-ion SOBP (Publication IV). However, a drawback of this approach is the need to establish separate calibration curves for each particle species that may be encountered. Additionally, each of these calibration curves must cover the entire range of possible LET values.

The results obtained from the simulations indicate agreement for L_F but significant differences for L_D between the two implemented scoring methods. The latter, despite applying the same filters to score only particles with atomic numbers equal to or less than the primary particles, as recommended for protons [25]. Overall the differences between both implemented methods were larger for the ^{4}He-ion SOBP. Compared to the particle spectra scoring approach, the method based on scoring the energy deposition generally predicts higher and lower L_D values at the entrance channel and the distal dose-falloff, respectively. These differences can be attributed to two independent factors. First, the particle energy scoring approach relies on updated electronic stopping power data, which differs from that defined internally in the simulation code. Second, the energy deposition is scored in finite volumes, where the particles lose some of their energy, resulting in volumetric averaging. The fact that two commonly applied scoring techniques can render such differences shows the importance of developing suitable experimental devices for the comparison and/or validation of computational tools. However, besides comparing simulations against experimental techniques for their validation, LET scoring techniques must be standardized to improve comparisons of clinical observations between different centers [25].

The LET spectra obtained from FNTDs show good agreement with those obtained from simulations in terms of the position of the maxima. However, there are noticeable differences in their shape. Specifically, the measured LET spectra tend to be wider than the ones obtained from simulations. This difference can be attributed to energy straggling in the scanned thin crystal layers, fluctuations in fluorescence emissions, and the quantum efficiency of the detector that collects the fluorescence light. All of these effects combine to deliver LET values that

may appear to be either lower or higher than their actual values, thereby widening the LET spectra. To reduce the effect of energy straggling, more slices can be acquired at different depths to average over a larger sample of track-spots, at the expense of increasing the imaging time. Another approach would be to increase the pinhole aperture to image thicker slices, but this would also reduce the overall spatial resolution of the images. Rescanning the same area can reduce fluctuations in fluorescence emission and detection, but it also increases imaging times proportionally to the number of rescanning cycles. Spectra covering a wide range of values tend to exhibit more signal noise, which may require scanning a larger area to reduce it, with the drawback of longer imaging times. Therefore, it is advisable to carefully optimize the scanning parameters for each application.

In summary, the results of the clinical tests with proton and ^{4}He-ion SOBPs demonstrate that FNTDs are suitable for LET measurements in clinically relevant proton and He-ion beams. However, it is important to note that the studied beams represent highly idealized scenarios, consisting of single beams with regular shapes. If the complexity of the beam arrangement and/or the phantom geometry are increased, careful consideration of the detector position is essential to avoid tracks with steep angles relative to the FNTDs surface. Additionally, the beam fluences should be appropriately scaled while maintaining the relative weights of the fields to prevent track overlapping in the images. Both angled and overlapping tracks can lead to failures in the track reconstruction algorithm or inaccuracies in the results.

4.2.2. RBE measurements in clinical proton and ^{4}He-ion beams

The trends of the RBE values calculated from the FNTD-based LET measurements are consistent with those obtained from the clonogenic cell survival assays. However, for the proton SOBP, the FNTDs predicted RBE values that were systematically higher than the ones obtained from the cell experiments. This overestimation can be explained by the method used to derive the RBE models. Particularly, the parameters for $\mathrm{RBE}_{\mathrm{max}}$ and $\mathrm{RBE}_{\mathrm{min}}$ (Equation 2.19) in the models were obtained through best fitting techniques to sets of cell survival data for a wide variety of cell lines from different laboratories, which are characterized by high dispersion [85, 86]. Therefore, due to biological and lab-to-lab variabilities, it cannot be expected that experiments with single cell lines will exactly match the model predictions. Overall, there was good numerical agreement between the RBE values predicted by the FNTDs and those derived from the clonogenic cell survival assays for the ^{4}He-ion SOBP. However, an exception occurred at the distal dose-falloff, where the RBE was underestimated by the FNTDs by a factor of almost 0.8. The RBE results for the ^{4}He-ion SOBP are consistent with previous reports for the same cell line [83, 87]. The better correlation of the RBE between FNTDs and cells for the ^{4}He-ion SOBP than for the proton SOBP can be attributed to data used to derive the parameters for $\mathrm{RBE}_{\mathrm{max}}$ and $\mathrm{RBE}_{\mathrm{min}}$ in the applied model. Specifically, the derivation of these parameters relied on a relatively large dataset for A549 cells [83, 87], which is the same cell line used in this work for *in-vitro* validation.

To decouple the biological variability and further examine the RBE predictive capabilities of FNTDs, *in-silico* experiments were conducted. The RBE obtained from simulations showed remarkable quantitative consistency with the values obtained from the FNTDs. This supports the hypothesis that the discrepancies between clonogenic cell survival assays and FNTDs can be mostly attributed to biological variabilities. Additionally, this confirms that FNTDs are suitable for validating computational tools for RBE calculations in proton and He-ion beams. It is important to note that the relative differences between simulations and FNTDs in terms of RBE are lower than those for L_F and L_D. This is attributed to the robust stability of the RBE models in response to variations in the input LET quantities.

For both protons and He-ions, the LET spectra and L_D approaches resulted in nearly identical RBE values, except for the distal dose-falloff in the ^{4}He-ion SOBP. In the latter scenario, the L_D-based method yielded a higher RBE, which seems to be reasonable given that utilizing L_D overlooks the distinct contributions of H- and He-ions to the RBE. Based on these findings, the L_D approach appears to be adequate for protons across the entire range of potential RBE values. Additionally, this approach is simpler to implement and its computational cost is lower, when compared to the LET spectra approach. However, for He-ions, LET spectroscopic information may be necessary to accurately determine the RBE in regions characterized by a high mixture of H- and He-ions.

In the final step, the RBE-weighted doses obtained experimentally from the FNTD-based RBE values and ionization chamber dose measurements were compared against simulations. This scenario resembles what could be done in a clinical validation. Notably, the differences were below 0.1 Gy for a prescribed RBE-weighted dose of 2.0 Gy at the SOBP (assuming a constant RBE of 1.1 and 1.3 for protons and He-ions, respectively) at all studied positions along the proton and ^{4}He-ion SOBPs. These results confirm that FNTDs are a suitable tool for experimental validation of RBE-weighted dose distributions. However, further studies are required to investigate more complex scenarios, as is the case with LET.

4.2.3. Luminescent detectors comparison study

The comparison study reveals that all of the examined detectors have the potential to measure L_F and L_D in PBT. In all cases, the agreement between experiments and simulations was better for L_F than for L_D, irrespective of the detector type. It is worth noting that all detectors underestimated L_D at the distal falloff. For FNTDs, this is consistent with the results reported in Publication III and discussed in the previous subsection. When comparing with the simulations and considering both L_F and L_D, FNTDs provide the most accurate results, followed by Al_2O_3:C,Mg OSLDs. This supports the initial motivation to investigate Al_2O_3:C,Mg-based FNTDs and OSLDs.

TLDs and OSLDs offer the advantage of being capable to measure both LET and absorbed dose [32, 37]. However, for dose measurements, LET-dependent correction factors are necessary to correct for the quenching of luminescent signals due to increased ionization density. To obtain LET with TLDs in the comparison study, pairs of differently doped materials were used. Therefore, with this approach, two detectors must be exposed to accurately measure the absorbed dose [32]. On the other hand, OSLDs can measure LET and absorbed dose simultaneously with a single detector [37]. In principle, FNTDs can be used to measure the absorbed dose from the LET spectra [45]. However, this approach can only be used to measure doses several orders of magnitude lower than those used clinically due to track overlapping. Additionally, the precision of absorbed dose measurements with FNTDs is dependent on the precision of the LET-spectra.

The impact of ions heavier than protons, which can be generated by nuclear reactions in PBT, on L_F and L_D was investigated through Monte Carlo simulations. For this, both only protons and all ions including protons were considered in the calculation of L_F and L_D. The results indicate that L_F is nearly insensitive to nuclear fragments, while a significant increase in L_D was observed. This increase, consistent with nucleus-to-nucleus cross sections [241], was particularly pronounced at the entrance channel and decreased towards the protons end of range. L_D exhibits a greater sensitivity to the inclusion of heavier ions due to the quadratic increase with LET (Equation 2.14). The results show that TLDs and OSLDs can be used to measure L_F and L_D in PBT when considering only protons, as well as protons and all secondary heavier ions. However, specifically tailored calibration curves are necessary. Al-

though FNTDs have the potential to measure all ions that interact with the detector, the probability of detecting nuclear fragments in proton beams is low due to the small volumes that are imaged coupled with the low number of nuclear fragments relative to the number of protons. Therefore, for all practical purposes, it can be assumed that L_F and L_D measured with FNTDs correspond to that of only protons.

To estimate the RBE at the measurement positions, the L_D results obtained from all the studied detectors were used as input in the McNamara-RBE model. Despite the differences in L_D, the RBE values obtained from all detectors showed good agreement with each other, as well as with the simulations. This once again demonstrates the low sensitivity of the RBE model to variations in L_D. The calculations, assuming an α/β-ratio of 10 Gy for X-rays, yielded results consistent with the RBE values obtained from FNTDs exposed in the proton SOBP presented in Publication III, where the α/β-ratio for X-rays was (9.3 $\pm$ 1.1) Gy. However, the RBE values obtained using the L_D measured with all detectors used in the comparison study are systematically smaller than those observed in the *in-vitro* experiments reported in Publication III and previous studies with Chinese hamster ovary (CHO) cells (α/β-ratio of (11.5 $\pm$ 1.5) Gy for X-rays) [32].

Chapter 5 Summary and conclusions

In this thesis, novel methods for assessing linear energy transfer (LET) and relative biological effectiveness (RBE) in proton-beam therapy (PBT) and ion-beam therapy (IBT) using aluminum oxide doped with carbon and magnesium (Al_2O_3:C,Mg)-based fluorescent nuclear track detectors (FNTDs) and optically stimulated luminescence detectors (OSLDs) have been developed. These methods were tested in simplified clinical scenarios relevant to PBT and IBT, and systematically validated through *in-silico* and *in-vitro* techniques.

To enhance the accuracy and precision of LET measurements using FNTDs, a novel approach to derive a detector-specific sensitivity correction factor was developed. This method involves exposing the FNTDs to α-particles to indirectly assess the sensitivity of each crystal relative to a reference set. The results demonstrate that this correction results in a significant improvement in the accuracy and precision of the LET measurements utilizing FNTDs. Furthermore, the sensitivity correction establishes traceability to the reference set of detectors and the imaging system. With a reliable means to account for variable sensitivities, a calibration curve relating the fluorescence intensity of single light-ion tracks to the LET was established. This calibration is intended to measure LET spectra in unknown light-ion fields.

Motivated by previous research involving aluminum oxide doped with carbon (Al_2O_3:C) OSLDs, the feasibility of using Al_2O_3:C,Mg-based OSLDs for measuring LET and absorbed dose in PBT and IBT was explored. The results demonstrate that the blue- to UV-signal ratio of Al_2O_3:C,Mg can be correlated with both the track average linear energy transfer (L_F) and dose average linear energy transfer (L_D). Exploiting this relationship, calibration curves for measuring L_F and L_D in unknown light-ion fields were established. Additionally, the results indicate that the so-called Q_{eff} factor can serve as an ionization density descriptor, with the added advantage of reducing the dependence of the blue- to UV-signal ratio on the particle type. For Al_2O_3:C,Mg, both the blue- and UV-signals can be used to measure the absorbed dose. However, comparisons with ionization chamber measurements indicate that the UV-signal can provide more accurate results.

To investigate the capabilities of FNTDs in assessing both LET and RBE in clinically relevant scenarios, FNTDs were exposed to proton and ^{4}He-ion spread-out Bragg peaks (SOBPs) at various depths within a solid water phantom. The LET spectra, L_F, and L_D measured with FNTDs were compared with dedicated Monte Carlo simulations. When particle-specific calibration curves were applied to the FNTDs, an overall good agreement was found between measurements and simulations. To assess the RBE from the LET measurements, RBE models for protons and He-ions parameterized in terms of LET were integrated into the FNTD data analysis workflow. For both protons and He-ions, approaches based on LET spectra and L_D were implemented. The RBE values obtained from FNTDs were validated by comparison with clonogenic cell survival assays for a single cell line and Monte Carlo simulations. For consistency, in the latter case, the same models used with FNTDs were applied. The results demonstrate that FNTDs are suitable for assessing the RBE in proton and ^{4}He-ion clinical beams, which can be utilized to evaluate the RBE-weighted dose. The developed methods have the potential to facilitate future studies investigating more complex geometries and beam arrangements. Following a similar approach as the one developed, methods to

derive microdosimetric quantities using FNTDs have the potential to allow the integration of microdosimetric-based RBE models.

The comparison study represents the first dedicated effort to systematically evaluate different luminescent detectors with already proven capabilities to measure LET in proton beams under identical experimental conditions. This study demonstrated that FNTDs, OSLDs, and thermoluminescent dosimeters (TLDs) are potentially good candidates for L_F and L_D measurements in PBT. An additional advantage of OSLDs and TLDs is their capability to measure absorbed dose. However, for all studied detectors, enhanced techniques or calibration protocols may further improve their accuracy for LET measurements. The latter is particularly true for L_D at regions characterized by high-LET particles, such as the distal dose-falloff, where the largest deviations from Monte Carlo reference data were found.

Both FNTDs and OSLDs possess favorable characteristics for assessing LET and RBE in PBT and IBT. Both types of detectors are small-sized, which helps mitigate volume effects when measuring in regions characterized by steep LET gradients and prevents significant perturbations in the radiation fields that could lead to inaccurate results. Additionally, both FNTDs and OSLDs are capable of measuring the LET over a range that covers all possible values of both primary and secondary ions. In the case of FNTDs, the ability to derive LET spectroscopic information can be considered notable within the context of passive-luminescent detectors, and provides the means for handling mixed-ion fields. However, typical FNTD workflows can be labor-intensive and time-consuming. In contrast, measuring the LET in mixed-ion fields with OSLDs can be challenging due to the dependence of the blue- to UV-signal ratio on the type of particle. Nevertheless, fully automated end-to-end workflows for OSLDs, better suited for routine clinical applications, have been developed. Regardless of the detector type, standardized and robust protocols, as well as solid traceability chains, must be developed prior to routine clinical applications to ensure consistent and reproducible results.

Appendices

A. Specifications of the readout systems

Tables A.1 and A.2 respectively list the specifications and parameters of the devices used for imaging fluorescent nuclear track detectors (FNTDs) and for the readout of optically stimulated luminescence detectors (OSLDs) throughout this thesis.

Table A.1.: Details of the laser scanning confocal microscopy (LSCM) system for imaging fluorescent nuclear track detectors (FNTDs).

Characteristics	**Technical Details**
Manufacturer	Carl Zeiss Microscopy GmbH (Jena, Germany)
Model	LSM-710 equiped with the ConfoCor-3 module
Detector	Pixel wise avalanche photodiode in Geiger mode
Excitation source	HeNe laser (red, 633 nm wavelength)
Objective	Plan Apochromat 63x/1.4 Oil DIC M27
Beam splitter	Main dichroic beam splitter 488/562/633
Emission filter	Low-pass filter 655
Dwelling time	40.63 µs
Imaging area	135 µm × 135 µm (1280 × 1280 pixels)

Table A.2.: Details of the system for the readout of optically stimulated luminescence detectors (OSLDs).

Characteristics	**Technical Details**
Manufacturer	Technical University of Denmark Nutech (Roskilde, Denmark)
Model	Risø Reader (TL/OSL-DA-20)
Detector	Photomultiplier tube (PMD9107Q-AP-TTL)
Excitation source	Light emission diode (green, 525 nm wavelength)
Emission filter	UV band-pass filter (Hoya U-340)
Stimulation mode	Pulsed
Pulse duration	100 µs stimulation followed by 100 µs quiescence
Total readout time	300 s

B. Intersession correction factor

A daily quality assurance protocol was established to ensure the proper functioning of the laser scanning confocal microscopy (LSCM) system and to monitor its performance during all readout sessions. A single FNTD, previously exposed to α-particles from a ^{244}Cm radioactive source, served as the reference sample. This FNTD was irradiated using the same experimental setup as described in Publication I (Section 3.5). At the beginning of each readout session, the FNTD was imaged at least seven consecutive times, with 15-minute intervals between acquisitions. The initial four scans aimed to stabilize the system, particularly the laser-light source. Careful attention was given to consistently scan the same region of the FNTD to mitigate coloration-related luminescence variations. A well-known constellation of α-particle track spots, which was established in the initial stages of the investigation, served as a visual

reference for this purpose (Figure B.1(a)). It is worth noting that a relatively low laser power of 5 % was utilized to image the reference FNTD to prevent sample bleaching, which would render the correction ineffective. The last three readouts in a given readout session were utilized to determine the average fluorescence intensity for that specific session (I_d). A baseline average fluorescence intensity (I_B) was established during 10 dedicated readout sessions taking place after servicing the microscope, including the replacement of the focusing objective. To account for any variations between readout sessions, an intersession correction factor (k_d) was introduced. This correction was calculated for each readout session, as follows:

$$k_\mathrm{d} = \frac{I_\mathrm{B}}{I_\mathrm{d}}. \tag{B.1}$$

Figure B.1(b) displays an excerpt of the inverse of k_d obtained from November 2020 to July 2021. The complete dataset comprises over 90 readout sessions, continuing until March 2023. It is evident that around April and May 2021, the response of the imaging system began to consistently decrease. Upon investigation, a leakage of immersion oil was discovered in the focusing objective, resulting in oil accumulation and light attenuation. After replacing the defective objective and giving general service to the microscope, the relative response increased by over 40 %. These results underscore the importance of monitoring the readout system. Even under regular conditions, variations of up to 10 % were detected. However, these variations were effectively corrected in the measurements using k_d. Beyond ensuring accurate results, the intersession correction factor provides traceability to the moment when the FNTD calibration curve for linear energy transfer (LET) measurements was established, as well as facilitating cross-calibration between independent systems.

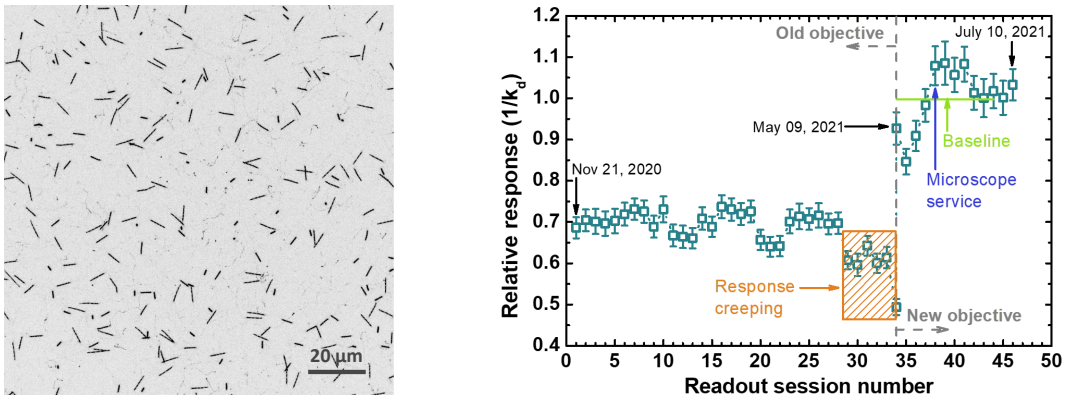

(a) Reference FNTD

(b) Microscope response

Figure B.1.: (a) Maximum fluorescence intensity projection image (1280 pixels × 1280 pixels) of the reference fluorescent nuclear track detector (FNTD) exposed to ^{244}Cm α-particles. **(b)** Inverse of the intersession correction factor (k_d) as a function of the session number. The gray dashed vertical line indicates the moment when the focusing objective was replaced, with arrows pointing towards the before and after of this event. The hatched box indicates the sessions where the relative response decreased and the malfunction was detected. The green horizontal line spans the sessions after the general service, when the baseline response was established. Reference dates are shown in black.

Bibliography

[1] H. Sung, J. Ferlay, R. L. Siegel, M. Laversanne, I. Soerjomataram, A. Jemal, and F. Bray. Global cancer statistics 2020: GLOBOCAN estimates of incidence and mortality worldwide for 36 cancers in 185 countries, *CA: a cancer journal for clinicians*; 71-3 (2021), 209–249. DOI: https://doi.org/10.3322/caac.21660.

[2] G. Delaney, S. Jacob, C. Featherstone, and M. Barton. The role of radiotherapy in cancer treatment: estimating optimal utilization from a review of evidence-based clinical guidelines, *Cancer: Interdisciplinary International Journal of the American Cancer Society*; 104-6 (2005), 1129–1137. DOI: https://doi.org/10.1002/cncr.21324.

[3] P. P. Connell and S. Hellman. Advances in radiotherapy and implications for the next century: a historical perspective, *Cancer research*; 69-2 (2009), 383–392. DOI: https://doi.org/10.1158/0008-5472.CAN-07-6871.

[4] International Atomic Energy Agency (IAEA) & International Commission on Radiation Units and Measurements (ICRU). Relative biological effectiveness in ion beam therapy. Technical Reports Series No. 461. Vienna, Austria: International Atomic Energy Agency, 2008.

[5] C. Grau, M. Durante, D. Georg, J. A. Langendijk, and D. C. Weber. Particle therapy in Europe, *Molecular oncology*; 14-7 (2020), 1492–1499. DOI: https://doi.org/10.1002/1878-0261.12677.

[6] O. Jäkel. Physical advantages of particles: protons and light ions, *The British journal of radiology*; 93-1107 (2020), 20190428. DOI: https://doi.org/10.1259/bjr.20190428.

[7] H. Paganetti. Relative biological effectiveness (RBE) values for proton beam therapy. Variations as a function of biological endpoint, dose, and linear energy transfer, *Physics in Medicine & Biology*; 59-22 (2014), R419. DOI: https://doi.org/10.1088/0031-9155/59/22/R419.

[8] Y. Furusawa, K. Fukutsu, M. Aoki, H. Itsukaichi, K. Eguchi-Kasai, H. Ohara, F. Yatagai, T. Kanai, and K. Ando. Inactivation of aerobic and hypoxic cells from three different cell lines by accelerated ^{3}He-, ^{12}C- and ^{20}Ne-ion beams, *Radiation Research*; 154-5 (2000), 485–496. DOI: https://doi.org/10.1667/0033-7587(2000)154[0485:ioaahc]2.0.co;2.

[9] Particle Therapy Cooperative Group (PTCOG). *Particle therapy facilities in clinical operation*. Retrieved February 25, 2024. n.d. https://ptcog.site/index.php/facilities-in-operation-public.

[10] E. J. Hall and A. J. Giaccia. Radiobiology for the radiologist. 7th. Philadelphia PA, USA: Lippincott Williams & Wilkins, 2012.

[11] H. Nikjoo and L. Lindborg. RBE of low energy electrons and photons, *Physics in Medicine & Biology*; 55-10 (2010), R65. DOI: https://doi.org/10.1088/0031-9155/55/10/R01.

[12] M. Krämer and M. Scholz. Treatment planning for heavy-ion radiotherapy: calculation and optimization of biologically effective dose, *Physics in Medicine & Biology*; 45-11 (2000), 3319. DOI: https://doi.org/10.1088/0031-9155/45/11/314.

[13] N. Bassler, O. Jäkel, C. S. Søndergaard, and J. B. Petersen. Dose-and LET-painting with particle therapy, *Acta oncologica*; 49-7 (2010), 1170–1176. DOI: https://doi.org/10.3109/0284186X.2010.510640.

[14] C. Grassberger, A. Trofimov, A. Lomax, and H. Paganetti. Variations in linear energy transfer within clinical proton therapy fields and the potential for biological treatment planning, *International Journal of Radiation Oncology* Biology* Physics*; 80-5 (2011), 1559–1566. DOI: https://doi.org/10.1016/j.ijrobp.2010.10.027.

[15] D. Giantsoudi, C. Grassberger, D. Craft, A. Niemierko, A. Trofimov, and H. Paganetti. Linear energy transfer-guided optimization in intensity modulated proton therapy: feasibility study and clinical potential, *International Journal of Radiation Oncology* Biology* Physics*; 87-1 (2013), 216–222. DOI: https://doi.org/10.1016/j.ijrobp.2013.05.013.

[16] M. Fager, I. Toma-Dasu, M. Kirk, D. Dolney, E. S. Diffenderfer, N. Vapiwala, and A. Carabe. Linear energy transfer painting with proton therapy: a means of reducing radiation doses with equivalent clinical effectiveness, *International Journal of Radiation Oncology* Biology* Physics*; 91-5 (2015), 1057–1064. DOI: https://doi.org/10.1016/j.ijrobp.2014.12.049.

[17] B. Kopp, M. Fuglsang Jensen, S. Mein, L. Hoffmann, H. Nyström, M. Falk, T. Haberer, A. Abdollahi, J. Debus, and A. Mairani. FRoG: An independent dose and LETd prediction tool for proton therapy at ProBeam® facilities, *Medical Physics*; 47-10 (2020), 5274–5286. DOI: https://doi.org/10.1002/mp.14417.

[18] S. Mein, T. Tessonnier, B. Kopp, C. Schömers, S. Harrabi, A. Abdollahi, J. Debus, T. Haberer, and A. Mairani. Biological dose optimization for particle arc therapy using helium and carbon ions, *International Journal of Radiation Oncology* Biology* Physics*; 114-2 (2022), 334–348. DOI: https://doi.org/10.1016/j.ijrobp.2022.04.025.

[19] H. Paganetti, E. Blakely, A. Carabe-Fernandez, D. J. Carlson, I. J. Das, L. Dong, D. Grosshans, K. D. Held, R. Mohan, V. Moiseenko, *et al.* Report of the AAPM TG-256 on the relative biological effectiveness of proton beams in radiation therapy, *Medical physics*; 46-3 (2019), e53–e78. DOI: https://doi.org/10.1002/mp.13390.

[20] Y. An, J. Shan, S. H. Patel, W. Wong, S. E. Schild, X. Ding, M. Bues, and W. Liu. Robust intensity-modulated proton therapy to reduce high linear energy transfer in organs at risk, *Medical physics*; 44-12 (2017), 6138–6147. DOI: https://doi.org/10.1002/mp.12610.

[21] A. Bertolet and A. Carabe. Proton monoenergetic arc therapy (PMAT) to enhance LETd within the target, *Physics in Medicine & Biology*; 65-16 (2020), 165006. DOI: https://doi.org/10.1088/1361-6560/ab9455.

[22] L. Heuchel, C. Hahn, J. Pawelke, B. S. Sørensen, M. Dosanjh, and A. Lühr. Clinical use and future requirements of relative biological effectiveness: Survey among all European proton therapy centres, *Radiotherapy and Oncology*; 172 (2022), 134–139. DOI: https://doi.org/10.1016/j.radonc.2022.05.015.

[23] D. A. Granville and G. O. Sawakuchi. Comparison of linear energy transfer scoring techniques in Monte Carlo simulations of proton beams, *Physics in Medicine & Biology*; 60-14 (2015), N283. DOI: https://doi.org/10.1088/0031-9155/60/14/N283.

[24] W. Y. C. Koh, H. Q. Tan, K. W. Ang, S. Y. Park, W. S. Lew, and J. C. L. Lee. Standardizing Monte Carlo simulation parameters for a reproducible dose-averaged linear energy transfer, *The British Journal of Radiology*; 93-1112 (2020), 20200122. DOI: https://doi.org/10.1259/bjr.20200122.

[25] C. Hahn, J. Ödén, A. Dasu, A. Vestergaard, M. Fuglsang Jensen, O. Sokol, C. Pardi, F. Bourhaleb, A. Leite, L. de Marzi, *et al.* Towards harmonizing clinical linear energy transfer (LET) reporting in proton radiotherapy: a European multi-centric study, *Acta Oncologica*; 61-2 (2022), 206–214. DOI: https://doi.org/10.1080/0284186X.2021.1992007.

[26] M. Desrosiers, L. DeWerd, J. Deye, P. Lindsay, M. K. Murphy, M. Mitch, F. Macchiarini, S. Stojadinovic, and H. Stone. The importance of dosimetry standardization in radiobiology, *Journal of research of the National Institute of Standards and Technology*; 118 (2013), 403. DOI: http://dx.doi.org/10.6028/jres.118.021.

[27] M. Hajek, T. Berger, R. Bergmann, N. Vana, Y. Uchihori, N. Yasuda, and H. Kitamura. LET dependence of thermoluminescent efficiency and peak height ratio of CaF_2:Tm, *Radiation Measurements*; 43-2-6 (2008), 1135–1139. DOI: https://doi.org/10.1016/j.radmeas.2007.12.015.

[28] G. Massillon-JL, I. Gamboa-deBuen, and M. E. Brandan. TL response of LiF:Mg,Ti exposed to intermediate energy ^{1}H, ^{3}He, ^{12}C, ^{16}O and ^{20}Ne ions, *Journal of Physics D: Applied Physics*; 40-8 (2007), 2584. DOI: https://doi.org/10.1088/0022-3727/40/8/025.

[29] P. Bilski. On the correctness of the thermoluminescent high-temperature ratio (HTR) method for estimating ionization density effects in mixed radiation fields, *Radiation Measurements*; 45-1 (2010), 42–50. DOI: https://doi.org/10.1016/j.radmeas.2009.11.006.

[30] T. Berger and M. Hajek. TL-efficiency—overview and experimental results over the years, *Radiation Measurements*; 43-2-6 (2008), 146–156. DOI: https://doi.org/10.1016/j.radmeas.2007.10.029.

[31] P. Bilski. Dosimetry of densely ionising radiation with three LiF phosphors for space applications, *Radiation protection dosimetry*; 120-1-4 (2006), 397–400. DOI: https://doi.org/10.1093/rpd/nci674.

[32] A. Parisi, S. Chiriotti, M. De Saint-Hubert, O. Van Hoey, C. Vandevoorde, P. Beukes, E. A. de Kock, J. Symons, J. N. Camero, J. Slabbert, *et al.* A novel methodology to assess linear energy transfer and relative biological effectiveness in proton therapy using pairs of differently doped thermoluminescent detectors, *Physics in Medicine & Biology*; 64-8 (2019), 085005. DOI: https://doi.org/10.1088/1361-6560/aaff20.

[33] G. O. Sawakuchi, N. Sahoo, P. B. R. Gasparian, M. G. Rodriguez, L. Archambault, U. Titt, and E. G. Yukihara. Determination of average LET of therapeutic proton beams using Al_2O_3:C optically stimulated luminescence (OSL) detectors, *Physics in Medicine & Biology*; 55-17 (2010), 4963. DOI: https://doi.org/10.1088/0031-9155/55/17/006.

[34] D. A. Granville, N. Sahoo, and G. O. Sawakuchi. Calibration of the Al_2O_3:C optically stimulated luminescence (OSL) signal for linear energy transfer (LET) measurements in therapeutic proton beams, *Physics in Medicine & Biology*; 59-15 (2014), 4295. DOI: https://doi.org/10.1088/1361-6560/acdfb0.

[35] E. G. Yukihara, B. A. Doull, M. Ahmed, S. Brons, T. Tessonnier, O. Jäkel, and S. Greilich. Time-resolved optically stimulated luminescence of Al_2O_3:C for ion beam therapy dosimetry, *Physics in Medicine & Biology*; 60-17 (2015), 6613. DOI: https://doi.org/10.1088/0031-9155/60/17/6613.

[36] J. B. Christensen, I. D. Muñoz, N. Bassler, C. Stengl, L. Bossin, M. Togno, S. Safai, O. Jäkel, and E. G. Yukihara. Optically stimulated luminescence detectors for dosimetry and LET measurements in light ion beams, *Physics in Medicine & Biology*; 68-15 (2023), 155001. DOI: http://dx.doi.org/10.1088/1361-6560/acdfb0.

[37] J. B. Christensen, M. Togno, L. Bossin, O. V. Pakari, S. Safai, and E. G. Yukihara. Improved simultaneous LET and dose measurements in proton therapy, *Scientific Reports*; 12-1 (2022), 8262. DOI: https://doi.org/10.1038/s41598-022-10575-4.

[38] Y. Miyamoto, H. Nanto, T. Kurobori, Y. Fujimoto, T. Yanagida, J. Ueda, S. Tanabe, and T. Yamamoto. RPL in alpha particle irradiated Ag^{+}-doped phosphate glass, *Radiation Measurements*; 71 (2014), 529–532. DOI: https://doi.org/10.1016/j.radmeas.2014.08.007.

[39] M. S. Akselrod, R. C. Yoder, and G. M. Akselrod. Confocal fluorescent imaging of tracks from heavy charged particles utilising new Al_2O_3:C,Mg crystals, *Radiation protection dosimetry*; 119-1-4 (2006), 357–362. DOI: https://doi.org/10.1093/rpd/nci664.

[40] S. Greilich, J. M. Osinga, M. Niklas, F. M. Lauer, G. Klimpki, F. Bestvater, J. A. Bartz, M. S. Akselrod, and O. Jäkel. Fluorescent nuclear track detectors as a tool for ion-beam therapy research, *Radiation Measurements*; 56 (2013), 267–272. DOI: https://doi.org/10.1016/j.radmeas.2013.01.033.

[41] M. Niklas, M. Henrich, O. Jäkel, J. Engelhardt, A. Abdollahi, and S. Greilich. STED microscopy visualizes energy deposition of single ions in a solid-state detector beyond diffraction limit, *Physics in Medicine & Biology*; 62-9 (2017), N180. DOI: https://doi.org/10.1088/1361-6560/aa5edc.

[42] D. W. M. Walsh, H. Liew, J. Schlegel, A. Mairani, A. Abdollahi, and M. Niklas. Carbon ion dosimetry on a fluorescent nuclear track detector using widefield microscopy, *Physics in Medicine & Biology*; 65-21 (2020), 21NT02. DOI: https://doi.org/10.1088/1361-6560/abb7c5.

[43] G. J. Sykora, M. S. Akselrod, E. R. Benton, and N. Yasuda. Spectroscopic properties of novel fluorescent nuclear track detectors for high and low LET charged particles, *Radiation Measurements*; 43-2-6 (2008), 422–426. DOI: https://doi.org/10.1016/j.radmeas.2007.11.009.

[44] G. O. Sawakuchi, F. A. Ferreira, C. H. McFadden, T. M. Hallacy, D. A. Granville, N. Sahoo, and M. S. Akselrod. Nanoscale measurements of proton tracks using fluorescent nuclear track detectors, *Medical physics*; 43-5 (2016), 2485–2490. DOI: https://doi.org/10.1118/1.4947128.

[45] G. Klimpki, H. Mescher, M. S. Akselrod, O. Jäkel, and S. Greilich. Fluence-based dosimetry of proton and heavier ion beams using single track detectors, *Physics in Medicine & Biology*; 61-3 (2016), 1021. DOI: https://doi.org/10.1088/0031-9155/61/3/1021.

[46] M. S. Akselrod, V. V. Fomenko, J. A. Bartz, and F. Ding. FNTD radiation dosimetry system enhanced with dual-color wide-field imaging, *Radiation measurements*; 71 (2014), 166–173. DOI: https://doi.org/10.1016/j.radmeas.2014.05.026.

[47] S. Rahmanian, M. Niklas, A. Abdollahi, O. Jäkel, and S. Greilich. Application of fluorescent nuclear track detectors for cellular dosimetry, *Physics in Medicine & Biology*; 62-7 (2017), 2719. DOI: https://doi.org/10.1088/1361-6560/aa56b4.

[48] A. Verkhovtsev, L. Zimmer, and S. Greilich. Calibration of intensity spectra from fluorescent nuclear track detectors in clinical ion beams, *Radiation Measurements*; 121 (2019), 37–41. DOI: https://doi.org/10.1016/j.radmeas.2018.12.006.

[49] M. Niklas, A. Abdollahi, M. S. Akselrod, J. Debus, O. Jäkel, and S. Greilich. Subcellular spatial correlation of particle traversal and biological response in clinical ion beams, *International Journal of Radiation Oncology* Biology* Physics*; 87-5 (2013), 1141–1147. DOI: https://doi.org/10.1016/j.ijrobp.2013.08.043.

[50] C. H. McFadden, S. Rahmanian, D. B. Flint, S. J. Bright, D. S. Yoon, D. J. O'Brien, A. Asaithamby, A. Abdollahi, S. Greilich, and G. O. Sawakuchi. Isolation of time-dependent DNA damage induced by energetic carbon ions and their fragments using fluorescent nuclear track detectors, *Medical physics*; 47-1 (2020), 272–281. DOI: https://doi.org/10.1002/mp.13897.

[51] B. G. Cartwright, E. K. Shirk, and P. B. Price. A nuclear-track-recording polymer of unique sensitivity and resolution, *Nuclear Instruments and Methods*; 153-2-3 (1978), 457–460. DOI: https://doi.org/10.1016/0029-554X(78)90989-8.

[52] S. Kodaira, K. Morishige, H. Kawashima, H. Kitamura, M. Kurano, N. Hasebe, Y. Koguchi, W. Shinozaki, and K. Ogura. A performance test of a new high-surface-quality and high-sensitivity CR-39 plastic nuclear track detector–TechnoTrak, *Nuclear Instruments and Methods in Physics Research Section B: Beam Interactions with Materials and Atoms*; 383 (2016), 129–135. DOI: https://doi.org/10.1016/j.nimb.2016.07.002.

[53] K. Ogura, M. Asano, N. Yasuda, and M. Yoshida. Properties of TNF-1 track etch detector, *Nuclear Instruments and Methods in Physics Research Section B: Beam Interactions with Materials and Atoms*; 185-1-4 (2001), 222–227. DOI: https://doi.org/10.1016/S0168-583X(01)00816-3.

[54] S. Kodaira, N. Yasuda, T. Konishi, H. Kitamura, M. Kurano, H. Kawashima, Y. Uchihori, K. Ogura, and E. R. Benton. Calibration of CR-39 with atomic force microscope for the measurement of short range tracks from proton-induced target fragmentation reactions, *Radiation measurements*; 50 (2013), 232–236. DOI: https://doi.org/10.1016/j.radmeas.2012.10.001.

[55] K. Brabcová, I. Jadrníčková, A. G. Molokanov, and F. Spurný. Dosimetry in heavy ion beams using various detectors, *Radiation Measurements*; 45-10 (2010), 1384–1386. DOI: https://doi.org/10.1016/j.radmeas.2010.06.004.

[56] Y. Hirano, S. Kodaira, H. Souda, A. Matsumura, and M. Torikoshi. Linear energy transfer (LET) spectra and survival fraction distribution based on the CR-39 plastic charged-particle detector in a spread-out Bragg peak irradiation by a 12C beam, *Physics in Medicine & Biology*; 63-18 (2018), 185006. DOI: https://doi.org/10.1088/1361-6560/aadaa6.

[57] H. H. Rossi and W. Rosenzweig. A device for the measurement of dose as a function of specific ionization, *Radiology*; 64-3 (1955), 404–411. DOI: https://doi.org/10.1148/64.3.404.

[58] P. Kliauga. Nanodosimetry of heavy ions using a miniature cylindrical counter of wall-less design, *Radiation Protection Dosimetry*; 52-1-4 (1994), 317–321. DOI: https://doi.org/10.1093/oxfordjournals.rpd.a082207.

[59] H. H. Rossi and M. Zaider. Microdosimetry and Its Applications. 1st. Berlin, Germany: Springer-Verlag Berlin Heidelberg, 1996.

[60] L. A. Braby *et al.* ICRU Report 98, Stochastic Nature of Radiation Interactions: Microdosimetry, *Journal of the ICRU*; 23-1 (2023), 1–168. DOI: https://doi.org/10.1177/14736691231211380.

[61] A. Bertolet, A. Baratto-Roldán, M. A. Cortés-Giraldo, and A. Carabe-Fernandez. Segment-averaged LET concept and analytical calculation from microdosimetric quantities in proton radiation therapy, *Medical Physics*; 46-9 (2019), 4204–4214. DOI: https://doi.org/10.1002/mp.13673.

[62] G. Martino, M. Durante, and D. Schardt. Microdosimetry measurements characterizing the radiation fields of 300 MeV/u ^{12}C and 185 MeV/u ^{7}Li pencil beams stopping in water, *Physics in Medicine & Biology*; 55-12 (2010), 3441. DOI: https://doi.org/10.1088/0031-9155/55/12/011.

[63] V. Conte, A. Bianchi, A. Selva, G. Petringa, G. A. P. Cirrone, A. Parisi, F. Vanhavere, and P. Colautti. Microdosimetry at the CATANA 62 MeV proton beam with a sealed miniaturized TEPC, *Physica Medica*; 64 (2019), 114–122. DOI: https://doi.org/10.1016/j.ejmp.2019.06.011.

[64] M. Missiaggia, G. Cartechini, F. Tommasino, E. Scifoni, and C. La Tessa. Investigation of in-field and out-of-field radiation quality with microdosimetry and its impact on relative biological effectiveness in proton therapy, *International Journal of Radiation Oncology* Biology* Physics*; 115-5 (2023), 1269–1282. DOI: https://doi.org/10.1016/j.ijrobp.2022.11.037.

[65] R. B. Hawkins. A microdosimetric-kinetic model for the effect of non-Poisson distribution of lethal lesions on the variation of RBE with LET, *Radiation research*; 160-1 (2003), 61–69. DOI: https://doi.org/10.1667/rr3010.

[66] T. Inaniwa and N. Kanematsu. Adaptation of stochastic microdosimetric kinetic model for charged-particle therapy treatment planning, *Physics in Medicine & Biology*; 63-9 (2018), 095011. DOI: https://doi.org/10.1088/1361-6560/aabede.

[67] A. B. Rosenfeld. Novel detectors for silicon based microdosimetry, their concepts and applications, *Nuclear Instruments and Methods in Physics Research Section A: Accelerators, Spectrometers, Detectors and Associated Equipment*; 809 (2016), 156–170. DOI: https://doi.org/10.1016/j.nima.2015.08.059.

[68] S. H. Lee, K. Mizushima, R. Kohno, Y. Iwata, S. Yonai, T. Shirai, V. A. Pan, D. Bolst, L. T. Tran, A. B. Rosenfeld, *et al.* Estimating the biological effects of helium, carbon, oxygen, and neon ion beams using 3D silicon microdosimeters, *Physics in Medicine & Biology*; 66-4 (2021), 045017. DOI: https://doi.org/10.1088/1361-6560/abd66f.

[69] C. Guardiola, D. Bachiller-Perea, J. Prieto-Pena, M. del C. Jiménez-Ramos, J. Garc'ıa López, C. Esnault, C. Fleta, D. Quirion, and F. Gómez. Microdosimetry in low energy proton beam at therapeutic-equivalent fluence rate with silicon 3D-cylindrical microdetectors, *Physics in Medicine & Biology*; 66-11 (2021), 114001. DOI: https://doi.org/10.1088/1361-6560/abf811.

[70] L. T. Tran, L. Chartier, D. Bolst, A. Pogossov, S. Guatelli, M. Petasecca, M. L. F. Lerch, D. A. Prokopovich, M. I. Reinhard, B. Clasie, *et al.* Characterization of proton pencil beam scanning and passive beam using a high spatial resolution solid-state microdosimeter, *Medical physics*; 44-11 (2017), 6085–6095. DOI: https://doi.org/10.1002/mp.12563.

[71] D. Bolst, S. Guatelli, L. T. Tran, L. Chartier, M. L. F. Lerch, N. Matsufuji, and A. B. Rosenfeld. Correction factors to convert microdosimetry measurements in silicon to tissue in 12C ion therapy, *Physics in Medicine & Biology*; 62-6 (2017), 2055. DOI: https://doi.org/10.1088/1361-6560/aa5de5.

[72] D. Wagenaar, L. T. Tran, A. Meijers, G. G. Marmitt, K. Souris, D. Bolst, B. James, G. Biasi, M. Povoli, A. Kok, *et al.* Validation of linear energy transfer computed in a Monte Carlo dose engine of a commercial treatment planning system, *Physics in Medicine & Biology*; 65-2 (2020), 025006. DOI: https://doi.org/10.1088/1361-6560/ab5e97.

[73] P. D. Bradley, A. B. Rosenfeld, and M. Zaider. Solid state microdosimetry, *Nuclear Instruments and Methods in Physics Research Section B: Beam Interactions with Materials and Atoms*; 184-1-2 (2001), 135–157. DOI: https://doi.org/10.1093/oxfordjournals.rpd.a006019.

[74] X. Llopart, R. Ballabriga, M. Campbell, L. Tlustos, and W. Wong. Timepix, a 65k programmable pixel readout chip for arrival time, energy and/or photon counting measurements, *Nuclear Instruments and Methods in Physics Research Section A: Accelerators, Spectrometers, Detectors and Associated Equipment*; 581-1-2 (2007), 485–494. DOI: https://doi.org/10.1016/j.nima.2007.08.079.

[75] J. Jakubek. Precise energy calibration of pixel detector working in time-over-threshold mode, *Nuclear Instruments and Methods in Physics Research Section A: Accelerators, Spectrometers, Detectors and Associated Equipment*; 633 (2011), S262–S266. DOI: https://doi.org/10.1016/j.nima.2010.06.183.

[76] T. Gehrke, L. Burigo, G. Aricó, S. Berke, J. Jakubek, D. Turecek, T. Tessonnier, A. Mairani, and M. Martišíková. Energy deposition measurements of single ^{1}H, ^{4}He and ^{12}C ions of therapeutic energies in a silicon pixel detector, *Journal of Instrumentation*; 12-04 (2017), P04025. DOI: https://doi.org/10.1088/1748-0221/12/04/P04025.

[77] C. Granja, C. Oancea, J. Jakubek, L. Marek, E. Benton, S. Kodaira, J. Miller, A. Rucinski, J. Gajewski, P. Stasica, *et al.* Wide-range tracking and LET-spectra of energetic light and heavy charged particles, *Nuclear Instruments and Methods in Physics Research Section A: Accelerators, Spectrometers, Detectors and Associated Equipment*; 988 (2021), 164901. DOI: https://doi.org/10.1016/j.nima.2020.164901.

[78] P. Stasica, H. Nguyen, C. Granja, R. Kopeć, L. Marek, C. Oancea, L. Raczyński, A. Rucinski, M. Rydygier, K. Schubert, *et al.* Single proton LET characterization with the Timepix detector and artificial intelligence for advanced proton therapy treatment planning, *Physics in Medicine & Biology*; 68-10 (2023), 104001. DOI: https://doi.org/10.1088/1361-6560/acc9f8.

[79] E. R. Benton, E. V. Benton, and A. L. Frank. Conversion between different forms of LET, *Radiation Measurements*; 45-8 (2010), 957–959. DOI: https://doi.org/10.1016/j.radmeas.2010.05.008.

[80] J. Tepper, L. Verhey, M. Goitein, H. D. Suit, D. Phil, and A. M. Koehler. In vivo determinations of RBE in a high energy modulated proton beam using normal tissue reactions and fractionated dose schedules, *International Journal of Radiation Oncology* Biology* Physics*; 2-11-12 (1977), 1115–1122. DOI: https://doi.org/10.1016/0360-3016(77)90118-3.

[81] T. L. Phillips, G. Y. Ross, L. S. Goldstein, J. Ainsworth, and E. Alpen. In vivo radiobiology of heavy ions, *International Journal of Radiation Oncology* Biology* Physics*; 8-12 (1982), 2121–2125. DOI: https://doi.org/10.1016/0360-3016(82)90555-7.

[82] B. G. Wouters, L. D. Skarsgard, L. E. Gerweck, A. Carabe-Fernandez, M. Wong, R. E. Durand, D. Nielson, M. R. Bussiere, M. Wagner, P. Biggs, *et al.* Radiobiological intercomparison of the 160 MeV and 230 MeV proton therapy beams at the Harvard Cyclotron Laboratory and at Massachusetts General Hospital, *Radiation Research*; 183-2 (2015), 174–187. DOI: https://doi.org/10.1667/RR13795.1.

[83] A. Mairani, G. Magro, I. Dokic, S. M. Valle, T. Tessonnier, R. Galm, M. Ciocca, K. Parodi, A. Ferrari, O. Jäkel, *et al.* Data-driven RBE parameterization for helium ion beams, *Physics in Medicine & Biology*; 61-2 (2016), 888. DOI: https://doi.org/10.1088/0031-9155/61/2/888.

[84] P. Choudhry. High-throughput method for automated colony and cell counting by digital image analysis based on edge detection, *PloS one*; 11-2 (2016), e0148469. DOI: https://doi.org/10.1371/journal.pone.0148469.

[85] M. Wedenberg, B. K. Lind, and B. Hårdemark. A model for the relative biological effectiveness of protons: the tissue specific parameter α/β of photons is a predictor for the sensitivity to LET changes, *Acta oncologica*; 52-3 (2013), 580–588. DOI: https://doi.org/10.3109/0284186X.2012.705892.

[86] A. L. McNamara, J. Schuemann, and H. Paganetti. A phenomenological relative biological effectiveness (RBE) model for proton therapy based on all published in vitro cell survival data, *Physics in Medicine & Biology*; 60-21 (2015), 8399. DOI: https://doi.org/10.1088/0031-9155/60/21/8399.

[87] A. Mairani, I. Dokic, G. Magro, T. Tessonnier, F. Kamp, D. J. Carlson, M. Ciocca, F. Cerutti, P. R. Sala, A. Ferrari, *et al.* Biologically optimized helium ion plans: calculation approach and its in vitro validation, *Physics in Medicine & Biology*; 61-11 (2016), 4283. DOI: https://doi.org/10.1088/0031-9155/61/11/4283.

[88] R. D. Stewart, D. J. Carlson, M. P. Butkus, R. Hawkins, T. Friedrich, and M. Scholz. A comparison of mechanism-inspired models for particle relative biological effectiveness (RBE), *Medical physics*; 45-11 (2018), e925–e952. DOI: https://doi.org/10.1002/mp.13207.

[89] S. Mein, I. Dokic, C. Klein, T. Tessonnier, T. T. Böhlen, G. Magro, J. Bauer, A. Ferrari, K. Parodi, T. Haberer, *et al.* Biophysical modeling and experimental validation of relative biological effectiveness (RBE) for ^{4}He ion beam therapy, *Radiation Oncology*; 14-1 (2019), 1–16. DOI: https://doi.org/10.1186/s13014-019-1295-z.

[90] A. Parisi, C. J. Beltran, and K. M. Furutani. The Mayo Clinic Florida microdosimetric kinetic model of clonogenic survival: Formalism and first benchmark against in vitro and in silico data, *Physics in Medicine & Biology*; 67-18 (2022), 185013. DOI: https://doi.org/10.1088/1361-6560/ac7375.

[91] O. Zlobinskaya, G. Dollinger, D. Michalski, V. Hable, C. Greubel, G. Du, G. Multhoff, B. Röper, M. Molls, and T. E. Schmid. Induction and repair of DNA double-strand breaks assessed by gamma-H2AX foci after irradiation with pulsed or continuous proton beams, *Radiation and environmental biophysics*; 51 (2012), 23–32. DOI: https://doi.org/10.1007/s00411-011-0398-1.

[92] J. Y. Tsai, F. H. Chen, T. Y. Hsieh, and Y. Y. Hsiao. Effects of indirect actions and oxygen on relative biological effectiveness: estimate of DSB induction and conversion induced by gamma rays and helium ions, *Journal of radiation research*; 56-4 (2015), 691–699. DOI: https://doi.org/10.1093/jrr/rrv025.

[93] J. J. Cuaron, C. Chang, M. Lovelock, D. S. Higginson, D. Mah, O. Cahlon, and S. Powell. Exponential increase in relative biological effectiveness along distal edge of a proton Bragg peak as measured by deoxyribonucleic acid double-strand breaks, *International Journal of Radiation Oncology* Biology* Physics*; 95-1 (2016), 62–69. DOI: https://doi.org/10.1016/j.ijrobp.2016.02.018.

[94] O. A. Sedelnikova, E. P. Rogakou, I. G. Panyutin, and W. M. Bonner. Quantitative detection of ^{125}IdU-induced DNA double-strand breaks with γ-H2AX antibody, *Radiation research*; 158-4 (2002), 486–492. DOI: https://doi.org/10.1667/0033-7587(2002)158[0486:qdoiid]2.0.co;2.

[95] E. C. Bourton, P. N. Plowman, S. A. Zahir, G. U. Senguloglu, H. Serrai, G. Bottley, and C. N. Parris. Multispectral imaging flow cytometry reveals distinct frequencies of γ-H2AX foci induction in DNA double strand break repair defective human cell lines, *Cytometry Part A*; 81-2 (2012), 130–137. DOI: https://doi.org/10.1002/cyto.a.21171.

[96] P. Rybak, A. Hoang, L. Bujnowicz, T. Bernas, K. Berniak, M. Zarebski, Z. Darzynkiewicz, and J. Dobrucki. Low level phosphorylation of histone H2AX on serine 139 (γH2AX) is not associated with DNA double-strand breaks, *Oncotarget*; 7-31 (2016), 49574. DOI: https://doi.org/10.18632/oncotarget.10411.

[97] J. L. Viovy. Electrophoresis of DNA and other polyelectrolytes: Physical mechanisms, *Reviews of Modern Physics*; 72-3 (2000), 813. DOI: https://doi.org/10.1103/RevModPhys.72.813.

[98] G. Esposito, M. Belli, A. Campa, R. Cherubini, G. Cuttone, V. Dini, Y. Furusawa, S. Gerardi, G. Simone, E. Sorrentino, *et al.* DNA fragments induction in human fibroblasts by radiations of different qualities, *Radiation protection dosimetry*; 122-1-4 (2006), 166–168. DOI: https://doi.org/10.1093/rpd/ncl389.

[99] V. Calugaru, C. Nauraye, G. Noël, N. Giocanti, V. Favaudon, and F. Mégnin-Chanet. Radiobiological characterization of two therapeutic proton beams with different initial energy spectra used at the Institut Curie Proton Therapy Center in Orsay, *International Journal of Radiation Oncology* Biology* Physics*; 81-4 (2011), 1136–1143. DOI: https://doi.org/10.1016/j.ijrobp.2010.09.003.

[100] M. Mognato, E. Bortoletto, P. Ferraro, L. Baggio, R. Cherubini, S. Canova, A. Russo, and L. Celotti. Genetic damage induced by in vitro irradiation of human G0 lymphocytes with low-energy protons (28 keV/μm): HPRT mutations and chromosome aberrations, *Radiation research*; 160-1 (2003), 52–60. DOI: https://doi.org/10.1667/0033-7587(2003)160[0052:gdibiv]2.0.co;2.

[101] T. E. Schmid, G. Dollinger, V. Hable, C. Greubel, O. Zlobinskaya, D. Michalski, S. Auer, A. A. Friedl, E. Schmid, M. Molls, *et al.* The effectiveness of 20 MeV protons at nanosecond pulse lengths in producing chromosome aberrations in human-hamster hybrid cells, *Radiation research*; 175-6 (2011), 719–727. DOI: https://doi.org/10.1667/RR2465.1.

[102] K. George, M. Durante, V. Willingham, H. Wu, T. C. Yang, and F. A. Cucinotta. Biological effectiveness of accelerated particles for the induction of chromosome damage measured in metaphase and interphase human lymphocytes, *Radiation research*; 160-4 (2003), 425–435. DOI: https://doi.org/10.1667/RR3064.

[103] K. George, H. Wu, V. Willingham, Y. Furusawa, T. Kawata, and F. A. Cucinotta. High-and low-LET induced chromosome damage in human lymphocytes: a time-course of aberrations in metaphase and interphase, *International journal of radiation biology*; 77-2 (2001), 175–183. DOI: https://doi.org/10.1080/09553000001003760.

[104] L. M. Green, D. K. Murray, D. T. Tran, A. M. Bant, G. Kazarians, M. F. Moyers, and G. A. Nelson. Response of thyroid follicular cells to gamma irradiation compared to proton irradiation. I. Initial characterization of DNA damage, micronucleus formation, apoptosis, cell survival, and cell cycle phase redistribution, *Radiation research*; 155-1 (2001), 32–42. DOI: https://doi.org/10.1667/0033-7587(2001)155[0032:ROTFCT]2.0.CO;2.

[105] T. E. Schmid, G. Dollinger, V. Hable, C. Greubel, O. Zlobinskaya, D. Michalski, M. Molls, and B. Röper. Relative biological effectiveness of pulsed and continuous 20 MeV protons for micronucleus induction in 3D human reconstructed skin tissue, *Radiotherapy and Oncology*; 95-1 (2010), 66–72. DOI: https://doi.org/10.1016/j.radonc.2010.03.010.

[106] A. Kowalska, E. Nasonova, P. Kutsalo, and K. Czerski. Chromosomal radiosensitivity of human breast carcinoma cells and blood lymphocytes following photon and proton exposures, *Radiation and Environmental Biophysics*; 62-1 (2023), 151–160. DOI: https://doi.org/10.1007/s00411-023-01016-5.

[107] A. Pantelias, D. Zafiropoulos, R. Cherubini, L. Sarchiapone, V. De Nadal, G. E. Pantelias, A. G. Georgakilas, and G. I. Terzoudi. Interphase cytogenetic analysis of G0 lymphocytes exposed to α-particles, C-ions, and protons reveals their enhanced effectiveness for localized chromosome shattering—a critical risk for chromothripsis, *Cancers*; 12-9 (2020), 2336. DOI: https://doi.org/10.3390/cancers12092336.

[108] C. P. Karger, P. Peschke, M. Scholz, P. E. Huber, and J. Debus. Relative biological effectiveness of carbon ions in a rat prostate carcinoma in vivo: comparison of 1, 2, and 6 fractions, *International Journal of Radiation Oncology* Biology* Physics*; 86-3 (2013), 450–455. DOI: https://doi.org/10.1016/j.ijrobp.2013.01.019.

[109] S. Koike, K. Ando, C. Oohira, T. Fukawa, R. Lee, N. Takai, M. Monobe, Y. Furusawa, M. Aoki, S. Yamada, *et al.* Relative biological effectiveness of 290 MeV/u carbon ions for the growth delay of a radioresistant murine fibrosarcoma, *Journal of radiation research*; 43-3 (2002), 247–255. DOI: https://doi.org/10.1269/jrr.43.247.

[110] J. T. Leith, K. H. Woodruff, J. Howard, J. T. Lyman, P. Smith, and B. S. Lewinsky. Early and late effects of accelerated charged particles on normal tissues, *International Journal of Radiation Oncology* Biology* Physics*; 3 (1977), 103–108. DOI: https://doi.org/10.1016/0360-3016(77)90235-8.

[111] C. Zhou, B. Jones, M. Moustafa, B. Yang, S. Brons, L. Cao, Y. Dai, C. Schwager, M. Chen, O. Jaekel, *et al.* Determining RBE for development of lung fibrosis induced by fractionated irradiation with carbon ions utilizing fibrosis index and high-LET BED model, *Clinical and Translational Radiation Oncology*; 14 (2019), 25–32. DOI: https://doi.org/10.1016/j.ctro.2018.10.005.

[112] L. Hintz, C. Glowa, M. Saager, R. Euler-Lange, P. Peschke, S. Brons, R. Grün, M. Scholz, S. Mein, A. Mairani, *et al.* Relative biological effectiveness of single and split helium ion doses in the rat spinal cord increases strongly with linear energy transfer, *Radiotherapy and Oncology*; 170 (2022), 224–230. DOI: https://doi.org/10.1016/j.radonc.2022.03.017.

[113] B. S. Sørensen, M. R. Horsman, J. Alsner, J. Overgaard, M. Durante, M. Scholz, T. Friedrich, and N. Bassler. Relative biological effectiveness of carbon ions for tumor control, acute skin damage and late radiation-induced fibrosis in a mouse model, *Acta oncologica*; 54-9 (2015), 1623–1630. DOI: https://doi.org/10.3109/0284186X.2015.1069890.

[114] S. Sténson. Effects of proton and roentgen radiation on the rectum of the rat, *Acta Radiologica: Therapy, Physics, Biology*; 8-4 (1969), 263–278. DOI: https://doi.org/10.3109/02841866909134458.

[115] Y. Kang, H. Ishikawa, T. Inaniwa, Y. Iwai, N. Matsufuji, G. Kasuya, N. Okonogi, Y. Liu, Y. Chao, M. Wakatsuki, *et al.* The clinical relative biological effectiveness and prostate-specific antigen kinetics of carbon-ion radiotherapy in low-risk prostate cancer, *Cancer Medicine*; 12-2 (2023), 1540–1551. DOI: https://doi.org/10.1002/cam4.5045.

[116] Y. Y. Zhang, W. L. Huo, S. I. Goldberg, J. M. Slater, J. A. Adams, X. W. Deng, Y. Sun, J. Ma, B. C. Fullerton, H. Paganetti, *et al.* Brain-specific relative biological effectiveness of protons based on long-term outcome of patients with nasopharyngeal carcinoma, *International Journal of Radiation Oncology* Biology* Physics*; 110-4 (2021), 984–992. DOI: https://doi.org/10.1016/j.ijrobp.2021.02.018.

[117] Y. Yang, O. M. Muller, S. Shiraishi, M. Harper, A. C. Amundson, W. W. Wong, L. A. McGee, J. C. M. Rwigema, S. E. Schild, M. Bues, *et al.* Empirical relative biological effectiveness (RBE) for mandible osteoradionecrosis (ORN) in head and neck cancer patients treated with pencil-beam-scanning proton therapy (PBSPT): a retrospective, case-matched cohort study, *Frontiers in Oncology*; 12 (2022), 843175. DOI: https://doi.org/10.3389/fonc.2022.843175.

[118] World Health Organization (WHO). *Cancer*. Retrieved June 07, 2023. n.d. https://www.who.int/news-room/fact-sheets/detail/cancer.

[119] D. Hanahan and R. A. Weinberg. The hallmarks of cancer, *cell*; 100-1 (2000), 57–70. DOI: https://doi.org/10.1016/S0092-8674(00)81683-9.

[120] Yuri Lazebnik. What are the hallmarks of cancer?, *Nature Reviews Cancer*; 10-4 (2010), 232–233. DOI: https://doi.org/10.1038/nrc2827.

[121] D. Hanahan and R. A. Weinberg. Hallmarks of cancer: the next generation, *cell*; 144-5 (2011), 646–674. DOI: https://doi.org/10.1016/j.cell.2011.02.013.

[122] Simiao Chen, Zhong Cao, Klaus Prettner, Michael Kuhn, Juntao Yang, Lirui Jiao, Zhuoran Wang, Weimin Li, Pascal Geldsetzer, Till Bärnighausen, *et al.* Estimates and projections of the global economic cost of 29 cancers in 204 countries and territories from 2020 to 2050, *JAMA oncology*; 9-4 (2023), 465–472. DOI: https://doi.org/10.1001/jamaoncol.2022.7826.

[123] Thomas Hofmarcher, Peter Lindgren, Nils Wilking, and Bengt Jönsson. The cost of cancer in Europe 2018, *European Journal of Cancer*; 129 (2020), 41–49. DOI: https://doi.org/10.1016/j.ejca.2020.01.011.

[124] João Pedro De Magalhães. How ageing processes influence cancer, *Nature Reviews Cancer*; 13-5 (2013), 357–365. DOI: https://doi.org/10.1038/nrc3497.

[125] Kevin Kinsella and Victoria A Velkoff. The demographics of aging, *Aging Clinical and Experimental Research*; 14-3 (2002), 159–169. DOI: https://doi.org/10.1007/BF03324431.

[126] Colin D Mathers, Gretchen A Stevens, Ties Boerma, Richard A White, and Martin I Tobias. Causes of international increases in older age life expectancy, *The Lancet*; 385-9967 (2015), 540–548. DOI: https://doi.org/10.1016/S0140-6736(14)60569-9.

[127] Lindsey A Torre, Rebecca L Siegel, Elizabeth M Ward, and Ahmedin Jemal. Global cancer incidence and mortality rates and trends—an update, *Cancer epidemiology, biomarkers & prevention*; 25-1 (2016), 16–27. DOI: https://doi.org/10.1158/1055-9965.EPI-15-0578.

[128] International Agency for Research on Cancer (IARC). *Global cancer observatory (GLOBOCAN 2020), Cancer today*. Retrieved October 07, 2023. n.d. https://gco.iarc.fr/.

[129] Kimberly D Miller, Rebecca L Siegel, Chun Chieh Lin, Angela B Mariotto, Joan L Kramer, Julia H Rowland, Kevin D Stein, Rick Alteri, and Ahmedin Jemal. Cancer treatment and survivorship statistics, 2016, *CA: a cancer journal for clinicians*; 66-4 (2016), 271–289. DOI: https://doi.org/10.3322/caac.21349.

[130] Brenda K Edwards, Martin L Brown, Phyllis A Wingo, Holly L Howe, Elizabeth Ward, Lynn AG Ries, Deborah Schrag, Patricia M Jamison, Ahmedin Jemal, Xiao Cheng Wu, *et al.* Annual report to the nation on the status of cancer, 1975–2002, featuring population-based trends in cancer treatment, *Journal of the National Cancer Institute*; 97-19 (2005), 1407–1427. DOI: https://doi.org/10.1093/jnci/dji289.

[131] Adrienne G Waks and Eric P Winer. Breast cancer treatment: a review, *Jama*; 321-3 (2019), 288–300. DOI: https://doi.org/10.1001/jama.2018.19323.

[132] Hassan Lemjabbar-Alaoui, Omer UI Hassan, Yi-Wei Yang, and Petra Buchanan. Lung cancer: Biology and treatment options, *Biochimica et Biophysica Acta (BBA)-Reviews on Cancer*; 1856-2 (2015), 189–210. DOI: https://doi.org/10.1016/j.bbcan.2015.08.002.

[133] Leonard G Gomella, James Johannes, and Edouard J Trabulsi. Current prostate cancer treatments: effect on quality of life, *Urology*; 73-5 (2009), S28–S35. DOI: https://doi.org/10.1016/10.1016/j.urology.2009.03.003.

[134] Vishal Madan, John T Lear, and Rolf-Markus Szeimies. Non-melanoma skin cancer, *The Lancet*; 375-9715 (2010), 673–685. DOI: https://doi.org/10.1016/S0140-6736(09)61196-X.

[135] Roberto Labianca, Giordano D Beretta, Basem Kildani, Laura Milesi, Federica Merlin, Stefania Mosconi, M Adelaide Pessi, Tiziana Prochilo, Antonello Quadri, Gemma Gatta, *et al.* Colon cancer, *Critical reviews in oncology/hematology*; 74-2 (2010), 106–133. DOI: https://doi.org/10.1016/j.critrevonc.2010.01.010.

[136] Michael B Barton, Susannah Jacob, Jesmin Shafiq, Karen Wong, Stephen R Thompson, Timothy P Hanna, and Geoff P Delaney. Estimating the demand for radiotherapy from the evidence: a review of changes from 2003 to 2012, *Radiotherapy and oncology*; 112-1 (2014), 140–144. DOI: https://doi.org/10.1016/j.radonc.2014.03.024.

[137] International Commission on Radiation Units and Measurements (ICRU), *Report 85, Fundamental Quantities and Units for Ionizing Radiation. Journal of the ICRU*, SAGE Publishing, 2011. Chap. 2. General Considerations, 7–9. DOI: https://doi.org/10.1093/jicru_ndr002.

[138] F. H. Attix. Introduction to radiological physics and radiation dosimetry. Weinheim, Germany: WILEY-VCH Verlag GmbH & Co. KGaA, 2004.

[139] E. B. Podgorsak. Radiation Physics for Medical Physicists. Biological and medical physics, biomedical engineering. Berlin, Germany: Springer-Verlag Berlin Heidelberg, 2006.

[140] International Commission on Radiation Units and Measurements (ICRU). *Report 19, Radiation quantities and units.* ICRU Report. Bethesda MD, USA: International Commission on Radiation Units and Measurements, 1971.

[141] J. T. Bushberg, J. A. Seibert, E. M. Leidholdt Jr., and J. M. Boone. The Essential Physics of Medical Imaging. 3rd. Philadelphia PA, USA: Lippincott Williams & Wilkins, 2012.

[142] M. J. Berger, J. H. Hubbell, S. M. Seltzer, J. Chang, J. S. Coursey, R. Sukumar, D. S. Zucker, and K. Olsen. *XCOM: Photon Cross Sections Database.* Retrieved October 10, 2023. November 2010. https://www.nist.gov/pml/xcom-photon-cross-sections-database.

[143] P. Andreo, D. T. Burns, A. Nahum, J. Seuntjens, and F. H. Attix. Fundamentals of ionizing radiation dosimetry. Weinheim, Germany: WILEY-VCH Verlag GmbH & Co. KGaA, 2017.

[144] International Commission on Radiation Units and Measurements (ICRU), *Report 90, Key Data For Ionizing-Radiation Dosimetry: Measurement Standards And Applications. Journal of the ICRU*, SAGE Publishing, 2014. Chap. 4. Charged-Particle Stopping Powers and Related Quantities, 21–30. DOI: https://doi.org/10.1093/jicru_ndw031.

[145] International Commission on Radiation Units and Measurements (ICRU), *Report 90, Key Data For Ionizing-Radiation Dosimetry: Measurement Standards And Applications. Journal of the ICRU*, SAGE Publishing, 2014. Chap. Appendix. Stopping Power and Range Tables for Charged Particles, 79–98. DOI: https://doi.org/10.1093/jicru/ndw030.

[146] J. F. Ziegler, M. D. Ziegler, and J. P. Biersack. SRIM–The stopping and range of ions in matter (2010), *Nuclear Instruments and Methods in Physics Research Section B: Beam Interactions with Materials and Atoms*; 268-11-12 (2010), 1818–1823. DOI: https://doi.org/10.1016/j.nimb.2010.02.091.

[147] M. A. Zucker M. J. Berger J. S. Coursey and J. Chang. *ESTAR: Stopping Powers and Ranges for Electrons.* Retrieved October 24, 2023. July 2017. https://physics.nist.gov/PhysRefData/Star/Text/method.html.

[148] F. Luoni, F. Horst, C. A. Reidel, A. Quarz, L. Bagnale, L. Sihver, U. Weber, R. B. Norman, W. De Wet, M. Giraudo, *et al.* Total nuclear reaction cross-section database for radiation protection in space and heavy-ion therapy applications, *New Journal of Physics*; 23-10 (2021), 101201. DOI: https://doi.org/10.1088/1367-2630/ac27e1.

[149] R. K. Tripathi, F. A. Cucinotta, and J. W. Wilson. Accurate universal parameterization of absorption cross sections, *Nuclear Instruments and Methods in Physics Research Section B: Beam Interactions with Materials and Atoms*; 117-4 (1996), 347–349. DOI: https://doi.org/10.1016/0168-583X(96)00331-X.

[150] A. Ingemarsson, J. Nyberg, P. U. Renberg, O. Sundberg, R. F. Carlson, A. J. Cox, A. Auce, R. Johansson, G. Tibell, D. T. Khoa, *et al.* New results for reaction cross sections of intermediate energy α-particles on targets from 9Be to 208Pb, *Nuclear Physics A*; 676-1-4 (2000), 3–31. DOI: https://doi.org/10.1016/S0375-9474(00)00200-1.

[151] F. Horst, C. Schuy, U. Weber, K. T. Brinkmann, and K. Zink. Measurement of charge-and mass-changing cross sections for ^{4}He + ^{12}C collisions in the energy range 80–220 MeV/u for applications in ion beam therapy, *Physical Review C*; 96-2 (2017), 024624. DOI: https://doi.org/10.1103/PhysRevC.96.024624.

[152] J. Jaros, A. Wagner, L. Anderson, O. Chamberlain, R. Z. Fuzesy, J. Gallup, W. Gorn, L. Schroeder, S. Shannon, G. Shapiro, *et al.* Nucleus-nucleus total cross sections for light nuclei at 1.55 and 2.89 GeV/c per nucleon, *Physical review C*; 18-5 (1978), 2273. DOI: https://doi.org/10.1103/PhysRevC.18.2273.

[153] E. Haettner, H. Iwase, M. Krämer, G. Kraft, and D. Schardt. Experimental study of nuclear fragmentation of 200 and 400 MeV/u ^{12}C ions in water for applications in particle therapy, *Physics in medicine & biology*; 58-23 (2013), 8265. DOI: https://doi.org/10.1088/0031-9155/58/23/8265.

[154] G. Aricò, T. Gehrke, R. Gallas, A. Mairani, O. Jäkel, and M. Martišíková. Investigation of single carbon ion fragmentation in water and PMMA for hadron therapy, *Physics in Medicine & Biology*; 64-5 (2019), 055018. DOI: https://doi.org/10.1088/1361-6560/aafa46.

[155] Particle Data Group (PDG): M. Tanabashi, K. Hagiwara, K. Hikasa, K. Nakamura, Y. Sumino, *et al.*, *Review of Particle Physics. Physical Review D*, American Physical Society, 2018. Chap. 33. Passage of Particles Through Matter, 1–36. DOI: https://doi.org/10.1103/PhysRevD.98.030001.

[156] P. V. Vavilov. Ionization losses of high-energy heavy particles, *Soviet Phys. JETP*; 5-4 (1957), 920–923.

[157] International Commission on Radiation Units and Measurements (ICRU), *Report 90, Key Data For Ionizing-Radiation Dosimetry: Measurement Standards And Applications. Journal of the ICRU*, SAGE Publishing, 2014. Chap. 2. Definitions of Basic Quantities and Terms, 9–13. DOI: https://doi.org/10.1093/jicru_ndw032.

[158] International Atomic Energy Agency (IAEA). Absorbed dose determination in external beam radiotherapy: An international code of practice for dosimetry based on standards of absorbed dose to water. Technical Reports Series No. 398. Vienna, Austria: International Atomic Energy Agency, 2000.

[159] International Commission on Radiation Units and Measurements (ICRU), *Report 85, Fundamental Quantities and Units for Ionizing Radiation. Journal of the ICRU*, SAGE Publishing, 2011. Chap. 5. Dosimetry, 22–28. DOI: https://doi.org/10.1093/jicru_ndr003.

[160] R. E. Zirkle, D. F. Marchbank, and K. D. Kuck. Exponential and sigmoid survival curves resulting from alpha and X irradiation of aspergillus spores, *Journal of Cellular and Comparative Physiology*; 39-S1 (1952), 75–85. DOI: https://doi.org/10.1002/jcp.1030390408.

[161] ICRU. *Linear Energy Transfer*. ICRU Report 16. Bethesda MD, USA: International Commission on Radiation Units and Measurements, 1970.

[162] M. Baumann *et al.* Basic Clinical Radiobiology. Ed. by M. Joiner and A. van der Kogel. 4th. London, UK: Hodder Arnold, 2009.

[163] J. A. Reisz, N. Bansal, J. Qian, W. Zhao, and C. M. Furdui. Effects of ionizing radiation on biological molecules—mechanisms of damage and emerging methods of detection, *Antioxidants & redox signaling*; 21-2 (2014), 260–292. DOI: https://doi.org/10.1089/ars.2013.5489.

[164] K. J. McKelvey, A. L. Hudson, M. Back, T. Eade, and C. I. Diakos. Radiation, inflammation and the immune response in cancer, *Mammalian Genome*; 29-11-12 (2018), 843–865. DOI: https://doi.org/10.1007/s00335-018-9777-0.

[165] L. Galluzzi, I. Vitale, S. A. Aaronson, J. M. Abrams, D. Adam, P. Agostinis, E. S. Alnemri, L. Altucci, I. Amelio, D. W. Andrews, *et al.* Molecular mechanisms of cell death: recommendations of the Nomenclature Committee on Cell Death 2018, *Cell Death & Differentiation*; 25-3 (2018), 486–541. DOI: https://doi.org/10.1038/s41418-017-0012-4.

[166] H. Okada and T. W. Mak. Pathways of apoptotic and non-apoptotic death in tumour cells, *Nature Reviews Cancer*; 4-8 (2004), 592–603. DOI: https://doi.org/10.1038/nrc1412.

[167] Research Collaboratory for Structural Bioinformatics (RCSB) Protein Data Bank (PDB). *5CBZ: AncMR DNA Binding Domain - (+)GRE Complex*. Retrieved October 12, 2023. July 2015. https://www.rcsb.org/structure/5CBZ.

[168] A. A. Edwards and D. C. Lloyd. Risks from ionising radiation: deterministic effects, *Journal of Radiological Protection*; 18-3 (1998), 175. DOI: https://doi.org/10.1088/0952-4746/18/3/004.

[169] N. Hamada and Y. Fujimichi. Classification of radiation effects for dose limitation purposes: history, current situation and future prospects, *Journal of radiation research*; 55-4 (2014), 629–640. DOI: https://doi.org/10.1093/jrr/rru019.

[170] P. L. Olive. The role of DNA single-and double-strand breaks in cell killing by ionizing radiation, *Radiation research*; 150-5s (1998), S42–S51. DOI: https://doi.org/10.2307/3579807.

[171] Y. Hagiwara, A. Niimi, M. Isono, M. Yamauchi, T. Yasuhara, S. Limsirichaikul, T. Oike, H. Sato, K. D. Held, T. Nakano, *et al.* 3D-structured illumination microscopy reveals clustered DNA double-strand break formation in widespread γH2AX foci after high LET heavy-ion particle radiation, *Oncotarget*; 8-65 (2017), 109370. DOI: https://doi.org/10.18632/oncotarget.22679.

[172] S. J. McMahon. The linear quadratic model: usage, interpretation and challenges, *Physics in Medicine & Biology*; 64-1 (2018), 01TR01. DOI: https://doi.org/10.1088/1361-6560/aaf26a.

[173] J. F. Fowler. 21 years of biologically effective dose, *The British journal of radiology*; 83-991 (2010), 554–568. DOI: https://doi.org/10.1259/bjr/31372149.

[174] M. Astrahan. Some implications of linear-quadratic-linear radiation dose-response with regard to hypofractionation, *Medical physics*; 35-9 (2008), 4161–4172. DOI: https://doi.org/10.1118/1.2969065.

[175] International Commission on Radiation Units and Measurements (ICRU), *Report 30, Quantitative Concepts and Dosimetry in Radiobiology. Journal of the ICRU*, SAGE Publishing, 1979. Chap. 2. Quantitative Concepts in Radiobiology, 3–15. DOI: https://doi.org/10.1093/jicru_os16.1.3.

[176] B. S. Sørensen, J. Overgaard, and N. Bassler. In vitro RBE-LET dependence for multiple particle types, *Acta oncologica*; 50-6 (2011), 757–762. DOI: https://doi.org/10.3109/0284186X.2011.582518.

[177] C. P. Karger and P. Peschke. RBE and related modeling in carbon-ion therapy, *Physics in Medicine & Biology*; 63-1 (2017), 01TR02. DOI: https://doi.org/10.1088/1361-6560/aa9102.

[178] T. Friedrich, U. Scholz, T. ElsäSser, M. Durante, and M. Scholz. Systematic analysis of RBE and related quantities using a database of cell survival experiments with ion beam irradiation, *Journal of Radiation Research*; 54-3 (2013), 494–514. DOI: https://doi.org/10.1093/jrr/rrs114.

[179] A. McNamara, H. Willers, and H. Paganetti. Modelling variable proton relative biological effectiveness for treatment planning, *The British journal of radiology*; 93-1107 (2020), 20190334. DOI: https://doi.org/10.1259/bjr.20190334.

[180] A. Carabe-Fernandez, R. G. Dale, and B. Jones. The incorporation of the concept of minimum RBE (RBE min) into the linear-quadratic model and the potential for improved radiobiological analysis of high-LET treatments, *International journal of radiation biology*; 83-1 (2007), 27–39. DOI: https://doi.org/10.1080/09553000601087176.

[181] M. Scholz and G. Kraft. Calculation of heavy ion inactivation probabilities based on track structure, x ray sensitivity and target size, *Radiation protection dosimetry*; 52-1-4 (1994), 29–33. DOI: https://doi.org/10.1093/oxfordjournals.rpd.a082156.

[182] R. B. Hawkins. A microdosimetric-kinetic theory of the dependence of the RBE for cell death on LET, *Medical physics*; 25-7 (1998), 1157–1170. DOI: https://doi.org/10.1118/1.598307.

[183] Y. Kase, T. Kanai, Y. Matsumoto, Y. Furusawa, H. Okamoto, T. Asaba, M. Sakama, and H. Shinoda. Microdosimetric measurements and estimation of human cell survival for heavy-ion beams, *Radiation research*; 166-4 (2006), 629–638. DOI: https://doi.org/10.1667/RR0536.1.

[184] T. Friedrich, U. Scholz, T. Elsässer, M. Durante, and M. Scholz. Calculation of the biological effects of ion beams based on the microscopic spatial damage distribution pattern, *International journal of radiation biology*; 88-1-2 (2012), 103–107. DOI: https://doi.org/10.3109/09553002.2011.611213.

[185] V. Nardone, E. D'Ippolito, R. Grassi, A. Sangiovanni, F. Gagliardi, G. De Marco, V. S. Menditti, L. D'Ambrosio, F. Cioce, L. Boldrini, *et al.* Non-Oncological Radiotherapy: A Review of Modern Approaches, *Journal of Personalized Medicine*; 12-10 (2022), 1677. DOI: https://doi.org/10.3390/jpm12101677.

[186] E. B. Podgorsak; sponsored by the International Atomic Energy Agency (IAEA). Radiation oncology physics: A handbook for teachers and students. Non-serial Publications. Vienna, Austria: International Atomic Energy Agency, 2005.

[187] International Atomic Energy Agency (IAEA). *DIrectory of RAdiotherapy Centres (DIRAC)*. Retrieved February 25, 2024. n.d. https://dirac.iaea.org/.

[188] R. R. Wilson. Radiological use of fast protons, *Radiology*; 47-5 (1946), 487–491. DOI: https://doi.org/10.1148/47.5.487.

[189] A. Konski, *Ion Beam Therapy: Fundamentals, Technology, Clinical Applications*. Berlin, Germany: Springer-Verlag Berlin Heidelberg, 2011. Chap. 3. Socio-Economic Aspects of Ion Beam Therapy, 31–41. DOI: https://doi.org/10.1007/978-3-642-21414-1_3.

[190] D. Sheikh-Bagheri and D. W. O. Rogers. Monte Carlo calculation of nine megavoltage photon beam spectra using the BEAM code, *Medical physics*; 29-3 (2002), 391–402. DOI: https://doi.org/10.1118/1.1445413.

[191] W. Schlegel, *New Technologies in Radiation Oncology*. Berlin, Germany: Springer-Verlag Berlin Heidelberg, 2006. Chap. 1. New technologies in 3D conformal radiation therapy: Introduction and overview, 1–6. DOI: https://doi.org/10.1007/3-540-29999-8_1.

[192] J. Staffurth on behalf of the Radiotherapy Development Board. A review of the clinical evidence for intensity-modulated radiotherapy, *Clinical oncology*; 22-8 (2010), 643–657. DOI: https://doi.org/10.1016/j.clon.2010.06.013.

[193] S. Łukomska, P. Kukołowicz, A. Zawadzka, M. Gruda, M. Giżyńska, A. Jankowska, and M. Piziorska. Evaluation of the usefulness of the electron Monte Carlo algorithm for planning radiotherapy with the use of electron beams, *Polish Journal of Medical Physics and Engineering*; 22-3 (2016), 49–54. DOI: https://doi.org/10.1515/pjmpe-2016-0009.

[194] J. R. Castro, J. M. Quivey, J. T. Lyman, G. T. Y. Chen, T. L. Phillips, C. A. Tobias, and E. L. Alpen. Current status of clinical particle radiotherapy at Lawrence Berkeley Laboratory, *Cancer*; 46-4 (1980), 633–641. DOI: https://doi.org/10.1002/1097-0142(19800815)46:4<633::aid-cncr2820460402>3.0.co;2-o.

[195] J. R. Castro, G. T. Y. Chen, and E. A. Blakely. Current considerations in heavy charged-particle radiotherapy: a clinical research trial of the University of California Lawrence Berkeley Laboratory, Northern California Oncology Group, and Radiation Therapy Oncology Group, *Radiation research*; 104-2s (1985), S263–S271. DOI: https://doi.org/10.2307/3583536.

[196] T. Tessonnier, S. Ecker, J. Besuglow, J. Naumann, S. Mein, F. K. Longarino, M. Ellerbrock, B. Ackermann, M. Winter, S. Brons, *et al.* Commissioning of helium ion therapy and the first patient treatment with active beam delivery, *International Journal of Radiation Oncology* Biology* Physics*; 116-4 (2023), 935–948. DOI: https://doi.org/10.1016/j.ijrobp.2023.01.015.

[197] H. Eickhoff, U. Weinrich, and J. Alonso, *Ion Beam Therapy: Fundamentals, Technology, Clinical Applications*. Berlin, Germany: Springer-Verlag Berlin Heidelberg, 2011. Chap. 20. Design criteria for medical accelerators, 325–343. DOI: https://doi.org/10.1007/978-3-642-21414-1_20.

[198] R. Mohan and D. Grosshans. Proton therapy–present and future, *Advanced drug delivery reviews*; 109 (2017), 26–44. DOI: https://doi.org/10.1016/j.addr.2016.11.006.

[199] T. Haberer, W. Becher, D. Schardt, and G. Kraft. Magnetic scanning system for heavy ion therapy, *Nuclear Instruments and Methods in Physics Research Section A: Accelerators, Spectrometers, Detectors and Associated Equipment*; 330-1-2 (1993), 296–305. DOI: https://doi.org/10.1016/0168-9002(93)91335-K.

[200] U. Linz, *Ion Beam Therapy: Fundamentals, Technology, Clinical Applications*. Berlin, Germany: Springer-Verlag Berlin Heidelberg, 2011. Chap. 4. Physical and biological rationale for using ions in therapy, 45–59. DOI: https://doi.org/10.1007/978-3-642-21414-1_4.

[201] J. J. Wilkens and U. Oelfke. Direct comparison of biologically optimized spread-out Bragg peaks for protons and carbon ions, *International Journal of Radiation Oncology* Biology* Physics*; 70-1 (2008), 262–266. DOI: https://doi.org/10.1016/j.ijrobp.2007.08.029.

[202] W. T. Chu, B. A. Ludewigt, and T. R. Renner. Instrumentation for treatment of cancer using proton and light-ion beams, *Review of Scientific Instruments*; 64-8 (1993), 2055–2122. DOI: https://doi.org/10.1063/1.1143946.

[203] U. Weber and G. Kraft. Design and construction of a ripple filter for a smoothed depth dose distribution in conformal particle therapy, *Physics in Medicine & Biology*; 44-11 (1999), 2765. DOI: https://doi.org/10.1088/0031-9155/44/11/306.

[204] S. H. Benedict, J. Cai, B. Libby, M. Lovelock, D. Schlesinger, K. Sheng, and W. Yang. SRT and SBRT: Current practices for QA dosimetry and 3D, 250-1 (2010), 012057. DOI: https://doi.org/10.1088/1742-6596/250/1/012057.

[205] M. Miften, A. Olch, D. Mihailidis, J. Moran, T. Pawlicki, A. Molineu, H. Li, K. Wijesooriya, J. Shi, P. Xia, *et al.* Tolerance limits and methodologies for IMRT measurement-based verification QA: recommendations of AAPM Task Group No. 218, *Medical physics*; 45-4 (2018), e53–e83. DOI: https://doi.org/10.1002/mp.12810.

[206] O. L. Green, L. E. Henke, and G. D. Hugo. Practical clinical workflows for online and offline adaptive radiation therapy, *Seminars in radiation oncology*; 29-3 (2019), 219–227. DOI: https://doi.org/10.1016/j.semradonc.2019.02.004.

[207] F. De Martino, S. Clemente, C. Graeff, G. Palma, and L. Cella. Dose calculation algorithms for external radiation therapy: an overview for practitioners, *Applied sciences*; 11-15 (2021), 6806. DOI: https://doi.org/10.3390/app11156806.

[208] B. Fraass, K. Doppke, M. Hunt, G. Kutcher, G. Starkschall, R. Stern, and J. Van Dyke. The report of Task Group 53 of the AAPM: Quality assurance for clinical radiotherapy treatment planning, *Medical physics*; 25-10 (1998), 1773–1829. DOI: https://doi.org/10.3390/app11156806.

[209] International Atomic Energy Agency (IAEA). Commissioning of radiotherapy treatment planning systems: testing for typical external beam treatment techniques. IAEA-TECDOC Series No. 1583. Vienna, Austria: International Atomic Energy Agency, 2008.

[210] J. B. Smilowitz, I. J. Das, V. Feygelman, B. A. Fraass, S. F. Kry, I. R. Marshall, D. N. Mihailidis, Z. Ouhib, T. Ritter, M. G. Snyder, *et al.* AAPM medical physics practice guideline 5. a.: commissioning and QA of treatment planning dose calculations—megavoltage photon and electron beams, *Journal of applied clinical medical physics*; 16-5 (2015), 14–34. DOI: https://doi.org/10.1120/jacmp.v16i5.5768.

[211] J. B. Farr, M. F. Moyers, C. E. Allgower, M. Bues, W. C. Hsi, H. Jin, D. N. Mihailidis, H. M. Lu, W. D. Newhauser, N. Sahoo, *et al.* The report of Task Group 185 of the AAPM: Clinical commissioning of intensity-modulated proton therapy systems, *Medical physics*; 48-1 (2021), e1–e30. DOI: https://doi.org/10.1002/mp.14546.

[212] S. W. S. McKeever. Thermoluminescence of solids. Cambridge, England: Cambridge University Press, 1985. DOI: https://doi.org/10.1017/CBO9780511564994.

[213] E. G. Yukihara, S. W. S. McKeever, C. E. Andersen, A. J. J. Bos, I. K. Bailiff, E. M. Yoshimura, G. O. Sawakuchi, L. Bossin, and J. B. Christensen. Luminescence dosimetry, *Nature Reviews Methods Primers*; 2-1 (2022), 26. DOI: https://doi.org/10.1038/s43586-022-00102-0.

[214] S. F. Kry, P. Alvarez, J. E. Cygler, L. A. DeWerd, R. M. Howell, S. Meeks, J. O'Daniel, C. Reft, G. Sawakuchi, E. G. Yukihara, *et al.* AAPM TG 191: Clinical use of luminescent dosimeters: TLDs and OSLDs, *Medical physics*; 47-2 (2020), e19–e51. DOI: https://doi.org/10.1002/mp.13839.

[215] E. G. Yukihara and S. W. S. McKeever. Optically stimulated luminescence: fundamentals and applications. Hoboken NJ, USA: John Wiley & Sons, 2011. DOI: https://doi.org/10.1002/9780470977064.

[216] G. Okada, T. Yanagida, H. Nanto, and S. Kasap, *Phosphors for Radiation Detectors*. Hoboken NJ, USA: Wiley Online Library, 2022. Chap. 9. Radiophotoluminescence (RPL), 247–281. DOI: https://doi.org/10.1002/9781119583363.ch9.

[217] M. Niklas, J. A. Bartz, M. S. Akselrod, A. Abollahi, O. Jäkel, and S. Greilich. Ion track reconstruction in 3D using alumina-based fluorescent nuclear track detectors, *Physics in Medicine & Biology*; 58-18 (2013), N251. DOI: https://doi.org/10.1088/0031-9155/58/18/N251.

[218] J. J. M. Kouwenberg, L. Ulrich, O. Jäkel, and S. Greilich. A 3D feature point tracking method for ion radiation, *Physics in Medicine & Biology*; 61-11 (2016), 4088.

[219] I. D. Muñoz, D. García-Calderón, R. Félix-Bautista, L. N. Burigo, A. Runz, S. Brons, S. Greilich, J. Seco, and O. Jäkel. Linear energy transfer measurements and estimation of relative biological effectiveness in proton and helium-ion beams using fluorescent nuclear track detectors, *International Journal of Radiation Oncology* Biology* Physics*; In Press (2024). DOI: https://doi.org/10.1016/j.ijrobp.2024.02.047.

[220] P. Bilski, B. Marczewska, W. Gieszczyk, M. Kłosowski, T. Nowak, and M. Naruszewicz. Lithium fluoride crystals as fluorescent nuclear track detectors, *Radiation Protection Dosimetry*; 178-3 (2018), 337–340. DOI: https://doi.org/10.1093/rpd/ncx116.

[221] S. Kodaira, T. Kusumoto, H. Kitamura, Y. Yanagida, and Y. Koguchi. Characteristics of fluorescent nuclear track detection with Ag^{+}-activated phosphate glass, *Radiation Measurements*; 132 (2020), 106252. DOI: https://doi.org/10.1016/j.radmeas.2020.106252.

[222] I. D. Muñoz, L. N. Burigo, T. Gehrke, S. Brons, S. Greilich, and O. Jäkel. Sensitivity correction of fluorescent nuclear track detectors using alpha particles: Determining LET spectra of light ions with enhanced accuracy, *Medical Physics*; 50-4 (2023), 2385–2401. DOI: http://dx.doi.org/10.1002/mp.16083.

[223] G. M. Akselrod, M. S. Akselrod, E. R. Benton, and N. Yasuda. A novel Al_2O_3 fluorescent nuclear track detector for heavy charged particles and neutrons, *Nuclear Instruments and methods in physics Research section B: beam interactions with materials and atoms*; 247-2 (2006), 295–306. DOI: https://doi.org/10.1016/j.nimb.2006.01.056.

[224] E. G. Yukihara, R. Gaza, S. W. S. McKeever, and C. G. Soares. Optically stimulated luminescence and thermoluminescence efficiencies for high-energy heavy charged particle irradiation in Al_2O_3:C, *Radiation measurements*; 38-1 (2004), 59–70. DOI: https://doi.org/10.1016/S1350-4487(03)00251-8.

[225] E. G. Yukihara, J. B. Christensen, and M. Togno. Demonstration of an optically stimulated luminescence (OSL) material with reduced quenching for proton therapy dosimetry: MgB_4O_7:Ce,Li, *Radiation Measurements*; 152 (2022), 106721. DOI: https://doi.org/10.1016/j.radmeas.2022.106721.

[226] M. Bobić, J. B. Christensen, H. Lee, E. Choulilitsa, K. Czerska, M. Togno, S. Safai, E. G. Yukihara, B. A. Winey, A. J. Lomax, *et al.* Optically stimulated luminescence dosimeters for simultaneous measurement of point dose and dose-weighted LET in an adaptive proton therapy workflow, *Frontiers in Oncology*; 13 (2024), 1333039. DOI: https://doi.org/10.3389/fonc.2023.1333039.

[227] F. Kalholm, L. Grzanka, I. Toma-Dasu, and N. Bassler. Modeling RBE with other quantities than LET significantly improves prediction of in vitro cell survival for proton therapy, *Medical Physics*; 50-1 (2023), 651–659. DOI: https://doi.org/10.1002/mp.16029.

[228] A. Lühr, C. von Neubeck, S. Helmbrecht, M. Baumann, W. Enghardt, and M. Krause. Modeling in vivo relative biological effectiveness in particle therapy for clinically relevant endpoints, *Acta Oncologica*; 56-11 (2017), 1392–1398. DOI: https://doi.org/10.1080/0284186X.2017.1356468.

[229] E. G. Yukihara and S. W. S. McKeever. Spectroscopy and optically stimulated luminescence of Al_2O_3:C using time-resolved measurements, *Journal of applied physics*; 100-8 (2006). DOI: https://doi.org/10.1063/1.2357344.

[230] N. Shrestha, E. G. Yukihara, D. Cusumano, and L. Placidi. Al_2O_3:C and Al_2O_3:C,Mg optically stimulated luminescence 2D dosimetry applied to magnetic resonance guided radiotherapy, *Radiation Measurements*; 138 (2020), 106439. DOI: https://doi.org/10.1016/j.radmeas.2020.106439.

[231] G. Denis, M. G. Rodriguez, M. S. Akselrod, T. H. Underwood, and E. G. Yukihara. Time-resolved measurements of optically stimulated luminescence of Al_2O_3:C and Al_2O_3:C,Mg, *Radiation measurements*; 46-12 (2011), 1457–1461. DOI: https://doi.org/10.1016/j.radmeas.2011.06.054.

[232] A. Muneem, J. Yoshida, H. Ekawa, M. Hino, K. Hirota, G. Ichikawa, A. Kasagi, M. Kitaguchi, S. Kodaira, K. Mishima, *et al.* Study on the reusability of fluorescent nuclear track detectors using optical bleaching, *Radiation Measurements*; 158 (2022), 106863. DOI: https://doi.org/10.1016/j.radmeas.2022.106863.

[233] G. O. Sawakuchi, E. G. Yukihara, S. W. S. McKeever, and E. R. Benton. Overlap of heavy charged particle tracks and the change in shape of optically stimulated luminescence curves of Al_2O_3:C dosimeters, *Radiation measurements*; 43-2-6 (2008), 194–198. DOI: https://doi.org/10.1016/j.radmeas.2007.11.030.

[234] C. Grassberger and H. Paganetti. Elevated LET components in clinical proton beams, *Physics in Medicine & Biology*; 56-20 (2011), 6677. DOI: https://doi.org/10.1088/0031-9155/56/20/011.

[235] E. V. Bellinzona, L. Grzanka, A. Attili, F. Tommasino, T. Friedrich, M. Krämer, M. Scholz, G. Battistoni, A. Embriaco, D. Chiappara, *et al.* Biological impact of target fragments on proton treatment plans: An analysis based on the current cross-section data and a full mixed field approach, *Cancers*; 13-19 (2021), 4768. DOI: https://doi.org/10.3390/cancers13194768.

[236] J. Ödén, K. Eriksson, and I. Toma-Dasu. Incorporation of relative biological effectiveness uncertainties into proton plan robustness evaluation, *Acta oncologica*; 56-6 (2017), 769–778. DOI: https://doi.org/10.1080/0284186X.2017.1290825.

[237] D. Sánchez-Parcerisa, M. López-Aguirre, A. Dolcet Llerena, and J. M. Udías. MultiRBE: Treatment planning for protons with selective radiobiological effectiveness, *Medical physics*; 46-9 (2019), 4276–4284. DOI: https://doi.org/10.1002/mp.13718.

[238] L. Polster, J. Schuemann, I. Rinaldi, L. Burigo, A. L. McNamara, R. D. Stewart, A. Attili, D. J. Carlson, T. Sato, J. R. Méndez, *et al.* Extension of TOPAS for the simulation of proton radiation effects considering molecular and cellular endpoints, *Physics in Medicine & Biology*; 60-13 (2015), 5053. DOI: https://doi.org/10.1088/0031-9155/60/13/5053.

[239] A. Bertolet, M. A. Cortés-Giraldo, and A. Carabe-Fernandez. Implementation of the microdosimetric kinetic model using analytical microdosimetry in a treatment planning system for proton therapy, *Physica Medica*; 81 (2021), 69–76. DOI: https://doi.org/10.1016/j.ejmp.2020.11.024.

[240] A. Mairani, S. Brons, F. Cerutti, A. Fassó, A. Ferrari, M. Krämer, K. Parodi, M. Scholz, and F. Sommerer. The FLUKA Monte Carlo code coupled with the local effect model for biological calculations in carbon ion therapy, *Physics in Medicine & Biology*; 55-15 (2010), 4273. DOI: https://doi.org/10.1088/0031-9155/55/15/006.

[241] H. Paganetti. Nuclear interactions in proton therapy: dose and relative biological effect distributions originating from primary and secondary particles, *Physics in Medicine & Biology*; 47-5 (2002), 747. DOI: https://doi.org/10.1088/0031-9155/47/5/305.

Acknowledgements

Professional

I would like to express my most sincere gratitude to **Prof. Dr. Oliver Jäkel**, head of the division of Medical Physics in Radiation Oncology at the German Cancer Research Center (DKFZ; Heidelberg, Germany), for giving me the oportunity to carry out my doctoral research project at his group, for accepting being my supervisor and part of my Thesis Advisory Committe (TAC).

I would like to thank **Prof. Dr. Joao Seco**, head of the division of Biomedical Physics in Radiation Oncology at DKFZ, **Dr. Steffen Greilich** from Berthold Technologies GmbH & Co. KG (Bad Wildbad, Germany) and **Dr. Lucas N. Burigo** from the division of Medical Physics in Radiation Oncology at DKFZ for accepting being part of my TAC and their valuable feedback and guidance during the TAC meetings.

I extend my deep gratitude to **Dr. Eduardo G. Yukihara** (head) and **Dr. Jeppe Brage Christensen** from the Radiation Metrology Section and Dosimetry Group at the Paul Scherrer Institute (PSI; Villigen, Switzerland) for their advice and extremely fruitful collaborations, always characterized by an outstanding sense of collegial teamwork.

I would like to thank **Dr. Felix Bestvater** (head) and **Manuela Brom** from the Light Microscopy Core Facility at DKFZ, for their unwavering support, providing of excellent working conditions at the microscopes, and willingness to answer my numerous inquiries.

I want to express my gratitude to the **staff of the Heidelberg Ion Beam Therapy Center** (HIT; Heidelberg, Germany) for granting all the beam time required to develop this thesis and providing the conditions to perform the experiments. Especially, I would like to thank **Dr. Stephan Brons** for all his help and support for the experiments and taking care that everything that was required to be in place or at hand.

I would like to thank **Dr. Peter Häring**, **Mona Lifferth** and **Clemens Lang**, all from the division of Medical Physics in Radiation Oncology at DKFZ, for their support with the experiments at the ETHOS. Also, I express my gratitude to **Armin Runz**, for designing and printing all the holders and parts used during the experiments.

I would like to thank **Dr. Tim Gehrke** and **Dr. Renato Félix-Bautista**, both from the division of Medical Physics in Radiation Oncology at DKFZ, for their support during the experiments at HIT. Also, I would like to thank **Daniel García-Calderón** from the division of Biomedical Physics in Radiation Oncology at DKFZ for his support during the irradiations at HIT and DKFZ, and all his hard and careful work with the cell experiments.

I would like to express my gratitude to **Dr. Liliana Stolarczyk**, **Dr. Anne Vestergaard**, and **Dr. Niels Bassler** from the Danish Center for Particle Therapy (DCPT; Aarhus, Denmark) for organizing and facilitating the LET measuring campaign and, of course, for their generous invitation to participate in it. Furthermore, I extend my thanks to them for their invaluable support during the preparation of the manuscript reporting the initial results.

I would like to express my sincere appreciation to the **German Academic Exchange Service** (DAAD; Bonn, Germany) for their exceptional financial support during my doctoral project through the "Research Grants – Doctoral Programmes in Germany" program (program number: 57440921). Particularly, I want to extend my thanks to the **staff of Unit ST31** –

Latin America for their assistance and support over the years, as well as the DAAD offices at Mexico (Mexico City, Mexico).

Personal

I would like to express my deep gratitude to **Oliver** for his invaluable guidance and mentoring. Above all, I appreciate his unwavering commitment to make time for me as my advisor, without fail, despite his busy schedule. Furthermore, I am grateful for his trust in my ability to independently pursue my project. Lastly, I am thankful for his skillful balancing act between providing me with the freedom to work autonomously and offering his supervision when needed.

I would like to thank **Eduardo** for consistently being open to providing his – always very accurate – advice, for reading my drafts, and, above all, for fostering the highly fruitful collaborations I maintained with his group.

I want to extend my gratitude to **Jeppe** for his invaluable assistance throughout this journey. It is truly difficult to overstate his impact on shaping my project – it was a real game changer. I am also thankful for the valuable skills I have gained through our collaboration. And lastly, I appreciate all the enjoyable experiments we conducted together (though perhaps not the candies!).

I would like to express my gratitude to my 'foster group' at the very beginning of my project: **Tim**, **Renato**, and **Laura**. They provided invaluable help and guidance during the initial stages. In particular, I want to extend my thanks to **Tim** for our insightful and stimulating discussions about LET when we were desk neighbors, for his selfless assistance during my first experiments at HIT, and for the bottle of champagne in Frankfurt. Similarly, I would like to thank **Renato** for bringing such a positive atmosphere to the seemingly endless experiments at HIT, for all the enjoyable coffee breaks we shared together, and for his friendship.

I would like to express my gratitude to **Lucas** for welcoming me into his group and for his invaluable guidance during our meetings, which significantly pushed my project forward in a positive direction. Additionally, I am grateful for his outstanding efforts to understand everything, even the most intricate aspects of my project. For introducing me to TOPAS and sharing his enthusiasm for Monte Carlo simulations, teaching me so many valuable techniques.

I would like to thank **Pamela**, **Antoni**, **Tim**, and **Renato** for their support and presence at one of the most important events of my life. Quite literally, without you it simply would not have been possible.

I would like to thank my *amigos* **Daniel**, **Nina**, and **Luis** for their sincere friendship and the wonderful times we shared, where we could forget about everything else. Individually, I want to thank **Daniel** for being the glue that held our group together, **Nina** for her patience in dealing with our messiness, and **Luis** for his positive and mellow presence.

I would like to express my deep gratitude to **my family** for their unwavering support at the distance. Particularly, I would like to thank my **mom (Consue)** and **brother (Poncho)** for their encouragement, blind trust and the countless sacrifices they made to enable me to pursue my PhD. Additionally, I extend my thanks to **Toño** and **Paquita** for their encouragement, assistance, and for welcoming me into their family.

I reserved the last sentences to express my heartfelt gratitude to **Lety (my wife and life partner)**. For everything she has provided – unwavering support, patience, inspiration, companionship, and love – no amount of written space and ink would be sufficient to express all my gratitude and love towards her.